XEROGEL-BASED Cu ELECTRODE INKJET PRINTED ON PLASTIC SUBSTRATE

SHUAICHEN WANG

PhD

The Hong Kong Polytechnic University

2022

The Hong Kong Polytechnic University

Institute of Textiles and Clothing

Xerogel-based Cu Electrode Inkjet Printed on Plastic Substrate

Shuaichen Wang

A Thesis Submitted in Partial Fulfillment of the
Requirements for the Degree of Doctor of Philosophy

Aug 2021

CERTIFICATE OF ORIGINALITY

I hereby declare that this thesis is my own work and that, to the best of my knowledge and belief, it reproduces no material previously published or written, nor material that has been accepted for the award of any other degree or diploma, except where due acknowledgement has been made in the text.

_____________________________ (Signed)

Shuaichen Wang (Name of Student)

ABSTRACT

Inkjet-printed Cu electrodes can replace noble metals (e.g., Au or Ag) to fabricate high-quality flexible electronic devices. However, the inkjet-printed Cu electrodes prepared by nanoparticle ink still need a sintering process (e.g., intense light irradiation) with high energy consumption. Moreover, these kinds of sintering processes still exert instant high-temperature on the surface of the substrate, damages the flexible substrate (e.g., polyethylene (PE) and polyethylene terephthalate (PET)), the stretchable substrates, and the biological substrates. On the contrary, polymer-assisted metal deposition (PAMD) is a room-temperature metal deposition method that enables low-cost Cu electrodes to grow on plastic substrates. Nevertheless, these inkjet-printed Cu electrodes usually have a rough surface uniformity and are difficult to be used as the bottom electrodes for the fabrication of thin-film electronic devices. And the current inkjet-printing ink and appropriate treatments for the PAMD technique cannot deal with the coffee-ring effect and irregularly growing Cu.

First, we found that the mesoporous xerogel, generated from the EtOH treatment, could improve the quality of the inkjet-printed Cu electrode's smoothness, surface morphology, and graphics retention. The EtOH treatment removed the pore liquid of the gel and the copolymer cluster that did not well-bond to the overall copolymer network. The gel thin film shrunk to around half of its original thickness for converting to mesoporous xerogel after the EtOH treatment. The initial unevenness of the surface morphology of the inkjet-printed gel pattern can be reduced to half of its original after this conversion. In addition, the xerogel thin film also reduced the occurrence probability of irregular Cu that grew on the peripheral of the inkjet-printed patterns. Then, we also found 4-extra-treatments to smooth further the deposition uniformity of the inkjet-printed xerogel-based Cu electrode. This is the first report in history to show an inkjet-printed Cu electrode has a smooth surface morphology. We also found that the high-quality xerogel-based Cu electrode had a strong adhesiveness to the plastic substrate. As a proof-of-concept, we carried out a TEM cross-sectional test to demonstrate the interpenetration network of the xerogel-based Cu electrode and the Cu nanoparticles. Compared with the original gel-based Cu electrode, the xerogel-based Cu electrode had a relatively stronger polymer cluster that may help it firmly attach to the plastic substrate without the broken of the polymer cluster. The adhesive energy of the

xerogel-based Cu electrode to the plastic substrate (PET) is 0.7 J/m^2, which is much higher than the thermal evaporated Cr adhesively layer for thermally evaporated Cu electrode (0.06 J/m^2).

Second, we used the three-solvent copolymer system as a sample to prove a new concept that a thin sheet of liquid, difficult to evaporate, can help to level the join of the inkjet-printed patterns. Besides the primary solvent, two special cosolvents were added. One cosolvent modulates the copolymer ink's viscosity, while another cosolvent, with a slow-evaporation rate, generates the thin sheet of liquid that is difficult to evaporate. As a proof of concept, we observed the drying process of the liquid sheet and the morphology of the final deposited film by an optical microscope. And the thin sheet of liquid formed a smooth joint of two inkjet-printed patterns. In addition, we found that when we inkjet-printed the patterns in a specific sequence, a well-controlled boundary will appear. Initially, only the line-shaped pattern (formed by a row of droplets with similar spacing) can create an almost perfectly border by verifying the droplet spacing. The inkjet-printed 2D pattern usually has an uncontrollable boundary due to the complex drying process of the inkjet-printed droplets. Furthermore, two of these well-controlled boundaries can form a uniform channel structure with a channel length of 15 μm without the help of any evaporation or etching techniques.

Finally, we prepared multi-layer devices, including organic thin-film transistors (OTFTs) and organic electrochemical transistors (OECTs), by only solution methods. The functional layers of the thin film devices can be directly inkjet-printed or be spin-coated on the top of the inkjet-printed Cu electrode without short current between layers benefit from the smooth surface morphology of the Cu electrode.

We also printed this kind of xerogel-based Cu electrodes onto commonly used plastic shopping bags without damaging the hate-sensitive plastic bag. This metal deposition method, powered by pure chemical energy, may replace many traditional methods in the industry of printed electronics and bring hope to human beings in the age of global warming.

LIST OF PUBLICATIONS

Qiuna Zhuang, Zhijun Ma, Yuan Gao, Yaokang Zhang, Shuaichen Wang, Xi Lu, Hong Hu, Chifai Cheung, Qiyao Huang,* and Zijian Zheng* Liquid-metal-superlyophilic and Conductivity-strain-enhancing Scaffold for Permeable Superelastic Conductors

Paper in preparation

Shuaichen Wang, Anneng Yang, Xuyun Guo, Xing Ju, Xiao Xiang, Yaokang Zhang, Lina Chen, Hong Hu, Dongdong Chen, Peng Li, Qiuna Zhuang, Yuan Gao*, Ye Zhu,* Feng Yan,* and Zijian Zheng*, Inkjet-printed Xerogel Scaffolds enabled Room-temperature Fabrication of High-quality Copper Electrodes for Flexible Electronics

Conference Participation

1. Shuaichen Wang, poster presentation, *IDTechEx Printing Electronics EUROP,* **International meeting connecting emerging technologies with global brands**, April 10 – 11, 2019, Estrel Conversation Center, Berlin, Germany.

2. Shuaichen Wang, poster presentation, **Collaborative Research Fund Symposium,** Dec 7, 2017, the Hong Kong University of Science and Technology, Clear Water Bay, Hong Kong, China.

3. Shuaichen Wang, participation, *Flexible and Wearable Devices*, **Small sciences symposium**, May 14–17, 2017, the Polytechnic University of Hong Kong, Hung Hom, Hong Kong, China.

ACKNOWLEDGEMENTS

I would like to express my sincerest thanks to my supervisor Prof. Zijian Zheng and co-supervisor, Prof. Feng Yan, for their guidance and insightful enlightenment. Their comprehensive knowledge of science and rigorous attitude to scientific research has always been motivating me. My study period became a valuable time of my life, during which I learnt the correct writing methods and expression ways in academic areas. And enriched my knowledge and broadened my horizons in the scientific world. And I knew the appropriate way to experiment, overcoming difficulties, and the ability of data analysis.

I've also been grateful to all members of Prof. Zheng's research group during these three years: Dr Yiyi She, Dr Liyong Niu, Dr Lina Chen, Dr Xiang Xiao, Dr Yang Yu, Dr Jian Chang, Dr Guoqiang Liu, Dr Ting Xiao, Dr Dongrui Wang, Dr Dongdong Chen, Dr Zhongwei Wu, Dr Lei Yao, Dr Qi Gan, Dr Zhijun Ma, Dr Chaojian Chen, Dr Kate Yip, Ms Casey Yan, Dr Xiang Xiao, Dr Younseon Wang, Dr Shijin Zhu, Dr Yuqi Zhang, Dr Yuan Gao, Dr Wenshuo Wang, Dr Dongdong Li, Dr Hong Hu, Dr Lei Wang, Dr Sze Wing Ng, Dr Yujing Zhu, Dr Qiyao Huang, Dr Peng Li, Dr Xi Lu, Mr Shang Jian, and Mr Chuan Xie. Ms. Qianyi Guo, Ms. Mingming Rong, Ms. Huixin Wang, Ms. Qiuna Zhuang. They are my reliable partners in my research life. In the meantime, I would like to thank the facilitation of Prof. Feng Yan and Dr Zhu Ye in the Department of Applied Physics of the Polytechnic University of Hong Kong. And Dr Shengdong Zhang in the School of Electronics and Computer Engineering, Shenzhen Graduate School, Peking University, for testing help. And Dr Anneng Yang and Dr Xuyun Guo in the department of Applied Physics of the Polytechnic University of Hong Kong for their technical assistance.

I also gratefully acknowledge the financial support from the GRF of Hong Kong (PolyU 5036/13P) and GRF of Hong Kong (grant number C5015-15G).

TABLE OF CONTENTS

LIST OF FIGURES

LIST OF TABLES

LIST OF ABBREVIATIONS

AFM	Atomic force microscope
ABS	Acrylonitrile butadiene styrene
APTES	Aminopropyl triethoxysilane
BFTEM	Bright field transmission electron microscope
CNT	Carbon nanotubes
DW	Microdissection direct-write
DNA	Deoxyribonucleic acid
DFTEM	Darkfield transmission electron microscope
EELS	Electron energy loss spectroscopy
EDS	Energy-dispersive X-ray spectroscopy
EG	Ethylene glycol
ELD	Electroless deposition
FIB	Focused Ion beam
FOTS	(Tridecafluoro-1,1,2,2-tetrahydrooctyl) trichlorosilane
FHSS	Frequency-Hopping Spread Spectrum
P(g2T-TT)	Poly(2-(3,3′-bis(2-(2-(2methoxyethoxy)ethoxy)ethoxy)-[2,2′-bithiophen]-5-yl)thieno[3,2-b]thiophene)
HAADF	High-angle annular dark-field
HAADF -STEM	High-angle annular dark-field scanning transmission electron microscope
ITO	Indium tin oxide
IDTBT	Indacenodithiopheneco- benzothiadiazole
LIFT	Laser-induced forward transfer
MAPLE	Matrix-assisted pulsed laser capture microdissection
METAC	[2- (methacryloyloxy) ethyl] trimethyl ammonium chloride
NMNPs	Noble metal nanoparticles
OECT	Organic electrochemical transistors
OTFT	Organic thin-film transistor
PA	Poyamide
PLD	Pulsed laser deposition
PI	Polyimide

PET	Poly(ethylene terephthalate)
PEG	Poly(ethylene glycol)
PEDOT:PSS	Poly(3,4-ethylenedioxythiophene):polystyrene Sulfonate
PDMS	Polydimethylsiloxane
PAMD	Polymer-assisted metal deposition
RH	Relative humidity
RFID	Radiofrequency identification
R2R	Roll-to-roll
RR-P3HT	Regioregular poly(3-hexylthiophene)
SEM	Scanning electron microscope
SI-ATRP	Surface-initiated atom transfer radical polymerization
SHF	Super high frequency
STEM	Scanning transmission electron microscope
SAM	Self-assembled monolayer
TENG	Triboelectric nanogenerator
TMCS	Trimethylchlorosilane
XRD	X-ray diffraction
XPS	X-ray photoelectron spectroscopy

CHAPTER 1. INTRODUCTION

1.1 Background and Challenge

The printing technology characterized by energy-saving and material-saving has developed rapidly in recent decades and has attracted many scientists' attention.[1] However, traditional fabrication methods for electrodes have disadvantages, such as energy waste and material waste. Because these techniques, including chemical vapor deposition (CVD)[2] or physical vapor deposition (PVD),[3] usually evaporate the metal at extremely high temperatures in an absolute vacuum environment. In addition, the traditional patterning methods are polluting and wasteful because they rely on strong acids (e.g., sulfuric acid) to remove the unnecessary part of the electrode.

On the contrary, inkjet printing is a digitally controlled printing technique, can "direct write" micron-scale electrodes by solution ways on various substrates in ambient conditions.[4]

However, the inkjet-printable nonmetallic materials, such as carbon-based materials (carbon nanotubes (CNT)[5] and graphene[6]) and conductive polymers[7], have low conductivity. Therefore, the most popular way is to inkjet-print and sinter the ink formed by dispersed noble metal nanoparticles. Highly conductive electrodes were fabricated benefit from Noble metal's inherent chemical stability and excellent conductivity.[7e] However, the inkjet-printed metal nanoparticle ink has to be sintered at least 150^{o}C, reported by Zou et al.[8] and Hu et al.,[9] to form a highly uniform electrode that can attach[10] to the plastic substrate. Some organic additives in ink provide the adhesiveness of the metal electrode to the substrate.[11] However, the adding of the organic additive will sacrifice the electrical conductivity of the metal electrode.

In addition, the 150^{o}C sintering process can lead to the deformation of low-cost plastic substrates (e.g., PE and PET), stretchable substrates, and biological substrates. The printed noble metal nanoparticles can only join together after a high-temperature sintering process (> 150 °C). This operation step will increase the limitations of the choice of flexible substrates, including polyethylene, polyamide, polyvinyl alcohol, acrylonitrile butadiene styrene, polyethylene terephthalate, etc. In addition, the utilization of Ag and Au significantly increased the production cost that prevented this technique from being widely used., Therefore, the preparation of the inkjet-printing ink by Cu, a low-cost and high conductive metal, has received significant attention from scientists to reduce the production cost of the printed electronics. However, these non-Noble metals (e.g., Cu and Ni) are prone to form un-conductive oxides[12] during nanoparticle deposition and the high-temperature sintering process. Scientists invented unique sintering processes, such as quick laser[13], intense pulsed light[14], flashlight [15], and sintering Cu under the production of oxalic acid[12], aiming to prevent the oxidation of Cu nanoparticles. However, most of these techniques still rely on an energy-intensive step, with instantaneously increased surface temperature.[14, 16] Such electrodes can also form cracks or even getting off during bending due to the limited adhesiveness provided by organic additives.[17] Besides, the inkjet-printed Cu electrodes usually have a rough surface due to the utilization of larger-sized Cu particles (difficult to be oxidized). In the coffee-ring effect, the inkjet-printed Cu electrode usually has an extremely rough surface morphology. Furthermore, nanoparticle ink technology also has the problems of electrode melting at high temperatures [12] and short-term storage of the ink.[17c]

Polymer assisted metal deposition (PAMD) techniques is a full-solution strategy that can achieve accurate room-temperature preparation of non-Noble-metal (e.g., Cu and Ni) electrodes of various substrates. In PAMD techniques, the Cu electrode can grow on a polymer buffer layer in the electroless deposition solution at room temperature.[18] However, three problems appear on the PAMD-based Cu electrodes. First, there is still a lack of efficient inkjet-printing ink to eliminate the coffee-ring effect. Second, there are randomly appeared extra-Cu deposition in the places without the copolymer thin film patterned by inkjet-printer. Finally, there are irregular holes, and pinholes appear on the surface of Cu electrodes. Therefore, such Cu electrodes are challenging to achieve downscaling and fabrication of multilayer devices by solution methods, since it is easy to cause short current between layers.[19] To tackle these issues, we firstly invented a three-solvent cosolvent system to suppress the coffee-ring effect. Then, we designed a vital solution replacement step to convert the crosslinked gel thin film to a xerogel. The uniform xerogel matrix with a 3D structure can fabricate Cu electrodes with smooth surface morphology and high adhesiveness to the plastic substrate. We also developed 4-extra-treatments to eliminate the coffee-ring stain, irregularly grown Cu particles, holes, and pinholes on the surface of Cu electrodes. Three-solvent copolymer ink using slow-evaporation-rate cosolvent ethylene glycol (EG) can optimize the surface uniformity of the inkjet-printed patterns by generating the Marangoni flow that can compensate the capillary flow (the cause of the coffee ring stain).[20] This precaution significantly reduced the appearance rate of the diffusion of the pattern. This solvent replacement step removed the redundant cosolvents and un-fixed P[MBP-co-METAC] groups entrapped in the gel matrix to form a well-crosslinked copolymer network with a larger porous size. It is allowing Cu nanoparticles to grow inside, forming an interpenetrating network of Cu and polymer matrix. In addition, nano-indentation and nano-scratching tests investigated the plastic substrate's mechanical strength and adhesiveness to a plastic substrate. The xerogel-based Cu electrodes show high adhesiveness to the plastic substrate compared to the Cu electrodes prepared by vapor deposition or other PAMD techniques. Then, the TEM, for the first time, demonstrated the cross-sectional structures of PAMD-based Cu electrodes by explaining the principle of the structural advantage of xerogel-based Cu thin film. As this inkjet-printed electrode has a uniform surface topography, the materials of interest can be spin-coated on the surface of the printed electrodes. This technique can directly inkjet-print high-quality electrodes with smooth surface morphology to fabricate multilayer electronic devices, such as an organic thin-film transistor (OTFTs) and organic electrochemical transistors (OECTs). This uniform Cu electrode enables the preparation of electronic devices by solution ways, greatly reducing the production cost and equipment requirements.

In addition, this sticky Cu electrode inkjet-printed on the plastic substrate possess an electrical conductivity of 1.2 ± 0.05 × 10^7 S/m in the upper, pure metal layer. The conductivity only decreased to around 1.18 of this original resistivity after 10000 cycles of bending at the bending radius of 1 mm. The Cu electrode has the adhesiveness of 0.7 J/m^2 to the plastic substrate and can pass a scotch tape test with ease. Furthermore, this Cu electrode was directly inkjet printed onto plastic shopping bags benefit from the possibility of room-temperature preparation of the Cu electrode. This inkjet-printable Cu electrode is suitable for large-volume industrial production with less production cost and small energy consumption. We propose inkjet printing of xerogel-based Cu electrode powered by only chemical energy (redox reaction). This technique can be applied to many applications, including smart packaging, wearable electronics, flexible RFID antennas, sensing, biocompatible sensing, etc.

1.2 Research Objectives

This study focused on developing methods to enable inkjet printing of high-quality Cu electrodes with smooth surface morphology and uniform boundary.

The research objectives are defined as follows:

1. To develop stable copolymer inks with good inkjet printability.
2. To suppress coffee-ring effect by solvent exchange and addition of co-solvents.
3. To study the surface morphology and microstructure of inkjet-printed copolymer thin films.
4. To demonstrate the remarkable electronic properties and mechanical properties of the inkjet-printed metal thin films on various substrates.
6. To fabricate thin-film devices, such as OECTs and OTFTs, with the inkjet-printed high-quality Cu electrode to replace the previously commonly used Au or Pt thin-film electrodes.

1.3 Research Originality

For the first time, this study reports the inkjet-printed Cu electrodes with a high surface uniformity applicable for a wide range of electronic devices.

First, we developed the appropriate inkjet-printing ink for the PAMD technique to fulfil the requirement of good inkjet printability, accuracy, and stability. This inkjet printing ink also achieved coffee-ring free inkjet printing of copolymer thin films on plastic substrates.

Second, we carefully investigated the mechanism of diffusion of patterns and an irregular pinhole that frequently appeared on the inkjet-printed Cu electrodes during the metal electroless deposition process. And we proposed four effective strategies to tackle these problems.

Third, we investigated the cross-sectional nanostructure of the PAMD-based Cu electrodes by TEM. This study verified the interpenetrating network of Cu and copolymer in the Cu electrodes prepared by PAMD-techniques.

Fourth, we tested the mechanical strength of the PAMD-based Cu electrode by nanoindentation and nano-scratching analyzer for the first time. And demonstrated the excellent performance of the adhesiveness of the PAMD-based Cu electrode, especially for the newly invented xerogel-based based Cu electrodes, incorporated with the Cu electrodes prepared by the traditional thermal evaporation techniques.

Finally, we realized the application of the inkjet-printed xerogel-based electrodes for many aspects. First, we achieved all-solution fabrication of electronic devices using inkjet-printed xerogel-based Cu electrodes without the help of any evaporation or etching techniques. Second, we achieved inkjet printing of xerogel-based Cu electrode on a low-cost shopping plastic bag. Third, we inkjet-printed functional RFID antenna using the PAMD-based Cu electrodes. Due to the smoothness and flatness of the xerogel-based Cu electrode, it can form the bottom electrodes of thin-film devices with triode structures. The upper film layer can be prepared by simple solutional methods, e.g., spin coating or drop-casting.

1.4 Outline of the Thesis

This thesis described follows content:

Chapter 1 introduces the background of inkjet printing of metal electrodes. Then it states the research gap, the objectives as well as the value of this study.

Chapter 2 gives a brief introduction to the structures, properties, and electronic applications of OECTs. After that, it comprehensively reviews the inkjet-printed electronics, nanoparticle inkjet-printing inks, polymer-assisted metal deposition (PAMD), gel structure of inkjet-printed patterns, and the suppression and utilization of the coffee-ring effect.

Chapter 3 elaborates the research methodology, including materials, fabrication, apparatus, and characterization techniques.

Chapter 4 demonstrates the newly invented xerogel-based Cu electrode and its advantages in structural mechanics. This low-cost operations method prepared highly flat and high-quality electrodes.

Chapter 5, the strategies in uniformly inkjet printing of high-quality electrode and the role of the liquid sheet of low evaporation cosolvent played in the droplet merging process and its possible future applications.

Chapter 6, using this high-quality electrode, OECTs and OTFTs can be made by simple solutional methods. And we demonstrated many meaningful attempts, such as inkjet-printed PAMD-based Cu electrodes on thin latex film, plastic bags. Finally, the inkjet-printed Cu electrode formed functional devices such as inkjet-printed RFID tape, the triboelectric generator.

Lastly, Chapter 7 lists the results, conclusions, and perspectives to the future.

CHAPTER 2. LITERATURE REVIEW

2.1 Chemical and Biological Sensors Based on the Structure of Thin-film Transistors

A chemical sensor can analyze valuable signals of the system by converting its chemical information, e.g., concentration, to digital signals. Biosensors are analytical instruments based on physicochemical measurements to detect biological and protein moieties. They apply to different areas, including environmental monitoring, medical analysis, medical products, agricultural productions, and safety food safety testing.

This chapter reviews two types of organic thin-film transistors (OTFTs) for chemical sensing systems. They are organic field-effect transistors (OFETs) and organic electrochemical transistors (OECTs).[21]

2.1.1 Working Principle of OFETs

OTFTs have developed into different applications in the biological and medical areas. The basic structure of OTFTs can make highly sensitive sensors benefit from their advantages including bendability, and low production cost. It takes advantage of a tiny signal vibration analyzer's sufficient gate voltage, resulting in significant changes in the channel current.

OFETs usually has three electrodes: source (s), drain d), and gate g).[21b] Like traditional field-effect transistors (FETs), the gate voltage can control the channel current of OFETs. Compared to conventional rigid-type silicon-based FETs, OFETs features good flexibility and biocompatibility and a low-cost solution-based process. The following equation describes the working principle of OFETs:

$$I_{DS} = \begin{cases} \frac{W}{L}\mu C_i(V_G - V_t)V_{DS} \quad V_{DS}\text{"}V_G - V_t \\ \frac{W}{2L}\mu C_i(V_G - V_t)^2 \quad V_{DS} > V_G - V_t \end{cases} \qquad (1)$$

I_{DS} and V_{GS} represent channel current and gate voltage, respectively. μ represents carrier mobility, which can be affected by the diffusion of the analyte.[21c] C_i is the capacity. V_t is the threshold voltage. W and L represent channel width and channel length, respectively.

2.1.2 Application of OFETs in Chemical and Biological Sensing

OFET was first used as the electrochemical sensor to detect the humidity by Zhu et al. in 2002[22]. The carrier mobility decreased during the detection process due to the diffusion of polar water molecules into the active layers closed to the gate electrodes. Ji et al. later successfully developed highly sensitive OFET-based ion and pH sensors, as shown in Figures 2.1a and 2.1b. It used valinomycin monolayer and tantalum pentoxide (Ta_2O_5) layer as the active layer, respectively. The OFET-based ion sensor can mainly detect a low concentration of K^+ ion (~33 mM) [23]. Many other groups further developed electrochemical OFETs for biological and medical applications such as rapid molecular diagnosis and genotyping.[24] For instance, Hadayat et al. have successfully created OFETs sensors for selective detection of target DNA sequences (Figure 2.1c).[25] In this technique, sensitive PNA-DNA hybridization assays (15-base PNA strands) can modify the channel structure of OFETs.

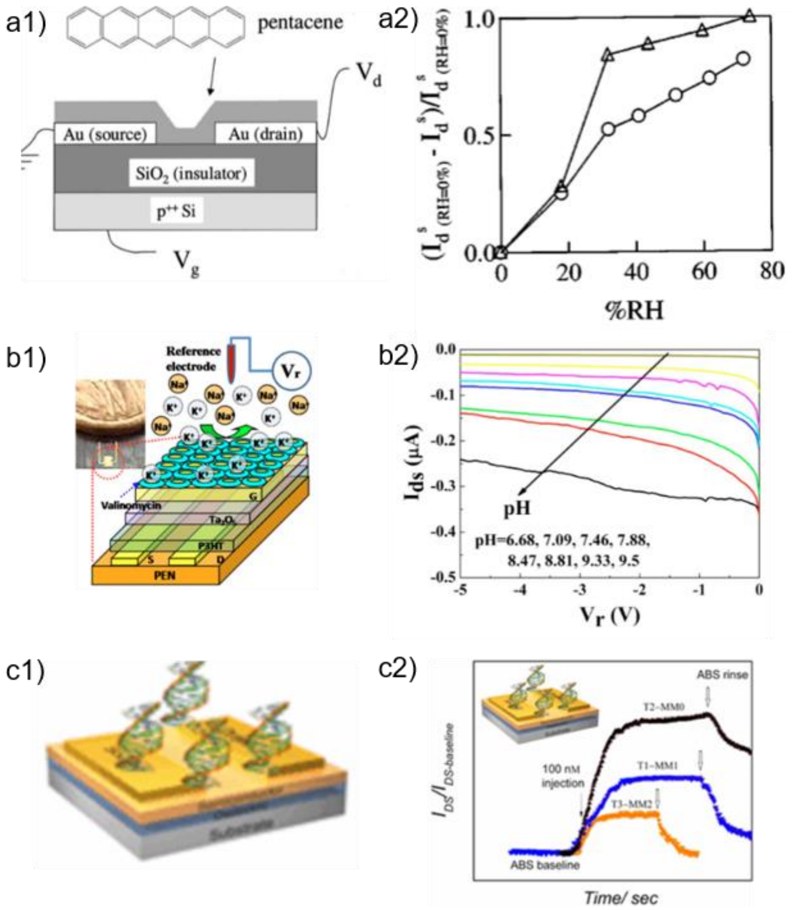

Figure 2.1 (a1) Diagram of the pentacene TFT for humidity detection. The channel size is 100 µm x 3 mm. (a2) The saturation current measured at V_g= -100 V and V_d =100 V is related to humidity.[22] (b1) Enlarged diagram of the ion-sensitive FETs (ISFET) for K^+ sensing. The valinomycin monolayer and Ta_2O_5 gate modified the device. (b2) Drain

current can detect the PH level.[23] (c1) Schematic diagram and c2) curves of channel current vs time for the OFET modified by DNA to test the electrical signal response of T_2-MM_0, T_1-MM_1, and T_3-MM_2.[25]

However, OTFT does not have obvious structural advantages when measuring the ion concentration in the liquid. For example, the biosensors with the structure of OFETs have a relatively high operation voltage (>1V). And their sensitivity is not high.

2.1.3 Working Principles of the OECTs

Organic semiconductors are sensitive to water and oxygen. On the contrary, the OECTs can stably work in a liquid environment. The first OECT, reported by Wrighton et al., uses polypyrrole oxidization to modify its conductivity.[26] The gate voltage can modulate the channel current of an OECT due to the electrochemical doping in the active layer by the electrolyte. Therefore, it can form chemical and biological sensors. The working principles of OECTs are:

$$I_{DS} = \frac{q\mu p_o tW}{LV_p}\left(V_p - V_g^{eff} + \frac{V_{DS}}{2} + \frac{V_{DS}}{2}\right)V_{DS}\left(\text{when}|V_{DS}|\text{"}\left|V_p - V_g^{eff}\right|\right)$$

$$V_p = qP_o t/C_i$$

$$V_g^{eff} = V_G + V_{effset}$$

t is the length of active material. C_i represents the gate capacitance. V_P represents the pinch-off voltage. V_g^{eff} represents the effective gate voltage. V_{offset} represents the offset voltage related to the potential drop at the interface between gate and electrolyte and electrolyte and channel. q represents the electronic charge, while μ is the hole mobility. Po is the intrinsic hole density in a semiconductor.[27]

The PEDOT: PSS is a promising semiconducting material for OECTs in applying chemical and biological sensing. The applied gate voltage can reject cations. The de-doting phenomenon will happen, which will decrease the S and D current.[27]

Advantages of OECTs compared to OFETs

- Better compatibility with the aqueous and liquid environment
- Less than 1 V threshold voltage.
- Analytes can directly dissolve in the electrolyte
- Distance between gate and channel can reach several centimeters range of

activity

2.1.4 Application of OECTs in Chemical and Biological Sensing

The OECT electrochemical sensors were successfully applied to detect humidity in 1987 by Chao et al., where polyaniline and poly(vinyl alcohol)/phosphoric acid as active layers and solid-state electrolytes, respectively[28]. Yan et al. [21a]systematically investigated using noble metals as electrodes for source and drain. When increased the cation concentration of electrolyte, the gate voltage will decrease. Therefore, the curve can demonstrate the concentration signal, as shown in Figure 2.2a. The glucose sensor was reported by Yang et al., which using the organic semiconductor to grasp signal from the liquid. This experiment using only PEDOT: PSS to fabricate almost all the components, including the S&D and semiconductive layer, of the device. After that, a (tridecafluoro-1,1,2,2-tetrahydrooctyl) trichlorosilane (FOTS) monolayer coated on the surface of the printed electrodes. as shown in Figure 2.2b.[29]

However, the sensitivity is not high enough for many biological applications, such as applying for tiny concentration detections. As shown in Figure 2.2c, a biological friendly chemical, chitosan, was deposited on the gate electrode. Then the enzyme was deposited in the matrix. As the surface of the gate has nanostructures, which plays an extremely important role in increasing the sensitivity of the device[30]. As shown in Figure 2.2d, an organic semiconductor-based OECT can be a DNA sensing device. It can be applied in the same solution environment like the living body. They have excellent mechanical stability, even deformed from the outside. DNA probes based on the gold electrode (gate) can achieve testing with high sensitivity (1nM). The device was able to detect complementary DNA targets down to 1 nM. A mechanical way called pulse enhancement can further enhance sensitivity. This sensor detects the signal by the verification of the work function of the OECT device. The major change happened in the DNA modified gate electrode. Therefore a high-sensitive biological sensor becomes a powerful detection way been applied in the clinical and medical field.[31]

Organic Thin-Film Transistors (OTFTs), including OFETs and OECTs, have broad chemical and biological sensing applications.

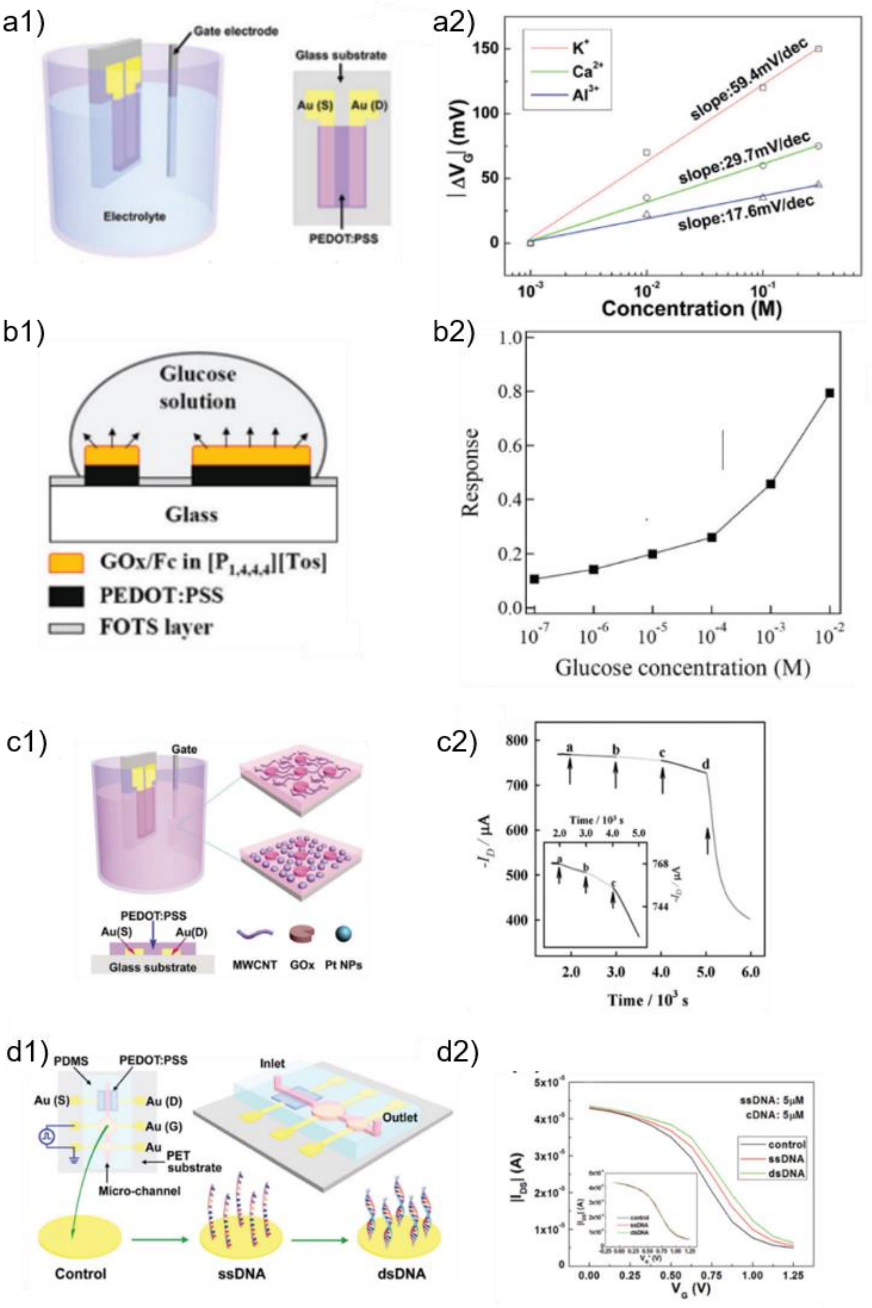

Figure 2.2 (a1) Schematic diagram of the basic structure of OECTs for biological and chemical sensing. (a2) Transfer curve to detect potassium chloride, calcium nitrate, and aluminium sulphate in the solvent.[21a] (b1) Schematic diagram of the mechanical structure and (b2) concentration-response of an OECT for detection of the concentration of the glucose.[29] (c1) Schematic diagram of an OECT with a nanostructure immobilized gate electrode and the (c2) signal response for a long-term during the trace addition of a target solvent.[30] d1) Diagram of an OECT on the plastic substrate for signal detection underwater. (d2) I_d-V_g Curve of OECT-based DNA sensor.[31]

2.1.5 Summary

The OECTs, as an attractive type of OTFTs, can display excellent performance in aqueous environments. OECTs can form chemical and biological sensing sensors, including DNA testing, ion and pH sensing, glucose sensing, etc. However, their challenge lies in the improvement of sensitivity and stability. Also, the fabrication of OECTs relied on a vacuum environment and poisonous etching techniques. These techniques will cause energy waste and environmental pollution. Therefore, various printing techniques will apply to fabricate low cost, environmentally friendly, flexible, and wearable OECTs.

2.2 Additive Printing Technologies for Fabrication of Electronics

Printing technologies, including flexographic, gravure, and inkjet printing, can fabricate various electronic and electrochemical devices. Printing technologies feature low cost, high volume, and high throughput. Generally, printed thin-film materials on a plastic substrate layer by layer can manufacture functional devices. And the pattern compacted with the structure of the functional material, forming an apparatus with specific functions. The active materials, such as organic semiconductors and dielectric materials, are easily printed because they are intrinsically suitable for preparing a solution system. On the contrary, the metallic material for electrodes' formation is naturally incompatible with the liquid environment and difficult to fit into printers. Therefore, the metallic material must form metal nanoparticles or nanowires to fabricate inks for compatibility with the printing techniques.

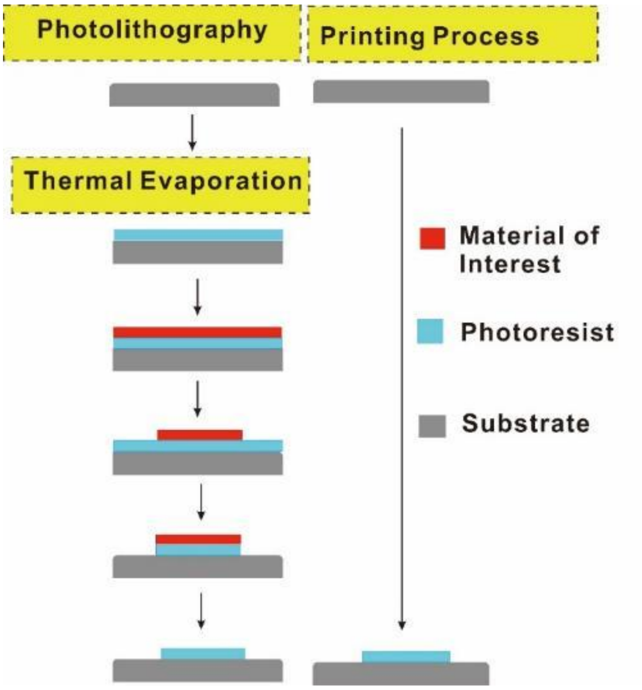

Figure 2.3 Operation steps for the traditional subtractive patterning methods and in comparison to additive printing technologies.

Printing technologies are superior to the traditional manufacturing technologies, such as photolithography, low equipment requirements, low energy consumption, low pollution, streamlined preparation process. The traditional photolithography technic for electrode fabrication is a subtraction process, which requires the deposition of materials (by sputtering, thermal evaporation, or chemical vapor deposition) on the whole substrate, followed by removing unnecessary material corrosive solutions.[32] In comparison, the printing process is a one-step additive process, depositing the tiny amount of ink accurately on a specific position to form the thin film pattern of the material of interest. The inkjet printer can work on the ambient conditions without the requirement of extreme conditions such as high vacuum and extremely high temperature.

The printing limits the unnecessary expense of material and significantly decreased the operation complexity by directly depositing functional materials onto various flexible and stretchable substrates without masks. In addition, printing technology applies to a broader range of materials than photolithography. For instance, bioactive fluids can coat on the substrates by printing. Still, they cannot undertake UV lithography (accelerate the aging) and strong corrosive liquid used in the etching step for photolithography technique.[33] In the following part, we will focus on describing several printing techniques.

2.2.1 Contact Printing Technologies

Contact printing, also known as the roll-to-roll (R2R) printing technique, features high production speed and low production cost. Nowadays, the R2R strategy is the main printing process in the PE industry. However, direct contact with the surface will impose some restrictions on materials and printing resolution. The following is a brief overview of several common contact printing techniques.

Flexography

The flexographic printing uses a series of rotating cylinders to absorb and print metals in the correct position during the rotation period shown in Figure 2.4.[34] The printing plate with a prepared depression cylinder can act as a mask during printing. And an ink supplying cylinder with an ink supplier can transfer the liquid material onto the printing plate with lots of elastic concaves.[35] In this way, the ink amount can be in a suitable range because only the outer wall of the micro-projection can carry the ink with a limited amount.

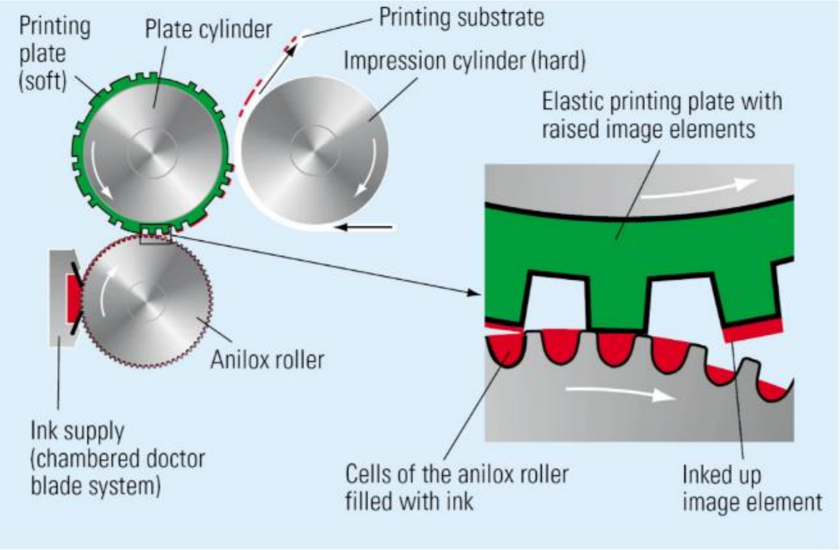

Figure 2.4 Schematic image of the printing process of a flexography.[34]

Finally, the material printing in the correct place by contacting the substrate film by rotating the impression cylinder.[36] The disadvantage of this technique is the low resolution of the pattern. Because of a compression interaction of two-cylinder, i.e. the diffusion of the ink outside the image area.[37] Various plastic substrates and foils can be a substrate in this printing technique.[36]

Gravure Printing

Different from the previous technique, gravure printing relies on the wetting of the substrate. Unlike the flexographic printing process, the gravure printing process does not require the deformable part of the impression cylinder. Instead, all the printing cylinders are rigid. Gully of the tooth on the rotating gravure plate formed by laser or photolithography was used to obtain the liquid ink for printing during rotating. Finally, the ink can transfer to the substrate by the surface energy of the liquid. This method enables high-volume printing of patterns with high resolution. Also, this technique can print most of the organic and inorganic solvent-based ink.

Soft Lithography

Soft lithography is contact printing ways that utilized the moulded elastic mould. The mould with different patterns can be a stamp. Typically, the reusable stamp formed by electron light or lithography techniques is applicable for many materials. The soft plastic materials formed the templates. The stamped form by pouring liquid precursor into a model. The precursor is the polydimethylsiloxane (PDMS) mixed with the catalyst or curative. The curative may be a platinum complex and a copolymer of methyl hydrogen siloxane and dimethylsiloxane. A subsequent heating treatment formed a reusable stamp.[38] The soft lithography can achieve micro/nanostructures patterning relies on the inherent properties of PDMS elastomers. It can make positive contact with the surface of the substrate. The positive connection is shown, in fact, adaptable solid to some slightly rougher substrates.

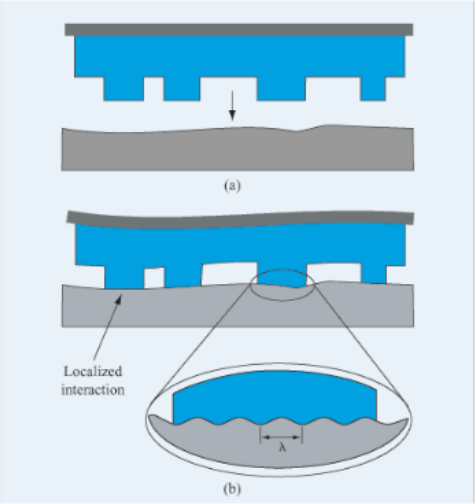

Figure 2.5 Schematic diagram of soft lithography process for a PDMS stamp. a) A large-scale, and b) a micro-scale of self-adjusting of the elastomer stamp can be compatible with the rough substrate.[39]

Soft lithography provides a cost-effective solution for large volume printing of patterns with various high-resolution substrates, even with some irregularity in the surface morphology. But its printing production speed is not as high as the R2R methods. [40]

2.2.2 Non-contact Patterning Techniques

Non-contact printing techniques are methods to maskless patterning the material of interest with no physical contact with the substrate by any part of the patterning machine. The patterning ways allow precise alignment with computer-designed patterns, which can fabricate complicated devices with multiple layers. Besides, as there is no contact between the templet mode with the substrate, the restrictions on the substrate have become extremely loose. Many substrates, including organic (e.g., plastic or rubber) and inorganic materials (e.g., ceramics or metals), are contact sensitive substrates. Because of the utilization of mask easy to damage the surface structure of the substrate during contact. Generally, it can print material of interest onto contact-sensitive substrates besides, as the patterns design are represented in digital form and verify from batch to batch. The changing of patterns has no extra cost for the templet of mask preparation.

Laser Direct Writing

As early as the 1960s and 1970s, laser generators have already become a functional tool for material treatments, such as etching, annealing, cutting, and some photochemical reactions. Generators were invented.[41] As early as the 1980s, the laser generator has already become a functional tool for subsequent processing of materials, e.g., photolithography and laser patterning. The last stage of study developed in recent decades; the secondary product was designed to interact with novel materials. It developed into a matrix-assisted pulsed laser capture microdissection (MAPLE) and a MAPLE direct-write (MAPLE DW).[41]

The laser capture microdissection technology can help to develop high-quality coatings. Pulsed laser deposition (PLD) is a deposition technology with the advantages of excellent compatibility in various environments, and the laser technique does not introduce any impurities to the fabricated surface. The laser beam has an adjustable wavelength that can lead to the decomposition of specific chemicals or chemical reactions.

McGill et al. demonstrated the first PLD strategy could use organic materials as MAPLE.[41-42] This process used the focused laser to partially react with the polymer film deposited on the surface in advance. The regional high-temperature curing will form high-resolution patterns. During the printing process, the laser beam will increase the temperature, which is much larger than that the pre-deposited thin film can withstand but not reach the level of evaporation temperature of the film molecules. The solvent collaborating with the matrix will deposit on the target region. Finally, since the printing substrate cannot absorb the liquid entrapped in the gel pores, only the polymer matrix can be deposited onto the target substrates. This technology is also can be laser-induced forward transfer (LIFT) technology.[43] On the contrary, the MAPLE can only pattern organic thin films in a vacuum environment.

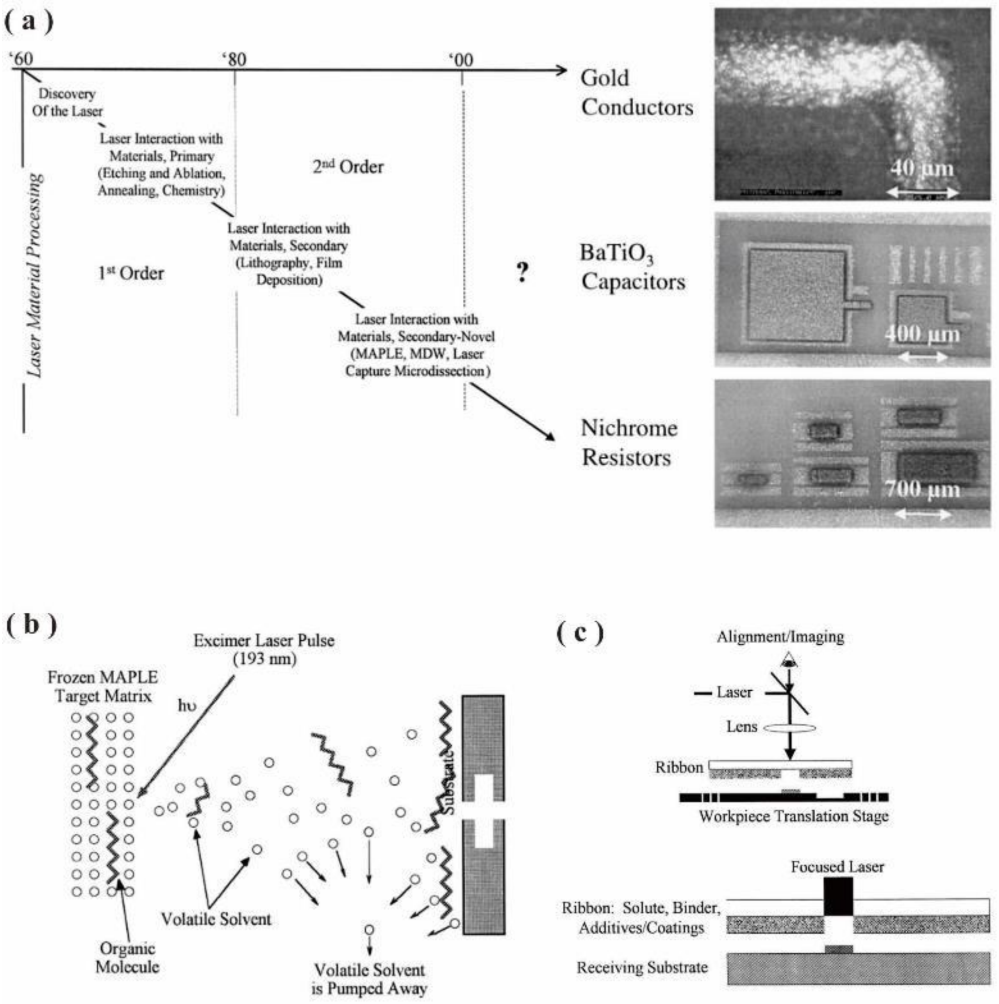

Figure 2.6 a) Laser processing technique using different organic materials. Right: MAPLE DW result of Au lines, an energy storage device made by barium titanate and five electronic devices made by nichrome. b) Operation principle of MAPLE. The liquid material was removed quickly in a recycling system. c) Schematic diagram showing the working principle of the laser-induced additive patterning process.[41, 43]

As shown in the Figure above, the matrix-assisted pulsed laser capture microdissection direct-write (MAPLE DW) technology can work in the air without the requirement of a vacuum environment. The advantages of MAPLE DW include attaching and depositing various materials on a different substrate at room temperature. Since MAPLE DW is a technique without liquid printing materials, without a drying process, therefore, the MAPLE DW technique can achieve high-speed patterning of the material of interest. The resolution of the MAPLE DW method can be minimized to 1 or 3 millimeters. The technology is computer-controlled and handles multiple layers of different materials with a precise thickness control using a wide variety of sources.[41]

Aerosol Printing

Aerosol printing is a non-contact direct-write technique that can print metal electrodes,[44] dielectric layers[1d] and seal [45] in the application of electronic fabrication. It consists of three distinct steps: first, place the ink in a nebulizer and atomizes it into liquid drops. Drops can exhibit different sizes. Inks can compose of polymers, adhesives, metal oxides, some biomaterials, and metals. Second, large amounts of particles are generated in the atomizer and are then delivered to the deposited head by a stream of nitrogen. Finally, the aerosol is on depositing of the material of interest onto the target substrate.

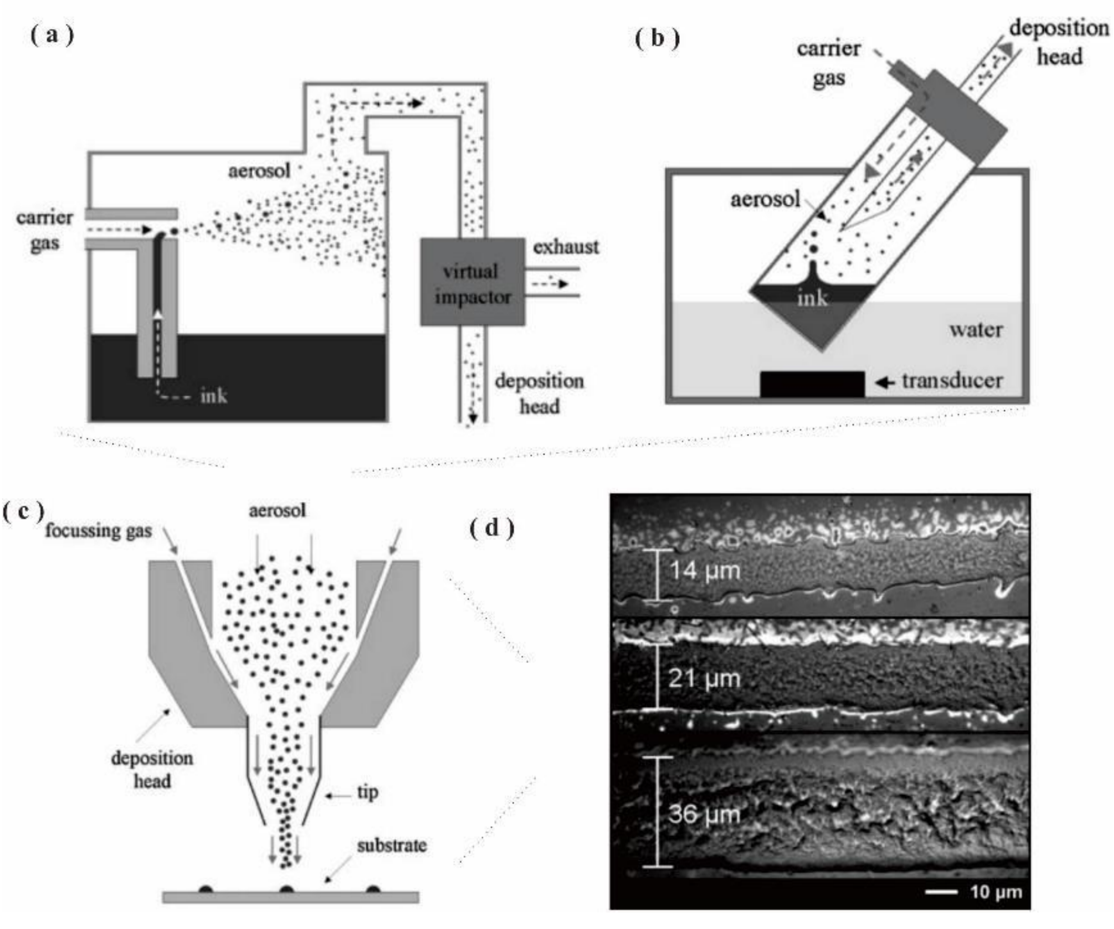

Figure 2.7 a-c) schematic diagram showing the working principle of a) atomizer, b) ultrasonic atomizer, and c) deposition head for aerosol printing. d) Optical microscopic images of the printed line using an aerosol printing technique. [45]

The aerosol-printed pattern has low contact resistance and nice mechanical adhesion to the silicon surface. The focused gas avoids the contact between the aerosol and the nozzle tip. Besides, the line width of the printed pattern is significantly narrow than the outlet diameter of the nozzle tip. However, this technique still has the disadvantage of low printing resolution (up to the centimeter level) and rough surface morphology.[44] The printed patterns usually have a rough surface due to the utilization of solid airflow.

Inkjet Technology

Modern inkjet-print technology stems from the miniature tubular pump developed in 1987.[4a] With the continuous development of piezoelectric material[46] and a deeper understanding of mechanical properties of fluid[47], modern inkjet printing technology has the ability to precisely depositing picolitre volume of functional material droplets onto various substrates. It became a powerful tool to "direct write"[48] solution-based material with accurately controlled patterns by a computer program with the help of ink-dispensers and translation stages. It is a mask-less technique that can additively printing thin film patterns on a substrate with less material and energy waste.

Drop-on-demand (DOD) is the commonly used inkjet print technology for an inkjet printer.

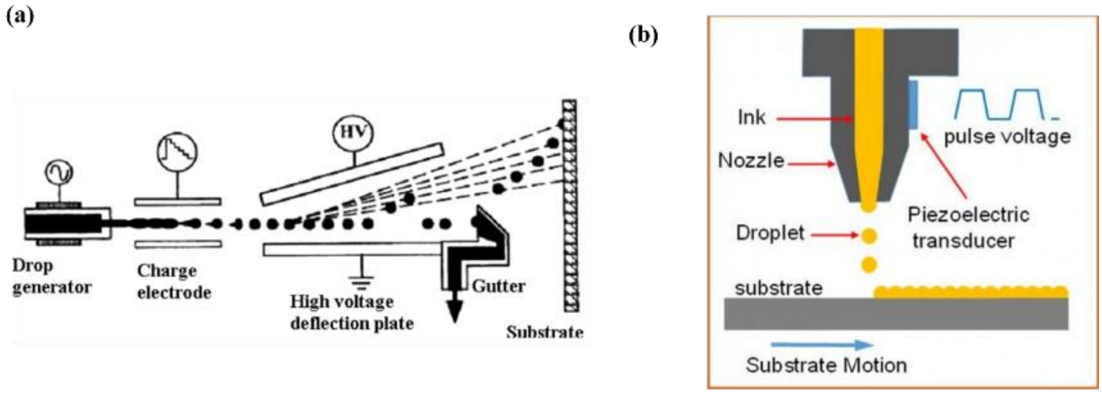

Figure 2.8. Working principle of a) continuous inkjet printer[1c] and b) drop-on-demand inkjet printer.

As shown in Figure 2.8, a continuous inkjet printer has a drop generator to generate droplets consistently. Once the droplets fly across the electrostatic field, most of them will get an electrostatic charge when they depart from the charged electrodes. After flying across the voltage deflection plate, the charged droplets can deposit on the desired location of the substrate and the uncharged droplet will be collected by the gutter and entering the recycling system. This technology can initiate high-speed printing for graphics because continuous droplets can appear at a frequency ranging from 20 to 80 kHz.[1c] Besides, this technology can deal with stocking the jetting head due to solvent drying in the intermittent printing task.

The inkjet-printed droplets have uniform volume, jetting time, and falling speed for the drop-on-demand inkjet printer. This technique requires jetting head and strictly controlled electrical pulses to generate precise droplets. During inkjet printing, when the constant voltage pules, was added to the piezoelectric ceramics on the jetting head, the fluid obtained outward kinetic energy to overcome the surface tension of the ink. The generated droplet has a falling speed of more than one m/s to resist the air resistance. The falling rate of the ejected droplets depends on the kinetic energy that transforming into the liquid droplet.[48] The drop-on-demand inkjet printing technology becomes an important technology that can easily print materials in liquid form, including solutions or suspension, onto various substrates, including flexible thin-film,[49] textiles,[50] papers,[51] etc. This well-developed technology is easy to operate and has diverse, successful applications.

2.2.3 Summary

Table 2.1 shows the advantages and disadvantages of various printing technologies. The Table also demonstrates the and scope of application for each technique. Additive printing technologies developed rapidly in the past few decades aiming to replace the traditional subtractive patterning strategies. It enables high-speed printing of flexible and wearable electronics with little material waste and energy consumption. With these printing techniques, the development of additive printing technology opens the door for the mass production of low-cost, high-quality, flexible, and wearable electronics for the application, including energy storage, digital display, medical and biological sensing, and energy harvesting. Contactless additive printing technologies have developed quickly because the original printing techniques rely on masks or stamps to print patterned, causing material waste and the difficulty of changing the print template.

On the contrary, the non-contact printing techniques usually can be " direct write" onto the substrate without utilizing a mask. The computer-designed pattern can be changed with ease from batch to batch for these technologies. Laser direct-write technologies need to rely on a ribbon" or target matrix as the source of the material. For the ribbon" or target matrix, the printing process can also rely on subtractive printing. Therefore, it generated extra material waste and energy waste. In addition, the printed patterns usually have rough surfaces and unclear boundaries due to the airflow of the aerosol printing technique.

The inkjet printing technique, especially the drop-on-demand inkjet printing technique, has its special status. Among all the additive printing techniques, inkjet printing is a non-contact maskless printing strategy. Also, it allows high-speed printing of various functional materials on multiple substrates, including flexible thin-film,[49] textiles,[50] papers,[51], etc. The inkjet printing technique is a technology that may enable the large-volume fabrication of low-cost sensors or other electronic devices.

Table 2.1. Properties of additive printing strategies showing advantages of the inkjet printing techniques.

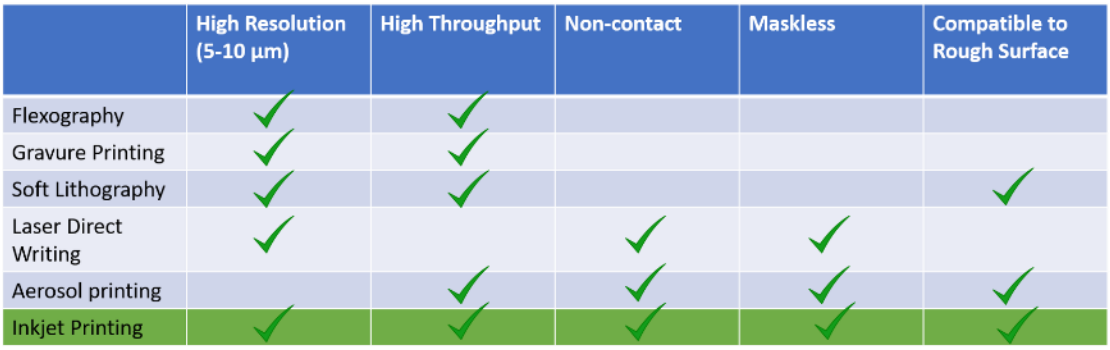

	High Resolution (5-10 μm)	High Throughput	Non-contact	Maskless	Compatible to Rough Surface
Flexography	✓	✓			
Gravure Printing	✓	✓			
Soft Lithography	✓	✓			✓
Laser Direct Writing	✓		✓	✓	
Aerosol printing		✓	✓	✓	✓
Inkjet Printing	✓	✓	✓	✓	✓

2.3 Printable Ink with Nanosized Metal Dispersions

Nanostructured noble metallic materials, especially silver, can form electronics by printing techniques. Nanosized metals have various types, including nanospheres, nanoplates, silver nanowire (NW), nanobelts.[52] To use these nanomaterials for the printing of the electronic devices, an essential operation, i.e., joining nanoscale building blocks, should be carried on, creating a permanent connection among these nanomaterials. The perfect relationship between nanomaterials and the formation of the bulk components is where the challenge lies.

2.3.1 Joining Processes for Metallic Interconnects

The technique of micro joining and micro-welding can trace from the 1950s.[53] There are many different ways to attempted to connect the printed separated metallic particles.

Fusion Welding

Fusion welding requires localized heating impute by various energy suppliers such as laser beam, plasma, microwave, and electron beam. The micro/nanostructures coalescence with each other by high energy imputation.[54]

Soldering and Brazing

Soldering and Brazing without the essential melting component of metal but introducing another type of molten filler metal to form an alloy by the metallurgical reaction.[55] Metals with low liquidus ranging from 200 to 600 °C[56] are utilized as a filter material for micro-joining. Although well-developed lead-free soldering technology has is multifunctional, it still 'cannot be used on heat-sensitive plastic substrates.

Solid-state Bonding

Solid-state bonding requires the introduction of strain or deformation to the particles, including friction, pressure, to induce high strain and plastic deformation of the building bulks. The building bulks operated in an inert or vacuum environment and bond at high temperatures (half of the melting point) and high-pressure environments.[57]

This solid-state bonding technique can develop into low-temperature or even room-temperature bounding of bulk metals due to the utilization of heat-sensitive materials. Since the material is for the nanoscale, the surface energy increased dramatically, leading to a heat-sensitive property. As described by Qi in 2014[58]

$$T_m = T_{mb}\left(1 - \frac{\delta}{D}\right)$$

The material melting point (T_m) is related to the bulk material melting point (T_{mb}). The particle diameter D. Material-dependent parameter δ is dependent on the properties of specific metals.

Nanostructured noble metallic materials, especially silver, have been developed into various types, including nanospheres, nanoplates, silver nanowire (NW), nanobelts, which have been applied in this way for the application of electronics fabrications.[11a] To apply these nanomaterials for printing electronic devices, an essential operation, i.e., joining nanoscale building blocks, should be carried on creating a permanent connection among these nanomaterials. The formation of bulk components is where the challenge lies.

Silver, with its distinguished electrical conductivity and mechanical flexibility, has been developed into various nanoparticle pastes in the application of bulk metal bonding. Silver joints via nano-sintering processes were well-developed in the past decade.

2.3.2 Silver Joints via Nanosintering

Porosity Reduction

In the process of sintering, some porosity of sintered nanomaterials has been maintained due to the need to release organic binder and solvent. Usually, the gas or vacuum should be shielded to suppress oxidation.

The formation of this bond is usually carried out in two steps. First, the partial bond-forming, then the interaction between the two parts begins to break apart, and there is a residual space between the asperities connected.[11a] Then, a complete bond is formed under high-temperature conditions for a relatively long time so that diffusion increases the contact area. Figure 2.9a shows filler nanoscale silver to bond two components together. External pressure is being exerted on the joining materials and increasing the joining properties to suppress the porosity.

Coverage

During the joining process, there are two types of interconnection, namely self-bonding and substrates bonding. Theoretically, the connecting material to the substrate is only an ultra-thin-metal layer.[11a] Peng et al. have reported that the following equation can describe the coverage rate C.:

$$\mathrm{C} = \left(1 - \frac{x}{y}\right)$$

x represents the uncovered length, while y is the nuclear length of the dispersed kernels. x needs to be a low value to improve the real contact areas. Adding pressure is also impossible to implement a dense interface.[9]

Optical Nanowelding

Light causes the heating produced by radiation absorption [59] using the silver plasma effect. The concentrated light in the gaps between two adjacent particles or fibres of the silver in nanoscale can sinter the pattern. This beam generates heat in a tiny area without exerting influence on the surrounding environment.[60] As shown in Figure 2.9b, twenty-five mega Pa pressure also can initiate the nanowire cross-linking and forming connections, offering a very low surface resistivity. [61]

Ion-Activated Joining

The nanosized Ag act as plastic particles, which will be bonded together when they encounter opposite polyelectrolytes.[62] Therefore, this technique can generate conductive plastic substrate by joining the nanosized Ag. Another advantage of this technology is that it can be operated at room temperature.

In ion-activated joining, a single layer of nanoparticle materials was coated on the substrate and then printed the electrolyte on its surface. As shown in Figure 2.9c, an ion-activated joining technique joined the silver nanoparticles. The relatively high surface energy will prevent molecular diffusion. Besides, the nanoparticles can be sintered at room temperature and potentially derived in various applications.

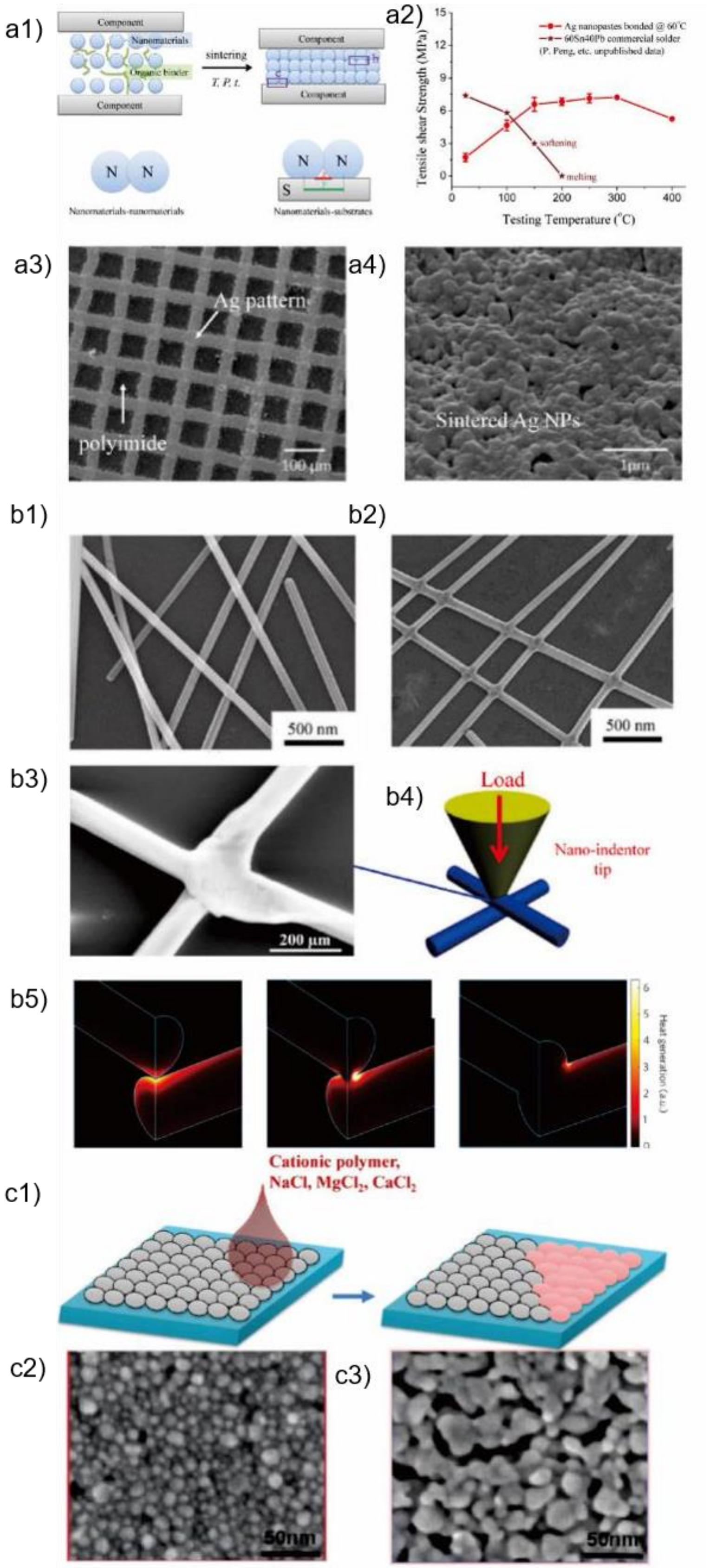

Figure 2.9 a1). Diagram of the sintering process of printable nanoparticle inks under pressure, with high sintering temperature. (a2) Comparison of joining strength using Ag NP paste and commercial Sn−Pb alloy. (a3-a4) SEM images showing the surface

uniformity of the AgNP ink formed pattern after the sintering process. [11a] SEM image of AgNW b1) before and b2-b3) after applying a twenty-five mega Pa pressure for sintering. (b4) The computer-simulated sintering process. [61] (c1) Schematic diagram and SEM images of the ionic jointing of silver nanoparticles using inkjet-printed solution drops. [62]

2.3.3 Summary

As the separated nanoparticle conductors do not have high conductivity, many techniques can join the isolated nanoparticles. Among these, the porosity reduction technique and the optical molding technique requires huge pressure. Although the ion-active joining technique can operate in ambient conditions, the joined electrode have rough surface morphology and cannot merge all the points into a uniform and smooth film electrode. More investment in silver nanomaterials to enable silver NP or ink to form conductive thin film electrodes to fabricate various flexible electronics. In addition, a new kind of inks for printing technology will have future development.

2.4 Polymer Assisted Metal Deposition (PAMD)

2.4.1 PAMD Based on Polymer Brushes

Zheng's group has developed a solution strategy to fabricate highly conductive flexible, foldable, stretchable, and compressible metal electrodes, contacts, interconnects, and textiles. The solution method at room temperature can manufacture the cost-effective Cu electrode, which addresses the challenges mentioned above. For example, they have developed a solution-processable chemical approach to fabricate highly flexible and durable conductive textiles, including cotton, nylon, polyester, and Kevlar[18f]. In this method, a thin layer of poly[2-(methacryloyloxy)ethyl-trimethylammonium chloride] (PMETAC) was mounted on the surface of the substrate by surface-initiated atom transfer radical polymerization (SI-ATRP) or free-radical polymerization. The conductive metal was subsequently deposited onto the PMETAC layer by ion exchange with palladium complexes and electroless deposition (ELD). The as-made conductive textiles exhibited metallic conductivity and were durable in mechanical and washing tests. In addition, this technique can print conducting wires for wearable electronics.

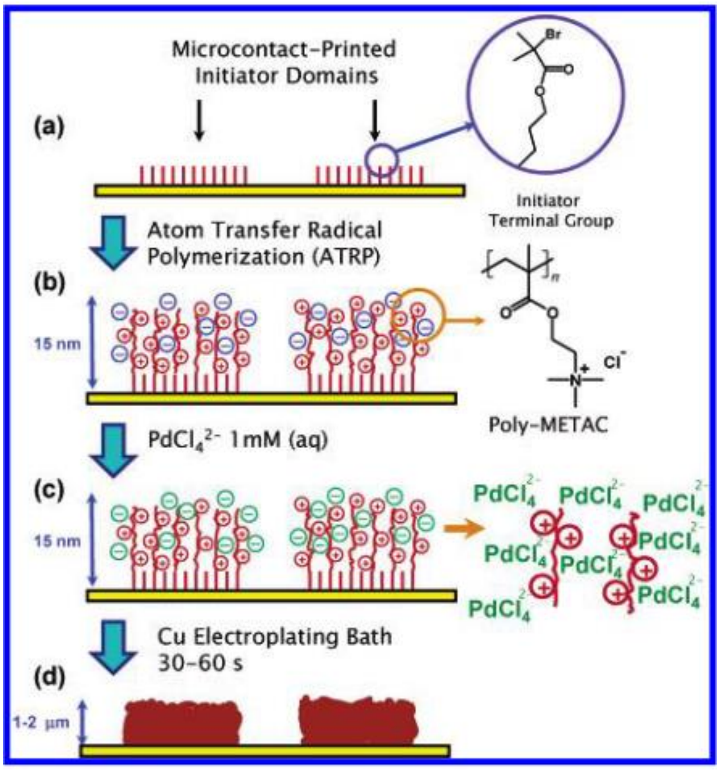

Figure 2.10. Diagram of the preparation process of a conductive plastic substrate.[18h]

On top of this metal deposition technique, the project team further developed a universal printing method, namely "matrix-assisted catalytic printing" (MACP), which allows patterning metal interconnects ranging from nanoscale to macroscale.[18e] In MACP, palladium catalytic species were printed onto the PMETAC modified flexible substrates to form a designed pattern (Figure 2.10). By adjusting the concentration, molecular weight, and solvent of the carrying polymer, one can easily tune the printing ink to fit the requirements of different printing technology. The printed metal structures on various compliant substrates showed remarkable adhesion and conductivity against repeating bending, folding, and fatigue tests.

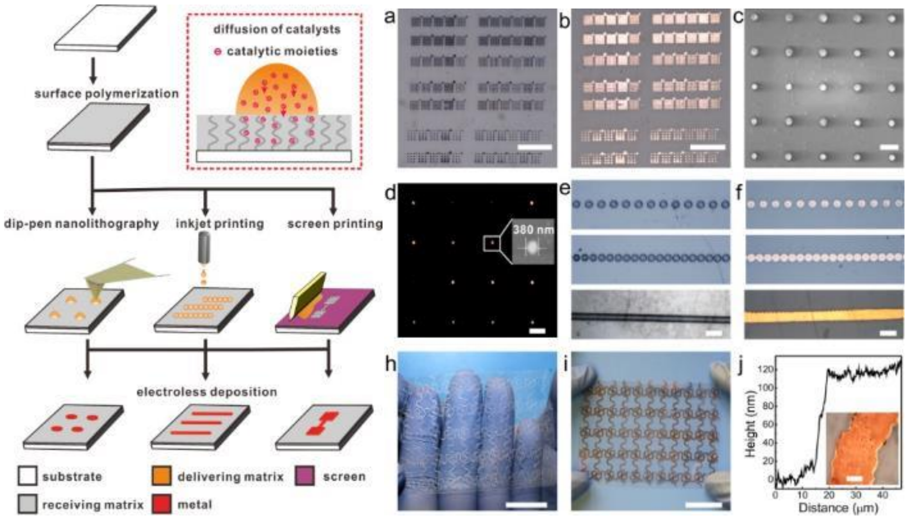

Figure 2.11 Left: schematic of the fabrication process of MACP. Right: SEM, optical, and AFM images of as-made metal structures on various substrates with the resolutions from manometer to sub-mm using MACP. [18d]

Zheng's group reported an efficient way to deposit metal thin-film electrodes on plastic substrates. In addition, they invented a poly (4-methacryloyl benzophenone-co-2-methacryloyloxy ethyltrimethylammonium chloride) [P(MBP-co-METAC)], which can serve as a buffer median to carry out electroless metal deposition.

Professor Feng Yan (co-supervisor) and his research team in applied physics, famous for TFT-based sensor detection. Prof. Feng reported lots of crucial scientific research based on OECTs to biological and ionic sensing.

The dielectric material can effectively screen the dipole field and optimized low-voltage mobility. The dielectric layer can be indacenodithiopheneco- benzothiadiazole (IDTBT) and poly (vinylidene fluoridetrifluoroethylene-chlorofloroethylene) [63].

2.4.2 PAMD Based on Metal Platable Copolymer Ink

P(MBP-co-METAC) has been developed into the copolymer ink to directly copolymer buffer layer for offering sits for metal thin-film electrode growth in a solutional environment. Compared with the MACP technique that requires coating of METAC thin film onto the entire substrate. This copolymer is suitable for various printing techniques, including spin-coating, screen printing, and inkjet printing. It is a versatile technique to print a highly conductive metal thin-film electrode at room temperature. This inkjet-printed Cu electrode became electrodes for solar cells, flexible a-IGZO

TFTs, flexible electronic circuits, etc. The thin film has promised a plastic adhesion substrate that can pass the scotch tape test.[19a]

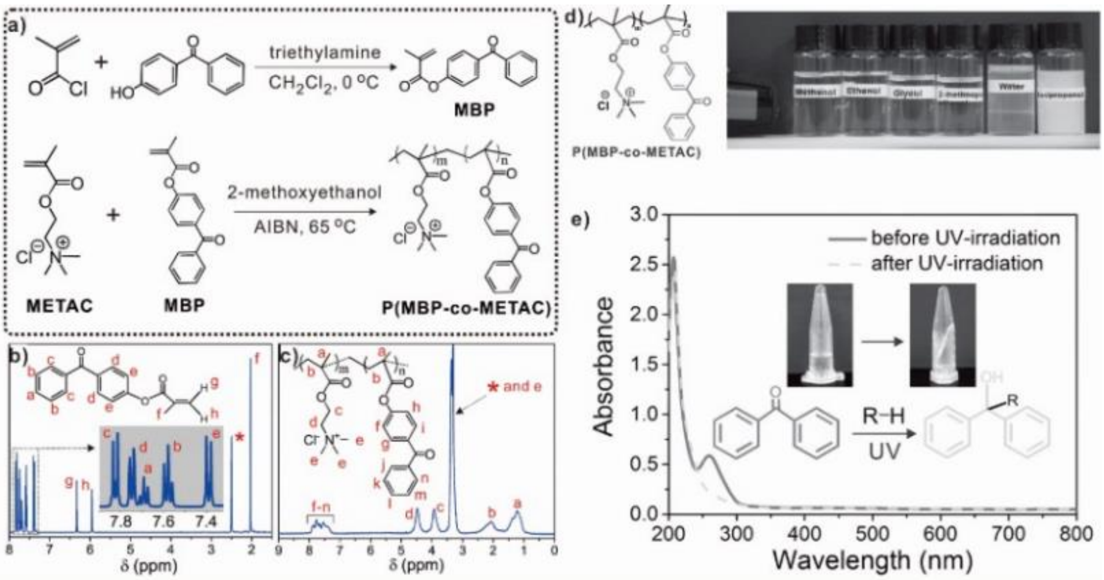

Figure 2.12. Synthesis and characterization of P(MBP-co-METAC) as solute of the inkjet print-printable copolymer ink. a) Synthetic route of P(MBP-co-METAC). The 1H-NMR spectrum of b) MBP in d6-DMSO and c) P(MBP-co-METAC) in d4-methanol. d) Chemical structure and P(MBP-co-METAC) in a different solvent. e) UV spectrum of copolymer ink.[19a]

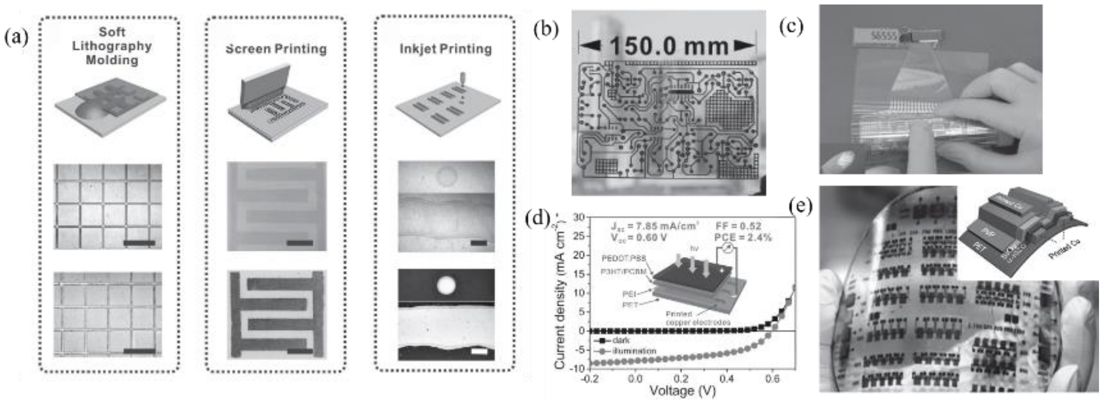

Figure 2.13 a) Different printing ways for the metal-platable copolymer ink.[19a] b) Inkjet-printed flexible circuit board on a transparent PET substrate. c) The inkjet-printed flexible keyboard of a calculator. d) *I-V* curve of the organic solar cell with printed Cu electrodes. e) TFTs using inkjet-printed flexible Cu electrode. The thermally evaporated a-IGZO was the semiconductive material.[19a]

2.4.3 PAMD on Soft Substrates

As shown in Figure 2.14a, the METAC polymer brush can grow on the surface of the cotton fibres in advance. Then, the catalyst modified METAC polymer brush can be used as a buffer layer to fabricate a thin-film Cu electrode to attach to the surface of the cotton. And this conductive cotton showed excellent conductivity and flexibility. Therefore, this conductive cotton has the potential to be applied to the fabrication of a new generation of flexible and wearable electronic devices.

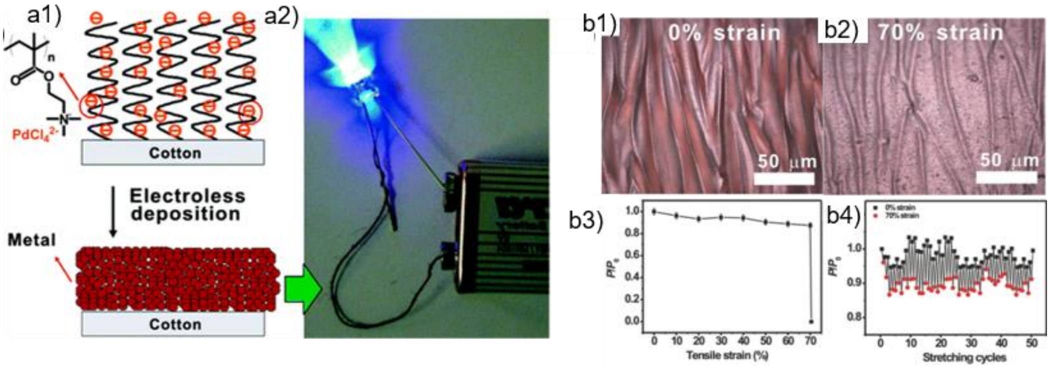

Figure 2.14. (a1) Schematic diagram showing the preparation process of conductive cotton yarns. (a2) Optical image of a cotton yarn forming a closed circuit for powering a LED. Optical microscopy images of the surface morphologies of the buckled Cu layer on PDMS at 0% (b1) and 70% (b2) strain. c) Electrical conductivity verification along with the application of different tensile strains for the stretchable conductor. d) Conductivity stability for the stretchable conductor under repetitive stretching and relaxing tests.[18b]

As showing in Figure 2.4.3b, the stretchable electrodes can attach to the PDMS substrate with a stretchability of 70%. The PDMS substrate is pre-stretched to around 300% and then carry out the polymer brush grow.[18b] This PDMS-based stretchable conductor can maintain stable electronic conductivity during stretching and releasing. Therefore, this may be an ideal flexible conductive material to develop flexible robots and flexible sensors.

2.4.3 Summary

Polymer assisted metal deposition is a high-volume technique that can prepare thin-film metal electrodes on flexible substrates at room temperature. It generally includes the formation of polymer coatings, immobilization of catalyst moieties, and subsequent ELD processes. This innovative technique can overcome unmatched natural properties between the thin metal film and a flexible substrate. Finally, this kind of polymer coating technique can help inkjet print directly on flexible substrates. In addition, this technology can fabricate various types of wires and electrodes with low production cost and energy consumption.

2.5 Gel with Porous Structure

As early as the 1930s, Hurd has demonstrated the network microstructure of gels.[64] Then, in 1932, Kistler initiated research about the supercritical drying condition and unique properties of aerogels.[65] In the 1950s, Roy and his colleges have popularized the ceramic industry's sol-gel process for uniform porous structure fabrication.[66] When we come to gel structure, we must mention a well-developed technique called the sol-gel process that became a ceramic preparation technique that benefits humanity for decades.

2.5.1 Sol-gel Process

Definition of the noun of the sol-gel system:[67]

Colloid: a suspension with small (~1-1000 nm) dispersed materials. In a colloid, the short-range force, e.g., van der Waals force and ionic force, are the major interactions of particles because the gravitational is ignorable. The particles also have the Brownian motion because of the collisions of suspending particles.

Sol: a colloid that suspends solid particles in the liquid.

Aerosol: a colloid that suspends solid particles in the air.

Emulsion: a colloid that suspends liquid droplets in another liquid.

Ceramic: nonmetallic inorganic material.

Osmosis: ceramics that include organic or organically modified materials.

Alkoxide: most common precursors used in the sol-gel process.

Alkane: molecules formed by only C and H atoms.

Alkyl: An *Alkane* that removes hydrogen (e.g., $\bullet CH_3$). The interpunction • is indicating one electron that can form a bond.

Alcohol: Adding a hydroxyl (OH) group to the *Alkyl*, such as methanol (CH_3OH).

Alkoxy: Removing a protein from alcohol, e.g., methoxy ($\bullet OCH_3$), forming the most used ligand group in the sol-gel process.

Lots of metal oxides can be processed at high temperatures and then forming glasses or ceramics. The sol-gel process is a relatively “soft” [68] technique to prepare various glasses or ceramics by preparing precursors surrounded by different ligands. A list of commonly used ligands, including Alkyl and Alkoxy, can be found in table 2.1. In the 1950s, Roy and his colleges have popularized the ceramic industry's sol-gel process for uniform porous structure fabrication.[66] Besides, the most widely used silicon for precursor fabrication, such as non-silicates materials, Ti and V, and Group IIIB metals (e.g., B and Al), can be fabricated as precursors. This sol-gel process can generally be described as several independent steps, as shown in Figure 2.14.[67]

Table 2.2 Commonly used ligands.[67]

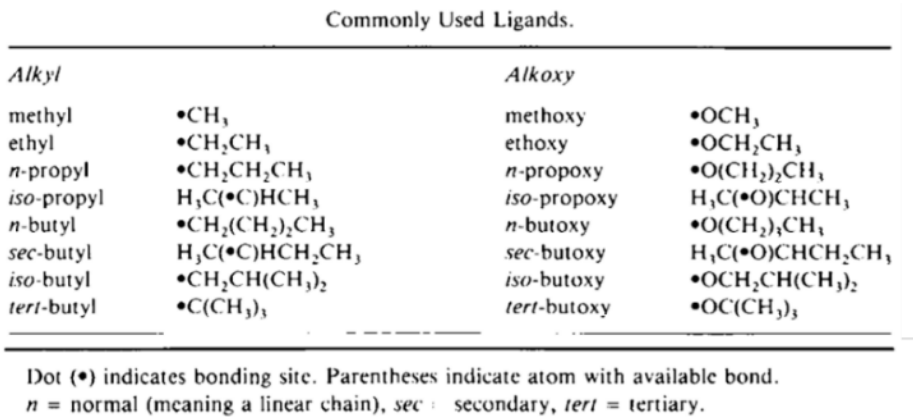

Commonly Used Ligands.

Alkyl		*Alkoxy*	
methyl	$\bullet CH_3$	methoxy	$\bullet OCH_3$
ethyl	$\bullet CH_2CH_3$	ethoxy	$\bullet OCH_2CH_3$
n-propyl	$\bullet CH_2CH_2CH_3$	*n*-propoxy	$\bullet O(CH_2)_2CH_3$
iso-propyl	$H_3C(\bullet C)HCH_3$	*iso*-propoxy	$H_3C(\bullet O)CHCH_3$
n-butyl	$\bullet CH_2(CH_2)_2CH_3$	*n*-butoxy	$\bullet O(CH_2)_3CH_3$
sec-butyl	$H_3C(\bullet C)HCH_2CH_3$	*sec*-butoxy	$H_3C(\bullet O)CHCH_2CH_3$
iso-butyl	$\bullet CH_2CH(CH_3)_2$	*iso*-butoxy	$\bullet OCH_2CH(CH_3)_2$
tert-butyl	$\bullet C(CH_3)_3$	*tert*-butoxy	$\bullet OC(CH_3)_3$

Dot (•) indicates bonding site. Parentheses indicate atom with available bond.
n = normal (meaning a linear chain), *sec* = secondary, *tert* = tertiary.

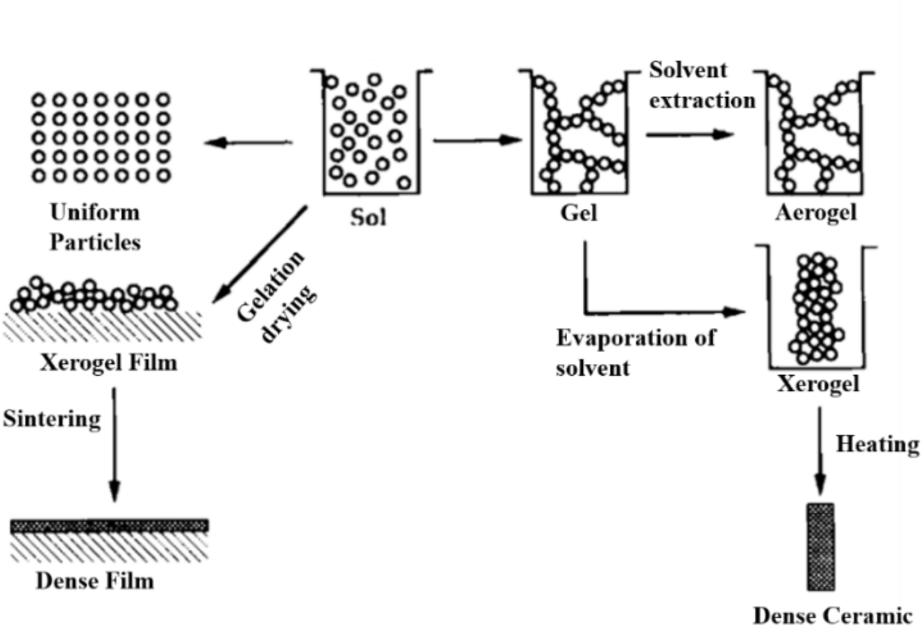

Figure 2.15 Schematic diagram of the fabrication process of the sol-gel process to form a thin film and dense ceramic. [67]

The study of polymer can trace back to the 1930s. In 1953, Flory reported that the polymer is a material that has a 3-dimensional network made up of random branches.[69] Gelation reactions usually form polymers. In the sol-gel process, the gelation passed two stages: hydrolysis and decomposition. Take the metallic alkoxides, for example:

An OH group will replace the ligand group in hydrolysis reaction, forming a chemical with ROH, where the R represents different ligands.

$$\mathrm{Si(OR)_4 + \ H_2O \rightarrow HO - Si(OR)_3 + ROH}$$

In a condensation reaction, two hydrolyzed molecules can link together to form bigger molecules that contain silicon.

$$\mathrm{(OR)_3Si - OH + HO - Si(OR)_3 \rightarrow (OR)_3Si - O - SiOR_3 + H_2O}$$

In the polymerization process, the branched amount that an atom can serve is f. Therefore, if f is bigger than 2, the cross-linking can successfully build three-dimensional structures.

2.5.2 Interpenetrating Organic/Inorganic Sol-Gel

Between the 1930s and 1980s, the sol-gel system usually prepares non-composite materials such as glasses and ceramics. Huge developments have been made in both non-silicates and silicates sol-gel processes to fabricate ceramics with excellent chemical durability, transparency, and optical properties.[70] The sol-gel process can also make specific applications such as heat reflection and car windshield by coating or laminating with organic materials.[68] A similar case is showing in Figure 16a. In 1985, Schmidt report the first composite sol-gel in the combination of the organic and inorganic material on the atomic scale.[68]

Mary et al. reported the first Si grains that crosslinked by the amines in the epoxy. This organic and inorganic bounded particle can form strong, lightweight xerogels and aerogels. In this way, the gel material features better elastic properties and bigger pores.[71] As shown in Figure 2.16b, adding different epoxy groups with different functions can modify the porous size and gel structure.

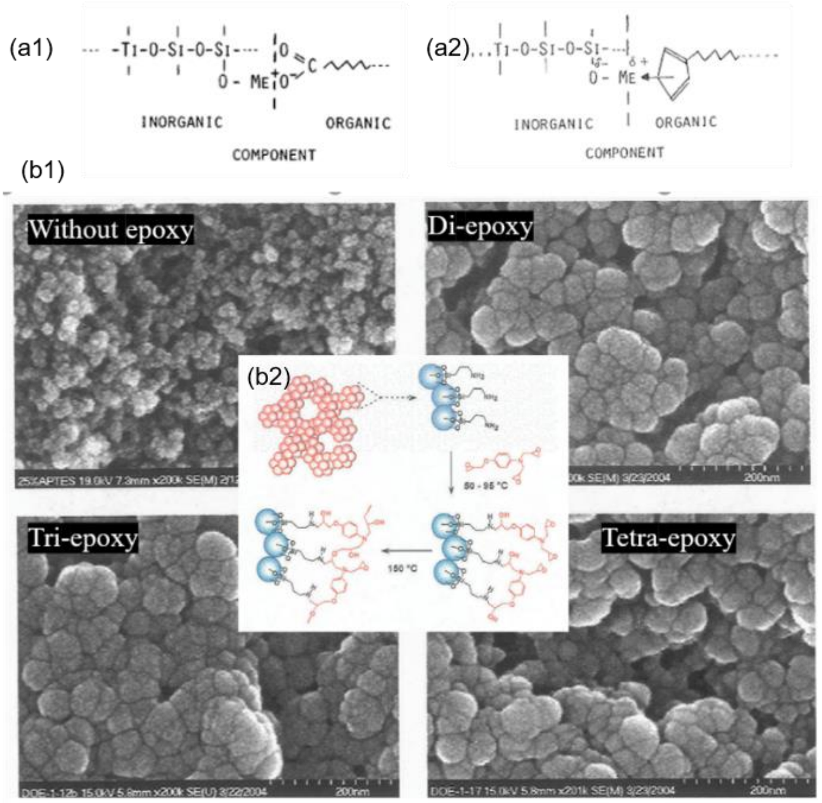

Figure 2.16 (a1) Crosslinking by ionic force between polymer groups and metal oxide particles. (a2) Crosslinking point with specific inorganic ligands. (b1) SEM images of ionic crosslinking of 25% aminopropyl triethoxysilane (APTES) with different epoxy groups. (b2) Diagram showing interaction formula of the amines crosslinking of Tri-epoxy groups.[71]

Aging Process Before Drying

Aging is a necessary treatment for enhancing the strength of a gel structure.[72] Various studies focused on measuring the strength of the gel agents at the senior level. The lower the bulk density of the gel, the lower capillary pressure it needs to undertake. The gels with lower bulk density also have higher permeability and lower obesity. As shown in Figure 2.16, the stronger the network is, the less shrinkage the gel will be after the drying process. The shrinkage of the volume after drying is related to the pore size.

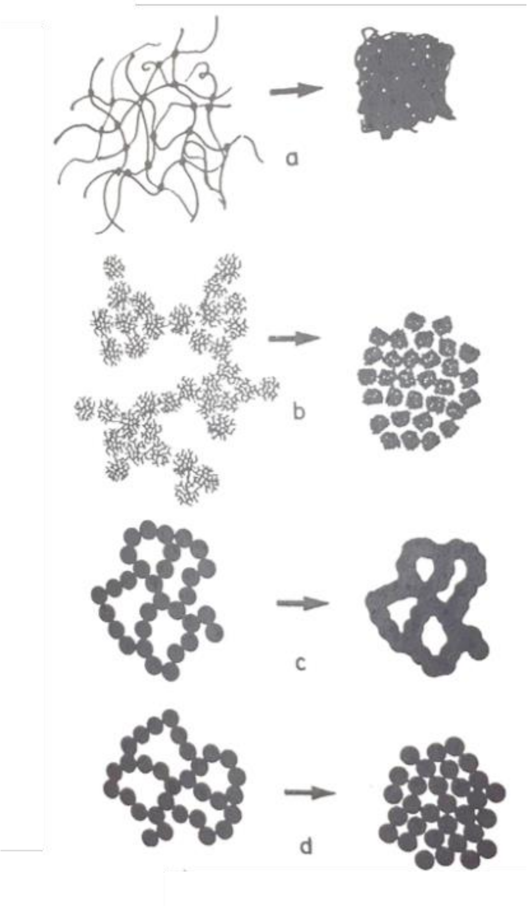

Figure 2.16 Schematic diagram showing the drying of the gel for a) gel-forming crystalized structure after acid treatment b) catalyzed treatment. c) high and d) low solubility influence the aging result. [73]

Drying

Besides, polymerization and aging can strengthen the gel materials, drying process that also provides another choice. During the drying process, the liquid boundary is first approaching the main body of the gel matrix. Then, in the transition stage, the gel matrix containing the liquid solvent began to shrink till the last stage. In the transition stage, the liquids recede inside the skeleton of the polymer structure, and the liquid becomes isolated to form a pore liquid. Finally, in the second stage, the pore liquid will dry and diffuse to be excreted from the polymerized system. As showing in Figure2.17a, the rate of water evaporation variation chart can demonstrate the drying process.

As showing in Figure 2.5.4b, the drying front is usually rough. When enlarged the boundary of liquid during the drying process, the nanosized pore liquid can be detected.

Shaw et al. have derived the function of express the maximum capillary pressure of the pore liquid during the drying process, as shown in Figure 2.17c.[74]

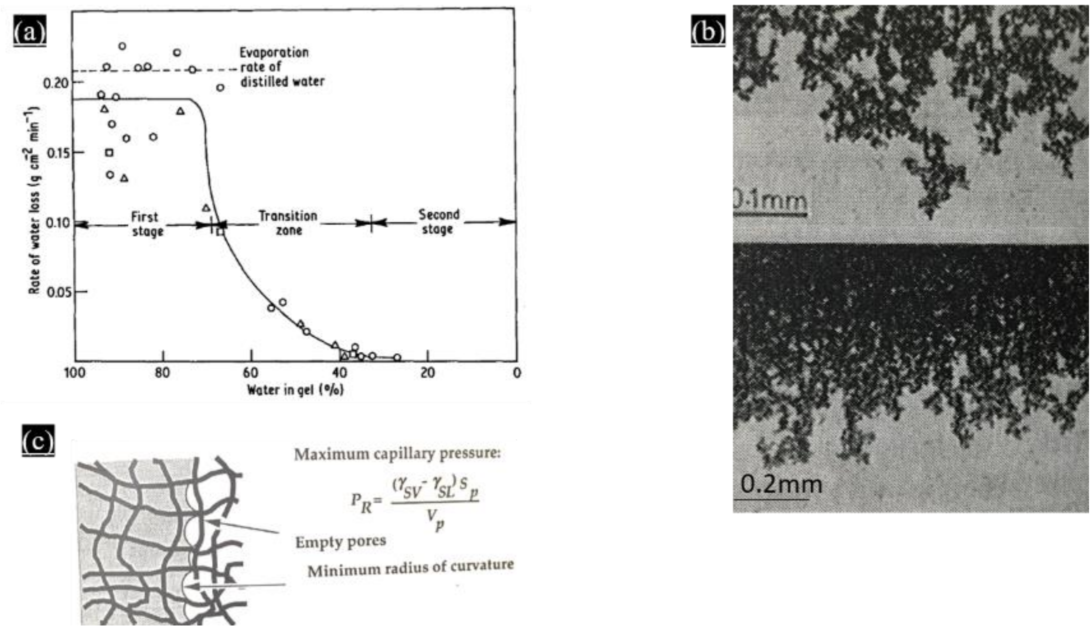

Figure 2.17 a) The curve of the rate of water evaporation vs the water proportion for a gel with the initial thickness of o 7.5 mm, ◌ 3.0 mm, □1.8, ▲ 0.8mm.[75] b) Cross-sectional view of the gel drying process. The white areas represent the region with liquid, whiles the dark areas represent the polymer matrix without pore liquid.[74] c) Schematic illustration of the pore liquid evaporation during the transition zone.[76]

2.5.3 Xerogel

Xerogel and aerogel can fabricate condensed ceramics. But they are gradually found to have a wide range of catalytic substrates filters because of their high porosity and large surface areas. Drying of gel to xerogel formed a 5 to 10 times shrinkage compared to the sample's original volume.

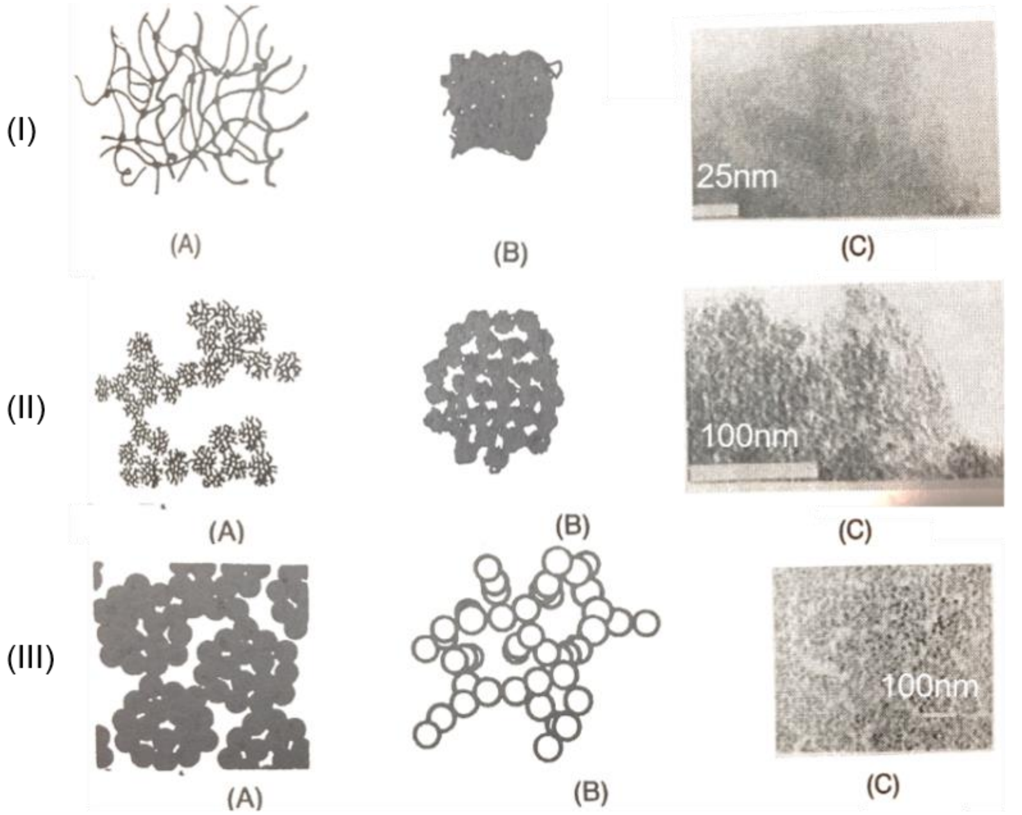

Figure 2.18 Schematic diagram of transfer between a) gel catalyzed under acid environment to b) xerogel catalyzed under essential acid-formation and dried at 50^{o}C for i) week branched, (II) normal branched, and (III) highly branched system. c) The TEM micrographs of xerogel showing the hierarchical gelation of colloidal particles.[77]

As shown in Figure 2.18I, the polymer with a week branched system, difficult to be penetrated by water after drying, namely acid-catalyzed silica. The gel structure is hydrophilic and has a low condensation rate. That structure is freely shrinking due to solvent evaporation. In addition, acid-based-catalyzed silica, a polymer formed by a highly branched system, exhibit higher absorbability of water and higher rigidity, as shown in Figure 2.18 b.[77] The drying of the solvent generated relatively big pores. During which, the individual cluster shrunk to rearranged the gel matrix.[77] Big-sized pores will reduce the capillary pressure, which largely decreases the shrinkage. In this structure, the porosity has two length scales. TEM identified the uniform particles in xerogels. The pore size is also related to the particle size. The big pore size will reduce the capillary force during solvent evaporation.[77]

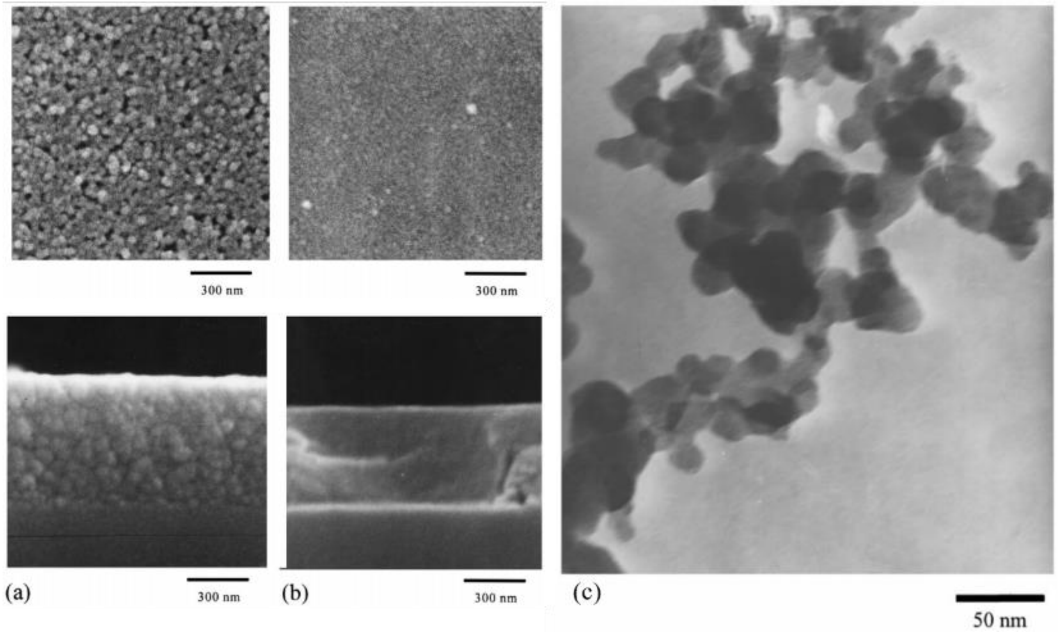

Figure 2.19. SEM images of silicon oxide xerogel a) with and b) without Trimethylchlorosilane (TMCS) modification. c) high-resolution TEM image of this xerogel.[78]

As shown in Figure 2.19, the modified film has high porosity and a low dielectric constant. TMCS treatment can transfer the original small-sized SiO4 gel into a mesoporous gel with a porous size of around forty nanometers and a porosity of about 50%.[78]

2.5.3 Summary

The gel is a solid material that has a matrix structure in nano/micro-scale. There usually exists pore liquid in the gap of the network structures. This special structure helps increase structural strength and structural toughness. The component can be a pure organic material or a combination of organic and inorganic material. There also have a pure-inorganic-material formed gel with excellent structural strength.

2.6 Coffee-ring Effect

Inkjet printing is a maskless printing technique with great potential to be the next to generate primary electrode fabrication methods. However, the deposition morphology of printing results is a big challenge for this technology. A drying droplet is a very complex system with lots of internal flows. It is very vulnerable to outside influences, including the temperature of the substrate, airflow above the droplet, surface properties of solid substrate, etc. Therefore, the deposition morphology is not uniform due to the coffee ring effect. In addition, the residual challenge of controlling inkjet printing results proposed, and the prospect of using inkjet printing to control deposition morphology is presented.

2.6.1 Formation Principle of Coffee Ring Effect

When a droplet is dry on the substrate, the internal solute deposits along the edge, leaving a ring deposition. It is the phenomenon of the so-called coffee ring effect.

Deegan et al.[20c] has revealed that capillary flow forms a coffee ring stain when a droplet is drying on a solid substrate as early as 1997.

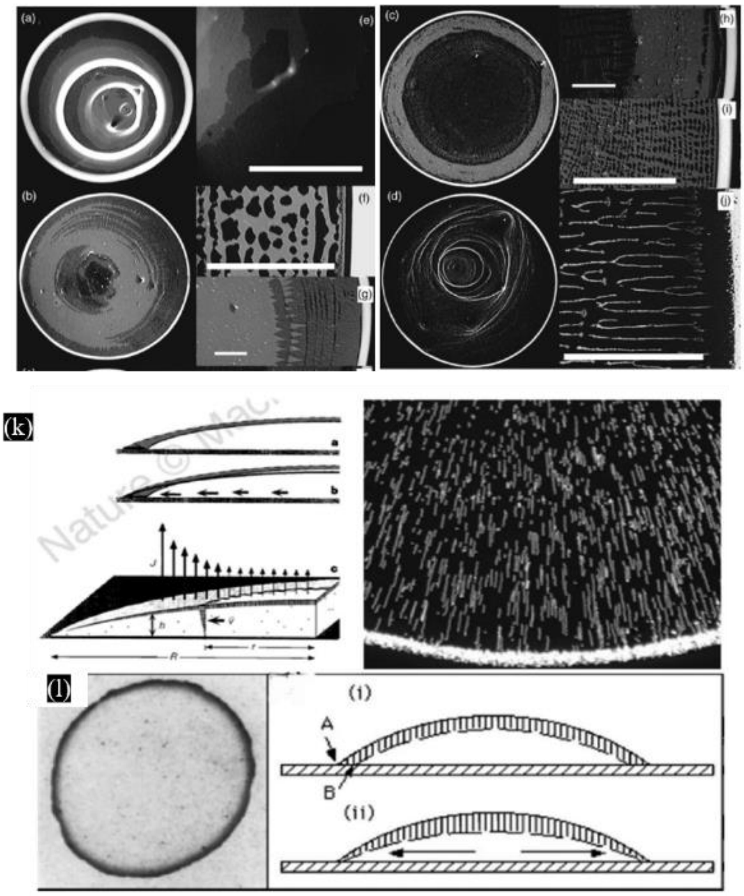

Figure 2.20. “Coffee ring” effect and its forming process. (a-d) Drying of a drop of liquid with different concentrations. This drop has a radius of six millimeters.[79] (k) The formation mechanism of coffee ring stain. The generation mechanism of capillary flow.[20c] (l) The top view of coffee ring stain with a diameter of five centimeters formed i) without and ii) with pinning of TCL line.[79]

Then, in 2000, Deegan et al. have introduced the concept of a three-phase contact line (TCL) to explain the coffee-ring formation mechanism. They have demonstrated that the solvent evaporation speed in TCL is much higher than in other places. As a result, the solution in the center will flow to the edges to replenish the lost solution. This flow is called capillary flow, which will carry the solute to deposit on the boundary and left a ring-shaped stain.

2.6.2 Methods to Suppress Coffee Ring Effect.

Suppression of the Outward Capillary Flow

Many methods can reduce the coffee ring effect. Soltman et al. have demonstrated that the excellent environment will suppress the capillary flow and deposit uniform patterns in 2008.[80] Then, Kukuda et al. have shown that increasing ambient humidity can modify the deposition morphology of the inkjet-printed ways.[19b] Then, in 2010, the connection of the droplet scale with topography has been investigated.[81]

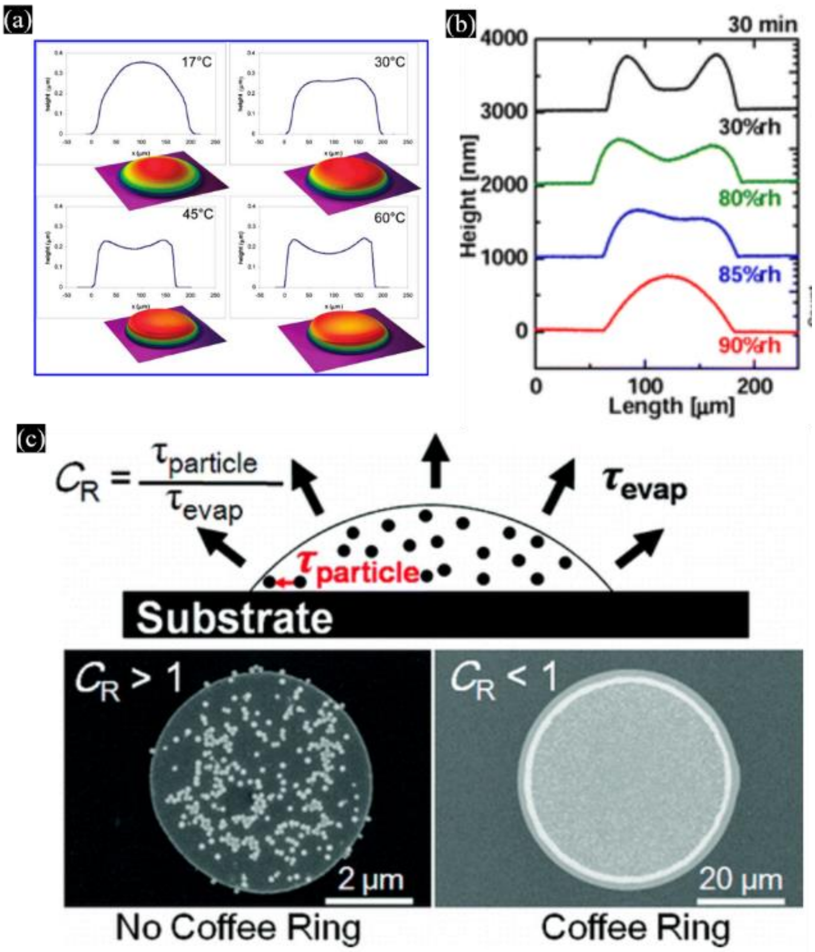

Figure 2.21 a) Optical profiler of the morphology of droplet deposit at different temperatures.[80] b) Profiles for the same electrodes with different humidifies.[19b] c) Diagram showing that the minimally sized droplet does not have a coffee ring effect. Using C_R as an evaporation rate-related stander to determine the possibility of forming a coffee ring stain.[81]

Besides these sample condition verification strategies, there were various of an attempt to eliminate the coffee ring effect. As shown in Figure 2.22a, as the outward capillary flow forms the coffee ring effect during drying, scientists using nanoparticles with different shapes as solutes to investigate the deposition result of the liquid droplet. As shown in Figure 2.22a, nanoparticle ink with a long strip shape and spherical shape have different deposition results. As shown in Figure 2.22b, Song et al. prepared microparticles as a solute of different sizes to study the coffee-ring formation mechanism in 2009.[82] Furthermore, Jaeger et al. have developed a unique way of eliminating the rough morphology based on decanethiol-ligated gold nanocrystal. This kind of nanocrystal can float to the surface of a liquid drop, as shown in Figure 2.22c.

In this way, capillary flow can hardly influence the deposition morphology of the inkjet-printed patterns. Therefore, a highly ordered monolayer structure would generate.[83] Anyfantakis et al. have reported the surfactant-mediated that interacted with particles modified the performance of colloidal suspension drops. As shown in Figure 2.22d, surfactants exert influence on the capillary flow achieved the perfect control of the strength of the coffee ring effect.[84]

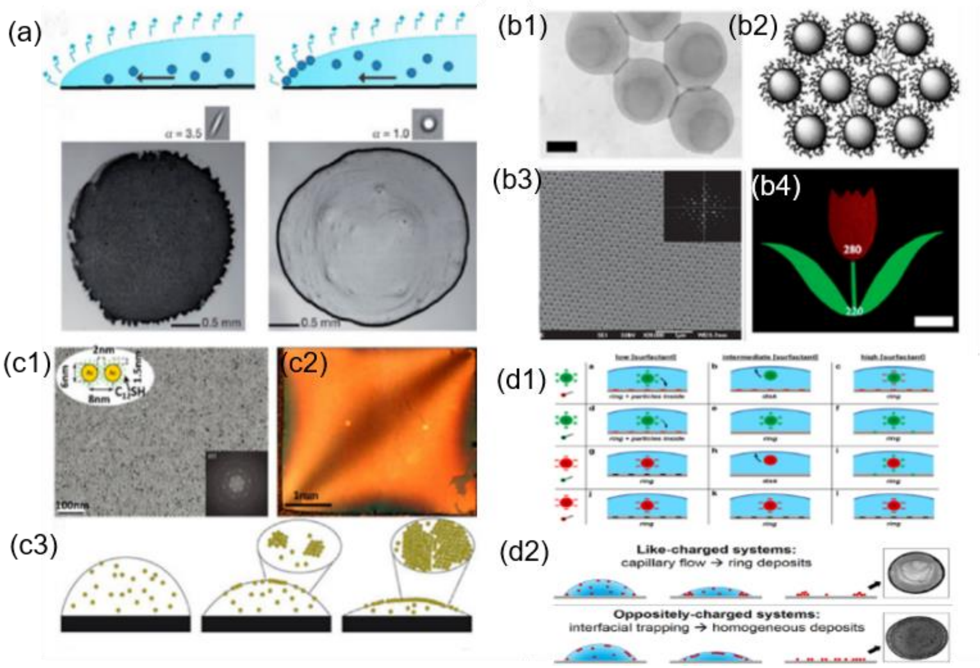

Figure 2.22 a) Schematic diagram and the optical image of the depositing result for nanoparticle solute with different three-dimensional shapes.[85] (b1) TEM organic balls. The unmarked scale size is100 nm. (b2) Scheme of the printed latex spheres bound together. (b3) Image of an inkjet-printed rouse-shaped pattern. (b4) SEM images of pattern region.[82] (c1) TEM image of droplet drying with dispersed Au crystals. Insert is the diffraction pattern of the inkjet-printed Au thin film. (c2) Optical microscopic image of the inkjet-printed crystals after drying. (c3) Schematic diagram showing the principle of forming the uniform layer of Au crystal.[83] (d1) Function of surfactants in the droplet drying system. (d2) Coffee-ring formation experiment showing the relationship of the formation of coffee-ring stain with the concentration of surfactants in ink.[84]

Increasing Inward Marangoni Flow

Another leading technology for Homogenization of the surface topography of the inkjet-printed patterns is by generating the Marangoni flow that can compensate the outward capillary flow. As early as 1865, C. Marangoni et al. discovered a higher force exerted on the surrounding fluid for liquid with higher surface tension.[86] The concentration gradient will generate an inward flow, namely Marangoni flow, by which particles near the droplet's surface are carried to the top, as shown in 2.6.4a.[86] This fluid is opposite to the capillary flow, which can carry the solute from the center region to the droplet edge and suppress the coffee-ring effect.

Researchers have developed various ways to generate and utilize the Marangoni flow. Moon et al. have added ethylene glycol (EG) in ink, aiming to form uniform surface morphology for inkjet-printed electrodes. The low evaporation rate of MEG is a critical component of the ink. The MEG component will be cumulated in the region near the TCL and form a MEG concentration gradient during drying. The concentration gradient will generate a Marangoni flow, which can transport the solute toward the center area of the printed pattern. As shown in Figure 2.23b, the high-quality design can coat the substrate by direct-write and coffee-ring suppression.[20b] As shown in Figure 2.23c, Cho et al. also successfully generated the Marangoni flow by adding dodecane, which also has low surface tension and high boiling point, to a chlorobenzene-based inkjet-printing ink.[87]

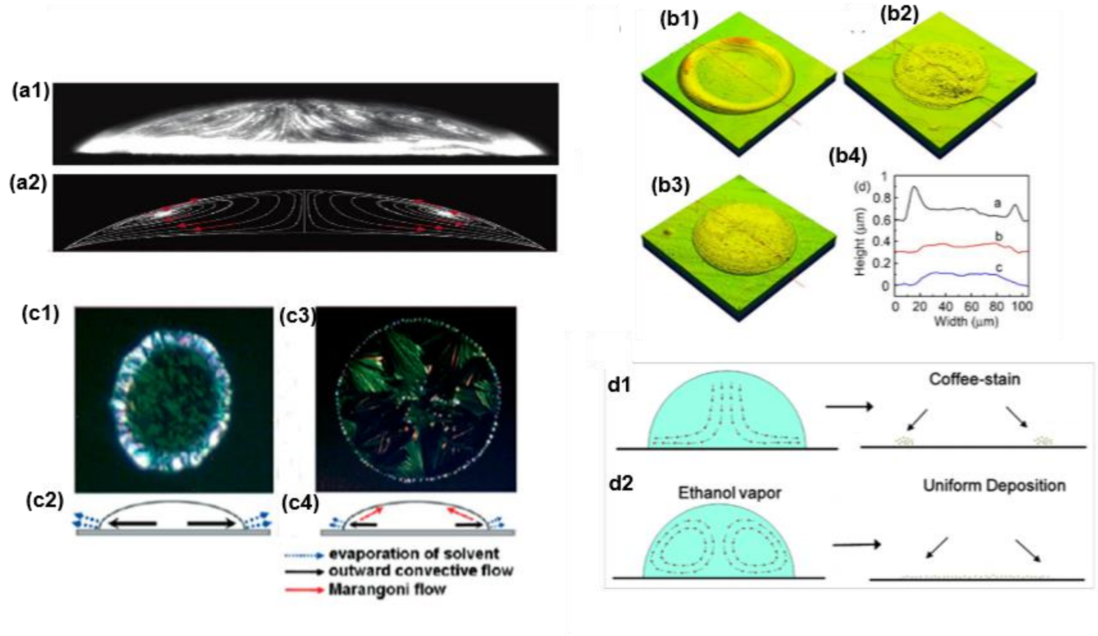

Figure 2.23 (a1) A drop of octane drying on the substrate. (a2) Predicted image showing the Marangoni vortex.[20a, 86] Confocal laser scattering microscopic image of the deposited strain of the ink with b1) 0%, b2) 16%, and b3) 32% of EG. (b4) Cross-

sectional image of the droplet stain with varying solvent composition.[20b] c) The polarized images and the schematic diagrams showing the distribution of the solute stain after drying of the ink droplets for (c1-c2) chlorobenzene solution and (c3-c4) mixed-dodecane solution.[87] (d1) Flows inside the drop during dying ambient conditions. (d2)flows inside the drops in the EtOH vapor environment.[88]

The generation of Marangoni follows we are not only can be formed by adding co-solvent into the inks. Majumder et al. have successfully generated Marangoni flow by verifying the drying environment.[88] As shown in Figure 2.23d, drying the droplet in an environment with EtOH vapor can form smooth surface morphology. This technique can increase the surface gradient of EtOH. The internal flow can offset the outward capillary flow.

Sliding of Three-Phase Contact Line

The coffee ring effect happened due to the enormous solvent evaporation rate in the three-phase contact line (TCL). As early as 2004, Young Ko et al. have studied the material deposition by a droplet with a movable TCL line.[89] As shown in Figure 2.24a, the hydrophilicity of the substrate made the TCL line subtract. The solute accumulated in the central area during droplet drying. As shown in Figure 2.24b, Minxuan et al. reported the first inkjet-printed pattern to simulate high height-to-diameter ratio deposition with a dome structure.[90] Tsao et al. have tried to print polymer matrix on different substrates, showing the receding of the TCL line. As shown in Figure 2.24c, a series of an image showing the verification of the contact angle during the drying process.[91] The receding of the TCL line can form polymer residue with a dome shape instead of a coffee ring effect.

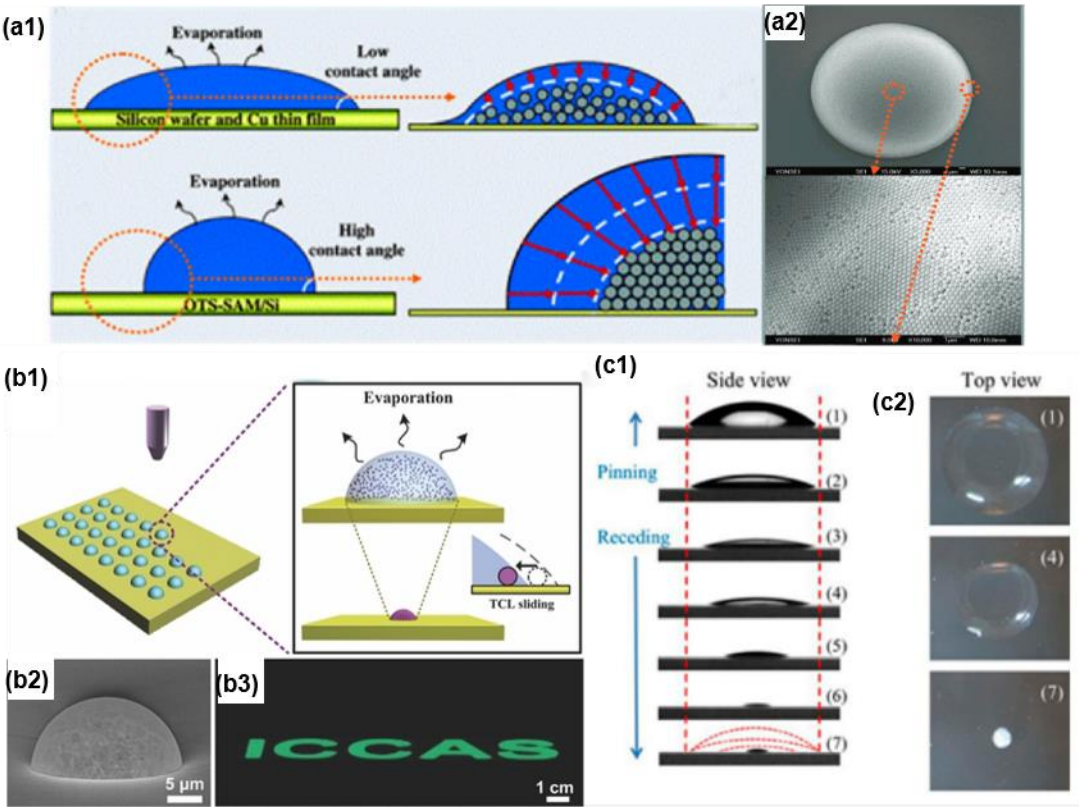

Figure 2.24. The sliding TCL controls depositing morphologies. (a1) Sketch of the self-assembling process of the droplet drying on a substrate with extremely high hydrophobicity of the substrate. (a2) SEM image of the gathered nanoparticles formed by the receding TCL.[89] b) Schematic diagram of regulating the deposition result of the self-assembly of the solvent during the droplet drying of the inkjet-printed droplets by the receding of the contact line. [90] c1) Images of the contact angle and c2) top view photos illustrating the receding of the TCL line for the polymer solution during droplet drying.[91]

2.6.3 Utilization of the Coffee Ring Effect.

The coffee ring effect naturally exists. Researchers made attempts to develop methods to utilize the coffee-ring product to form better patterns.

Magdassi et al. reported that the inkjet-printed silver nanoparticle ink could form nanotubes 150-meters-sized transparent conductive layer for electronics. It comprises countless ring-shaped conductive patterns in the ring of around 300 nm, as shown in Figure 2.25 a,[92]. Furthermore, instead of ring-shaped coffee ring stain, Zhang et al. have successfully printed line stains with the help of the coffee ring effect.[93] Therefore, inkjet printing technology can fabricate uniform, transparent messes with the use of coffee ring stain.

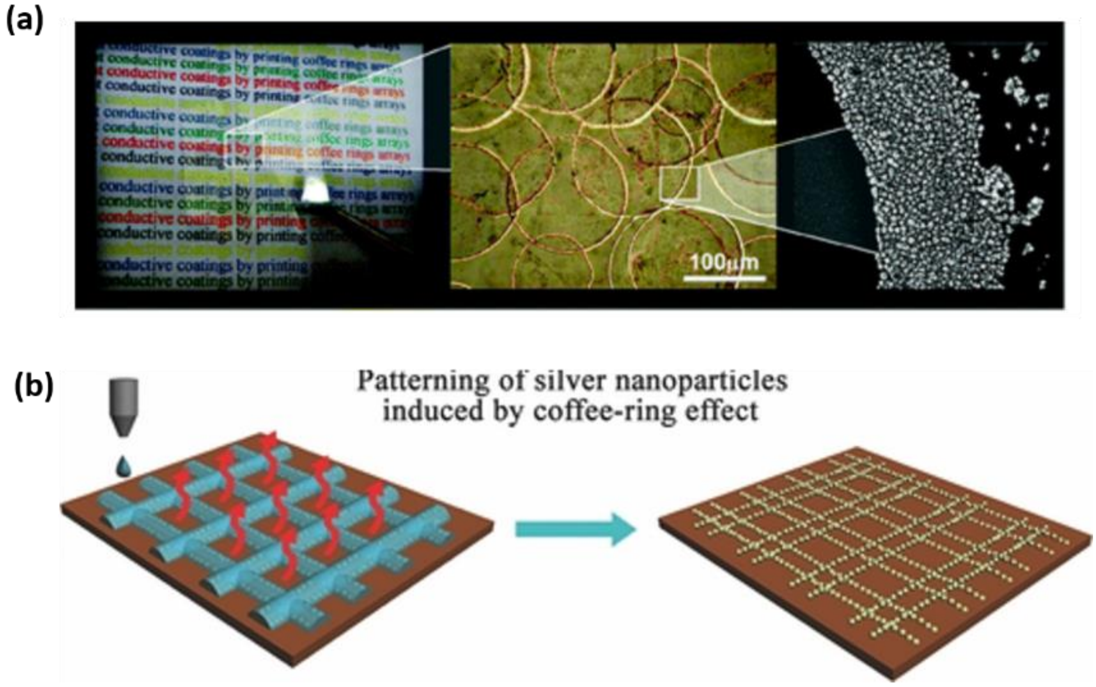

Figure 2.25 a) Optical and SEM images of the transparent conductive film formed by countless overlapped coffee ring stains of the silver nanoparticles. The width of the coffee ring stain is only around 300 nm.[92] b) Schematic diagram of inkjet printing of the transparent Ag electrode mash with the help of the coffee ring effect.[93]

2.6.4 Inkjet Printing with the Help of Patterned Substrate

Stringer described the inkjet-printing resolution as limited by the size of each droplet, which is usually bigger than 20 µm.[94] In addition, complicate drying processes also lead to irregular patterns. Inkjet-printing techniques have tried to fabricate electronics with higher resolutions to tackle these problems. The patterned substrate was able to control the deposition of the solution precisely. The hydrophobic and hydrophilic patterns are prepattern. When a droplet falls onto the substrate, the surface energy will exert an effect to prevent the overspreading of the droplet. The resolution increased dramatically.[95] Similarly, a 500-nm-long channel was inkjet-printed through surface energy-assisted inkjet printing. As shown in Figure 2.26b, the inkjet-printed materials on a hydrophilic substrate with an ultra-thin hydrophobic line.[96] The nanoparticle ink was dropped on the substrate with hydrophobic-hydrophilic patterns to make different forms of inkjet-printed droplets. The patterned substrate can induce a regulation function for the inkjet-printed droplets. As shown in Figure 2.26c, the assembled nanoparticles from the ink droplet can obtain various compact forms.[97] Mahajan et al. have demonstrated the first inkjet-printed droplet was deformed by high-resolution channels and left a high--resolution pattern. As shown in Figure 2.26d, the ink will automatically fill the channel driven by capillary forces. The combination of different length and width provide different maximum travelling length.[98]

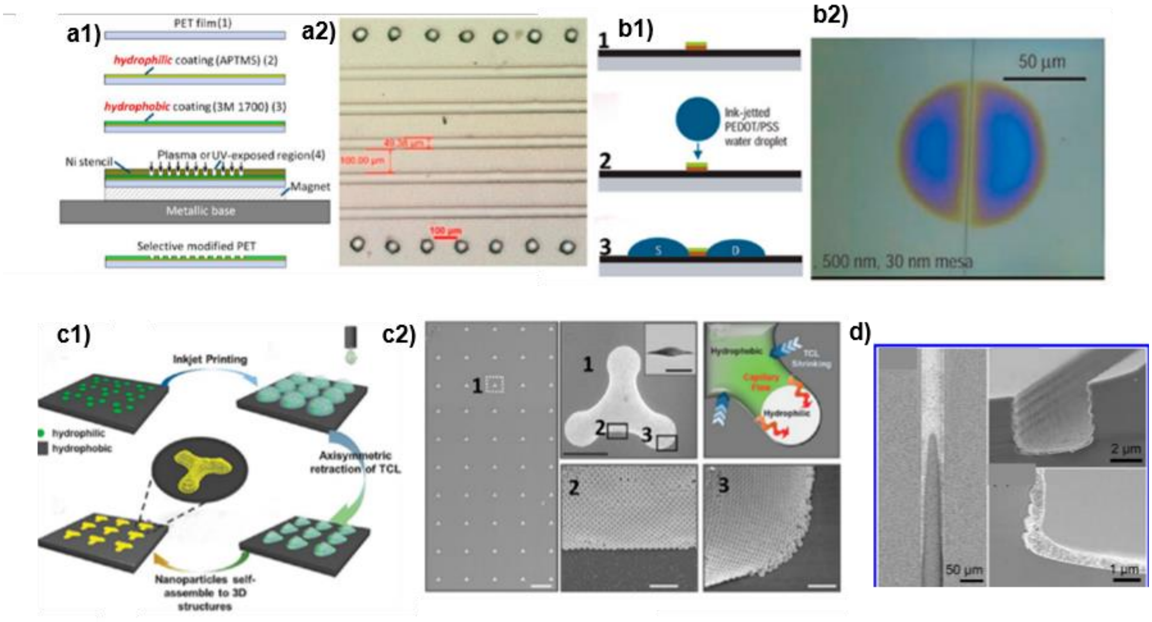

Figure 2.26 a1) Schematic diagram showing the fabrication process of the pre-patterned substrate, with the regional-change of hydrophilic, to improve the inkjet-printing resolution. a2) Optical microscopic image of the uniform lines formed by spreading the ink on the hydrophilic area.[95] b1) Schematic diagram showing the inkjet-printing of the ultra-narrow channel by pre-deposited hydrophobic line. b2) Optical microscopic image of on drop of inkjet-printed pattern divided into two parts by a hydrophobic line, with the line width of around 500 nm.[96] c1) Schematic diagram of the formation process of a three-dimensional structure by preparing the substrate with specific regional hydrophilic. c2) SEM images demonstrating the pattern with a clear 3D design after drying.[97] d) A pre-etched channel allows inkjet-printed ink to flow inside and form an electrode with a uniform boundary.[98]

2.6.5 Summary

The inkjet-printed pattern is rough due to the coffee ring effect. But the nature of drying droplets is difficult to be controlled. An outward capillary flow formed the coffee ring stain, which carried the solute to the TCL line. Various strategies, including weakening the capillary flow, increasing Marangoni flow, sliding of the three-phase contact lines, etc., were invented to improve the printing result. The slow-evaporation-rate cosolvent is the simplest method to suppress the coffee-ring effect and has almost the least equipment requirements. As the coffee ring effect is an intrinsically existing phenomenon, the scientist also attempted to utilize it to inkjet print ultra-thin patterns, with the line width of ~500 nm, to form transparent electrodes. The study and utilization of the coffee ring effect provide the foundation for the possible improvements in the inkjet-printed electronics' quality.

CHAPTER 3. METHODOLOGY

This section discussed the general methodology for the experiments. The project involves the fabrication of the inkjet-printable copolymer ink, and the Cu electrodes were grown based on the inkjet-printed gel and xerogel patterns. Furthermore, methods for demonstrating mechanical porosity, such as adhesiveness, roughness, crystal forms of the thin films, will be elaborated.

3.1 Inkjet Printing Technique

The inkjet printing technique is a maskless, non-contact, additive patterning approach allowing the deposition of low-cost thin films materials with variable computer designs for flexible and wearable electronic devices. As shown in Figure 3.1.1b, the regular voltage pules exerted on the piezoelectric part of the printing tube generated the uniform droplets. This printing method enables multi-nozzles, large-area, high-volume printing of high-resolution patterns, and system error around 5µm.[99]

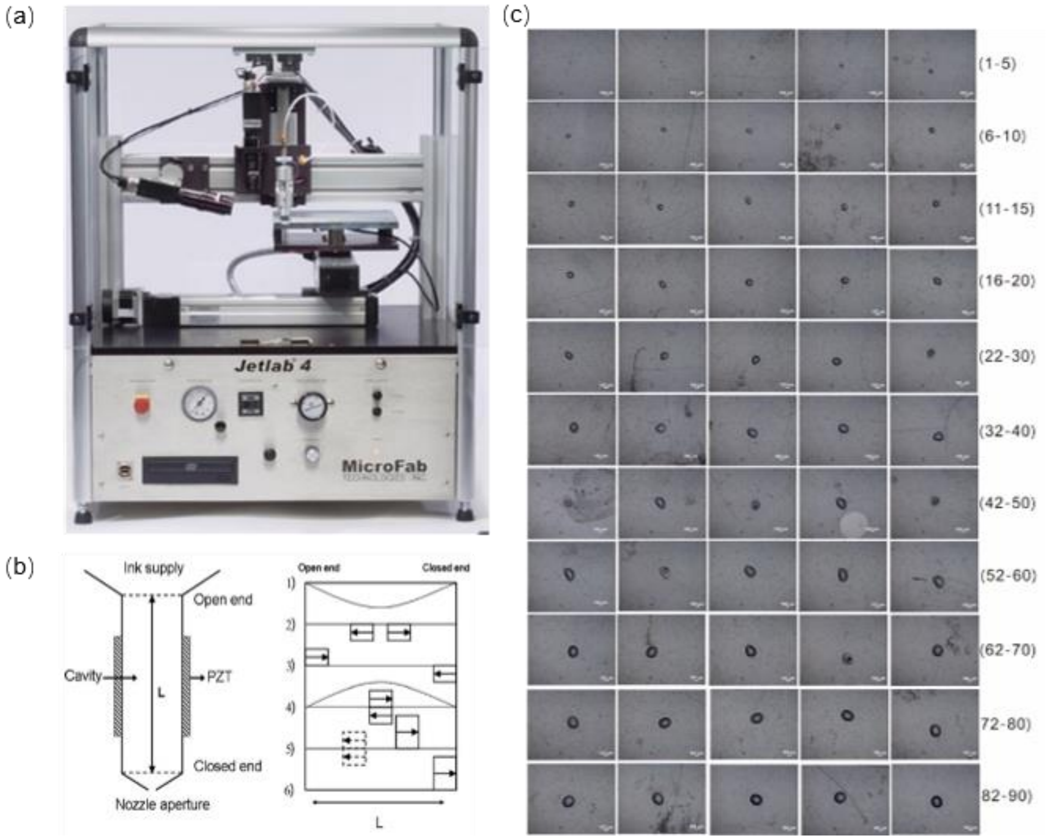

Figure 3.1. a) Inkjet Printer of Jetlab@4. b) Sketch demonstrating the working principle of the inkjet printing head and the electric signal exerted on the piezoelectric unit of the tube to the regular jet droplet. c) Drop size control by in-situ printing. Optical

microscopic images show the inkjet-printed aqueous ink printed with variable spot size controlled by script syntax on the PET substrate. The drop number is on the right side. For example, the diameter of the smallest drop is around 35µm made by one inkjet-printed drop. The biggest one is 216 µm in diameter, formed by 90 drops.

The well-designed pattern, stored in Bitmap, can be installed on the Jatlab®4 inkjet printer to carry out the drop-on-demand mode of printing. But this kind of regulation is still relatively rough. It may cause imprecisely printing of patterns due to irregular immerging of the inkjet-printed drop arrays. Nevertheless, the flying mode can control the number of drops, jetting frequency, and flying speed at the same time for precise control of the printed drops. In addition, as shown in Figure 3.1c, a script syntax controlled the spot size of the inkjet-printed pattern achieved by inkjet printing a series of droplets in the same place.

3.2 Preparation of Three-solvent Copolymer Ink

Preparation of copolymer ink: Dimethylformamide (DMF), ethylene glycol (EG), and deionized water, mixed in a weight ratio of 89:4:7. Then 0.5 w% pin-needle-shape copolymer (P[MBP]-co-[METAC]) was added to the cosolvent system and fully dissolved under an ultrasonic bath for about 30 min. Then, filtered by a Teflon filter (a pore size of 0.45 µm).

3.3 Droplet Monitoring System to Detect Droplet Formation

To avoid the “drop formation problem,” a part view CCD camera on one side of the inkjet-printing head captures the digital image during the inkjet-printing process. The side view of the CCD camera to study the drop formation.

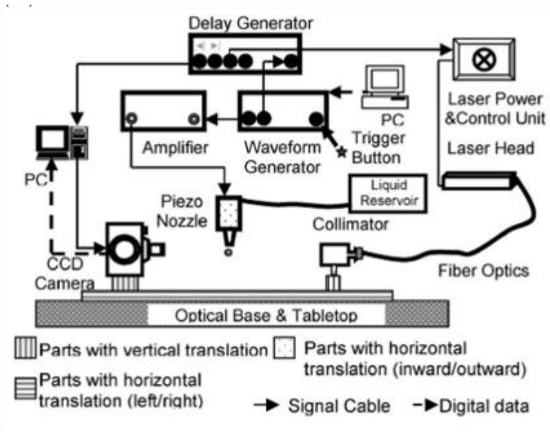

Figure 3.2. a) Experimental setup of the inkjet printing system.[100] The CCD camera on one side of the inkjet-printing head captures the digital images of the droplet formation.

3.4 Highly Conductive Flexible Metal Electrodes Prepared by PAMD Techniques

3.4.1 Preparation of Traditional Cu Electrode Using Single-solvent Copolymer Ink

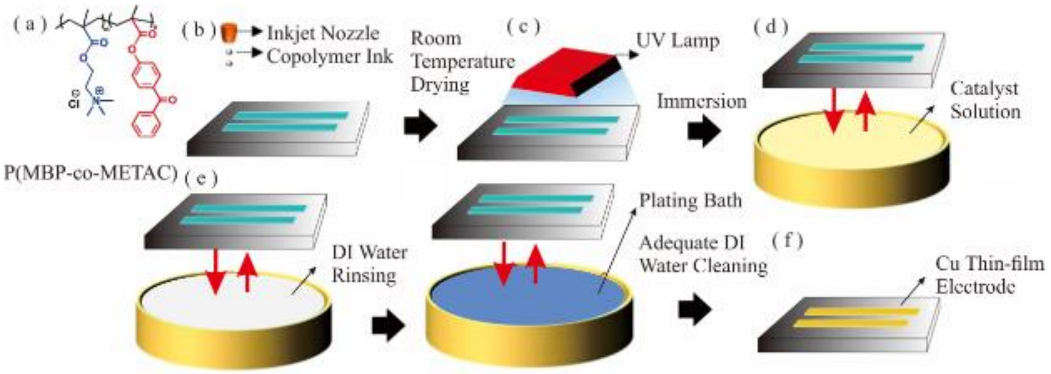

Figure 3.3. The original copolymer ink for inkjet-printing of the PAMD-based Cu electrode. a) The chemical formula of the P(MBP-co-METAC) copolymer. b) Inkjet printing of the copolymer patterns on flexible electronics. c) Exposure to UV light for copolymer cross-linking. d) Catalyst bath. e) DI water raining. f) Copolymer-gel-assisted metal electroless deposition.

As shown in Figure 3.3, the original copolymer ink, poly (4-methacryloyl benzophenone-co-2-methacryloyloxy ethyltrimethylam-monium chloride) [P(MBP-co-METAC)] solution (1% in 2 methoxyethanol), will be printed by the inkjet printer JetLab@4 MicroFab on plastic substrates, including PT, PS, PI, etc. After drying in the fume hood, the samples passed UV light treatment (e.g., 9W U-shape UV lamp) for about 45 min. Then the substrate with copolymer pattern passed a 45-min-catalyst bath in the 5 mM/L ammonium tetrachloropalladate solution. Finally, immerse the substrate in the electroless plating solution for copper growing in a liquid environment.

3.4.2 Preparation of Gal and Xerogel Based Cu Electrodes Using Three-solvent-Copolymer Ink

The freshly prepared three-solvent copolymer ink was mounted onto the Jatlab®4 inkjet printer and printed onto various plastic substrates with drop-on-demand mode. We set the dwell time, operation voltage, and backpressure of the inkjet printer to be 5 µs, 36 V, and 2.6, respectively. The droplet spacing of the pattern was ~45 µm when choosing the 50-µm-wide printing head. After drying the inkjet-printed gel paste at room temperature of around two h, the samples were exposed to a UV lamp (SB-100PA/F) for 45min at a distance <2 cm, make sure that the 365-nm-UV-light have the energy of ~20 mW cm^{-2}. A gel thin film that was well attached to the plastic substrate. Then the gel thin film was washed by running EtOH for around 8s to create xerogel. For the gel-based Cu electrode, the pattern carried out a catalyst bath directly, without EtOH treatment. The samples passed the treatment of immersing in the aqueous solution of 5 mM $(NH4)_2 PdCl_4$ (J&K) for 30 min. The sample thin film was then cleaned evenly in fresh DI water with the ultrasonication for 10s. After blowing dry by air gun, the sample thin film passed the immersion into freshly mixed electroless deposition solution A and B for metal electroless deposition. Solution A stands for an aqueous solution of sodium hydroxide (300mM, J&K), copper (II) sulphate pentahydrate (52 mM, J&K), and potassium sodium tartrate (126 mM, J&K) in DI water. Solution B stands for an aqueous solution of formaldehyde (315 mM, J&K). The substrate was then cleaned with DI water and dried with an air gun.

3.4.3 Preparation of Polymer-brush-based Cu Electrode

Firstly, the surface hydrophilic of the plastic and glass substrate passed the oxygen plasma for 4 min. Then immersed into MPS (0.5 w%) alcohol solution for one h. For Au substrate, the cleaned Au substrates passed the treatment by ethanol solutions of the ATRP initiator ω-mercaptoundecyl bromoisobutyrate (MUDBr) (2.5 mg/mL) at room temperature for 24 h to form a self-assembled monolayer (SAM). After ethanol rain and drying, we got the SAM modified Au substrate. Later, the polymer brush of METAC was grown in an aqueous solution of METAC (150 g/L, Sigma-Aldrich) with a concentration of 20 wt% blended with KPS (2.5 g/L, Sigma-Aldrich). The METAC was grown in an environment of 80 ^{o}C for one h. Then, the PMETAC modified substrates were cleaned with DI water and dried with a clean nitrogen spray gun. An aqueous solution of 5 mM ammonium tetrachloropalladate (II) treated the polymer-brush-based Cu electrode for 30 min. Then carry out electroless metal deposition by freshly prepared ELD solution. The thickness of the metal electrode changes with ease by verifying the duration of metal electrode deposition.

3.4 Material Characterization

The material component and electronic property of as-made metal electrodes were strictly tested by characterized. X-ray diffraction (XRD), atomic force microscope (AFM), optical microscope and scanning electron microscope (SEM) characterize the properties, including microstructures, morphology, and film thickness. The scotch tape test and the nanoindentation investigated the adhesion of the thin metal film to the substrate. The 4-point probe methods will first measure the conductivity of the electrodes. The Nikon Eclipse 80i optical microscope (Nikon, Tokyo, Japan) demonstrated the metal electrode. The transmission electron microscope (TEM) investigated the nanostructure of the cross-sectional image of the Cu and copolymer interpenetrating network. The sample milled by JIB-4510 of TEM sample, to a 100-nm-thick slice, is by, an act as, was made by a dual-beam multi-system FIB (JEOL Model JIB-4501).

3.4.1 Atomic force microscope (AFM)

Atomic force microscopy provides a three-dimensional profile of the surface on the nanoscale by measuring the force between a sharp probe (<10 nm) and the surface of the sample at a short distance (0.2-10 nm). The examination proves grown on a flexible cantilever. The AFM tip can detect the surface morphology of the sample and records the atomic force between the probe and the surface to depict the topographical image of the samples. The operation mode of AFM has two branches: contact mode and non-contact mode. Both can provide detailed information on the surface of the samples.

Tapping-mode AFM is a operation mode, different from the non-contact mode and the contact mode; The probe contacts the samples surface in an expeditious way by the oscillation of the cantilever. This way got rid of the possible damage of the brittle sample by the forces in the horizontal direction during testing. The laser was aligned on the cantilever portion of a probe (NP-S, standard, Bruker) for enabling the engage (automatic lowing) function. Then we used a drop of DI water to cover the sample (under the transparent fluid probe holder), followed by a careful lowing of the tip until the AFM tip was thoroughly immerged into the water drop. Then, the laser was re-aligned. The measurement can start after clicking of engage button for putting the probe to the tapping range. Then the tapping mode was chosen in software for scaning the profile of sample under water. The scanning rate was 1 Hz.

2.4.2 X-ray diffraction (XRD)

A beam of x-ray illuminated the sample in the x-ray diffraction instruments. The x-ray tube and detector move in a synchronized motion. The XRD can record and graph the peaks about the sample's atomic structure. Atoms are composed of a nucleus surrounded by a cloud of the electrode. If the wavelength of the incident x-ray is similar to the atoms' spacing of the specific sample, there will be a special interference effect, namely diffraction. Therefore, it can measure the distance between atoms. The angle between the incident and the scattered beam is called 2θ. According to Bragg's law:

$$n\lambda = 2dsin\theta$$

This value can reflect the crystal structure of the samples. This technique has been widely used for various materials, ranging from a single-crystal epitaxial thin film and the polycrystalline mixture of powder and even randomly oriented amorphous materials.

3.4.3 Scanning Electron Microscope (SEM)

Scanning electron microscope (SEM) can use electrons to replace optical light as the major medium to detect samples with higher resolution. Reducing the resolution limit from 400-700 nm to less than 1 nm. The electrons are accelerated away from the filament by an applied voltage. This voltage can go up to around 30000 V in a typical SEM. Then the electron passes through a serious magnetic lens to focus and initiate scanning operation on samples in different positions. A series of signals, including Auger electrons, secondary electrons, backscattered electrons, can be collected and be used to produce images. Secondary electron images show surface features of the sample; therefore, they look three-dimensional. Backscattered SEM images show fewer surface features. Majorly been used to detect embedded particles. And most of the modern SEM is equipped with energy-dispersive X-ray spectroscopy (EDS) to mapping the element distribution on the surface of samples.

3.4.4 Transmission Electron Microscope (TEM)

Similar to SEM, the transmission electron microscope uses electrons and a magnetic lens to scan and detect the micro/nanostructure of samples. In addition, the atomic structure of samples can be detected by various detection types, including parallel-beam diffraction, Kikuchi diffraction, and convergent beam diffraction, by TEM. And there are three types of contrast (i.e., mass-thickness difference, diffraction contract, and phase contract) to generate TEM images. The mass-thickness contrast can create biological ideas. Diffraction contracts can reflect topographic defects. And the phase contract is for studying the atomic structure. The diffraction of the sample can give the structure information of samples. And the spectroscopy of TEM can provide the chemical information of samples. The modern TEMs usually equipped with two spectroscopy techniques, including energy-dispersive x-ray spectroscopy (EDS) and electron energy loss spectroscopy (EELS). Using EDS, we can get the chemical information. While using EELS, we also can get the chemical bonding information. Combining EELS and EDS, we can generate the EELS spectroscopic mapping to demonstrate the regional distribution of specific atoms.

3.4.5 JIB-4510 Dual-beam Multi-system FIB

Multi-system focused ion beam (FIB) is an advanced milling technique with high operation speed, accuracy. It utilized an ion beam current to characterized and modify the topography of the sample. Therefore, it is usually to prepare TEM samples. The maximum energy is ~90 nA. The SEM component is to detect the real-time progress of the milling operation. The low-energy ionic Argon is commonly used to carry out fine polish of the TEM samples. There is also a high-resolution 3D reconstruction system using the working principle of FIB.

3.4.6 Nanoindenter

Triboindenter equipped with several individual functions, including nanoindentation, nanoscratching, and nanowearing, provide a strong ability to measure the mechanical properties of thin-film materials. The nanoindentater is used to measure the mechanical properties of a small amount of materials or for testing the thin film materials. The nanoindenter can grasp many mechanical properties, including elastic modulus, cracking toughness, viscoelastic properties, and hardness of the thin film materials. During the test, a rigid probe (made of diamond) applies vertical loading and reloading. The sensors on the probe measure the vertical displacement of the probe. For the nanoscratching test, a stylus scratches the substrate with the application of vertical ramping load in accompany with the horizontal displacement at a constant velocity. The scratching width data can derive out the hardness of samples according to the following function:

$$H_s = H_{ref}\left(\frac{L_s}{Lref}\right)\left(\frac{W_{ref}}{W_s}\right)^2$$

The H represents hardness, while L and W represent normal load and scratching width.

Nanoscratching test can test the adhesion of thin-film coatings to the substrate. The scratching head scratched the surface with a ramping load. The measured critical normal load Lc is related to the adhesiveness of the thin-film coating to the substrate. The interfacial adhesive energy can be further calculated by[101]:

$$G_c = \frac{\sigma_c^2 t}{2E}$$

Where t is the film thickness, and E is elastic modulus. σ_c Represent for the critical stress.

3.5 Durability Test for Metal Thin Film Electrode

The as made electrodes on an xyz mounting stage with bending ability. The bending varies from +180° to -180°. Two ends of the electrode are attached to 2-point probe measuring systems. The curve of bending cycles vs resistance demonstrates the durability of the electrode during bending. The fatigue tests usually have testing cycles ≥ 1,000.

3.6 Characterization of OTFTs and OECTs

The operation current and transfer current of the inkjet-printed organic thin-film transistors (OTFTs) can be measured by the micromanipulator probe station 450PM-B with Keithley 4200-SCS semiconductor parameter analyzer. This system detects the verification of voltage and current on three electrodes of the transistor. The electrical properties of semiconductor films and the performance of OECTs will be characterized at room temperature by a semiconductor parameter analyzer (KEITHLEY 2400). Parameters regarding the interpretation of OECTs, such as threshold voltage, sub-threshold swing, will be extracted from the *Id-Vg* curve to detect the working function of OECTs. The various solvent addition signals will be read by KEITHLEY 2400.

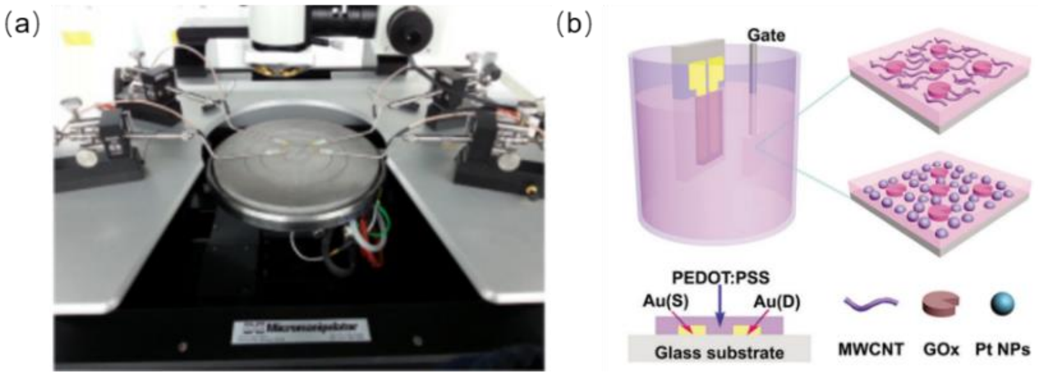

Figure 3.4. a) The micromanipulator probe station 450PM-B with Keithley 4200-SCS semiconductor parameter analyzer.[102] b) Schematic diagram of a measurement system for inkjet-printed disposable OECTs.[103]

3.7 Print PAMD-Based Cu electrode on Latex Substrate

Rubber balloon film was firstly cleaned by organic solvents, i.e. acton, isopropanol and alcohol, for 30 min with the treatment of ultrasonication. Then the 2-methoxyethanol based copolymer ink with 5w% was inkjet-printed on pre-cleaned latex substrate by the Jetlab@4 inkjet printer with a dwell time of 5µs and operation voltage of 35v. The droplet spacing was 50µm. After adequate drying at room temperature, an around 50-nm-thick polymer paste thin film is coated on the latex substrate. Then exposure the thin film under UV light, Spectroline MODEL SB-100PA/F, for 45 min for UV-crosslinking to form a gel thin film. The gel thin films passed the immersion treatment into a 5 mM ammonium tetrachloropalladate(II) aqueous solution for 30 min. After adequate DI water cleaning, the patterns on rubber film passed the immersion treatment in an electroless metal deposition bath for 30min electroless metal deposition.

CHAPTER 4. Smooth and Neat Cu Electrodes Grown on the Inkjet-printed Xerogel Scaffold that Attached to Plastic Substrate with High-adhesion Force

4.1 Introduction

The ever-increasing connection of people with the electronic world contributes to developing more low-cost electronic devices to meet people's increasing needs. Recently, the printed thin-film electronics are an attractive field aiming to allow low-cost electronic devices, such as smart packaging,[104] organic light-emitting diode (OLED),[105] wearable sensors,[106] and radio-frequency identifications (RFID),[107] to improve the living stander of human beings. However, the metal electrodes, one of the major components of electronic devices, are difficult to be printed on flexible substrates since metal material is intrinsically difficult to attach to normal plastic substrate substrates with smooth surface morphology. Nowadays, the mainstream technique for printing metal electrodes is by joining printed noble metal nanoparticle inks during a sintering process (>150 °C [11a]) on the plastic substrate. However, this high-temperature sintering process can cause deformation and aging of many heat-sensitive plastic materials such as polyethylene (PE) and polyethylene terephthalate (PET). Moreover, the utilization of noble metal (e.g., Ag and Au) enormously increased the cost of the printing industry, which violate the original intention of choosing printing technologies known for being cheap. However, non-noble metals (e.g., Cu and Ni) are difficult to form functional nanoparticle (NP) inks since they are easy to form unconducive oxidizes by the high-energy-consumption curing process. Aiming to prevent the oxidation of Cu nanoparticles during high-energy curing, scientists invented unique sintering methods, such as laser sintering,[13] pulsed-light curing,[14] flashlight curing,[16] and oxalic-acid-protected sintering of Cu NP.[12] However, most of these methods still require a rapid temperature rise on the surface area[14, 16] and negatively impact lots of heat-sensitive plastic or biological substrates. Moreover, these Cu NP inkjet-printing techniques also have problems such as rough surface morphology,[12] repeated merging and fracture at high temperature,[12] limited ink storage time,[17c] and low adhesiveness to the plastic substrate. Organic additives generate the additives after the sintering process.[17]

In contrast, the polymer assisted metal deposition (PAMD) technique prevented all the problems mentioned above, enabling room-temperature fabrication of non-noble-metal (e.g., Cu and Ni) electrodes on an inkjet-printed polymer matrix on a plastic substrate.[18b, 18e, 18h, 19a, 108] However, the current inkjet-printed PAMD-based copper electrodes have a sharp coffee-ring stain[20c] in boundary areas. This electrode needs to rely on vacuum evaporation methods to prepare the upper functional layer electronic devices without current leakage across the upper layers.[19a] Here, we report methods to grow uniform Cu electrode patterned by an inkjet printer on the plastic substrate.

The flatness of the xerogel-based Cu electrodes comes from the following ways. First, the coffee ring effect, originated by an outward trend of Capillary flow, was offset by adding a slow-evaporation-rate cosolvent to initiate an inward Marangoni flow in the inkjet-printed droplets.[20a, 20b] Secondly, the inkjet-printed gel thin film was converted into xerogel accompanied by overall shrinkage that achieved further smoothen of the polymer film. The inkjet-printed gel thin film was transformed to xerogel by an (EtOH) solution replacement. This operation removed the liquid entrapped in the gel pores. And the polymer cluster that not completely bonded to the overall polymer network. Finally, 4-extra-treatments, including flowing EtOH treatment, adequate cleaning after catalyst bath, intermittent immersion at the first half and second half of the Cu electroless deposition (ELD) process, ensured the uniformly growing of Cu on the inkjet-printed mesoporous xerogel. The final product Cu electrodes have a double-layer structure, consisting of an upper-pure Cu layer and a bottom interpenetrating copper and xerogel matrix network. The EtOH treatment also increased the thickness and strength of each polymer cluster that provided stronger toughness of the xerogel-based Cu electrodes. On PET substrate, the nano-scretching tests demonstrated that the xerogel-based Cu electrodes have higher adhesive energy (~0.7 J/m^2) when In comparison to the polymer-brush-based Cu electrode (a traditional PAMD technique) (≥ 0.06 J/m^2) or the thermal-evaporating technique (~ 0.06 J/m^2) with an adhesive layer of Chromium (Cr). Besides, this kind of inkjet-printed xerogel-based Cu electrode has a smoothed surface suitable for fabricating all-printed electronic devices.[19b] As a proof-of-concept, we directly spin-coated and printed functional materials on the top of the smooth Cu electrodes to form low-cost organic thin-film transistors (OTFTs) and organic electrochemical transistor (OECTs) without the help of any high-energy-consuming evaporation techniques. In addition, the EtOH operation step (transferring the gel thin film to xerogel) and specific precautions largely suppressed the immerging rate of the contamination. Therefore, the xerogel-gel based Cu electrode can use inkjet print precise electronic circuits with a condensed design. The xerogel-based Cu electrodes have a wide range of uses. It can be directly inkjet printed on the normal plastic bag for supermarket shopping. In addition, the xerogel-based Cu electrodes can be etched away with ease by dilute nitric acid solution so that it will not hinder plastic recycling. These high-quality Cu electrodes will replace many Noble-metal-NP inkjets for the printing industry and bring the low-cost electronic device to our side.

4.2 Fabrication of Xerogel-based Cu Electrode

Figure 4.1 demonstrates the significant operation steps for fabricating highly adhesive xerogel-based Cu electrodes, with no severe coffee ring effect[80], on the plastic substrate. Firstly, a slow-evaporation-rate cosolvent ethylene glycol (EG), with a slow-evaporation rate (i.e., 0.01 for nBuAC=1), initiated Marangoni flow for coffee-ring suppression. And a droplet, under the drying process, is unbalanced.[20c] The three-phase contact line (TCL) [79] region, close to the droplet edge, have a higher drying velocity. Therefore, the accumulation of EG, difficult to evaporate, can generate a concentration gradient, which will initiate Marangoni flow[20a] to compensate for the Capillary outward flow,[79] in Figure 4.1a.[20b] In a typical experiment, a dumbbell-shaped pattern was inkjet-printed (by Jetlab@4) on the surface of a polyvinylpyrrolidone (PVP) thin film that spin-coated on a polyethylene naphthalate (PEN) substrate to smooth the surface of PEN. The inkjet-printing ink, made by dissolving 0.5w% poly (4-methacryloyl benzophenone-co-2-methacryloyloxy ethyltrimethy-lammonium chloride) [P(MBP-co-METAC)] ink into a three-solvent system that composed of 4 w% of ethylene glycol (EG), 80 w% of dimethylformamide (DMF), and 16 w% of DI water. Figure 4.1e illustrates the cross-sectional profile (obtained by a Bruker DektakXT surface profiler) of an inkjet-printed gel pattern without a coffee-ring stain. Secondly, the inkjet-printed gel pastes crosslinked under ultraviolet radiation to form gel thin films. During the UV-crosslinking, the MBP group, a benzophenone moiety, of the copolymer [MBP-co-METAC],[109] was activated and provided covalent bonds to connect with various chemical groups, including plastic substrates (e.g., PET, polyethylene, and polyvinylpyrrolidone (PVP)), molecules of organic solvents, or the chains of the polymer itself (Figure 4.1b). This photochemical reaction for self-crosslinking generates a polymer network partially held with the plastic substrate by covalent bonds.

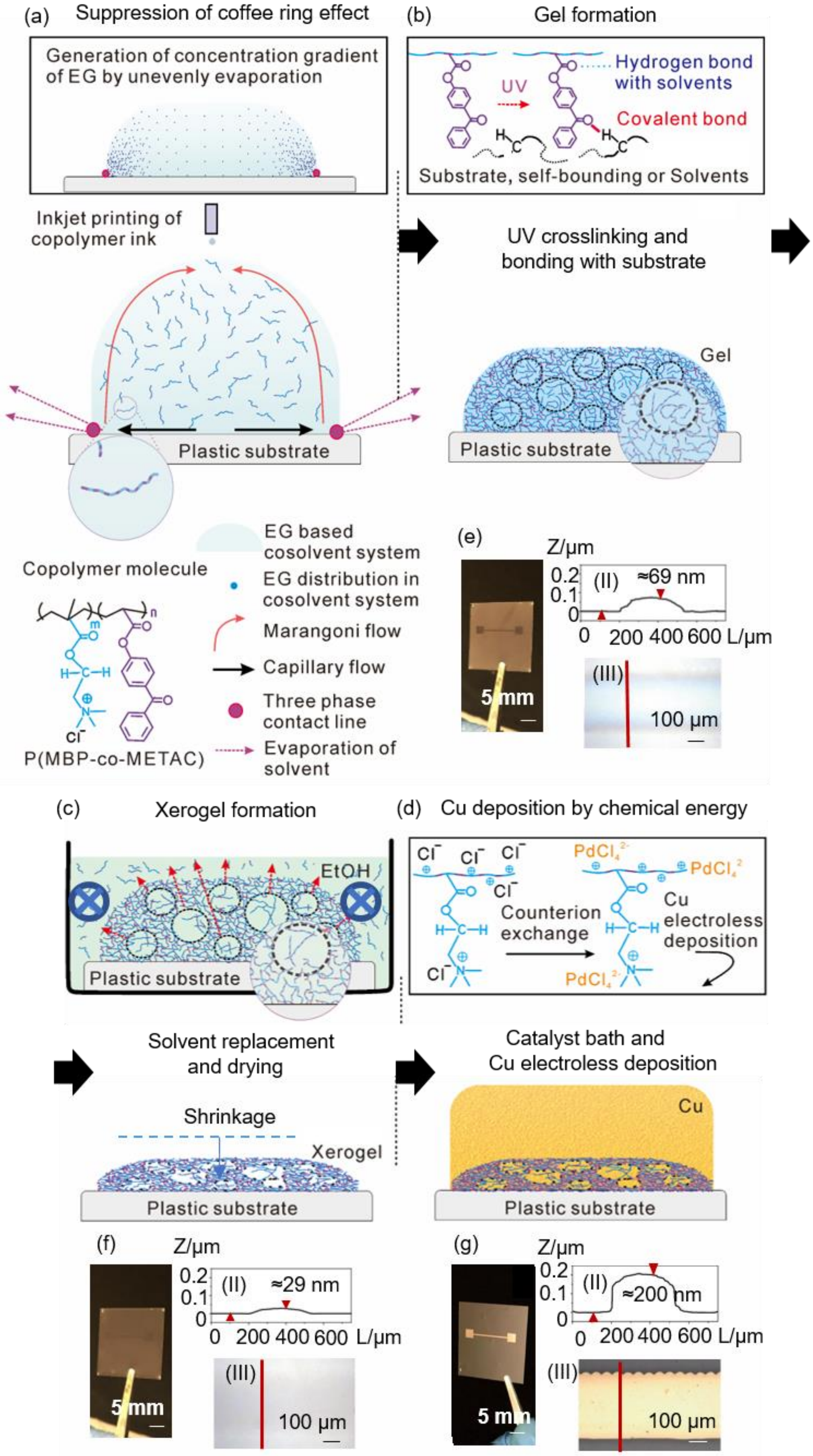

Figure 4.1. The fabrication process of the xerogel-based Cu electrodes. a) Schematic diagram of the cross-sectional view of the drying process of the inkjet-printed copolymer ink. The slow-evaporation-rate EG as a major cosolvent can generate a inward Marangoni flow to suppress the outward capillary flow (major causing effect of coffee-ring stain). b) Schematic diagram and the possible chemical reactions that happened during the UV-crosslinking process. The circular dotted lines surrounded the copolymer network either failed to bind to the overall copolymer matrix or were well crosslinked during the UV-crosslinking step. c) Schematic diagram of EtOH cleaning step for xerogel formation. The blue-cross sign demonstrates that the EtOH solution is flowing, not stagnant. d) Schematic of the catalyst immobilization and Cu electroless deposition to form xerogel-based Cu electrode. A typical xerogel-based Cu electrode’s I) optical photos, II) cross-sectional profile images, and III) optical microscopic image in different fabrication states, including e) gel states, f) xerogel states, and g) Cu electrode states. A spin-coated PVP thin-film covered the PEN substrate to improve the surface uniformity. The electroless deposition time was 5 min. The circular magnifying-glass-shaped areas provide a magnified view.

However, when we directly used gel thin film to grow Cu in electroless deposition (ELD) solution, a large extent of contamination appeared for both the original single solvent copolymer ink (Figure 4.2a) or the newly invented three-solvent copolymer ink (Figure 4.2b). Therefore, we invented a precaution step, namely EtOH treatment, that efficiently reduced the occurrence rate of contamination. Figure 4.1c illustrates the EtOH treatment's schematic concept that converts the gel thin film to the xerogel scaffold. During this process, the EtOH flow washed away liquid entrapped in the gel pores and copolymer clusters that are not well bonded to the overall copolymer network. Figure 4.1f demonstrates the remaining copolymer matrix, a so-called xerogel that shrunk to around half of the thickness. And the top view microscopic image of the xerogel shows the loss of the bluish-green luster after transferring from gel thin film. In addition, when applied a similar rate of shrinkage of the gel volume, the original thicker areas achieved a significant reduction in thickness, which further smoothed the inkjet-printed polymer thin film.

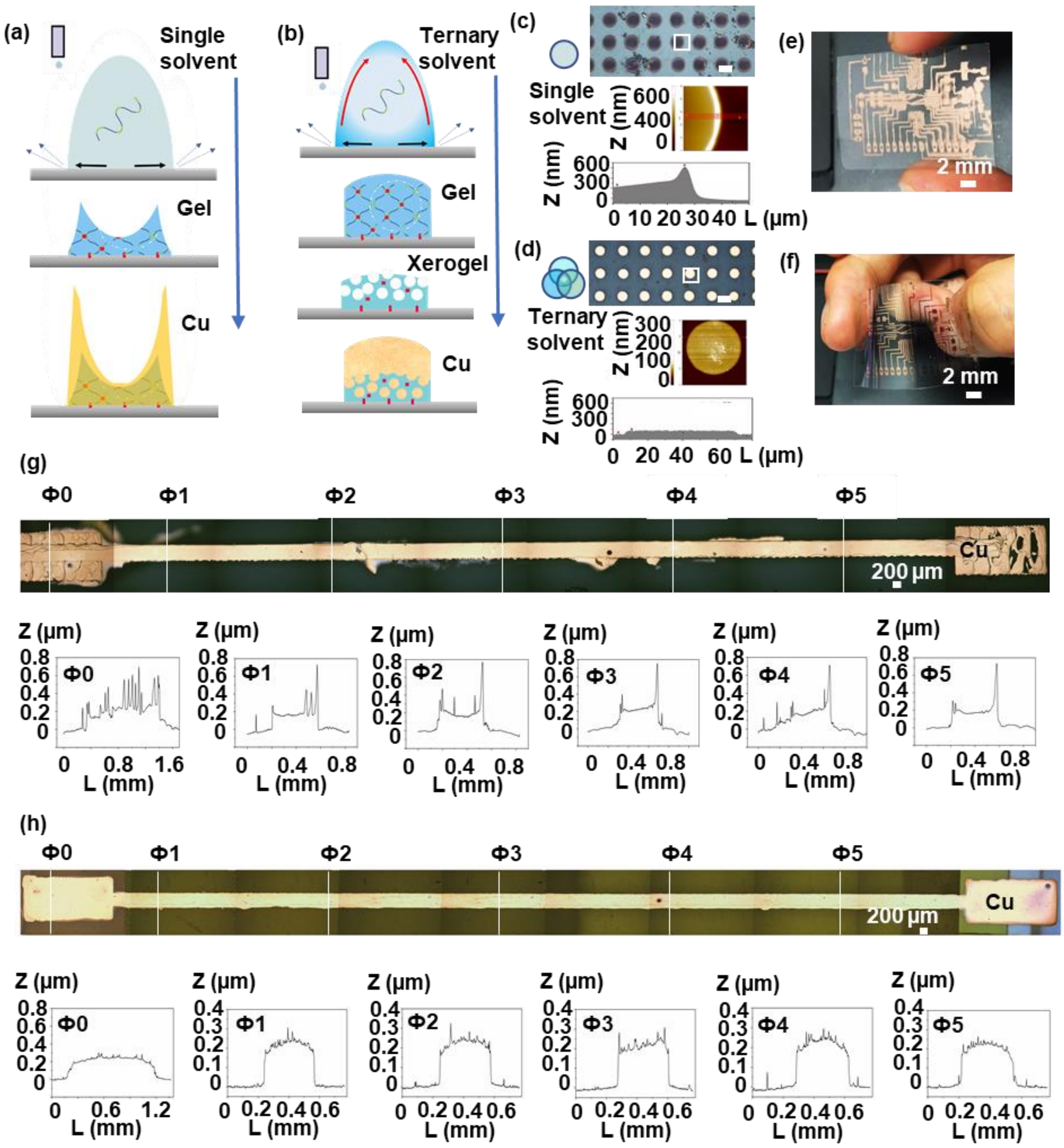

Figure 4.2. Three-solvent-based copolymer ink and EtOH cleaning step enable inkjet printing of Cu electrodes with no coffee-ring stain and less contamination of the pattern. Schematic diagram of Cu electrode preparation process using a) original copolymer ink and traditional treatments and b) ternary-solvent copolymer ink and treatments with EtOH cleaning step. Optical microscopic image and AFM cross-sectional profile of the inkjet-printed c) gel-based Cu dots and d) xerogel-based Cu dots. Optical microscopic image of the inkjet-printed e) gel-based Cu circuit and f) xerogel-based Cu circuit. Optical microscopic images and cross-sectional profiles of the g) gel-based Cu electrode and h) xerogel-based Cu electrode. Scale bars in (c-d) are 100 µm.

Finally, the metal can grow from inside of polymer matrix after a 30-min-catalyst bath in $(NH_4)_2[PdCl_4]$ aqueous solution and a 5-min-electroless deposition in ELD solution.

As shown in Figure 4.1d, the catalyst ion that binds with the METAC group of the copolymer network can initiate electroless metal deposition. Figure 4.1g illustrate a smooth Cu thin film grown on the xerogel. The diffusion of the pattern is a phenomenon that the growth of the metal become out of the control of the inkjet-printed polymer thin film underlying.

On the contrary, the xerogel-based Cu has no apparent diffusion of patterns, as shown in Figures 4.2. And the thickness distribution of the xerogel-based Cu electrode is uniform and have no coffee ring stain, regardless of the shape of the pattern and the testing position along a very long electrode, as shown in Figure 4.2. The cross-sectional details of the gel and xerogel are demonstrated in Figures 4.3 and 4.4. The average thickness of the gel and xerogel was identified in different testing positions along the line. It indicated that the height of the xerogel shrunk to around half of the gel thin film after EtOH cleaning. The shrinkage of the xerogel layer smoothed the electrode regardless of the thickness distribution along the long electrode.

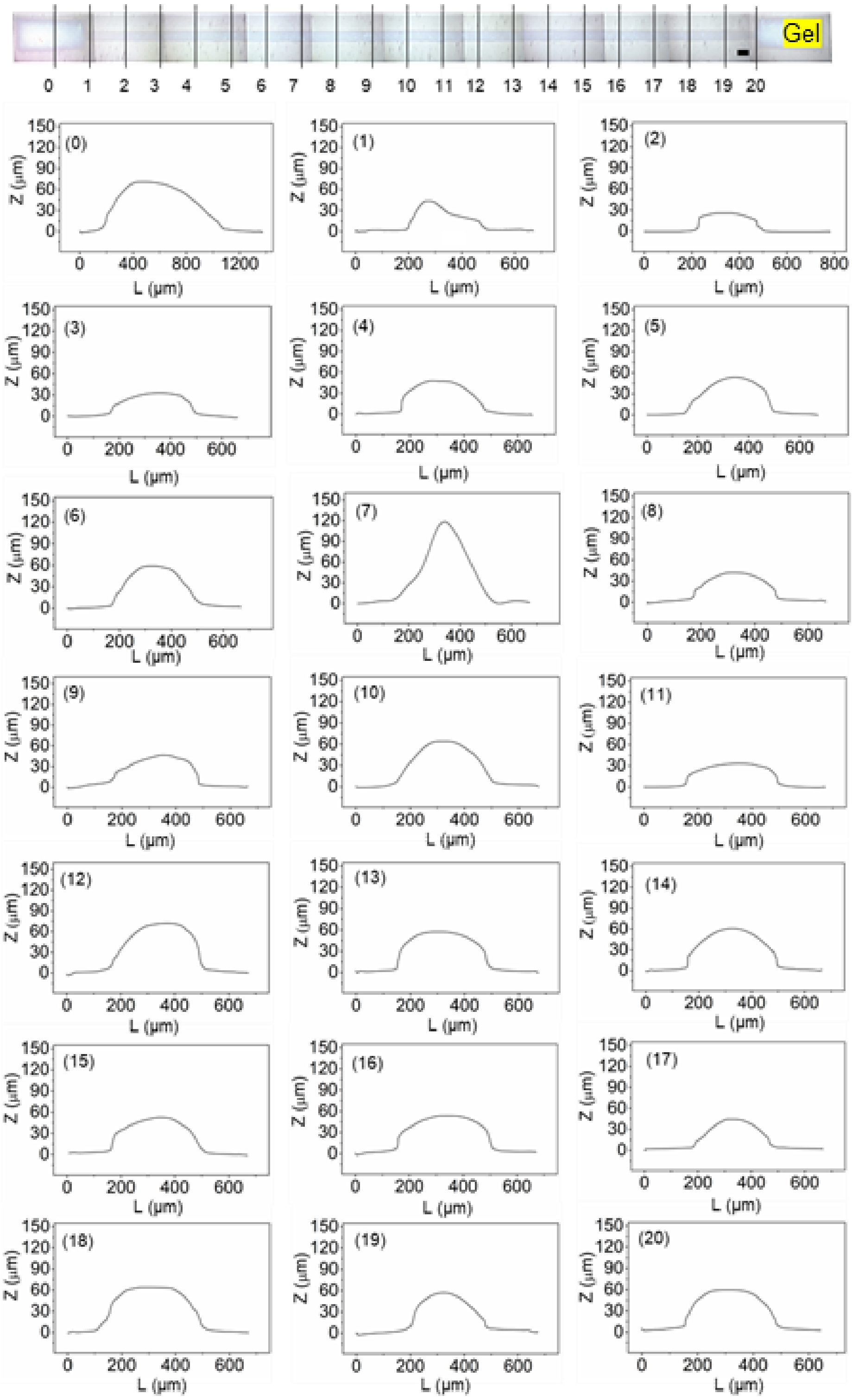

Figure 4.3. Optical microscopic images stitched together showing the thickness distribution of the inkjet-printed line-shaped (20.1 mm × 315 µm) gel patterns. The profile test was carried out every 1 mm along with the line-shaped pattern. The unmarked scale bar is 100 µm.

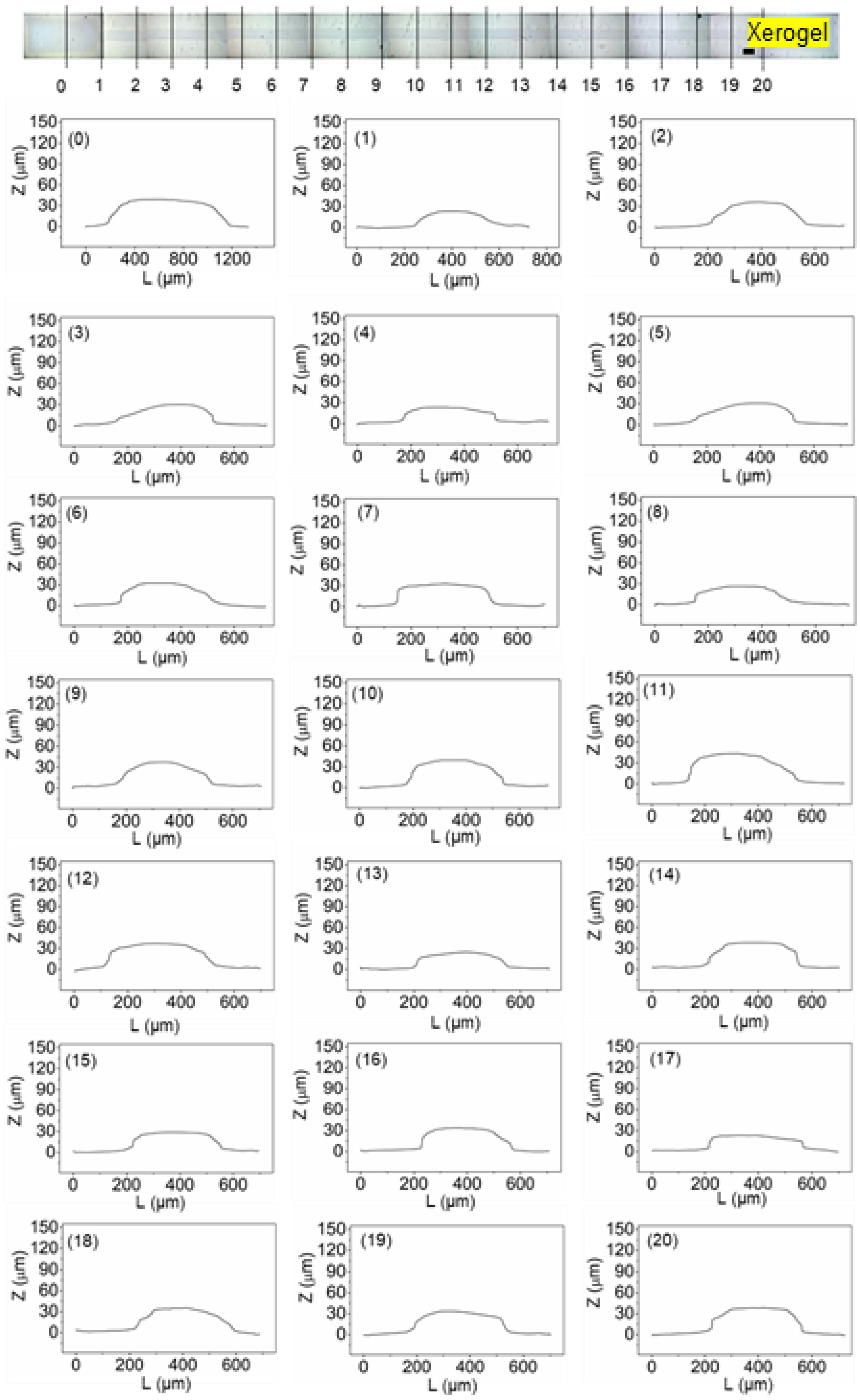

Figure 4.4. Optical microscopic images stitched together showing the thickness distribution of the inkjet-printed line-shaped (20.1 mm × 315 μm) xerogel patterns. The profile test was carried out every 1 mm along with the line-shaped pattern. The unmarked scale bar is 100 μm.

4.3 Morphological of Mesoporous Xerogel Film

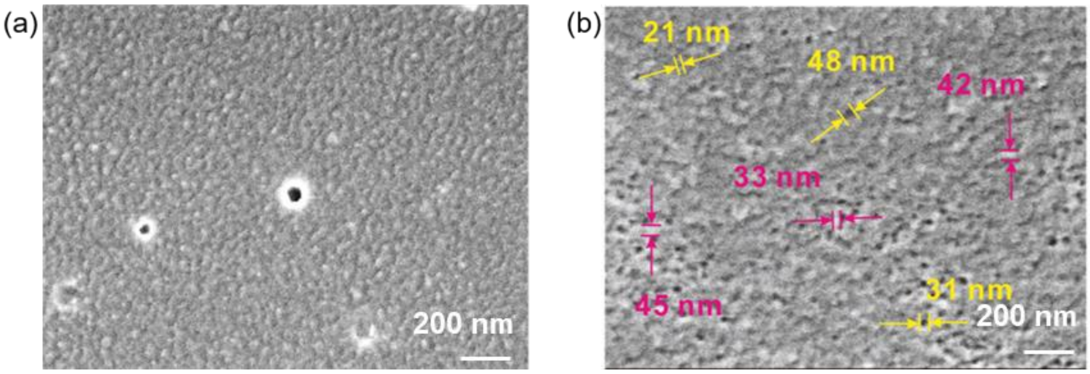

Figure 4.5. SEM image of the surface morphology of the a) gel and b) xerogel. A thin film of Au/Pt alloy (~ 2 nm) was sputtered on the polymer surface of the gel and xerogel for signal enhancement.

Figure 4.5 is a scanning electron microscope (SEM) image comparing surface morphology and a xerogel. The xerogel exhibits deeper concaves on the surface. The size of the concave and the polymer grits was ~ 25 nm and ~ 40 nm, respectively. The surface of the gel thin film seems a little bit smoother, while there appeared large-sized pits with a large depth. Therefore, we utilized the atomic force microscope (AFM) to investigate its morphology. As shown in Figure 4.6, these pits exhibited an almost perfect circular shape and descended to a depth of around 40 nm.

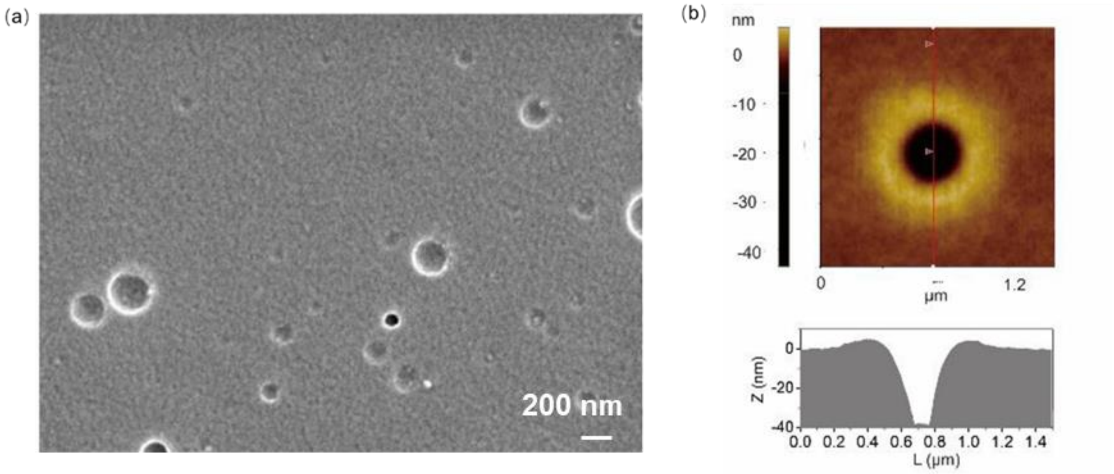

Figure 4.6. a) SEM image b) AFM cross-sectional image and cross-sectional profiles of deep pits appeared on the gel thin film after vacuum drying in the environment with a vacuum level of 10^{-6} Torr for 1 h.

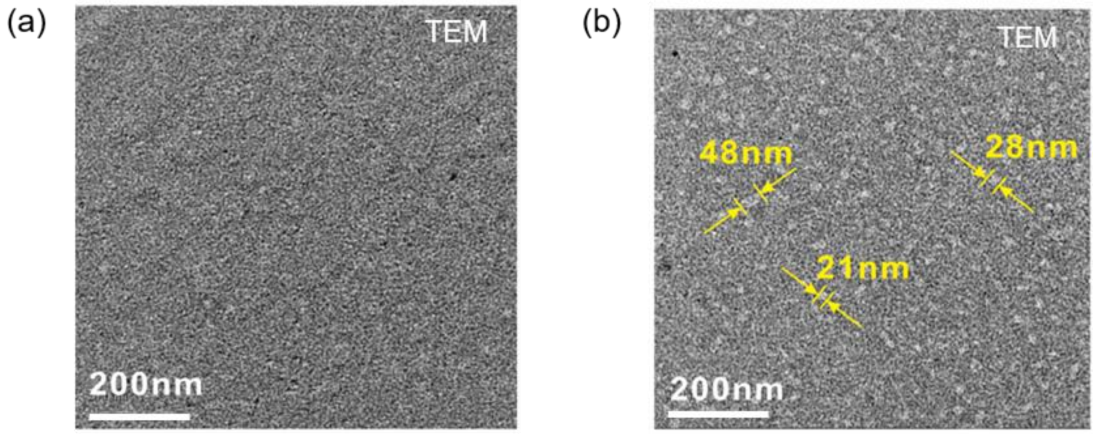

Figure 4.7. TEM images of the surface morphology of the a) gel and b) xerogel.

We assume the evaporation of liquid entrapped in the gel pores formed these pits during the vacuum environment in the SEM-testing chamber since they never appeared in ambient conditions. This phenomenon indirectly proves that there exists liquid entrapped in the gel pores inside the gel thin film. The transmission electron microscope (TEM) image investigated the gel and xerogel thin-film structure. As shown in Figure 4.7, the existence of the white dots indicated the uneven thickness of the xerogel. Because electrons easily penetrate the area with thinner coatings during TEM testing that shows brighter color. It clearly stated that the xerogel thin-film lost the liquid entrapped in the gel pores and missed polymer clusters that did not well bond to the overall xerogel matrix during the EtOH treatment. Both the TEM and SEM images demonstrated the concaves had a consistent size (around 50 nm), as shown in Figures 4.5 and 4.7.

Therefore, the xerogels have a mesoporous structure**.** Figures 4.3.4a and 4.3.4b compare the gel's schematic and optical microscopic images and xerogel. The xerogel lost the green luster in comparison to the gel thin film. Figures 4.8c and 4.8d compared the surface roughness of the gel and xerogel in an ambient environment. Figures 4.8e and 4.8f demonstrated the significant increase of the surface roughness of both the gel and xerogel when immersed in DI water. As the Cu electroless deposition occurs in an aqueous environment, the actual contact area of gel and xerogel with the upper Cu layer can extend considerably. Compared to the gel thin film, the xerogel formed an exceptionally rough structure in an aqueous environment that benefits from the EtOH treatment step that eliminated the filling copolymer clusters. Such structure may increase the contact force between the pure metal layer (top) and the Cu-polymer interpenetration layer (bottom).

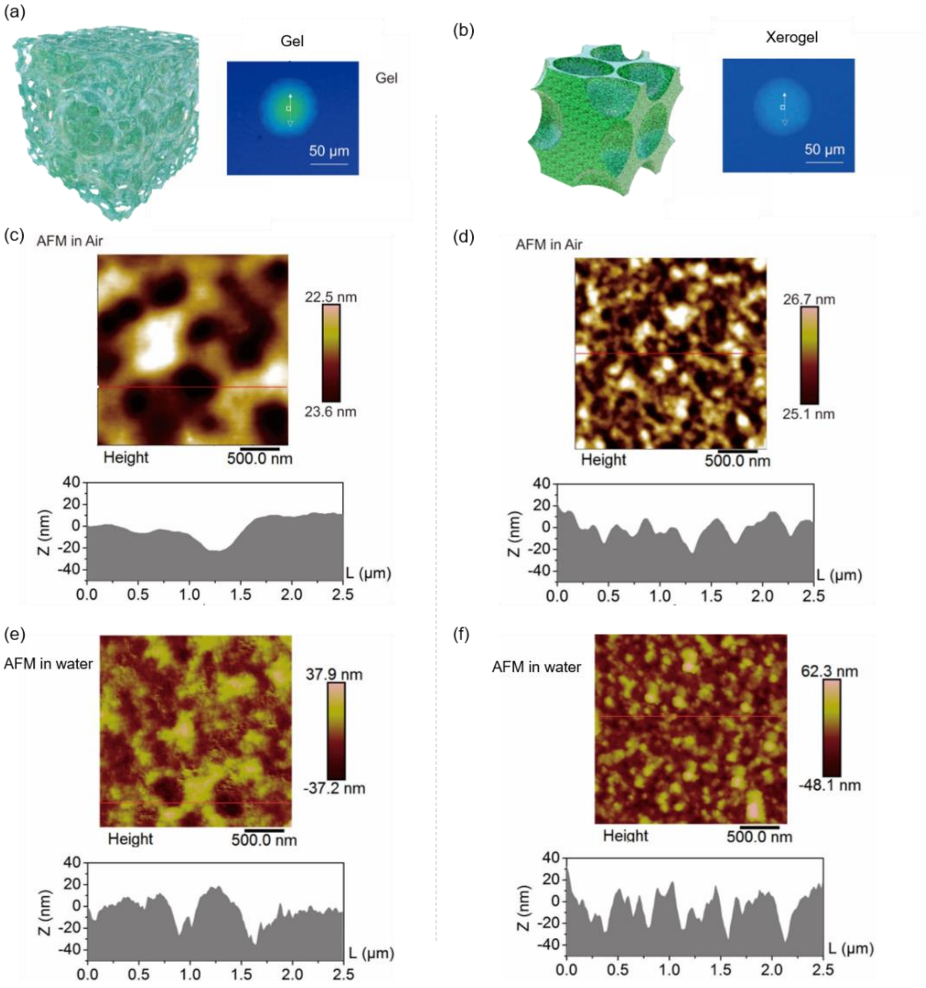

Figure 4.8. Surface morphology of the inkjet-printed gel and xerogel in air and aqueous environment. Schematic diagram and optical images of the inkjet-printed a) gel and b) xerogel on a silicon wafer with a 200-nm-thick SiO_2 layer. High-resolution AFM images and cross-sectional profiles showing the surface morphology of c) gel and d) xerogel. Under-water AFM images and cross-sectional shapes of the surface morphology of e) gel and f) xerogel in an aquatic environment.

4.4 Four-extra-precautions Future Improve the Quality of the Xerogel-based Cu Electrode

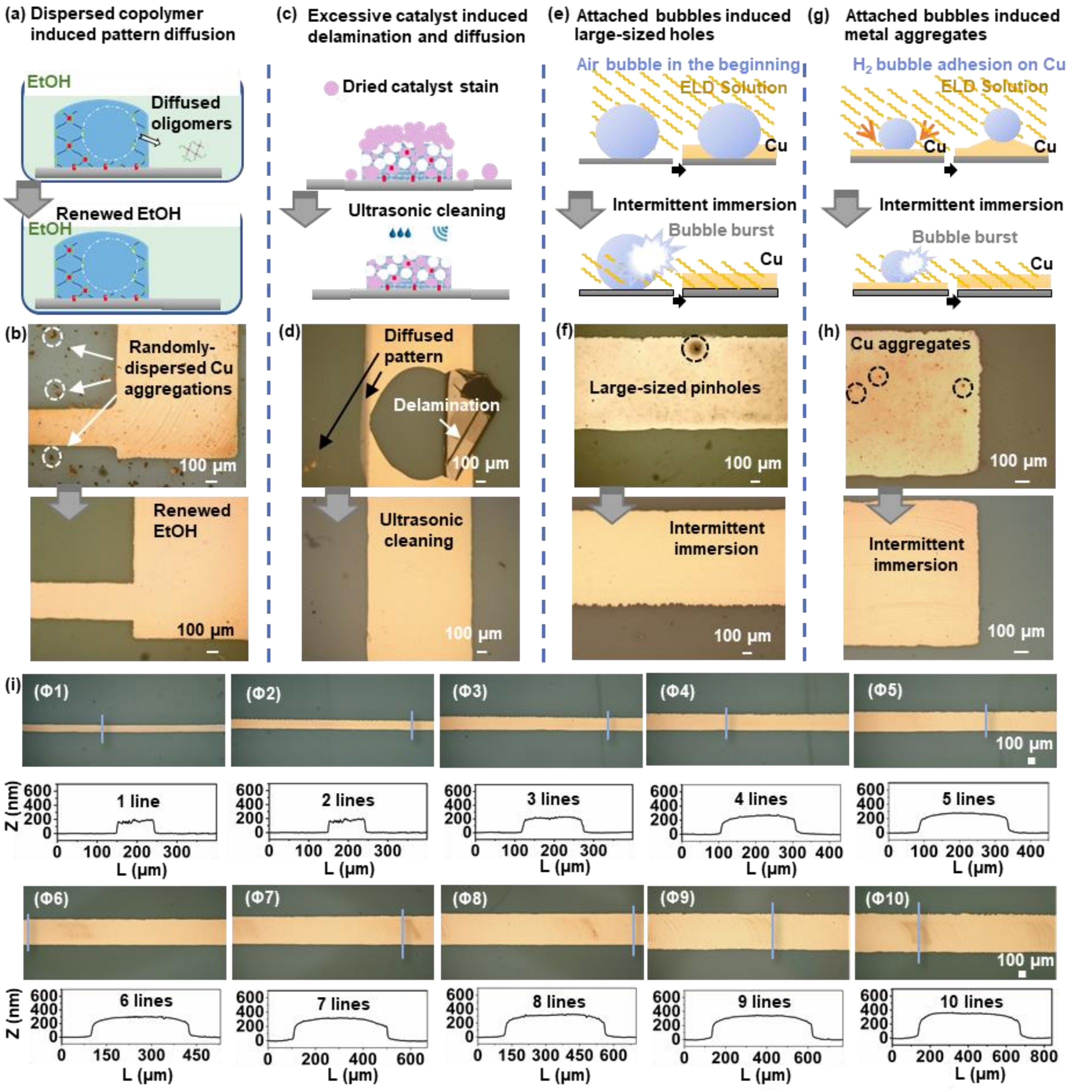

Figure 4.9. Four treatments help eliminate the contamination, holes, and protrusions on the xerogel-based Cu electrodes. a) Schematic diagrams, and b) optical images of the treatment of renewing the EtOH, which helps eliminate the contamination caused by randomly scattered uncrosslinked copolymers. c) Schematic diagrams and d) optical images of the adequate DI water cleaning (with ultrasonic cleaning) helps eliminate the contamination of the xerogel-based Cu electrodes. e) Schematic diagrams and f) optical images of the intermittent immersion at the beginning of the ELD process helped prevent the formation of pinholes on the xerogel-based Cu electrode. g) Schematic diagram and h) optical images of the intermittent immersion at the latter ELD period helped prevent the formation of Cu aggregations (formed by the babble attachment at the latter stages of the ELD process) on the xerogel-based Cu electrode. i) Optical

microscopic images and cross-sectional profile of the xerogel-based Cu electrodes with a smooth surface (without coffee-ring stain) and clear boundary (without pattern diffusion). All the samples were inkjet-printed on the PET substrates. The blue line marked the testing position of the profiler test. Different numbers of printed parallel lines of individual drops (i.e.,2, 4, 6 and 8) result in various widths of the line-shaped patterns. All the samples were additively fabricated on the transparent and flexible PET substrate at room temperature. The electroless deposition time of all the electrodes was 5 min.

In countless practices, we have summed up four precautions to ensure the smoothness and clarity of the electrode pattern. Firstly, we randomly found dirty spots in both the surface of the Cu electrodes and the plastic substrates. Figure 4.9a illustrates the schematic concept of the formation mechanism of the dirty spots generated by the dispersed copolymer. Some organic matter will be precipitated by EtOH solution and suspended in the solution. If we use stagnant EtOH (instead of running EtOH), dirty spots appear on both the Cu electrode and the plastic substrate, as shown in Figure 4.9a. The polymer group diffused out from the gel patterns formed this phenomenon. The color of the spots was dark yellow, similar to the color of a thin layer of Cu that grow on the polymer matrix. The EtOH is a volatile solution. Therefore, the copolymer matrix dispersed in the EtOH solution is likely to quickly attach to the substrate after rapid evaporation of the EtOH when released the EtOH solution. Therefore, we designed a flowing EtOH cleaning method, not allowing the long-term existence of a copolymer cluster in EtOH. We assume this can eliminate the appearance rate of this kind of impurities. As a proof-of-concept, we used flowing EtOH to replace the stagnant EtOH for cleaning the inkjet-printed gel pattern, and the randomly appeared dirty spots disappeared, as shown in Figure 4.9b.

Secondly, there exists excessive catalyst induced delamination and contamination, as shown in Figure 4.9c. Delamination is a phenomenon that the metal electrode will get off from the substrate after excessive electroless deposition time (Figure 4.10). Only the catalyst that is uniformly adherent to the METAC group can initiate a Cu electrode with a tight connection with the substrate. On the contrary, if the catalyst, potassium tetrachloropalladate (II), largely accumulate on the very top of xerogel or the surface of the plastic substrate (due to the inadequate DI-water cleaning), contamination and delamination will appear. As a proof-of-concept, we compared the line-shaped electrodes with and without adequate (with ultrasonication) DI water cleaning, as shown in Figure 4.9d. The not-well cleaned samples initiated the diffuse of the pattern at a random location and exhibited severe delamination only after 5-min-metal-electroless deposition. It is abnormal because the maximum deposition time for xerogel-based Cu electrodes is more than one h (Table 4.1). The maximum thickness of the xerogel-based Cu electrodes can reach ~1 μm (Figure 4.11). The catalyst crystal residue is very easy to accumulate on the top of the xerogel and the plastic substrate without adequate DI water cleaning. We assume the excess catalyst can initiate violent metal deposition to form the pure metal layer (upper) with less connection with the xerogel.

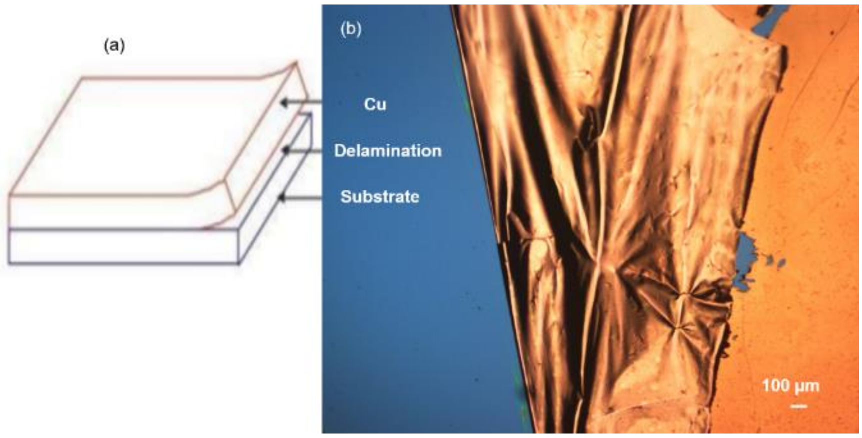

Figure 4.10. a) schematic diagram and b) optical microscopic image of xerogel-based Cu electrode on the silicon substrate delaminated after electroless metal deposition for 25 min.

Table 4.1. Maximum electroless deposition time before delamination of the PAMD-based Cu electrodes. All the experiments shared similar experimental conditions, such as ELD solutions, appropriate treatments, etc.

On different substrates	Gel-based Cu patterned by single-solvent ink	Gel-based Cu electrodes by three-solvent ink	Xerogel-based Cu electrodes by three-solvent ink	Polymer-brush-based Cu electrodes
SiO_2 (inorganic)	~ 8 min	~ 23 min	~25 min	~ 10 min
PET (organic)	~ 15 min	~2h	~ 1h 42 min	~28 min

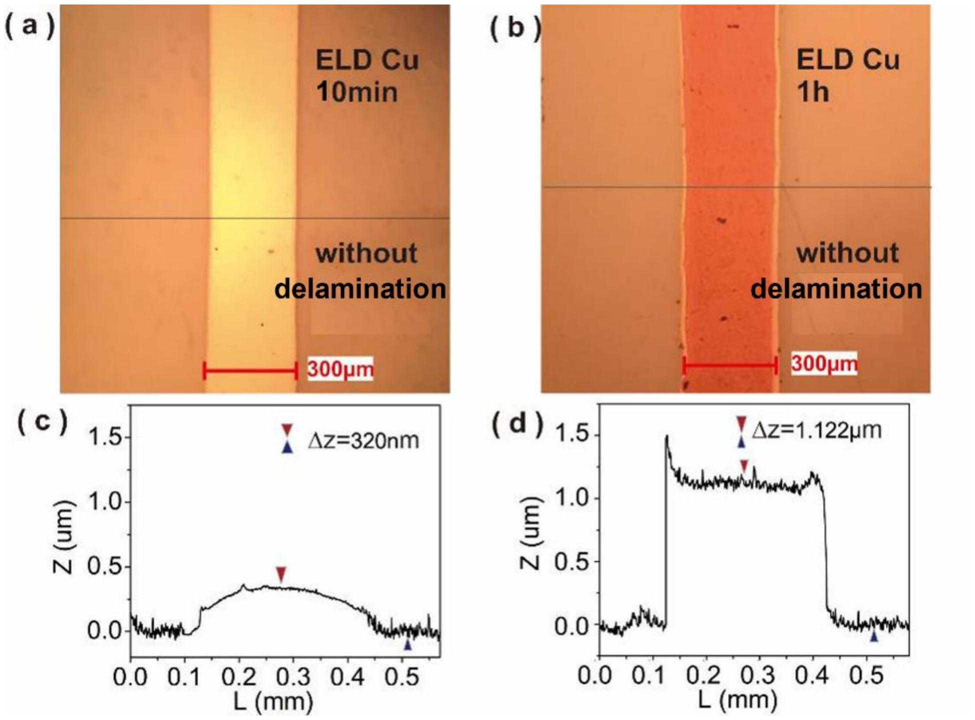

Figure 4.11. Ultra-long-time metal electroless deposition of Cu on xerogel that attached to PET substrate. Optical images of inkjet-printed metal thin-film electrode on PET substrate with an electroless deposited for a) 20min and b) 1h. Cross-sectional profiles of electrodes c) in a) and d) in b).

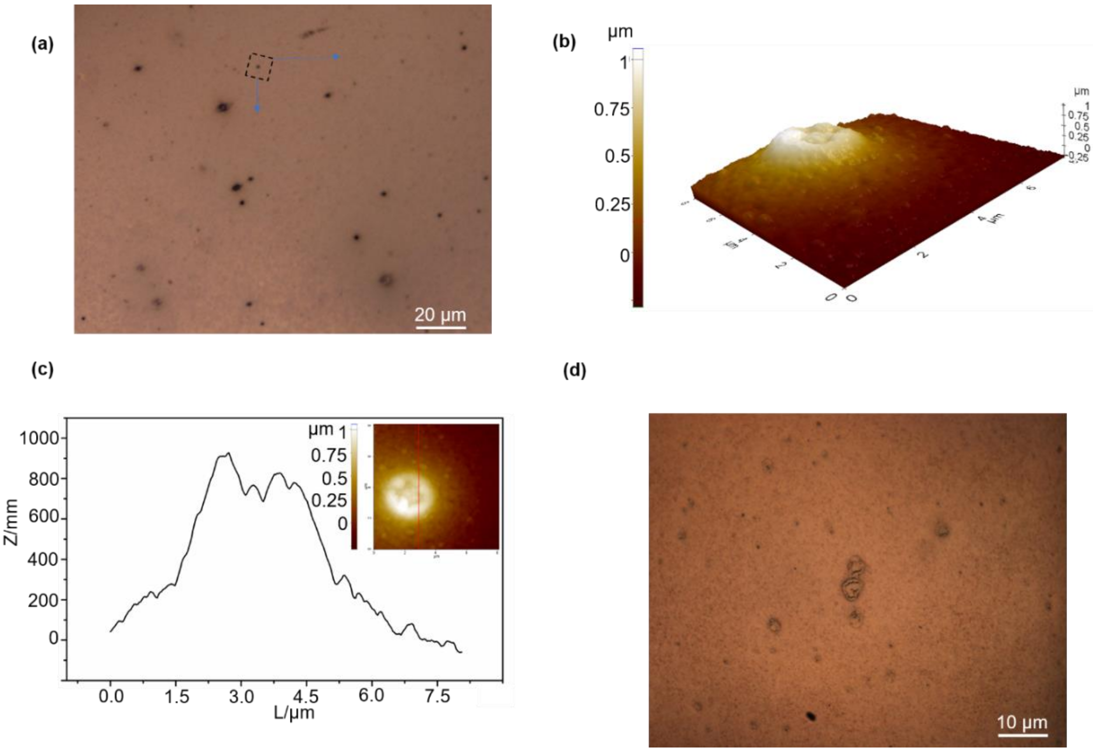

Figure 4.12. Bubble induced pinholes. a) Optical microscopic image of the inkjet-printed PAMD-based Cu electrode formed by traditional inkjet-printing ink. b) 3D AFM

image of one pinholes with a volcanic structure. c) 2D AFM image and its cross-sectional profile of the pinhole in b). d) Enlarged optical microscopic image showing several large-sized pinholes with volcanic structures.

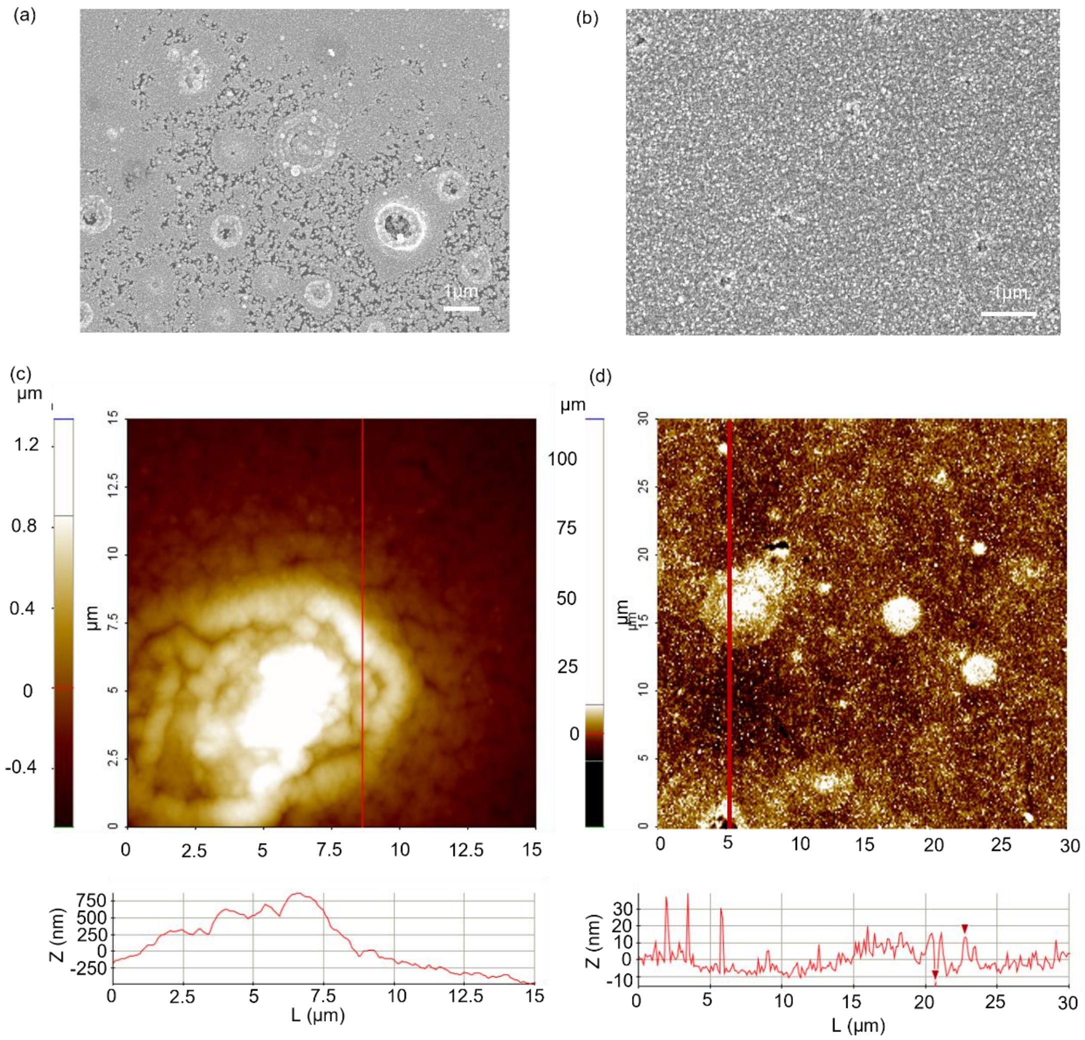

Figure 4.13. Top-view SEM image of Cu electrode prepared a) without and b) with intermittent-immersion operation in the second half of the Cu electroless deposition process. AFM image and cross-sectional profile image demonstrating the surface topography of pinholes in the c) sample a) and d) sample b).

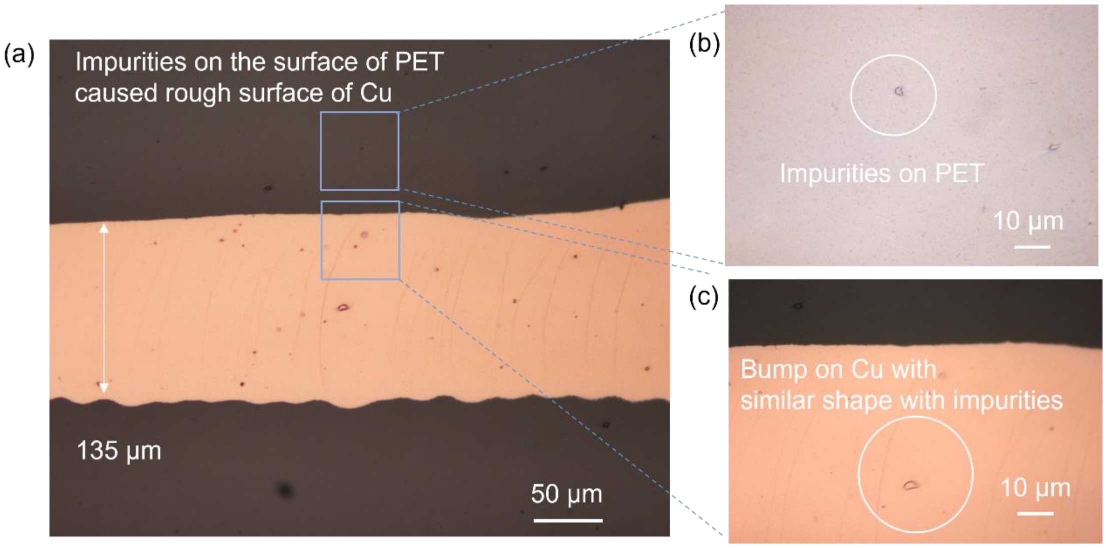

Figure 4.14. Randomly appeared impurities on the PET substrate, causing the rough surface morphology of the xerogel-based Cu electrode. a) Inkjet-printed xerogel-based thin film electrode on PET substrate. b) Enlarged-optical-microscopic image of the impurities that appeared on the surface of the PET substrate even after adequately cleaning by acetone, isopropanol, and DI water. c) Enlarged-optical-microscopic image of the surface of the xerogel-based Cu electrode. The white circle indicates the appearance of impurities (with a similar shape as the impurities that appeared on the bare PET substrate). The electroless deposition time was 3 min.

Thirdly, there are randomly appears circular holes on Cu electrodes (Figure 4.2a and 4.3c). We assume the air bubbles attached to the surface of the substrate at the beginning of the electroless metal deposition formed these pinholes. The bubbles prevented contact between xerogel and reaction solution, as shown in Figure 4.9e. These bubbles were possible formed by the sudden immersion of the substrate in the aqueous solution (electroless deposition solution). Therefore, we designed an operation step, namely intermittent immersion, to eliminate the bubbles attached to the substrate and the xerogel by repeatedly taking the plastic substrate out of the reactive solution. We assume break due to the absence of the solution environment. As a proof-of-concept, we compared the surface uniformity of the xerogel-based Cu electrode with and without the addition of intermittent immersion operation in the very beginning process of metal electroless deposition, as shown in Figure 4.9f. The intermittent immersion frequency was once every 5 seconds. It indicated that the intermittent-immersion operation efficiently stopped the growth of the large-sized circular holes on the surface of the electrodes.

Finally, we also found small-sized pinhole on the Cu electrode surface increased the surface roughness of the electrode. We assume they formed by the H_2 attached to the surface during electroless deposition, as shown in Figure 4.9g. Because the Cu electroless deposition process accompanies a release of H_2 due to the oxidation of the reducing agent.[110] Unlike the previous bubble we introduced, the H_2 bubbles are not attached to plastic substrates but connected to the surface of the newly formed Cu films. After scanning the surface morphology of the Cu electrode by atomic-force-microscope, we found the pinholes exhibit volcanic microstructures, as shown in Figure 4.12. And there was a tiny notch with an almost perfect circular microstructure on the top of the volcanic microstructure. We estimate that this volcanic structure formed by the accelerated Cu deposition on the edge of the bobble offered a cuspidal point in the reactive solution. As a proof-of-concept, we designed an experiment to test the effect of intermittent immersion treatment on eliminating small-sized pinholes. Most of the irregular pinholes disappeared when applied periodic immersion at the second half of the metal electroless deposition process, as shown in Figure 4.9h. Although some small-sized bubbles on the surface of the electrode, we found their height are all smaller than 30 nm (Figure 4.13.). It indicated that the continuous growth of the high pinholes was interrupted by the intermittent immersion operation. Theoretically, we can further increase the evenness of the electrode by simply increasing the frequency of the intermittent immersion operation.

Besides the 4-precaution steps, the surface roughness of the Cu electrode is also strongly related to the surface morphology of the electrodes, as shown in Figure 4.14. Therefore, the xerogel-based Cu electrodes with uniform surface morphology form thin-film devices. As a proof-of-concept, we inkjet-printed line-shaped Cu electrodes on the surface of a uniform PVP thin film that spin-coated on a PET substrate, shown in Figure 4.9i. The more delicate lines have little thickness difference in comparison to the broader lines. Because the wider xerogel pattern usually possess higher catalyst aggregation, that may trigger faster Cu deposition. Therefore, a thinner line pattern needs a slightly longer deposition time to compensate for this tiny height difference. We also found some wavy-shape marks with a dark color that small-scale-horizontal shrinkages of xerogel may form during the EtOH treatment. However, they cannot create optical thickness verification, as shown in Figures 4.9i8 and 4.9i10.

4.5 Microstructure of the Interpenetrating Network of Cu and Copolymer Matrix

We used TEM testing by JEOL JEM-2100F TEM/STEM (Tokyo, Japan) to investigate the cross-sectional area of Cu and polymer interpenetration networks. A Ga+ beam in a multiBeam SEM-FIB system (JEOL Model JIB-4501) milled the sample to form a thin cross-sectional sheet (with a thickness of less than 100 nm). Then the operating voltage of JEOL JEM-2100F TEM/STEM (Tokyo, Japan) was set to 200 kV for bright field transmission electron microscope (BFTEM), darkfield transmission electron microscope (DFTEM), high-resolution transmission electron microscope (HRTEM) testing.

4.5.1 HAADF Image and Elemental Mapping Showing the Existence of the Cu-and-polymer-interpenetration Network

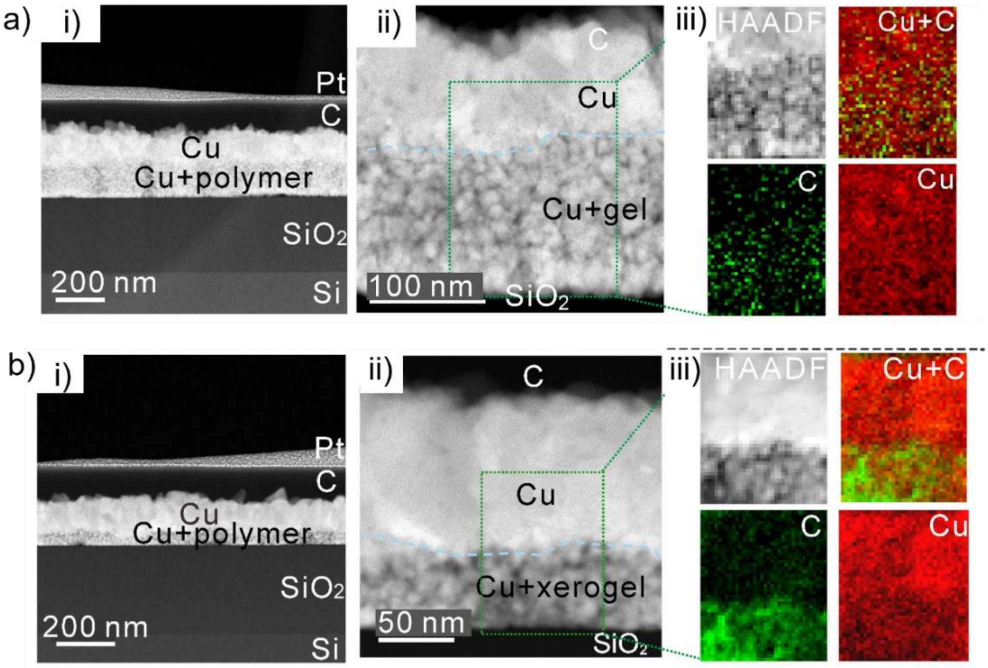

Figure 4.15. TEM analysis of the cross-sectional area of a) gel-based Cu electrode and b) xerogel-based Cu electrode. i-ii) HAADF-STEM image of the nanostructure of the Cu-and-polymer-interpenetration network in the cross-sectional view. iii) In-situ elemental map (by EELS) at the place circled by a green box in (ii).

A carbon layer and a platinum layer coated on the Cu metal surface to protect the original surface morphology of the Cu electrode from possible damage during the calibration process of the electron and gallium ion beam. We compare the cross-section structure of the xerogel-based Cu electrode by the high-angle annular dark-field scanning transmission electron microscope (HAADF-STEM). Both the gel and the xerogel possessed a bi-layer structure comprising an upper-pure metal layer and a Cu-and-polymer-interpenetrating network (Figure 4.15i-ii). And the gel-based Cu electrode had a thicker bottom layer (~132 nm) than the xerogel-based Cu electrode (~ 53 nm). There was a double thickness gap between them.

Figure 4.15 iii) is an elemental map acquired by electron energy loss spectroscopy (EELS). The green and red regions represent an accumulation of the element of carbon and copper, respectively. Carbon elements on the region of the bottom layer approved the existence of the Cu-polymer-interpenetrating network for the first time. The gel-based Cu electrode has a scattered carbon distribution, as shown in figure 4.15aiii. On the contrary, the xerogel-based Cu electrode showed a more concentrated C distribution in the Cu-polymer interpenetrating layer, as shown in Figure 4.15biii. The accumulation of C may originate from the shrinkage of a well-crosslinked polymer network that may offer stronger mechanical strength.

4.5.2 Cu Crystal Form in the Cu-and-polymer-interpenetration Network

The in-situ selected-area electron diffraction (SAED) patterns in Figure 4.16 indicated that the PAMD-based Cu is polycrystalline metal. Therefore, once we selected a specific white dot (circled by a yellow circle), indicates a particular diffraction orientation, the DFTEM image will highlight areas of similar lattice orientation. In this way, we can demonstrate the approximated grain size of copper.

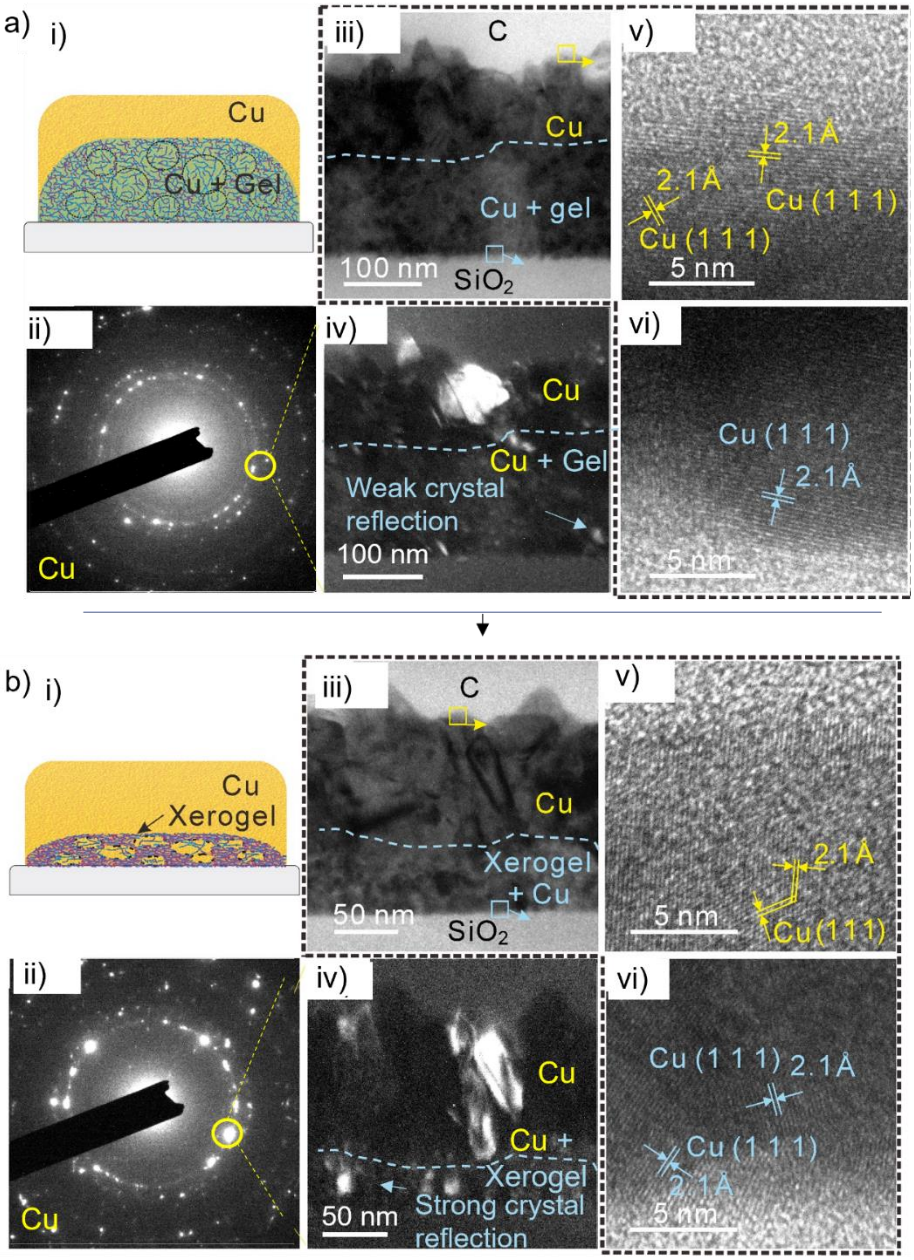

Figure 4.16. TEM analysis comparing the Cu crystal form of a) gel-based Cu electrode and b) xerogel-based Cu electrode in the cross-sectional view. i) Schematic concept, II) SAED pattern III) BFTEM image, IV) HFTEM image with the highlighted region with specific lattice orientation, V-VI) HRTEM image. The shattered blue lines marked the boundary between the upper-pure-Cu layer and the Cu-and-polymer-interpenetrating network

For the gel-based Cu electrode, the captured Cu particles on the top layer (pure metal layer) had a size of around 80 nm, while the Cu particles in the gel-and-Cu interpenetrating networks were dim and unclear in Figure 4.16iv. It is because the Cu nanoparticles were directly grown into the nanosized pores of the polymer matrix. And the thin polymer branches prevent the formation of the large-sized Cu crystal. On the contrary, a large-sized Cu crystal (shown as bright spots) formed in the xerogel-and-Cu-interpenetrating network, as shown in Figure 4.16iv. It is because of eliminating some of the pre-crosslinked polymer groups that are not well bonded to the overall polymer matrix during EtOH treatment. The absence of some large-sized polymer groups offered a place to form hollow structures in the xerogel. And it offered room for the growing of Cu crystals with a relatively larger size. And the Cu crystal size in the pure-metal layer on the top in xerogel-based Cu thin film was as large as the Cu crystal size in the gel-based Cu electrode. Therefore, the xerogel-based Cu electrode and gel-based Cu electrodes have a similar-upper-pure metal layer.

Figures 4.16av and 4.16vi were high-resolution transmission electron microscope (HRTEM) images indicating the diffraction fringes of the gel-based Cu electrode in both the upper-pure Cu layer (marked as yellow) and the bottom-Cu-polymer interpenetrating layer (marked as blue). All the detected regions had a crystal orientation of Cu (111). Similarly, Cu (111) lattice structure appeared in both the bottom layer and the upper layer for xerogel-based Cu electrodes (Figures 4.16bv and 4.16vi). Thus, the polymer matrix will not change Cu's essential chemical and physical nature.

4.5.3 Strong Cu cluster in Xerogel-based Cu Electrode May Offer Higher Mechanical Strength

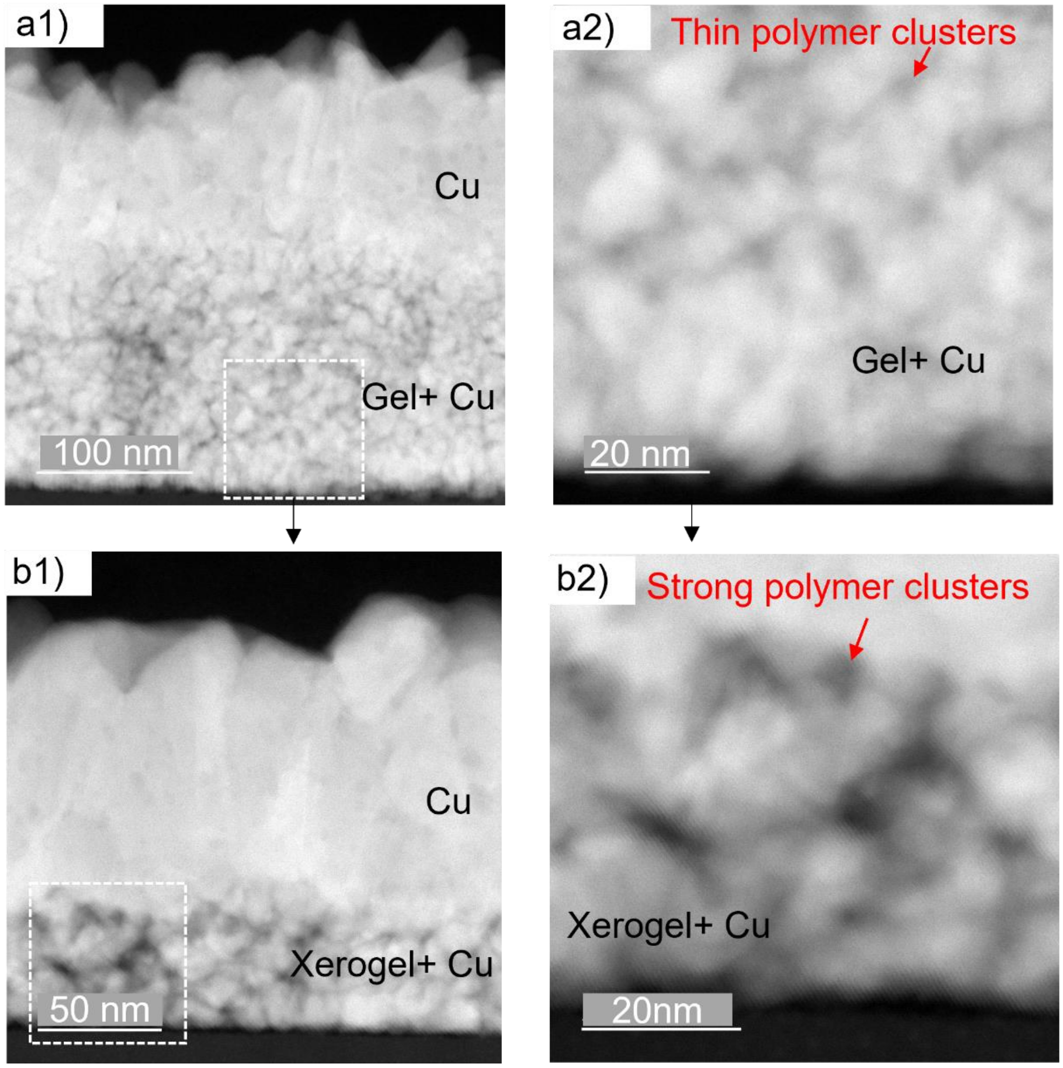

Figure 4.17. Enlarged HAADF-STEM images showing the Cu-and-polymer interpenetrating network of a) gel-based Cu, b) xerogel-based Cu. The xerogel-based Cu electrode had stronger polymer clusters compared to the gel-based Cu electrode. The Cu nanocrystal failed to penetrate the condensed region of the polymer clusters on the xerogel matrix.

The dark region in the HAADF-STEM image was the assembled polymer clusters that had less metal distribution because the metal crystal can reflect the electrons to make the area present high brightness. The formed polymer clusters in the gel-based Cu electrode were not clear (blur) compared with the copolymer cluster in xerogel-based Cu electrodes, as shown in Figure 4.17. This is because the Cu nanoparticle can penetrate the gel pore, whilst it cannot penetrate inside the condensed polymer clusters formed in xerogel. And the polymer cluster in xerogel was thicker and stronger than the polymer cluster in a gel. As each copolymer chain is comparatively fragile than the permission of the sharp and hard Cu particles with Young's modulus of >100 GP may make the thin polymer chains in the gel thin film become fragile in the case of external mechanical stress. On the contrary, we assume the EtOH treatment, converting the gel thin film to xerogel, can create a reunion of delicate copolymer clusters to form thicker and stronger polymer clusters. And this structure may improve the mechanical strength of the Cu-and-polymer interpenetrating network.

4.5.4 Cross-sectional Microscopic Image of Polymer-brush-based Cu Electrode

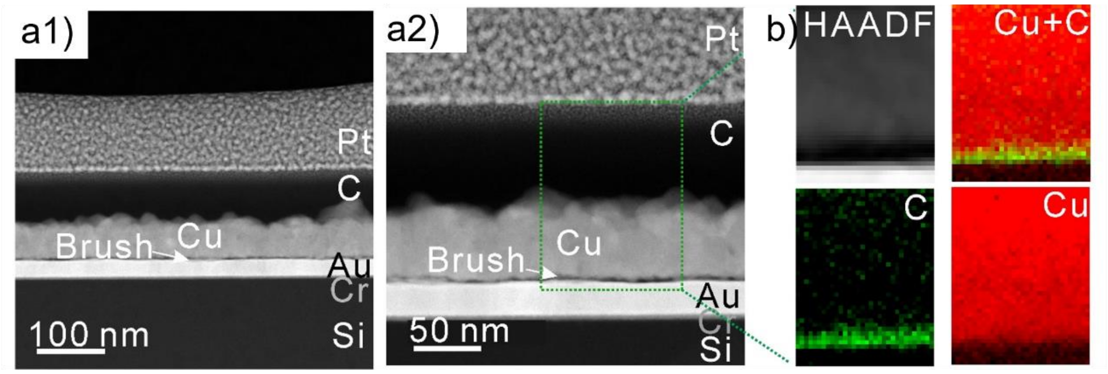

Figure 4.18. TEM analysis of the cross-sectional area of xerogel-based Cu electrode. a) HAADF-STEM image of the nanostructure of the Cu-and-polymer-interpenetration network in the cross-sectional view. b) In-situ elemental map (by EELS) at the place circled by a green box in (ii).

We also use TEM to analyze the cross-section microstructure of the Cu electrode formed by the grafting-from strategy (polymer-brush-based Cu electrode).[111] The grafting-from strategy has a thin Cu-and polymer interpenetration network compared to the grafting-to-strategy (gel-based Cu electrode and xerogel-based Cu electrode), as shown in Figure 4.18. Therefore, an Au layer coated on the non-metallic substrate increases the TEM image's contract, making the 3-nm-thick polymer brush easy to identify. The Cr layer is to increase the adhesiveness of the Au layer on the SiO_2 substrate.

The elemental map showed a C-rich zoon with less Cu penetration, as shown in Figure 4.18b. The polymer-brush-based Cu electrode formed on a relatively dense polymer brush, comprising an interpenetration network of Cu and polymer in a very narrow space.

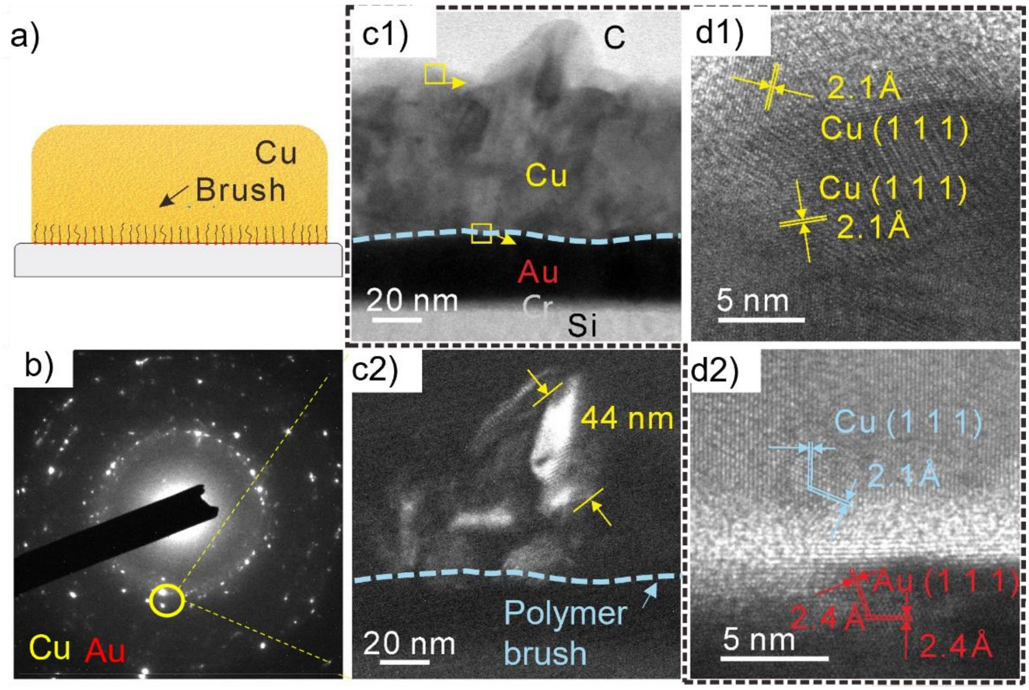

Figure 4.19. TEM analysis of the Cu crystal formed of polymer-brush-based Cu electrode in the cross-sectional view. i) Schematic concept, II) SAED pattern III) BFTEM image, IV) HFTEM image with the highlighted region with specific lattice orientation, V-VI) HRTEM image.

Figure 4.19c demonstrates the large-sized Cu particles that appeared on the upper layer of the polymer-brush based Cu electrode. It indicates that the different PAMD techniques can prepare Cu electrodes with a similar pure-metal layer on the top. And the detected Cu crystal orientation in both the upper-pure-metal electrode and the bottom Cu-and-polymer interpenetration network were all Cu (111) (Figure 4.19d). Thus, choosing the relatively dense polymer brush thin film as a buffer layer still cannot change Cu's basic chemical and physical nature.

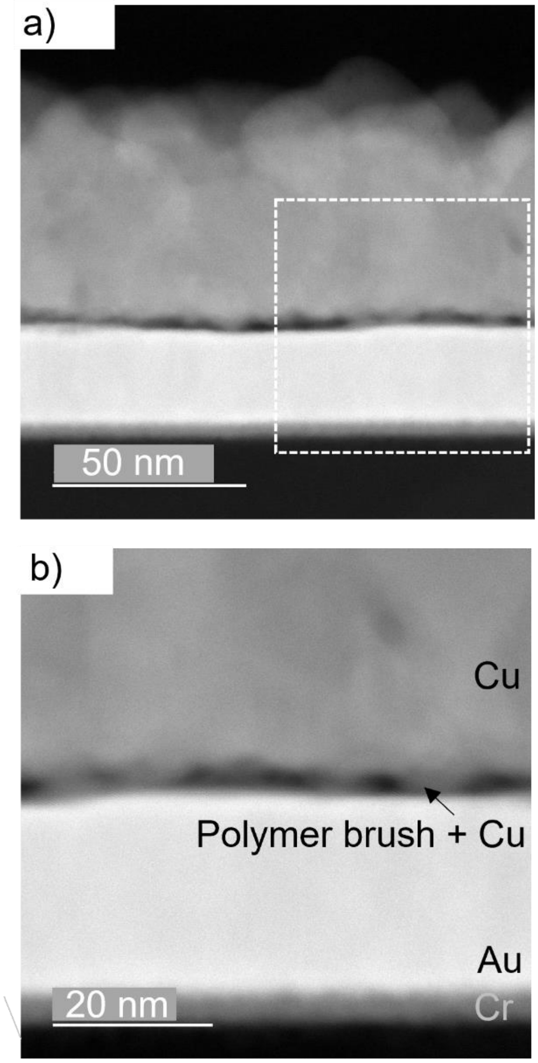

Figure 4.20. Enlarged HAADF-STEM images showing the Cu-and-polymer interpenetrating network of polymer-brush-based Cu electrode. The polymer-brush thin film still can form an interpenetration network with Cu nanoparticles.

Figures 4.20 indicated a clear nanostructure of an interpenetration network of Cu and polymer for the polymer-brush-based Cu electrodes.

4.6 Adhesiveness of the PAMD-based Cu Electrodes on the Plastic Substrate

4.6.1 Scotch Tape Test

As shown in Figure 4.21, a standard scotch tape test investigated the adhesiveness of both the thermal-evaporated Cu electrodes and the PAMD-based Cu electrodes (including xerogel) on PET substrate. Only the thermal evaporated Cu without the Cr layer was torn off by the scotch tape, as shown in Figure 4.21. Even the Cu crystal diffused to the PET substrate during the metal electroless deposition process, still difficult to be removed by the scotch tape.

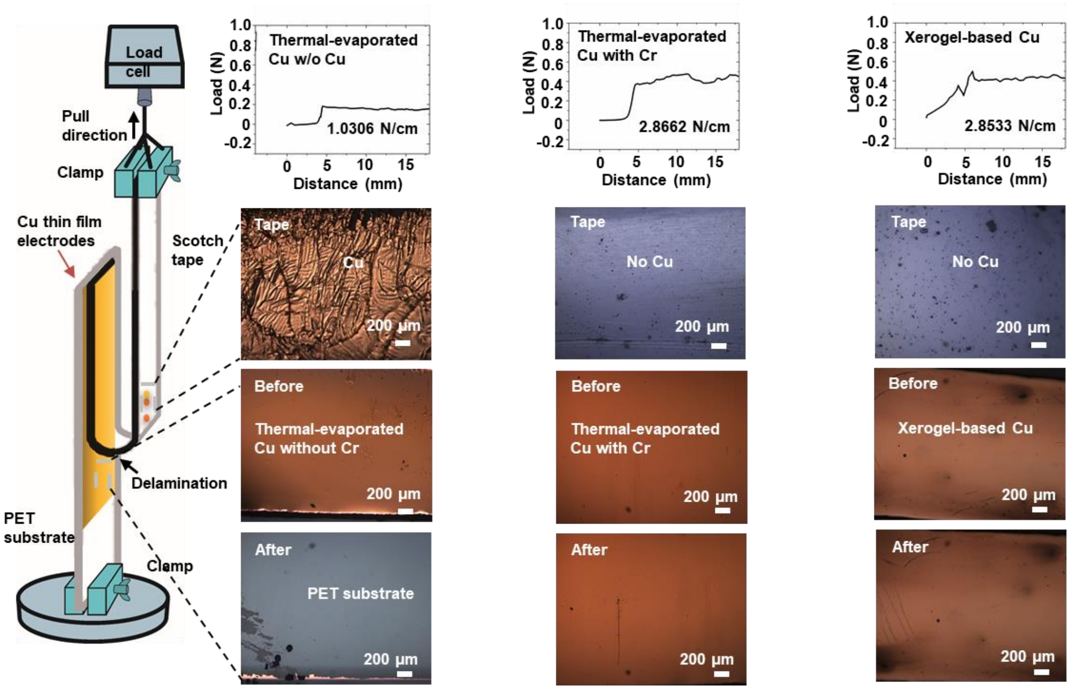

Figure 4.21. Scotch tape test of PAMD-based Cu electrode comparing with the thermal evaporated Cu electrodes. a) Schematic diagram of scotch tape testing. Insert image is a photograph of a thermal-evaporated Cu electrode coated on a PET substrate (with a thickness of 225 µm) after a scotch tape test. The load vs extension curve, microscopic images of Cu electrode before and after tearing the scotch tape, and the metal residue of the copper electrode on the tape for the thermal-evaporated Cu without Cr layer, thermal-evaporated Cu with Cr layer, and xerogel-based Cu electrode.

4.6.2 Nanoscratching Test for Traditional Thermal Evaporated Cu Electrode

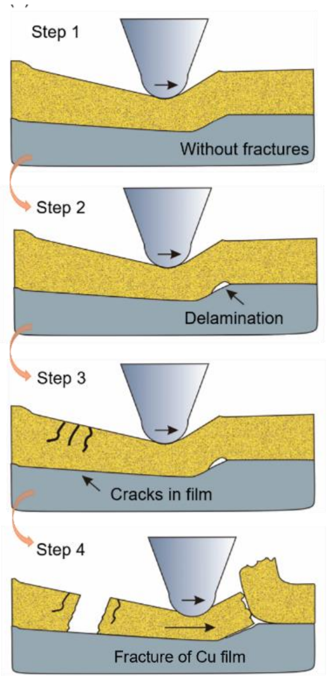

Figure 4.22. Four stages of nanoscratching process for thin-film coating on a plastic substrate. The delamination happened after entering stage 2. When entering stage 3, the cracks began to appear on the scratching trace. Stage 4 is demonstrating the scratching performance after the broken of the coating in a specific form.[112]

To further compare the adhesiveness of the electrodes on a plastic substrate, we carried out the ramping force nano-scratching test by a triboindenter (Hysitron TI 900) with a scratching length of 6 µm, and a maximum-scratching load of 3000 µN (Figure 4.22).

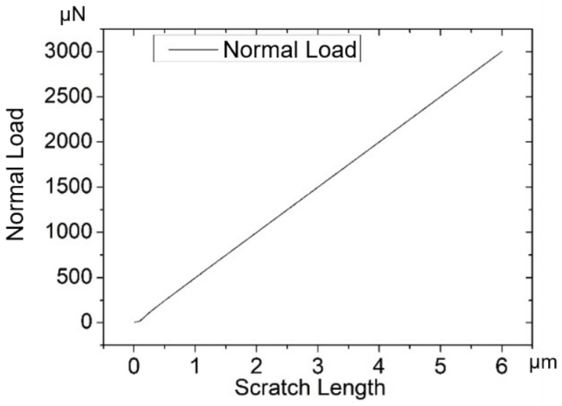

Figure 4.23. Relationship between average load and scratching length.

Figure 4.23 is the line-shaped relationship between average load (longitudinal pressure) and scratching length.

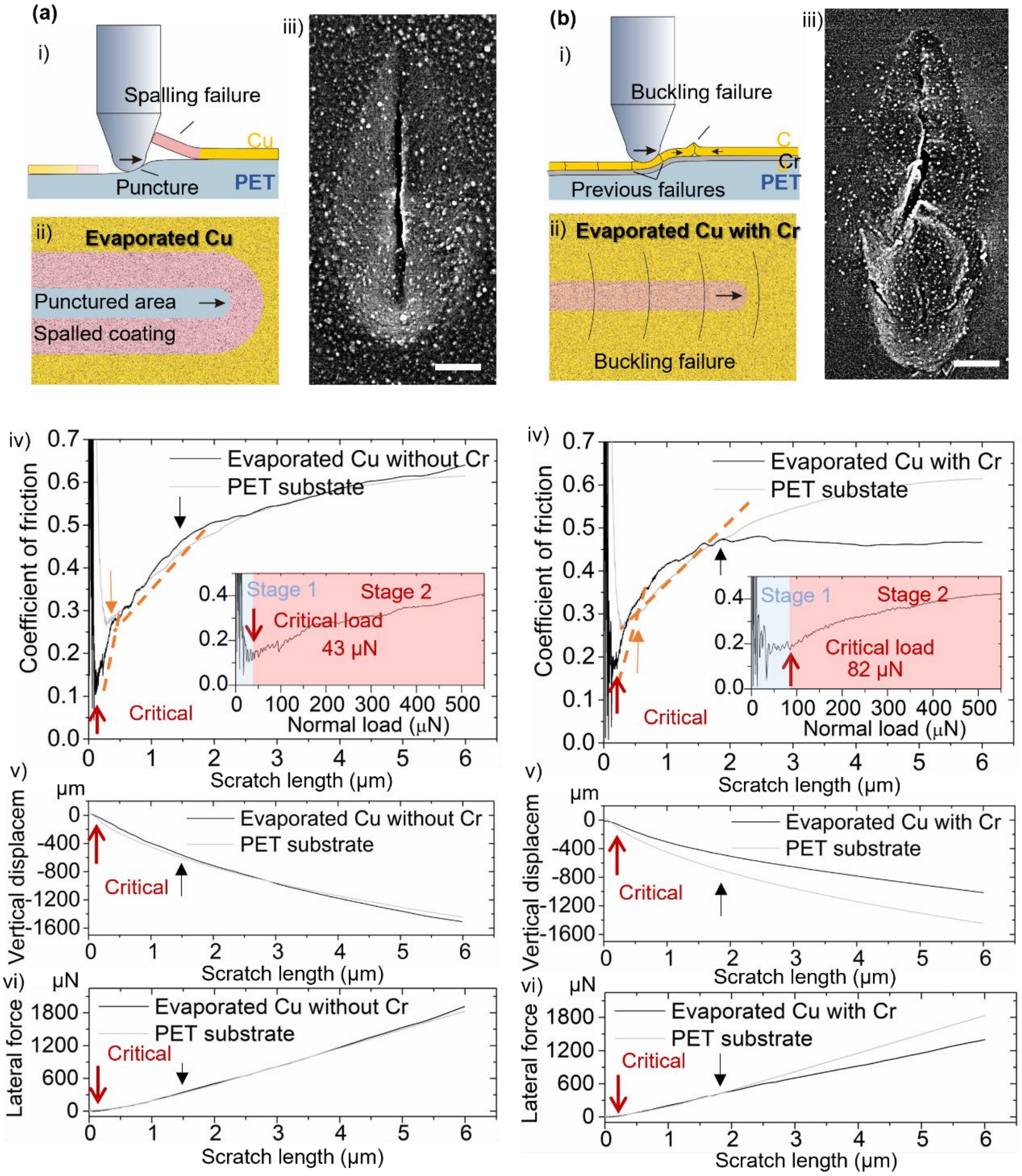

Figure 4.24. Nano-scratching test of the thermal-evaporated Cu electrodes a) without and b) with a 10-nm-thick Cr layer on the PET substrate. i) Side view, ii) top views of the schematics of the coating failure modes, iii) SEM image iv) typical (main plot) and enlarged (insets) coefficient of friction curve, v) vertical displacement curve, and vi) lateral force curve of the nano-scratching test. The red, orange and black arrows are on behalf of the borders of the 4-nanoscratching sections. The grey lines demonstrate the comparison experiment that scratched the surface of the pure PET substrate without any coatings. The unmarked scale bar is 1 μm. The thickness of all the Cu electrodes was ~200 nm.

Figure 4.24ai and 4.24aii show the spalling failure schematically. This failure has a semicircular arc region with delamination preceding the scratching head. According to the classification of coating failure mode by Burnett et al. [113], the coating failure of thermal evaporated Cu without Cr belongs to the failure mode of spalling generated by complete adhesive failure (delamination). As shown in Figure 4.24aiii, the delamination appeared on the peripheral of the clear scratch (at the center), formed by delamination between the Cu layer and PET substrate. The upper Cu layer did not form any deformation or cracks during the gradually increased deformation of the PET substrate. It approved the week adhesiveness between the Cu and the PET substrate. Figure 4.19aiv is the coefficient of friction curve showing the position of the critical point (initiation of delamination) was at the normal load of only 43 μN. Tanaka et al. has divided the failure of the thin-film coating on the plastic substrate into four different stages (Figure 4.22), and the critical point is where the coefficient of friction curve switches from stage 1 (oscillating) to stage 2 (rising at a particular slope).[112] In addition, the testing results, including coefficient of friction curve (Figure 4.24aiv), vertical displacement curve (Figure 4.24av), and lateral force curve (Figure 4.22avi), almost overlapped with comparative data scratching on a pure PET substrate without any coating. Thus, we speculate that the scratching stylus pierced the Cu coating and slipped on the pure PET substrate after the film-broken point marked by the black arrow.

On the contrary, the thermal-evaporated Cu with a Cr adhesive layer, commonly used in industrial production, shows bigger adhesiveness. Figures 4.24bi, ii, and iii demonstrate that this scratch trace has a different appearance from the spalling failure. Twists and cracks, with a semicircular shape, appeared in front of the stylus. The partial delamination must form this phenomenon. It indicated that this failure mode belongs to bucking failure.[113] The locality tear occurs on the Cu thin film electrodes, showing the interconnection between the Cu and PET substrates. Figure 4.19b④ is the coefficient of friction curve showing a larger critical load (~ 82 μN) in comparison to thermal evaporated Cu without Cr layer. And the sudden drop of the coefficient of friction curve indicating the possible position of film breaking.[112] This film breaking point was ~908 μN, marked by black arrows. And we found that the coefficient of friction did not increase along with the ramping longitudinal force after the broken point of the film. It may be because that the stylus did not penetrate the Cr layer and only glid on the surface of the Cr layer since the 10-nm-thick Cr layer has high mechanical strength. The lower level of the vertical displacement compared to the data of scratching on bare PET substrate, further approved this conclusion, as shown in Figure 4.24bv. And Figure 4.24bvi shows the lateral force curve of the sample. It further approved that the stylus may destroy the uppermost Cu thin film while it did not penetrate the Cr layer.

4.6.3 Nanoscratching Test for Gel-based Cu Electrode and Xerogel-based Cu Electrode

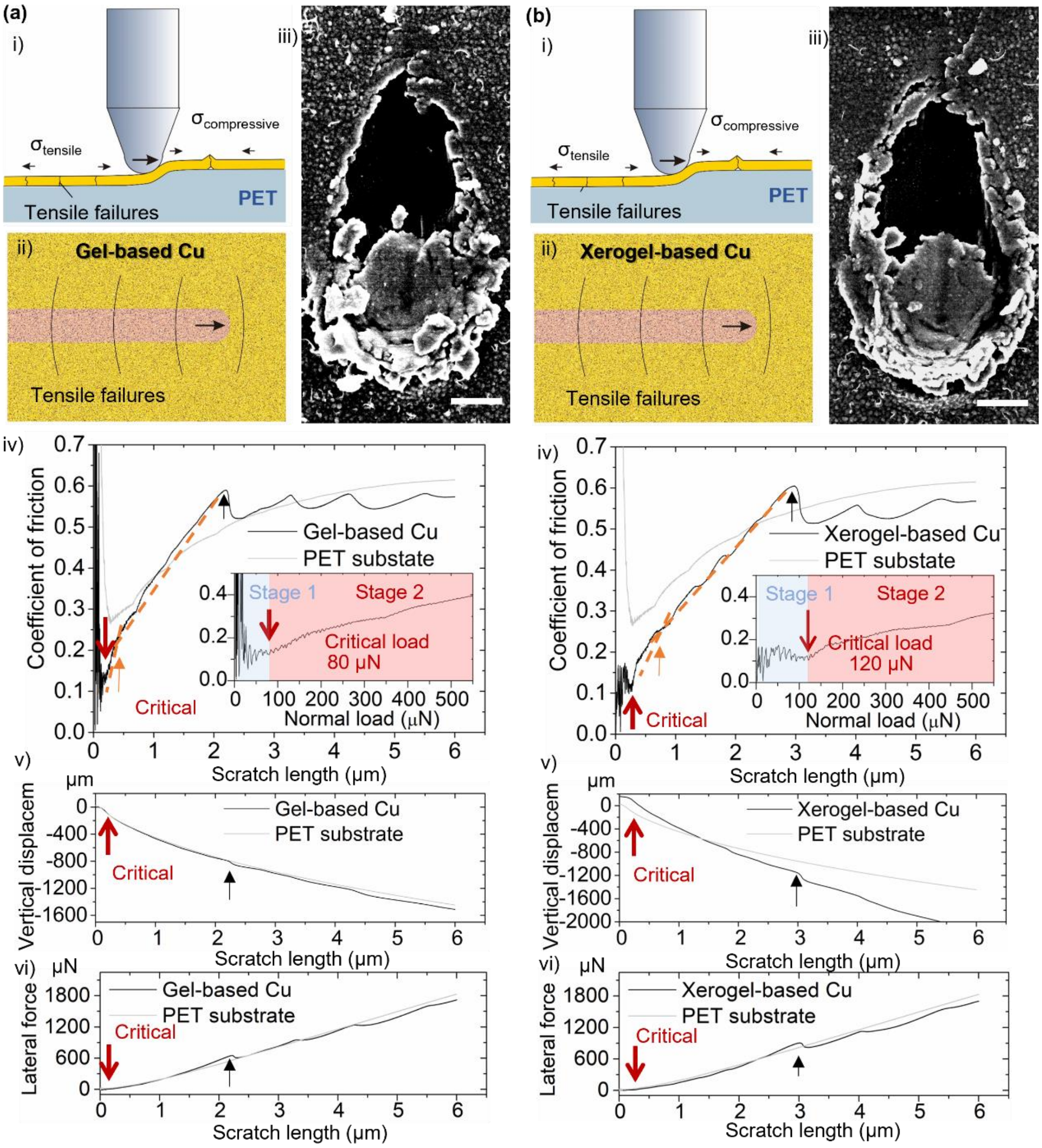

Figure 4.25. Nano-scratching test of PAMD-based Cu electrodes a) gel-based Cu electrode and b) xerogel-based Cu electrode on the PET substrate. i) Side view, ii) top views of the schematics of the coating failure modes, iii) SEM image iv) typical (main

plot) and enlarged (insets) coefficient of friction curve, v) vertical displacement curve, and vi) lateral force curve of the nano-scratching test. The red, orange and black arrows are on behalf of the borders of the 4-nanoscratching sections. The grey lines demonstrate the comparison experiment that scratched the surface of the pure PET substrate without any coatings. The unmarked scale bar is 1 µm. The thickness of all the Cu electrodes was ~200 nm.

Then, we tested the adhesiveness of the gel and xerogel-based Cu electrode prepared by three-solvent copolymer ink on the PET substrate. Both of them belongs to the tensile failure mode, [113] characterized by the immersion of cracks parallel to the trailing edge of the scratching head in the early stage of scratching (Figure 4.25ai, ii, and iii, Figure 4.25bi, ii, and iii).[113] The tensile force exerted to the scratch rear by the stylus formed the final film breaking. As shown in Figures 4.25aiii & 4.25biii, the stylus failed to penetrate the film under layer directly. Cu film with part of the scratching trace still attached on the drift disk, the fracture point may appear in the weakest area on the long-scratched trajectories by the tensile stress. The appearance of the weakest area is probably at the position of the first instantaneous slippage, i.e., the critical point.[112, 114] After the broken of the Cu film, the stylus slid on the PET surface, accompanied by the Cu film pressed underneath by the scratching stylus. During the whole scratching process, the scratching stylus, with a tip with a spherical structure of one-micron diameter, did not pierce the Cu film under the stylus. There left an exposed substrate at the rear and some stacking fractures at the front of the stylus. The Cu film under the stylus may drift as a whole on the PET substrate. This kind of film failure is unique and belongs to tensile failure. Therefore, this failure mode should belong to the tensile failure according to the taxonomy of Burnett et al.[113] that usually formed on fully adherent coating. This special failure mode indicated that the gel-and-xerogel-based Cu electrode has a strong mechanical strength making the Cu film difficult to be penetrated by the stylus even on a soft plastic substrate (PET substrate). In addition, the Cu film has good adhesiveness to the plastic substrate because of the Cu thin film failed in mode of the tensile failure. The critical load of gel and xerogel was confirmed to be 75 µN and 102 µN, respectively, according to the coefficient of friction curve (Figures 4.25aiv and 4.25biv). The possible film broke points of the gel-based and the xerogel-based electrode were ~1107 µN and ~1650 µN, respectively. The unprecedented adhesiveness of the xerogel-based Cu electrodes may be generated by its thicker and stronger polymer cluster.

4.6.4 Nanoscratching Test for Polymer-brush Based Cu Electrode

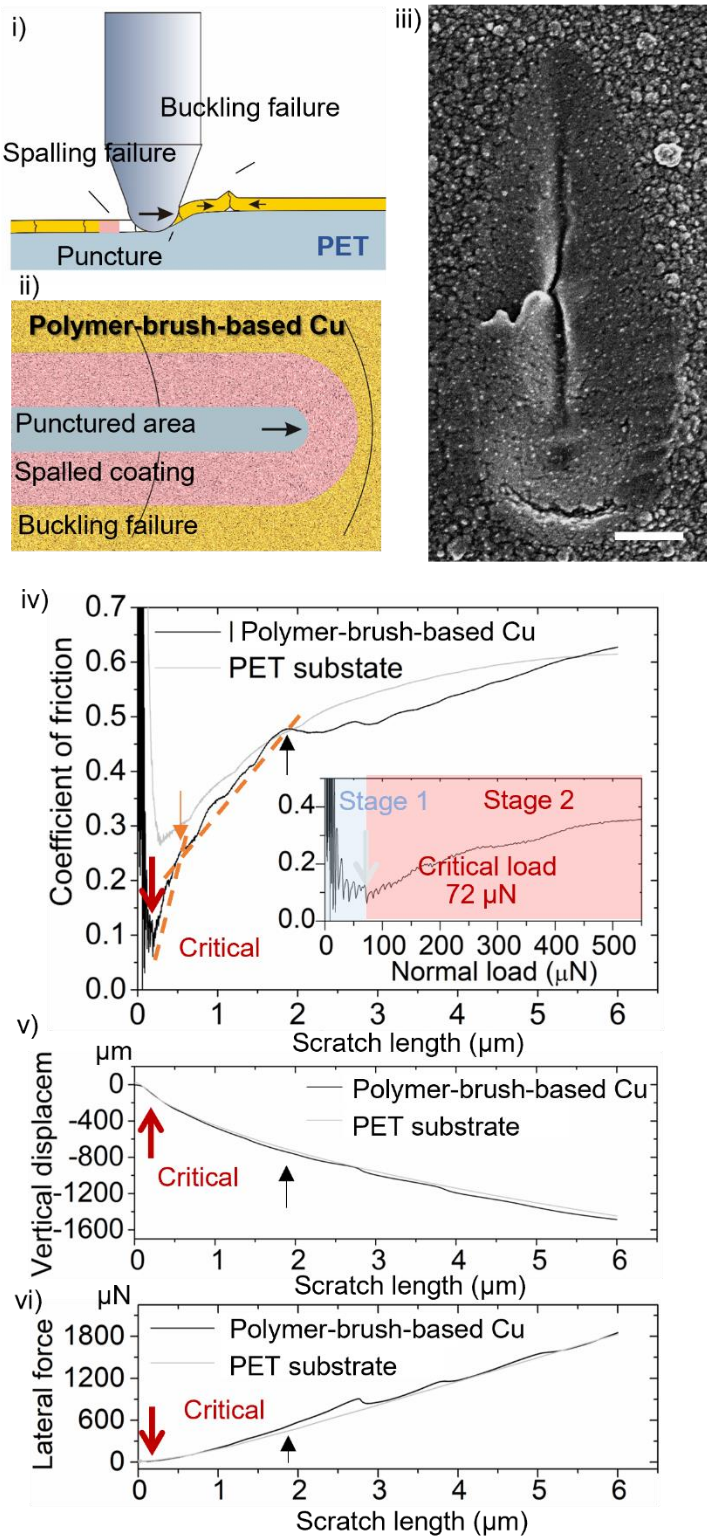

Figure 4.26. Nano-scratching test polymer-brush-based Cu electrode on the PET substrate. i) Side view, ii) top views of the schematics of the coating failure modes, iii) SEM image iv) typical (main plot) and enlarged (insets) coefficient of friction curve, v) vertical displacement curve, and vi) lateral force curve of the nano-scratching test. The red, orange and black arrows are on behalf of the borders of the 4-nanoscratching sections. The grey lines demonstrate the comparison experiment that scratched the surface of the pure PET substrate without any coatings. The unmarked scale bar is 1 µm. The thickness of all the Cu electrodes was ~200 nm.

We also carried out the nanoscratching test for the polymer-brush-based Cu electrode (Figure 4.26). The polymer-brush-based Cu is grown on a 3-nm-thick polymer brush. According to the number of twists and cracks (Figure 4.26i, ii, and iii) around the straight scratch, the failure mode should belong to the midway between the spalling failure and bucking failure.[113] Figure 4.26iv is the coefficient-of-friction curve demonstrating the critical load of the polymer-brush-based Cu thin film was ~ 72 µN, whilst the broken load was ~ 940 µ. It revealed the stronger mechanical strength of the polymer-brush-based Cu compared with the thermal-evaporated Cu films without the Cr adhesive layer. The vertical displacement curve (Figure 4.26v) and the lateral force curve (Figure 4.26vi) indicated that the stylus penetrated the Cu thin film instead of riding over it after the film breaking point because the curve overlapped with the comparative experiment data sliding pure PET substrate.

4.6.5 Nano Indentation Test

Nano-indentation can detect fracture toughness (K_c), indentation hardness h), and reduced elastic modulus (E_r) of coatings on the substrate.[115] We chose the Berkovich tip, with a three-sided pyramidal shape (with a radius of 150 nm), for a nano-indentation test. The schematic diagram of Oliver & Pharr can calculate Young’s modulus and hardness.[116] E_r is a concept, namely reduced elastic modulus, used to describe the non-perfectly plastic material. The reduced elastic modulus can be calculated by [117]:

$$\frac{1}{E_r} = \frac{(1-\upsilon^2)}{E} + \frac{(1-\upsilon_i{}^2)}{E_i}$$

υ and υ_i represent the Poisson ratio of sample and indenter. And the E & E_i are Young’s modulus of sample and indenter, respectively. Since the Berkovich tip was made of diamond, the E_i and υ_i were set to be 1140 GPa and 0.07, respectively. As the indentation happens on the very top of the metal layer, the Poisson ratio of υ 0.33 for Cu. E_r represents the reduced modulus. load vs displacement images can analyze various mechanical properties of the coatings, as early as the 1970s.[118]

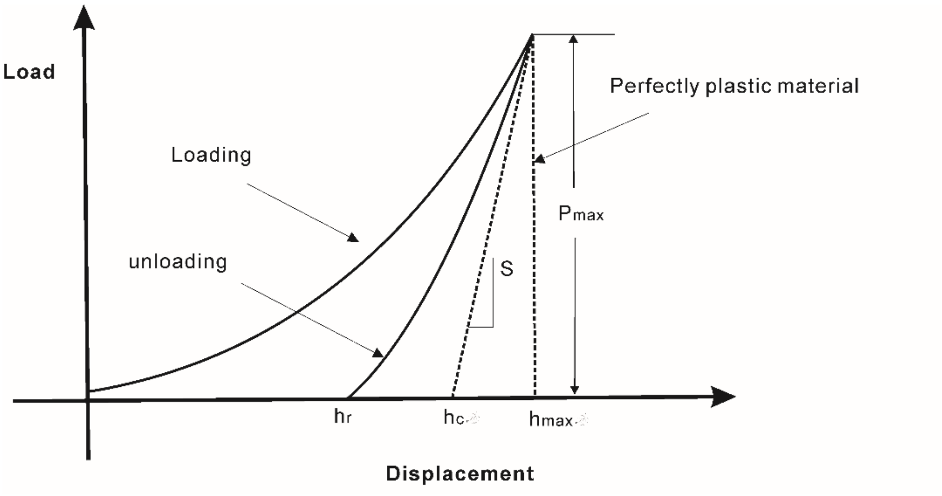

Figure 4.27. Schematic diagram of load vs displacement curve.[117]

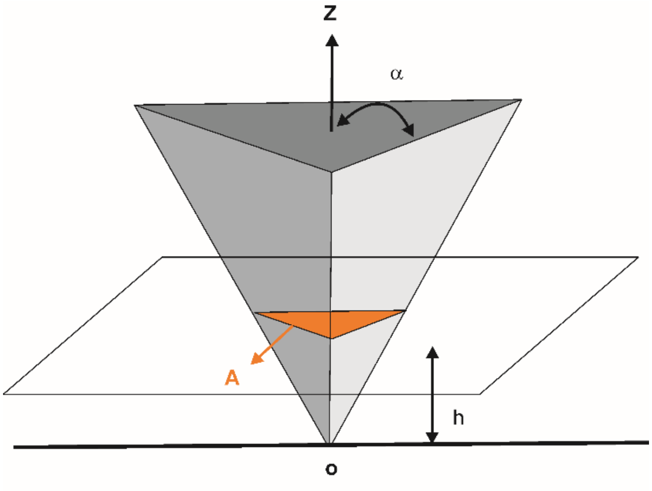

Figure 4.28. Schematic diagram of the Berkovich tip and the definitions of indentation area A, the indentation depth h, and the position of half-angle α.[119]

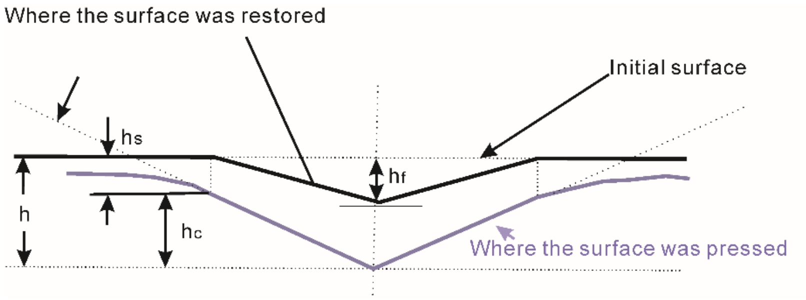

Figure 4.29. Schematic diagram of a cross-sectional view of the indentation process. [117]

As shown in Figure 4.27, the definition of h_{max} is the maximum depth that the tip has reached, while the h_r (alias h_f) representing the residual depth that the specimen can recover after the unloading curve. Thus, the stiffness of sample S follows the equation[120]:

$$S = \frac{dP}{dh} = \frac{2}{\sqrt{\pi}} E_r \sqrt{A}$$

As shown in Figure 4.28, A stands for the indentation area (projected area during the elastic contacting process), and h is the indentation depth.[120] The definition of P is the exerted load. Therefore, the initial data can calculate the stiffness and reduced elastic modulus.

Figure 4.29 expressed the cross-sectional view of the nano-indentation process.[117] The total displacement h equals the sum of h_c and h_s. h_c, namely contact depth, is the depth of specimen completely along the shape of indenter tip. And the h_s represents the depth of the surface sinking along the perimeter of the connecting area. h_c is the contact depth, can be expressed by:[119]

$$h_c = h_{max} - \varepsilon \times \frac{F_{max}}{S}$$

ε is a value demonstrating the possible range for the h_c, set to 0.75 for ones with a similar shape of a paraboloid.[117] The indentation hardness can be calculated by:[117]

$$H = \frac{P_{max}}{A}$$

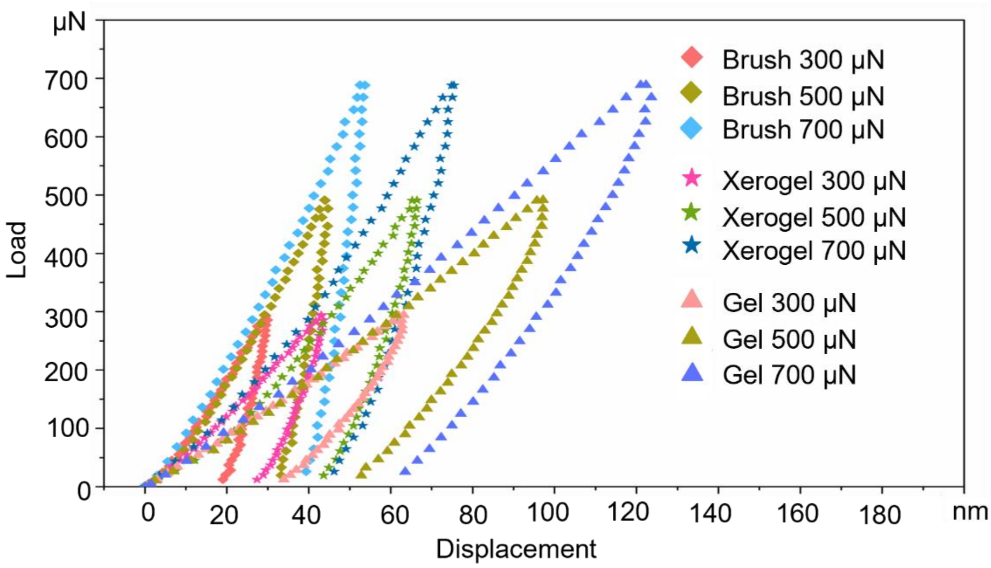

Figure 4.30. Load–displacement curves for the three different PAMD-based Cu electrodes after the nanoindentation test with an average load of 300 μN, 500 μN, and 700 μN.

Figure 4.30 is the load vs displacement curve of xerogel-based Cu electrodes, gel-based Cu electrodes, and polymer-brush-based Cu electrodes (on a rigid silicon wafer). As there are no apparent cracks around the indented boundary (Figure 4.31), these nano-indentation test data prove to be valid. From the formula listed above, we can calculate lots of physical properties of the three different Cu electrodes. Table 4.2 listed the mechanical properties, including reduced modulus (E_r), Young's modulus (E), hardness (H), reciprocal of hardness-to-modulus ratio (E/H), contact depth (h_c), stiffness (S), maximum indented depth (h_{max}), contact area (A), and fracture toughness $(k_c)$of the above mentioned three PAMD-based Cu electrodes.

Table 4.2. The mechanical properties of PAMD-based Cu electrodes were measured by Hysitron TI 900 nanoindentater when exerting different maximum loads.

Materials	Pmax [μN]	Er [Gpa]	E [Gpa]	H [Gpa]	E/H	hc [nm]	S [nN/nm]	Hmax [nm]	A [nm^2]	Kc [Mpam$^{1/2}$]
Polymer-brush-based Cu	700	155	124	4.20	29.5	46	71	53	164932	0.80954
	500	132	113	3.74	30.2	39	58	45	132361	0.70375
	300	130	104	3.78	27.5	25	41	30	78220	0.70356
Gel-based Cu	700	65	52	2.87	18.1	62	36	75	242001	0.55381
	500	71	57	2.71	21.0	50	34	61	183056	0.55226
	300	71	57	2.47	23.1	36	28	44	119867	0.54770
Xerogel-based Cu	700	23	18	1.5	12.0	96	17	126	462571	0.42070
	500	25	20	1.49	13.4	77	16	100	332291	0.47617
	300	31	25	1.64	15.3	50	15	64	180811	0.33456

4.6.6 Derivation of the Adhesive Energy

And fracture toughness is a value of the force the film can bear before the film crack, which can be derived from:[121]

$$k_c = \alpha\sqrt{\frac{E}{H}}\frac{P_{max}}{c^{\frac{3}{2}}}$$

Where c is the crack length on the surface measured by estimating the distance between the centre of the indent to the radical peak of the crack in the SPM images. Figure 4.31 is the cross-sectional profile of the Cu surface after the nano-indentation test.

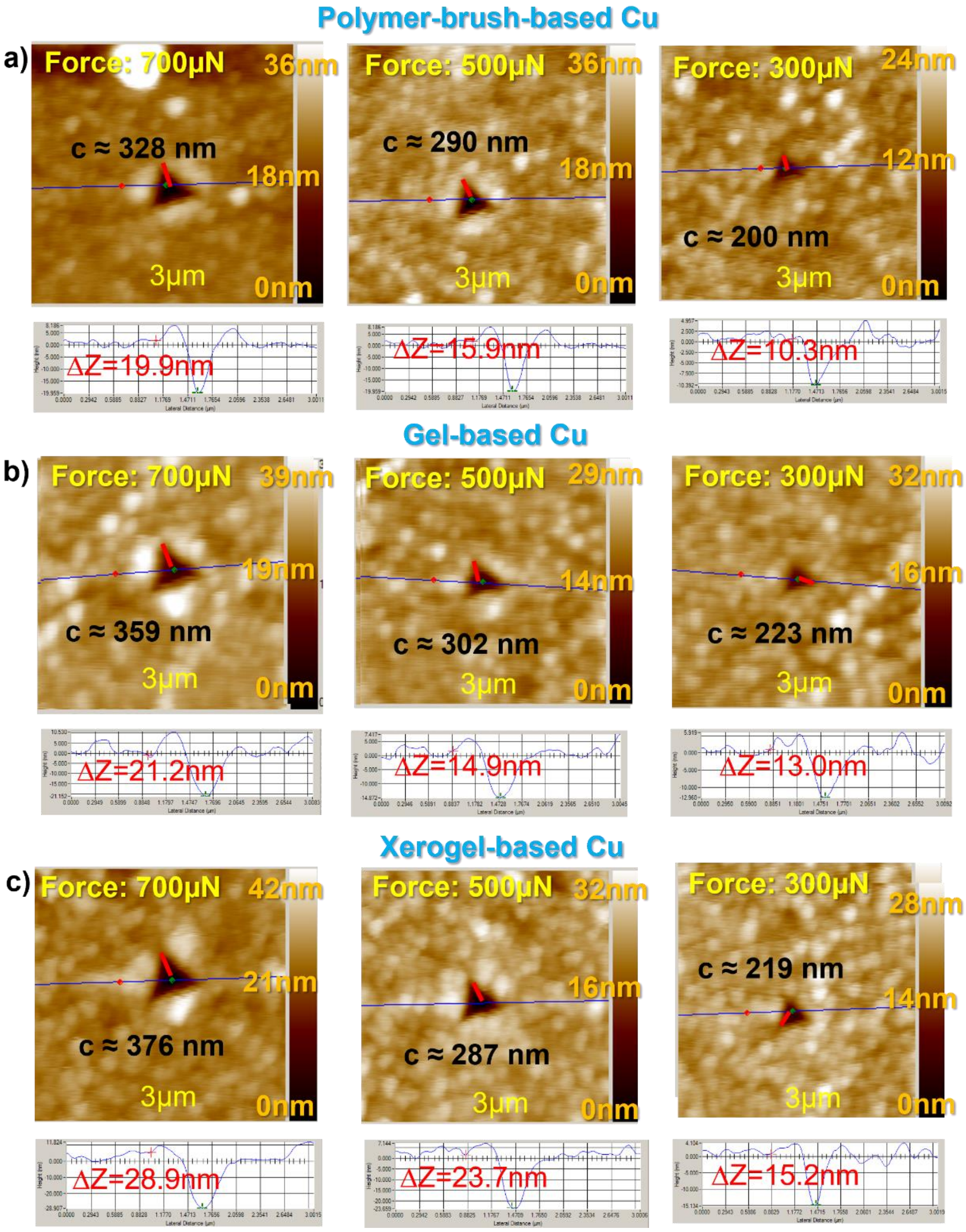

Figure 4.31. In-situ scanning probe microscopy (SPM) images and cross-sectional profiles of a) polymer-brush-based Cu electrode, b) gel-based Cu electrode and c) xerogel-based Cu electrodes after nanoindentation test under the maximum load of 300 µN, 500 µN, and 700 µN. The crack lengths, c, were marked by red lines.

The H/E is the hardness-to-modulus ratio. Pharr et al. defined the constant of α as 0.04 for sharp tips such as Berkovich.[122]

According to the previous TEM analysis (Figure 4.31), the polymer-brush-based Cu electrodes have an extremely thin polymer-Cu interpenetrating layer (~3-nm-thick). It is only 1.5% of the total thickness. Therefore, we can ignore this extremely thin buffer layer mechanical performance on the overall structure. The polymer-brush-based Cu electrode can be regarded as a template to study the mechanical properties of the upper-pure-Cu layer for PAMD-based Cu electrode. Simultaneously, the xerogel-based Cu electrode can have a bi-layer electrode with a polymer-Cu interpenetrating layer at the bottom. As shown in Table 4.2, Young's modulus and hardness of the xerogel-based Cu electrode, with a bi-layer structure, are around half of the pure Cu electrode. On a rigid substrate (e.g. a silicon wafer), the xerogel-based Cu electrode exhibit low fracture toughness (~0.4 Mpam$^{1/2}$), which means easy to form cracks when applying downward pressure with a sharp object.[123] However, on soft substrates (e.g. PET), the xerogel-based electrodes, with bi-layer structure, are difficult to break, as shown in the previous nanoscraching test. The larger fracture toughness not indicating better durability on a soft substrate like PET. Because the thermal-evaporated Cu film, with a fracture toughness of 3.8 MPam$^{1/2}$ (reported by Keller et al.[124]), was penetrated with ease by a semicircular stylus during the nano-scratching test. Therefore, the Cu-polymer-interpenetrating layer must play an important role in dealing with the tiny dispatching between the substrate and the upper-pure-Cu layer. This phenomenon is worth further investigation and study.

From the results of the nano-scretching test and nano-indentation test, the interfacial adhesive energy can be calculated by[101b, 125] :

$$G_c = \frac{\sigma_c^2 t}{2E}$$

Where t is the film thickness, and E is elastic modulus. σ_c represent for the critical stress of nano-scratching can be derived by[101b, 125]:

$$\sigma_c = \left(\frac{2P_c}{\pi d_c^2}\right)\left[\frac{(4+\nu)3\pi\mu}{8} - (1-2\nu)\right]$$

Where ν stand for Poisson ratio set to 0.33 for Cu thin film, µ is the friction coefficient on the critical point. P_c represents the value of the critical load. The d_c stands for critical scratching track width. All the samples shared the same d_c value (i.e., 200 nm) to simplify the calculation. The SEM image identified the d_c value for the polymer-brush-based Cu electrodes. Then, we set the elastic modulus of all the thermal-evaporated-Cu, to be 120 GPa, summarized by Qian et al.[126] The elastic modulus value was all selected to be the data under the maximum load of 300 µN. Then we got to know that the xerogel-based Cu electrode has the highest adhesive energy, i.e., 0.70147 J/m^2. It proved that the inkjet-printed copolymer matrix covalently bonded with PET substrate after the UV-crosslinking. In the same way, the polymer-brush-based Cu electrode also shown adhesive energy of up to 0.16482 J/m^2, and the gel-based Cu electrode (with a highly thick polymer-Cu-interpenetrating layer) have low adhesive energy (0.06250 J/m^2). It may be because the individual polymer clusters in xerogel film are thicker than the clusters in gel thin film. The cross-sectional TEM image demonstrated the increased thickness of the polymer cluster in the xerogel-based Cu electrode, in contrast with the thin cluster in the gel-based Cu electrode. The gel-based Cu electrode shown more considerable hardness. However, more brittle with the deformation of the substrate. The microstructure of the thick copolymer had better durability than the thinner copolymer cluster when combined with sharp Cu crystals with high Yong's modulus. Initially, the copolymer clusters were slender and fragile in gel thin film. The EtOH treatment, however, in the production process of xerogel-based, happened to complete the thickening and strengthening of the polymer cluster. Capillary action during the violent evaporation process of EtOH may group these well-crosslinked polymer clusters. Therefore, the xerogel-based Cu electrode with thicker and stronger polymer clusters gave full play to the advantages of covalent bonding with the plastic substrate making the upper-pure-metal electrode difficult to delaminate with the Cu-polymer-interpenetration layer. Regarding adhesive energy to a plastic substrate, the xerogel-based Cu electrode is far ahead of the traditional thermal-evaporated Cu electrodes, including those with a Cr adhesive layer (only 0.06073 J/m^2).

Table 4.3. Fracture strength and interfacial adhesive energy of PAMD-based Cu electrodes comparing with thermal evaporated Cu electrodes.

Sample	Thermal evaporated Cu without Cr	Thermal evaporated Cu with Cr	Polymer-brush-based Cu	Gel-based Cu	Xerogel-based Cu
μ	0.13	0.17	0.09	0.12	0.11
$\lvert\sigma_c\rvert$ [MPa]	53	270	414	189	419
G_c [J/m^2]	0.00225	0.06073	0.16482	0.06250	0.70147

4.7 Other Physical Properties of Xerogel Thin-films and Xerogel-based Cu Electrodes

The METAC groups with vital hydrophilicity offer water-absorption functions for their copolymers.[127] The xerogel is a well-crosslinked copolymer matrix of P[MBP-co-METAC], a copolymer with METAC group, should have good hydrophilicity. A proof-of-concept tested the thickness verification of an inkjet-printed copolymer-paste thin film in different humidity by a non-contact mode AFM.

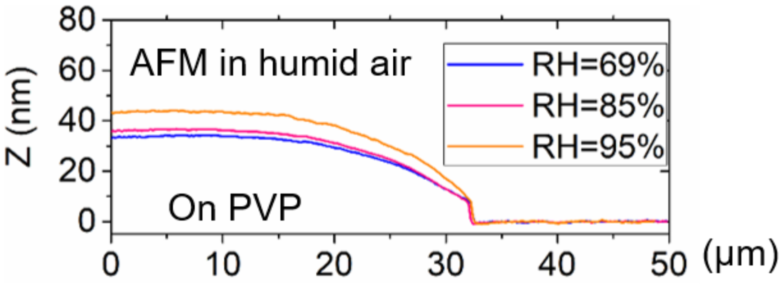

Figure 4.32. Thickness verification of an inkjet-printed copolymer paste pattern in an environment with different humidity. The substrate is PVP thin film, spin-coated on a silicon wafer.

As shown in Figure 4.32, when increased the relative humidity (RH) of the air from 69% (the original moisture in Hong Kong in October) to 95%, the thickness significantly increased. Therefore, the inkjet-printed P[MBP-co-METAC] can absorb moisture from the air, especially in a high humidity environment (>90 RH%).

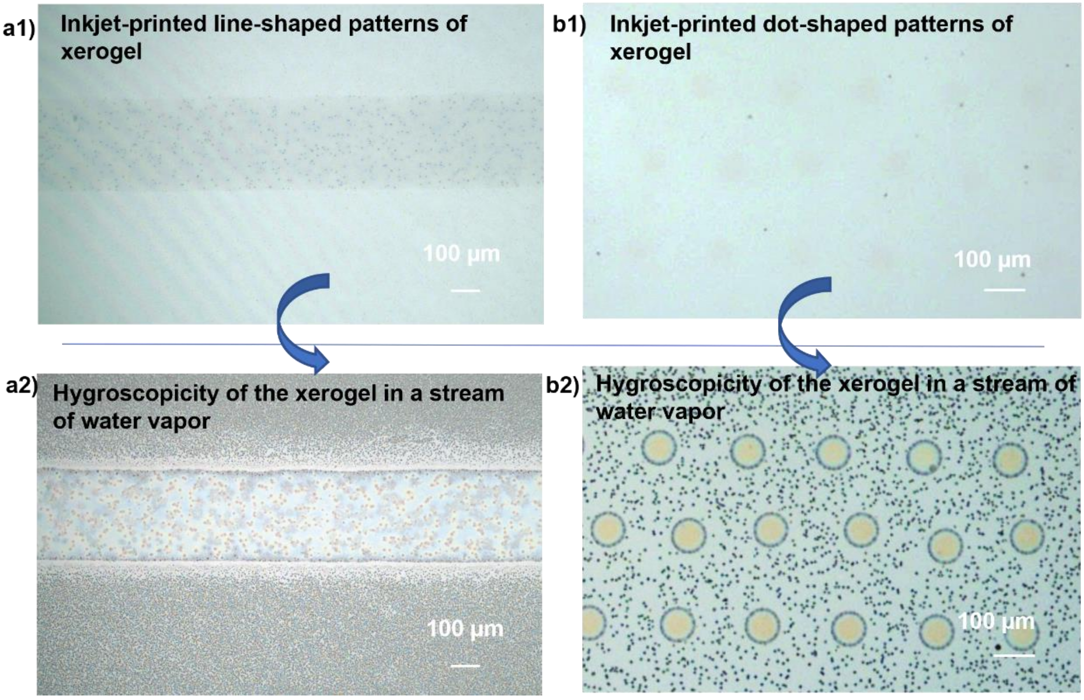

Figure 4.33. Optical microscopic images of the inkjet-printed xerogel patterns, with a) line-shape and b) dot-shaped pattern, before (upper) and after (bottom) been exposed to a stream of water vapor. The substrates of these printed patterns were PVP thin film that spin-coated on a glass slide.

Then we blew the xerogel patterns, coated on a PVP modified glass, with a stream of water vapor. Some water droplets evenly condense on the surface of the substrate. As shown in Figure 4.33, the tiny water droplets condensed on xerogel thin-film emerged with each other forming a liquid sheet. And the uniform color distribution of the water thin film demonstrating a uniform thickness distribution of the liquid sheet on the xerogel pattern since the color verification is formed by thin-film interference.[128]

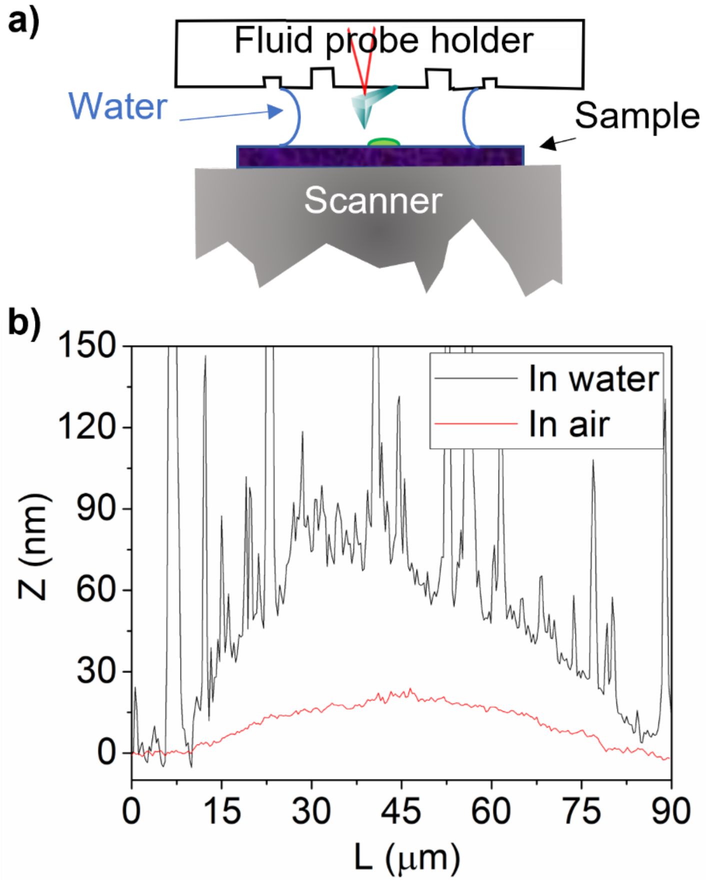

Figure 4.34. a) Schematic diagram of the fluid tapping mode AFM used to test surface topography of samples underwater. b) The cross-sectional AFM images showing the thickness verification when immerged the inkjet-printed xerogel into water.

The xerogel, even with the loose mesoporous structure, still shown good water-absorbing ability. We assume the xerogel can swell in these water films. As a proof-of-concept, we used fluid mode AFM to evaluate the morphology of the xerogel thin-film underwater. A drop of DI water occupied the space between the fluid probe holder and the sample's surface. The AFM tip dived into the DI water drop for testing. As shown in Figure 4.34, the xerogel thin-film swelled in water.

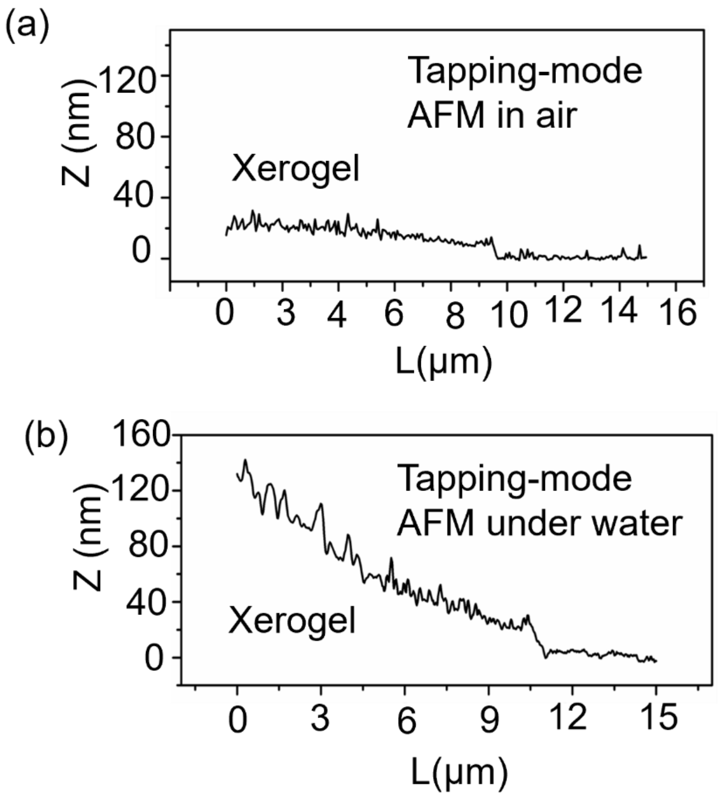

Figure 4.35. The cross-sectional AFM images (with a scanning scope of 15 μm) comparing the thickness of the inkjet-printed xerogel a) before and b) after been immersed in water.

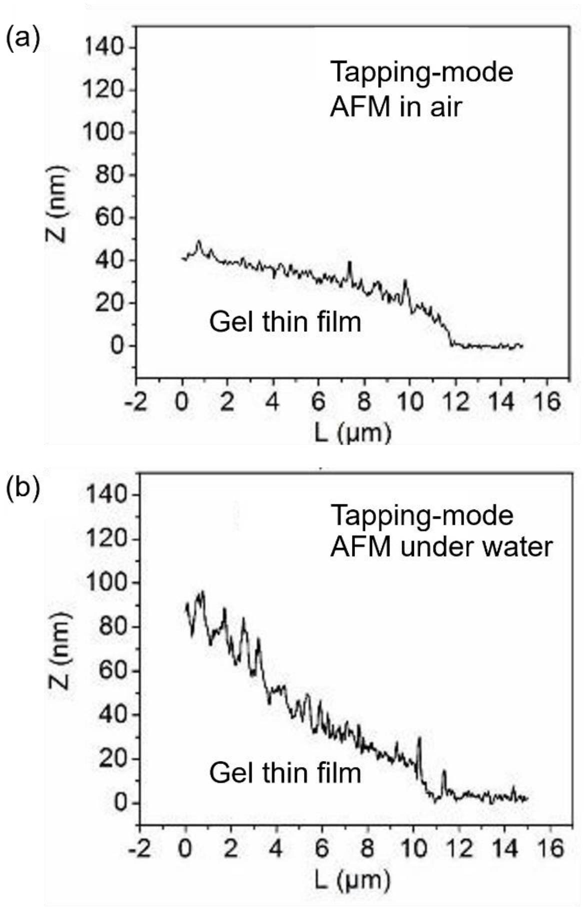

Figure 4.36. The cross-sectional AFM images (with a scanning scope of 15 μm) comparing the thickness of the inkjet-printed gel thin film a) before and b) after been immersed in water.

The copolymer thin film closes to the center area, swollen to around three times its original thickness. The boundary area, about 7-μm-wide, expanded by less than double the thickness, as shown in the fine scanning image (Figure 4.35). The boundary region of the inkjet-printed gel and xerogel patterns, close to the TCL line, usually has relatively condensed polymer deposition. We assumed they formed by the copolymer molecule with less molecular weight and are more likely to deposit on edge regions during the complicated drying process of the liquid droplets.[129] This extremely narrow transition area (In comparison to the 50-μm-wide printing orifice) offered a smooth boundary for the xerogel-based Cu electrode. Figure 4.36 is the cross-sectional AFM images showing the swollen gel-thin film (without EtOH treatment) in an aqueous environment. The degree of expansion is similar to that of the xerogel. It further confirmed that the xerogel copolymer skeleton is the main body that swells underwater.

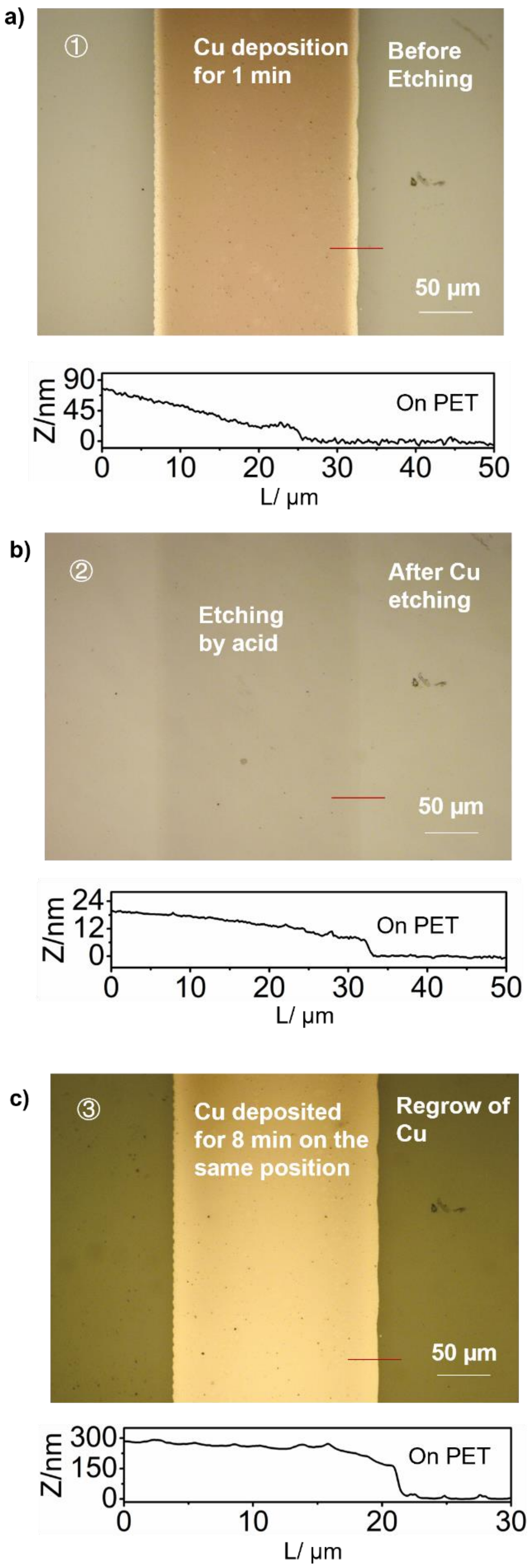

Figure 4.37. Optical microscopic images and AFM cross-sectional images of the xerogel-based Cu electrodes a) after 1-min-metal-electroless deposition, b) after

corroded by dilute nitric acid, and c) regrowing of Cu in the residual xerogel pattern for 8 min.

As shown in Figure 4.37, the Cu electrode can regrow on the xerogel matrix after being corroded by acid. Therefore, if such an electrode has rust due to long-term use, a new xerogel-based Cu electrode can be regrown on the residual xerogel matrix with ease by simply immersing the xerogel pattern into catalyst solutions the electroless deposition solutions in turn. The removable Cu layer is also good for plastic recycling. The xerogel electrode electroless deposited for 1 min shown dark color, whilst the electrodes with 8-min-electroless deposition have bright color, as shown in Figure 4.37.

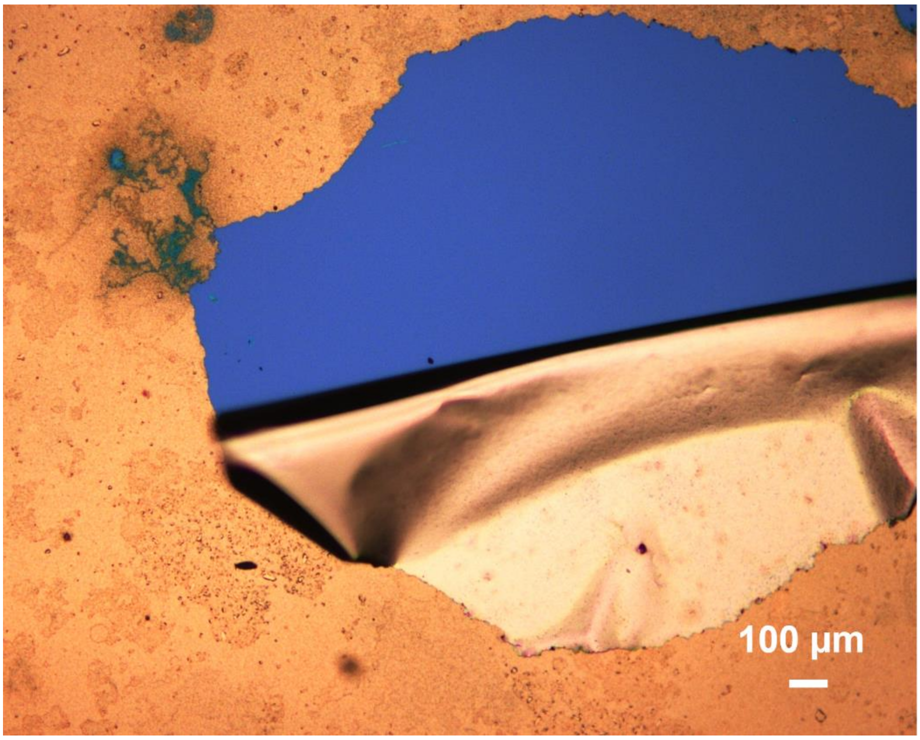

Figure 4.38. An optical microscopic image of the xerogel-based Cu electrode peels off from the silicon substrate showing the front and back of the Cu electrode.

Figure 4.38 shows the optical microscopic image of the xerogel-based Cu electrode deposited on the silicon wafer delaminated after 10 min metal electroless deposition. The surface of the upper-pure-Cu layer shows lighter color than the bottom interpenetration network of Cu and xerogel matrix.

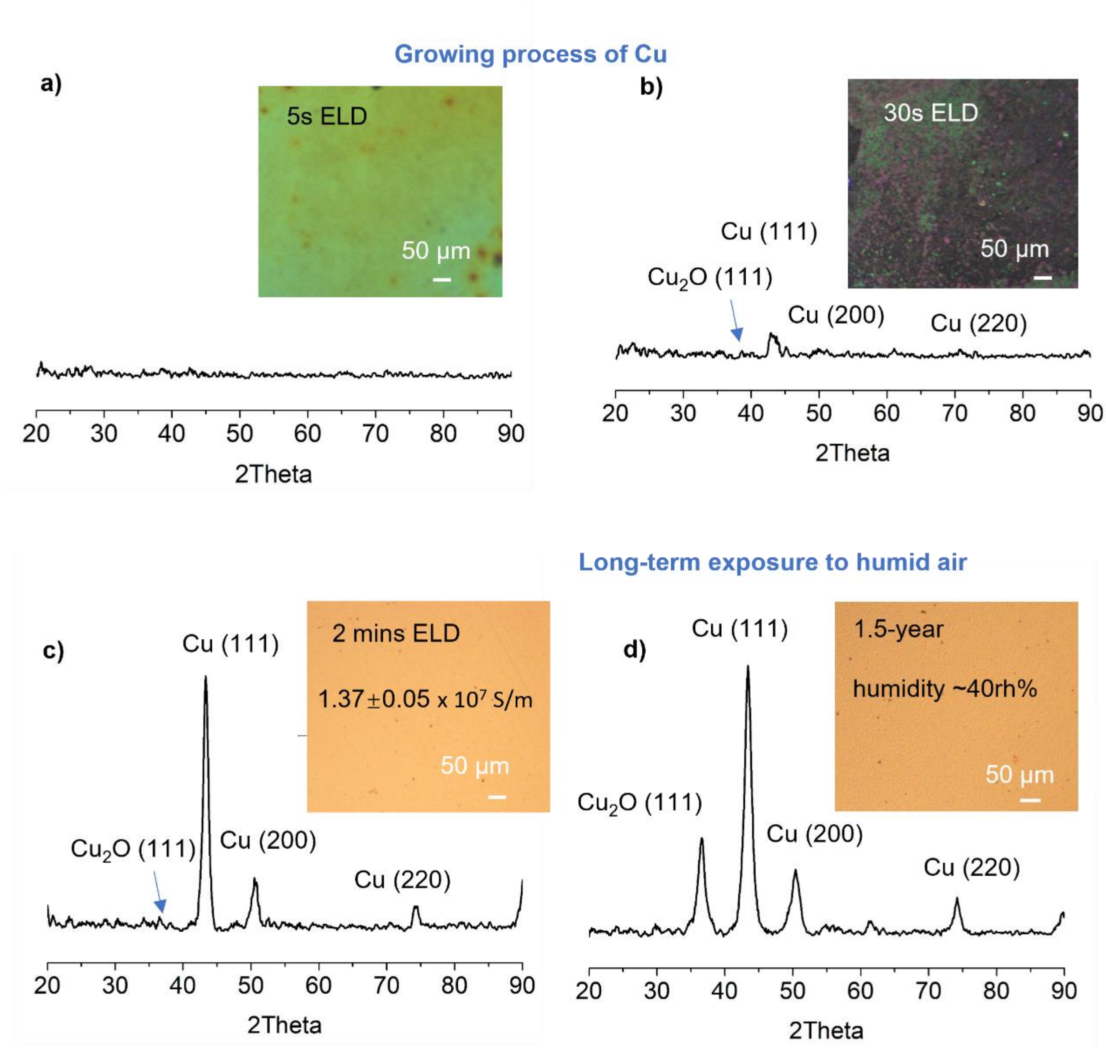

Figure 4.39. XRD spectra of the xerogel after a) 5 s, b) 30 s, c) 2-min-metal-electroless deposition. d) The XRD spectra of the xerogel-based Cu electrode, formed by 2-min-metal-electroless deposition after being placed in ambient condition (with humidity of more than 40% RH in Hong Kong) for half a year. Insect: optical microscopic image of the color verification of the xerogel, after different times of the electroless metal deposition. Silicon wafer with a 200-nm-thick layer of SiO_2 was the substrate.

We believe the dark formed by the reduced size of the Cu crystal when interacted with the xerogel matrix, not by the oxidation of the Cu crystal.[130] As a proof-of-concept, we investigated the material composition of the xerogel at the initial state of the electroless deposition process by x-ray diffraction (XRD) analysis. As shown in Figure 4.39a, 5-s-electroless deposition is too short for depositing enough Cu to generate a signal the XRD detector can detect. Nevertheless, after a 30-s-electroless deposition, the color of the xerogel thin-film converted to black. The Cu deposited in the pore of mesoporous xerogel was pure Cu without copper oxides. It proved our previous hypothesis. The nanosized Cu formed the dark color but not the copper oxide. When elongated the electroless deposition time to 2 min, a xerogel-based Cu electrode with a bright orange surface appeared. The relatively pure copper with a polycrystalline crystal can form an electrode with food electrical performance. However, when we placed it in the ambient condition (with humidity more than 40% RH in Hong Kong) for half a year, the Cu_2O appeared on its surface. The upper-pure-Cu layer of the freshly prepared xerogel-based Cu electrodes has an electrical conductivity of (1.2 ± 0.05) × 10^7 S/m and provides the electrode's major conductivity. In comparison, the conductivity of the bottom layer (Cu crystal + xerogel matrix) is negligible, maybe because polymer clusters separated most of the Cu particles.

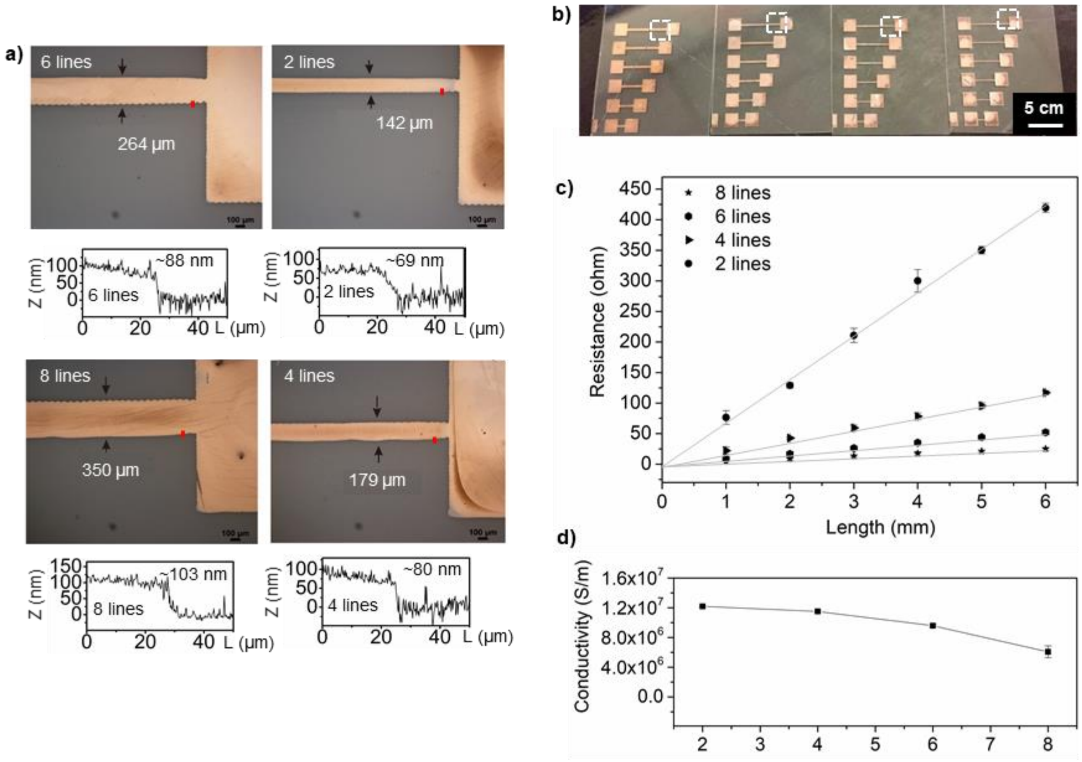

Figure 4.40. Identification of electrical conductivity of the inkjet-printed xerogel-based Cu electrode. a) Optical microscopy images with the AFM profiler tests and b) optical image of the inkjet-printed Cu line-shaped pattern used to measure electrical properties of the xerogel-based Cu lines with different widths and lengths. Choosing different numbers of printed parallel lines of individual drops (i.e.,2, 4, 6 and 8) results in various widths of the line-shaped patterns. The ELD time of all these electrodes was all set to

be 1 min. c) Measured resistance of the inkjet-printed Cu lines at different length and with various line widths. d) Calculated conductivity of the inkjet-printed Cu lines with various line widths.

Figure 4.40c shows the measured resistance of Cu lines for different lengths and various line widths collected from five batches of samples. The conductivity of the Cu electrode, σ, can be calculated according to the equation:

$$\sigma = \frac{L}{RA}$$

L is the length of the electrode, R is the detected resistance, A is the cross-sectional area of the upper-pure-Cu layer. The thickness of the upper-pure Cu layer can be obtained by subtracting 50 nm from the measured overall thickness (AFM cross-sectional profile in Figure 4.40a). Because the thickness of the bottom layer (the interpenetration network of Cu and the xerogel scaffold) was ~ 50 nm, which was identified by the TEM cross-sectional image of the xerogel-based Cu electrode.

Therefore, the average conductivity of the Cu lines was calculated to be $6.084 \pm 0.826 \times 10^6$, $9.595 \pm 0.201 \times 10^6$, $11.548 \pm 0.196 \times 10^6$, and $12.186 \pm 0.125 \times 10^6$ S/m for line width of 142, 179, 264, and 350 μm, respectively (Figure 4.40 d). It is interesting to note that the conductivity of the Cu lines increased slightly as the printed line width increased. It can be seen from Figure 4.40a that the line-shaped Cu electrode with thinner width has thinner intersection areas when contacting the large-size square electrode on the right-hand side. The thinner intersection area leads to the smaller electrical conductivity of the Cu electrode. We believe that the thinner intersection area was formed by the complicated immerging and drying process of the inkjet-printed ink droplets during the patterning process. The wider line with a uniform interconnection area showed good electrical conductivity. This conductivity can represent the real electrical conductivity of the upper-pure Cu layer of the xerogel-based Cu electrode after excluding the uncertainty caused by the intersection area.

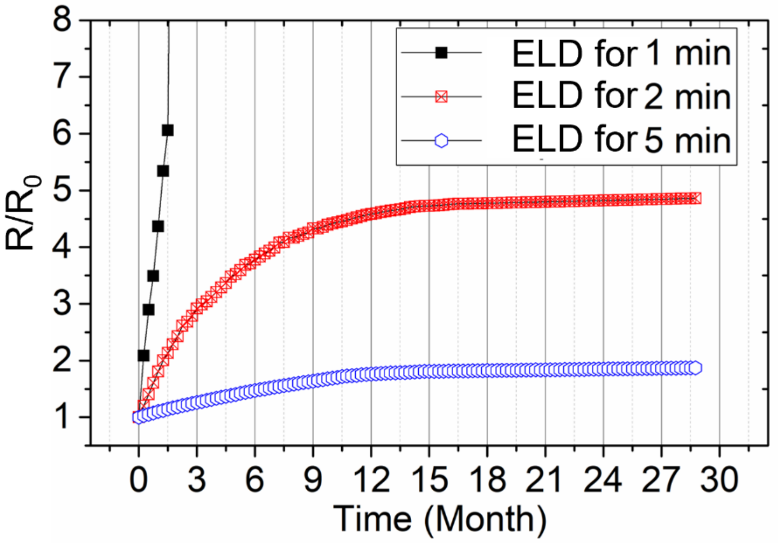

Figure 4.41. The verification of the electrical conductivity of the xerogel-based Cu electrodes, without any encapsulation, along the time in ambient condition (with humidity more than 40% RH in Hong Kong).

We assume that the conductivity will decrease slowly over time because the surface of the Cu layer can be oxidized for a long time placed in the ambient condition. As a proof-of-concept, we used nearly two and a half years to continuously record the changes in the conductivity of three sets of electrodes (without encapsulation), with different electroless deposition times (i.e., with different thickness), over time. We found that the electrode formed by 5-min metal electroless deposition had minimal verification of conductivity over time.

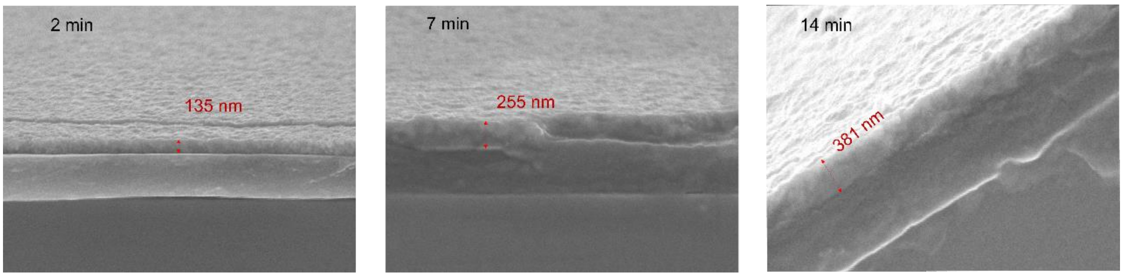

Figure 4.42. SEM images of the cross-sectional view of the xerogel-based Cu electrode on the PVP thin film show the thickness change along with the ELD duration.

Figure 4.42 is the SEM image of the cross-sectional view of the xerogel-based Cu electrode on a PVP thin film showing the thickness verification of the Cu electrode versus the electroless deposition time.

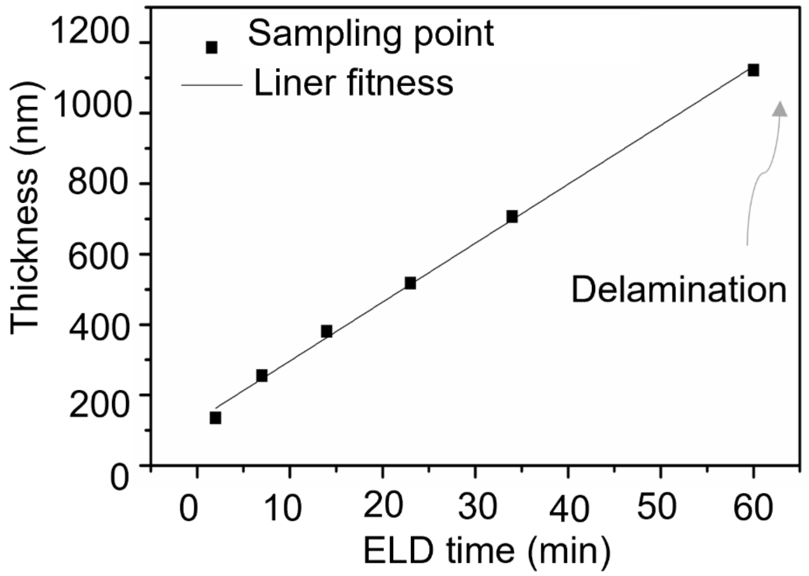

Figure 4.43. The thickness of the xerogel-based Cu electrode vs electroless deposition time.

We also assume that the thickness of the Cu electrode correlated with the electroless deposition time. Figure 4.43 is a diagram demonstrating the approximately linear relationship between the electroless deposition time and the thickness of the electrode. After more than 1-h-metal-electroless deposition, the Cu electrode tended to delaminate and get off from the substrate.

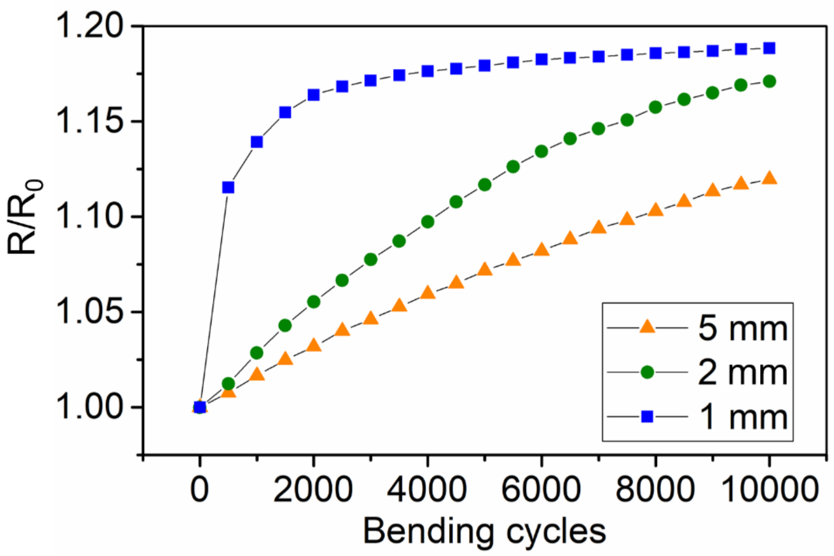

Figure 4.44. Resistance of xerogel-based Cu electrode during 10000 bending cycles with a 1 mm, 2 mm, and 5 mm bending radius.

Figure 4.44 shows the conductivity of the xerogel, deposited on a 50-µm-thick PET substrate during 10000 times bending at different radius. The electronic conductivity of the xerogel-based Cu electrodes tends to be stable after increasing. Therefore, we assume some tiny structure verification happened after the bending exercise, making the electrode adapted to the tiny surface mismatches. As a proof-of-concept, we scanned the surface of the electrode by a high precision optical microscope.

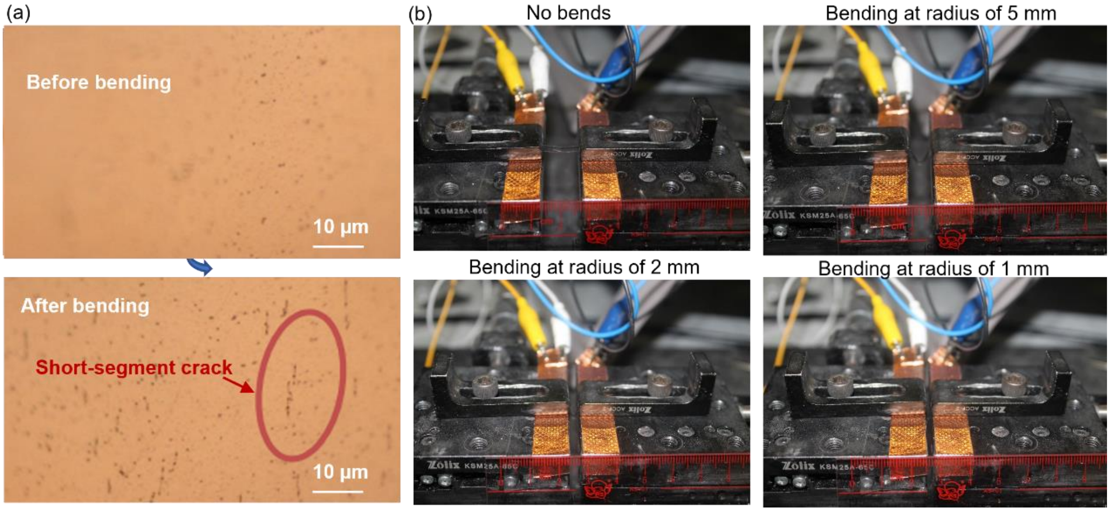

Figure 4.45. a) Optical microscopic image of the xerogel, deposited on a 50-µm-thick PET substrate, before (upper) and after (bottom) 10000 times electroless deposition. b) Displacement platform ensuring an electrode (1.8 cm × 300 µm), inkjet printed on a band of a 50-µm-thick PET substrate, bending at the radius of 1mm, 2 mm and, 5mm.

As a result, short-segment cracks appeared on the bending part of the electrode, as shown in Figure 4.45a. Figure 4.45b shows photos of the displacement platform used to ensure the PET substrate with the coating of the xerogel-based Cu electrode can bend at a radius of 1mm, 2 mm, and 5mm.

4.9 Conclusion

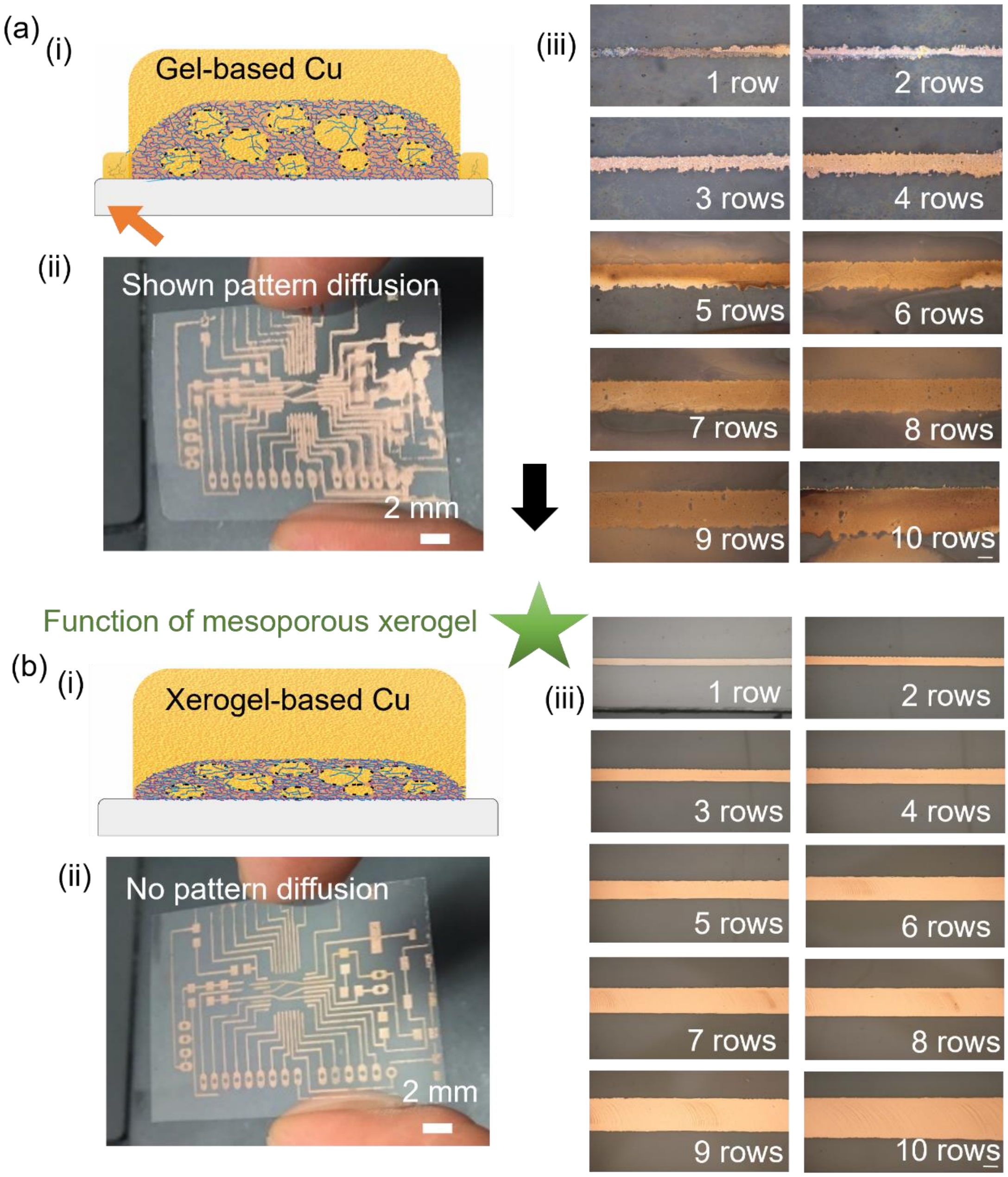

Figure 4.46 The function of mesoporous xerogel in suppression of the irregular Cu growing. i) Schematic diagram and optical images of the inkjet-printed a) gel-based Cu electrodes, b) xerogel-based Cu electrode forming ii) electronic circuit, and iii) line-shaped electrodes. The line-shaped electrodes were formed by ink arrays with different numbers of rows. The unmarked scale bar is 200 µm.

The mesoporous structure of the xerogel and its formation mechanism was discovered and proved by experiments. As shown in Figure 4.2, the xerogel and its corresponding treatment method eliminated the randomly grown Cu around the boundary of the inkjet-printed pattern. And this chapter reported the investigation of the nanostructure of the interpenetration network of the xerogel and the interpenetration of the xerogel matrix with the Cu nanoparticle by HAADF-STEM and elemental mapping (EELS). The nano-indentation and nano-scratching test indicated that the PAMD-based Cu electrodes, especially the xerogel based Cu electrode, have strong adhesiveness to the plastic substrate. After calculation, the adhesive energy of the PAMD-based Cu electrodes was 0.7 J/m^2 showing an advantage over the thermal-evaporated Cu electrodes (<0.06 J/m^2) even with the Cr adhesive layer. Unlike the gel-based Cu electrode with scattered and brittle copolymer clusters attached to the bottom plastic substrate, the xerogel with a thicker polymer cluster (generated by EtOH violate evaporation) makes the film softer (with a fracture toughness of only 0.3 Mpam$^{1/2}$) but captured large durability. This room-temperature prepared high-quality Cu electrode has the potential to reduce the production cost of the industry of printed high-quality electronic devices.

Chapter 5. A Thin Liquid Film that Difficult to Evaporate Helps Smooth the Intersections and Regulate the Boundaries of the Inkjet-Printed Pattern

5.1 Introduction

Inkjet-printing is a powerful technique that can fabricate thin-film electronic devices, taking the advantages such as low production cost, low material waste, low energy consumption, etc.[4a, 47, 131] However, the inkjet-printed pattern tolerate the coffee-ring effect and the low accuracy due to a complex droplet drying process.[20c, 79, 83] The rough surface morphology and low accuracy hindered the development of high-performance electronic devices by inkjet printing techniques.[19b]

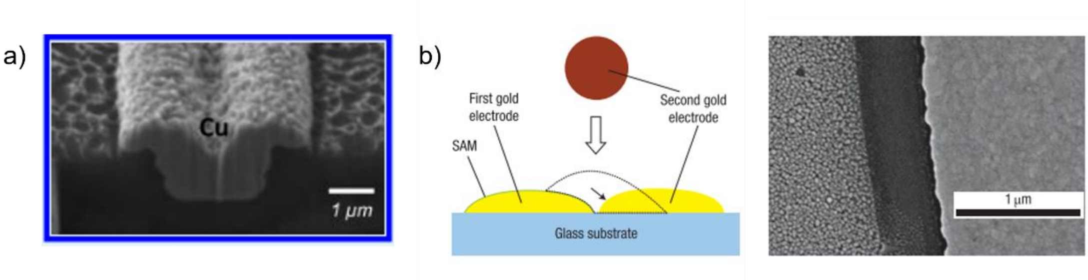

Figure 5.1 Inkjet printing with the help of evaporation or etching techniques with high-energy consumption. a) Cu electrode inkjet-printed in a channel formed by focused ion bean. [98] b) Schematic diagram (left) and SEM image (right) of the self-aligned inkjet-printed narrow channel between the first and second inkjet-printed gold electrodes.[132]

Many thermal evaporated techniques or subtractive etching techniques have been utilized to treat the printing substrate for improving the accuracy of the inkjet-printed patterns, as shown in Figure 5.1.[98, 132] Added high-energy-consumption thermal evaporation techniques or subtractive etching techniques would deviate the original intention in choosing inkjet printing techniques for energy saving and environmental protection.

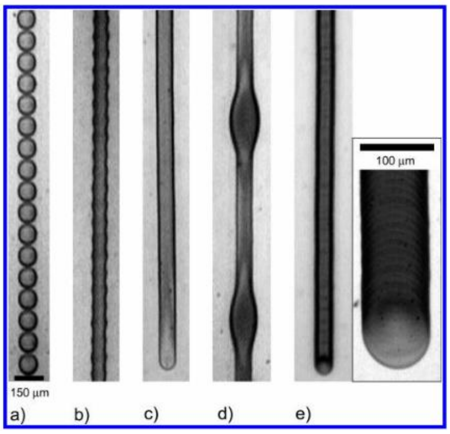

Figure 5.2. Forming uniform edge on the inkjet-printed single-line patterns. The changing droplet spacing can make line-shaped patterns have a structure of a) individual drops, b) scalloped, c) uniform, d) bulging, e) stacked coins.[80]

As shown in Figure 5.2, only the single line pattern can form a perfectly uniform boundary by simply verifying the droplet spacing. But for the two-dimensional design, people still don't have any methods to perfectly maintain the pattern boundary's uniformity. Patterns of different shapes and width have complex effects on the droplet immersion and drying process of the inkjet-printed single droplets and will result in non-uniform boundaries.

Another problem for the inkjet-printed pattern lies in the rough surface morphology induced by the coffee-ring effect. Especially in the joint, the newly inkjet-printed droplet can dissolve the previously printed pattern thin film, making more solutes deposited at the joint. This phenomenon can cause serious irregularity of the surface morphology, as shown in Figure 5.3.

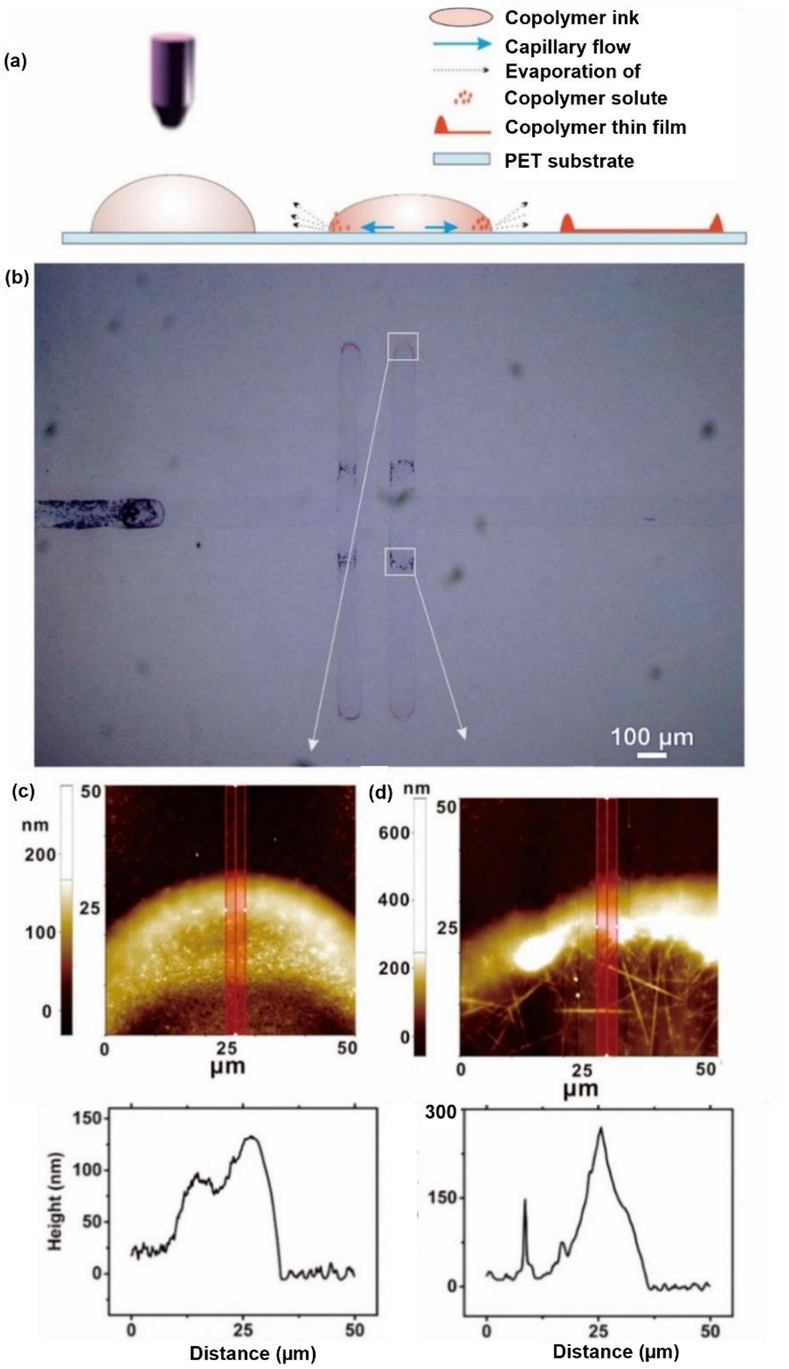

Figure 5.3. a) Schematic diagram showing the forming process of the coffee ring effect. b) Optical image of the inkjet-printed copolymer pattern on PET substrate with coffee ring stain at the boundary and the joint of the vertical and horizontal lines. AFM topographic images and cross-section profile of the copolymer ring stain formed at c) the end of a line and d) the joint.

As early as 1998, scientists found adding slow-evaporation-rate cosolvents in ink can improve the quality of the inkjet-printed pattern for the fabrication of LED lenses.[133] Kim et al. have systematically reported EG, a slow-evaporation-rate cosolvent, could suppress the coffee ring effect. However, that experiment only investigated the coffee-ring suppression phenomenon ion the impact on a drop of ink without studying the inkjet-printed pattern with a two-dimensional design.

Here, we report the ink with the addition of the slow-evaporation-rate cosolvent (EG) for inkjet printing of smooth and uniform xerogel-based Cu electrode. In the specific case of an experiment, we inkjet-print copolymer ink with EG as a slow-evaporation-rate cosolvent for obtaining the uniform boundary and smooth surface morphology of the xerogel-based Cu electrode. We found that the proportion of the slow-evaporation-rate cosolvent is crucial for uniform pattern deposition. On the other hand, excessive slow-evaporation-rate cosolvent leads to uneven thickness distribution of the pattern due to the flowing of the slow-evaporation-rate cosolvent. Furthermore, the insufficient slow-evaporation-rate cosolvent failed to suppress the coffee ring effect efficiently. In addition, a special printing sequence was invented, applying on the ink with slow-evaporation-rate cosolvent (EG), for inkjet-printing of patterns with controllable and uniform boundary, without the help of any evaporation or etching technique. Therefore, the inkjet-printed channel length can be suppressed to ~15 µm, while the diameter of each drop of ink is ~80 µm.

5.2 The Necessity of Using a Three-solution System for the Inkjet-printable Copolymer Ink for Metal Plating

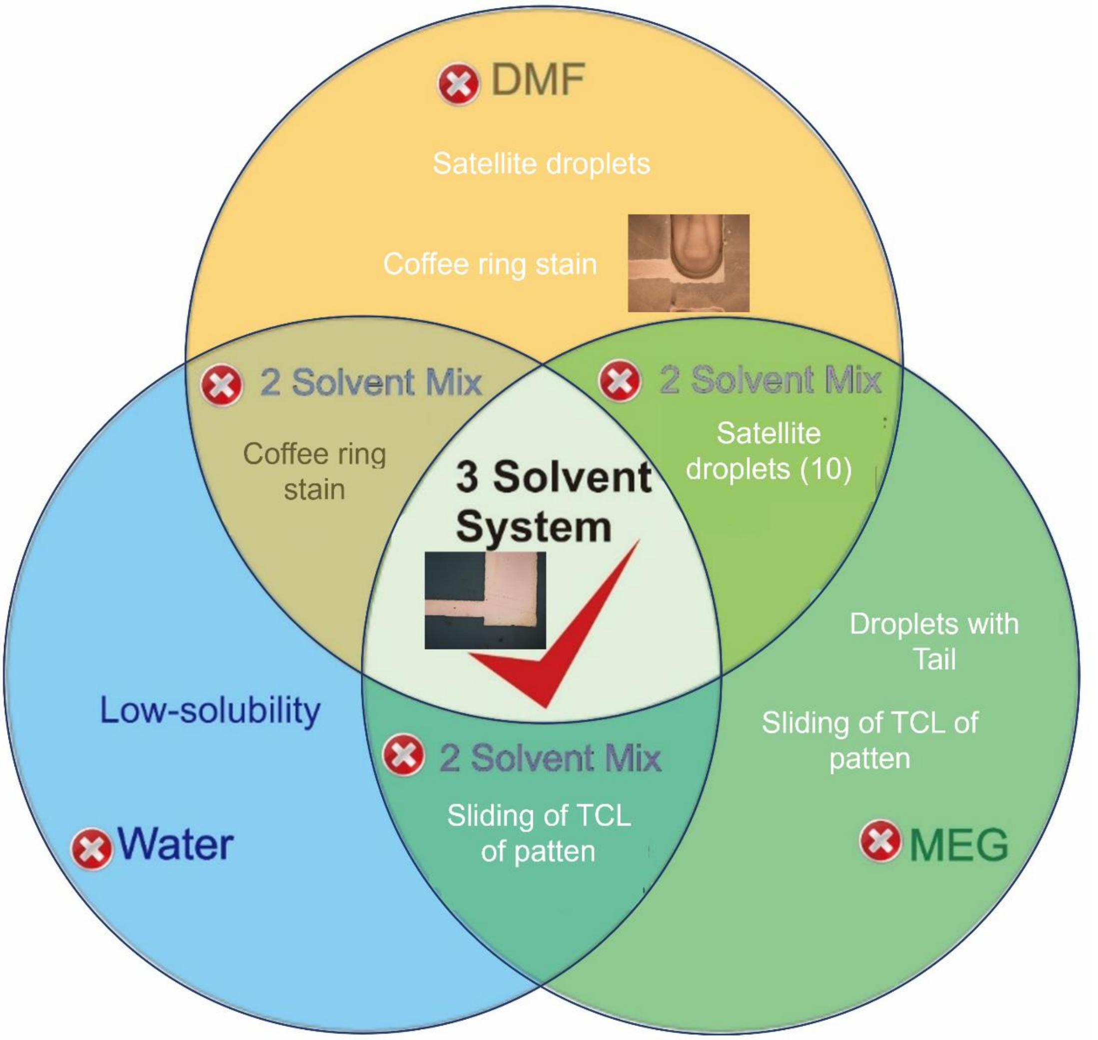

Figure 5.4. Schematic diagram shows the necessity of choosing the three solvent systems for inkjet-printing ink to fabricate copolymer (p[MBP-co-MATAC]) patterns without severe coffee-ring stain.

After countless experiments, we invented a three-solvent copolymer system to form the inkjet-printing ink of p[MBP-co-MATAC] for Cu electrode electroless deposition. The three-solvent cosolvent system, DMF, EG, and water, mixed at 89w%, 4w%, and 7w%, respectively. As shown in Figure 5.4, we listed why we use the three solvent systems instead of using a single-solvent system or two-solvent system. Table 5.1 lists the physical properties of the original single-solvent system for the formation of the metal-platable copolymer ink, which easy to generate coffee ring stain.[19a] Table 5.2 lists the physical properties of the three components of the 3-solvent system. Among these, the

EG with the evaporation rate of 0.01(nBuAc=1) belongs to the solvent with an ultra-low evaporation rate.

Table 5.1. Physical properties of the original single solvent preparing original metal-platable copolymer ink.

Single solvent system for copolymer ink	Boiling point	Evaporation rate (0.8< medium<3)	Surface tension 20°C	Viscosity m Pa·s
2-methoxyethanol	125oC	0.5	31.80 dyn/cm	1.72

Table 5.2. Physical properties of each component of the 3-solvent copolymer ink for coffee-ring free inkjet-printing of metal-platable copolymer thin film.

Three-solvent copolymer ink	Boiling point	Evaporation rate (0.8< medium<3)	Surface tension 20°C	Viscosity m Pa·s
Dimethylformamide (DMF)	153 ºC	0.2	36.42 dyn/cm	0.92 (25°C) 0.838 (30°C)
Mono ethylene glycol (MEG)	197 ºC	0.01	48.5 dyn/cm	25.66 (16°C) 10.38 (38°C)
Water	100ºC	0.3	72.86 dyn/cm	1.002 (20°C) 0.798 (30°C)

The following part discussed the determination of the composition of the three-solvent copolymer ink.

Why not use single solvent copolymer ink:

Figure 5.5 lists the reasons for choosing the three-solvent copolymer. Although p[MBP-co-MATAC] is dissolvable in dimethylformamide, it cannot become the only solvent for copolymer ink. Because such ink can form satellite droplets, as shown in Figure 5.6.[134] The satellites generation will influence the accuracy of inkjet printing.[134]

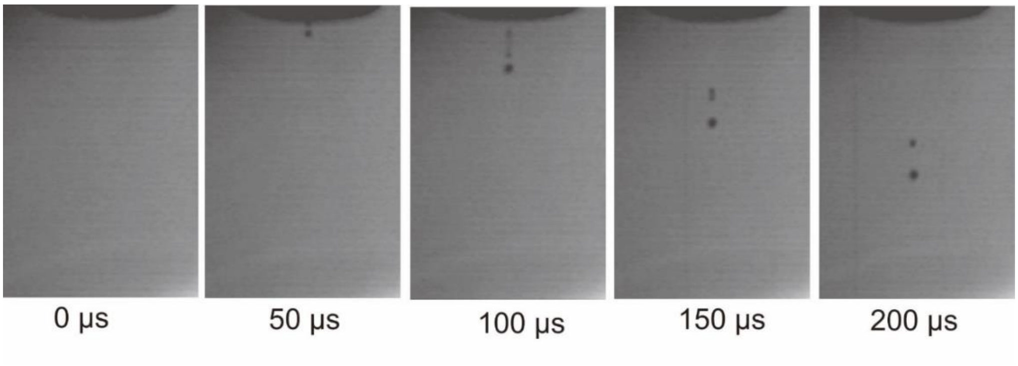

Figure 5.5. Photo sequence for droplet formation using 0.5w% copolymer ink with DMF as single solvent at a driving voltage of 33V. The pulse duration was five µs.

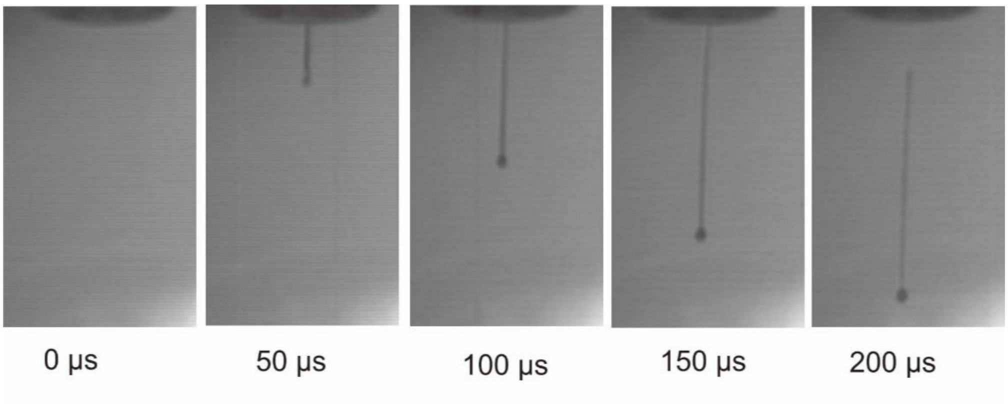

Figure 5.6. Photo sequence for droplet formation using 0.5w% copolymer ink with EG as single solvent at a driving voltage of 33V. The pulse duration was 5 µs.

Although the low-evaporation cosolvent EG is a suitable solvent of p[MBP-co-MATAC], it cannot be used as a single solvent to form high-quality inkjet printing ink. Because EG has a large viscosity, i.e., 18cp, it is easy to generate a long tail trajectory that will mismatch with the main droplet when they fall onto the substrate. As a result, as shown in Figure 5.7, the printed pattern cannot form a regular circular pattern. In addition, this low stability of the droplets reduced printing resolution.

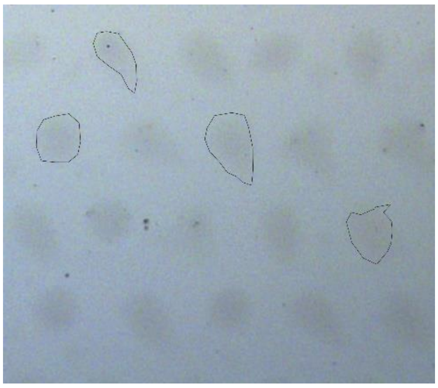

Figure 5.7 A optical microscopic image of the inkjet-printed droplet array on the PET substrate.

Also, the water-based single solvent copolymer ink is inapplicable because of the low solubility of p[MBP-co-MATAC] in water.

Why not use two-solvent system:

Two-solvent ink formed by only EG and DMF still cannot achieve inkjet printing of high-quality copolymer patterns. Because the satellite droplet always formed until the concentration of EG was 10% (Figure 5.8). However, the high concentration of the low-evaporation cosolvent (EG) in the cosolvent system will generate uneven thickness deposition during the drying process due to the excess EG flowing on the inkjet-printed patterns. The later chapters describe this part.

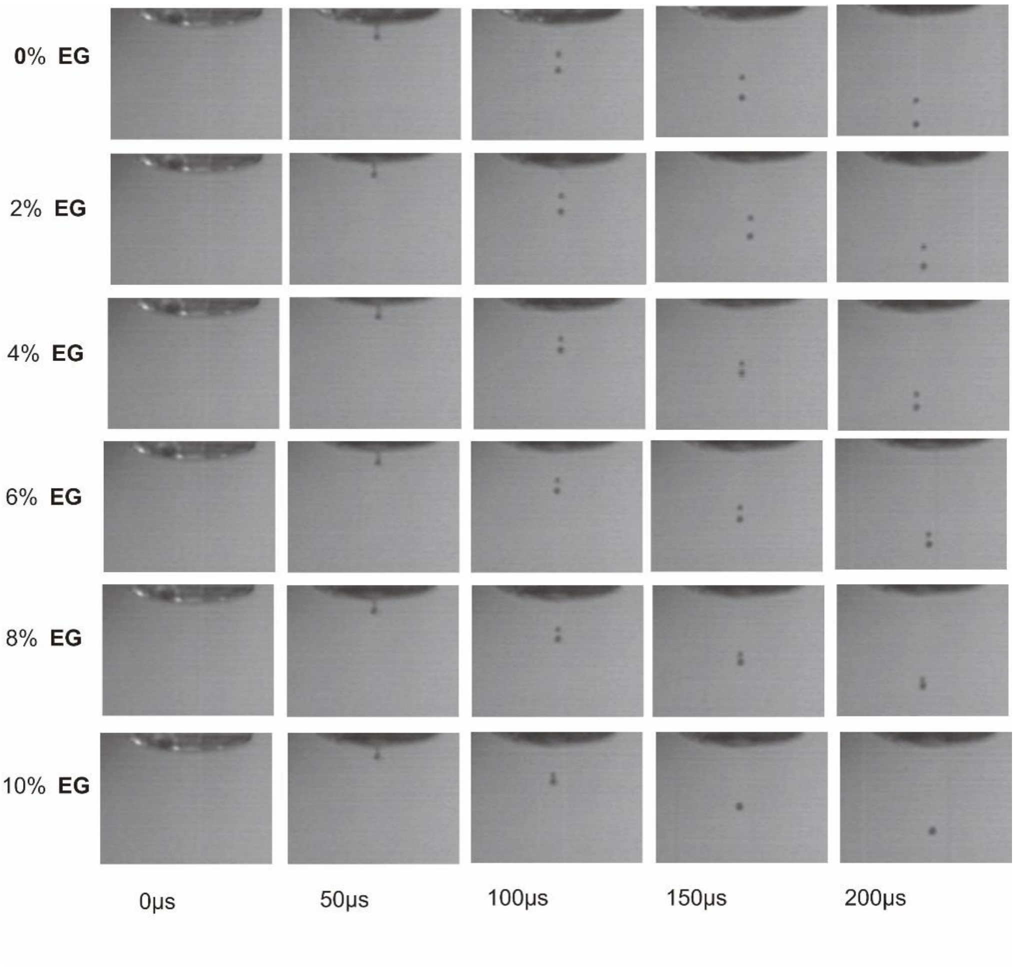

Figure 5.8. Photo sequence for the droplet formation using ink with two-solvent cosolvent system, formed by EG and DMF, with variable concentration of EG (from 0 w% to 10w%) at a driving voltage of 33V. The pulse duration was 5 µs.

The two solvent systems, made by DMF and water, still difficult to form reliable copolymer ink for inkjet-printing of high-quality patterns without the coffee-ring effect. Although the satellite droplet started to disappear (Figure 5.9), the coffee-ring suppression function was limited (Figure 5.10). In addition, without the existence of the slow-evaporation-rate cosolvent (EG), the joint's surface had a rough surface caused by a redissolving of the first inkjet-printed pattern on the bottom and an unbalanced solvent deposition driven by the coffee ring effect, as shown in the Figure 5.10.

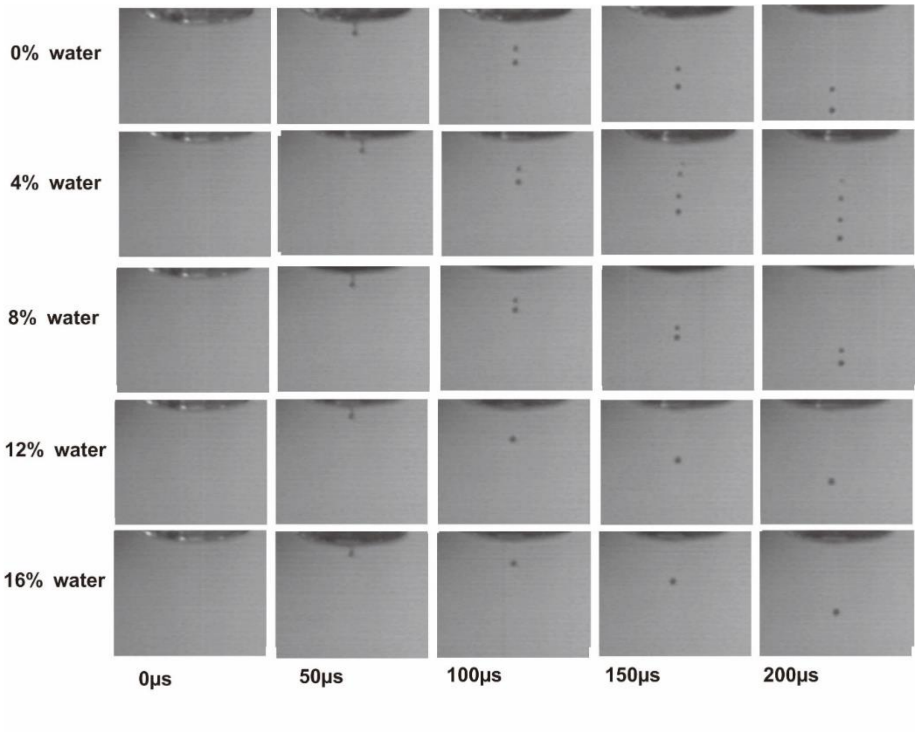

Figure 5.9. Photo sequence for the droplet formation using ink with two-solvent-based cosolvent system, formed by water and DMF, with variable concentration of water (from 0 w% to 16w%) at a driving voltage of 33V. The pulse duration was 5 μs.

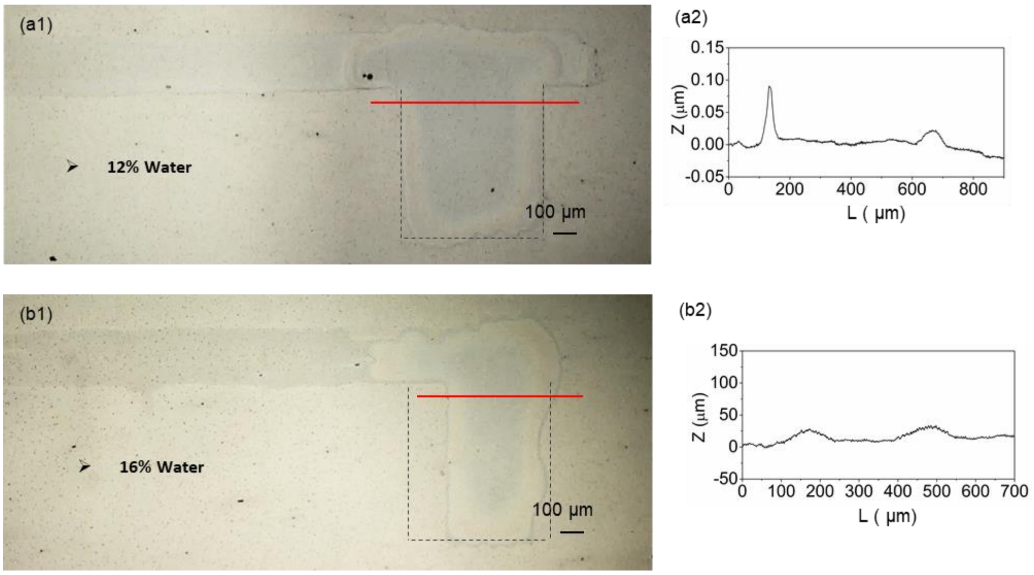

Figure 5.10. Optical microscopic image of a firstly inkjet-printed line-shaped pattern joined with a secondly inkjet-printed rectangular pattern using copolymer ink in a bi-solvent system made by DMF and water, with a water proportion of 12 v% (upper) and 16% (bottom). The droplet spacing of all the patterns was set to be 50 µm.

The EG-and-water-based dual solution system is still challenging to form inkjet-printable copolymer ink. The droplet generated by the inkjet printer easily forms tail trajectories and irregular printing results due to the high viscosity of EG (~18cp). And the water is not a suitable solvent for p[MBP-co-MATAC]. Although this two-solvent-system can form fine droplets (Figure 5.11), both the EG and the water have low wettability to the plastic substrate (e.g., PET). As a result, the inkjet-printed copolymer ink with EG&water-dual-solvent system flow on the PET substrate, making the initially complete line-shaped pattern separated into several sections, as shown in Figure 5.12.

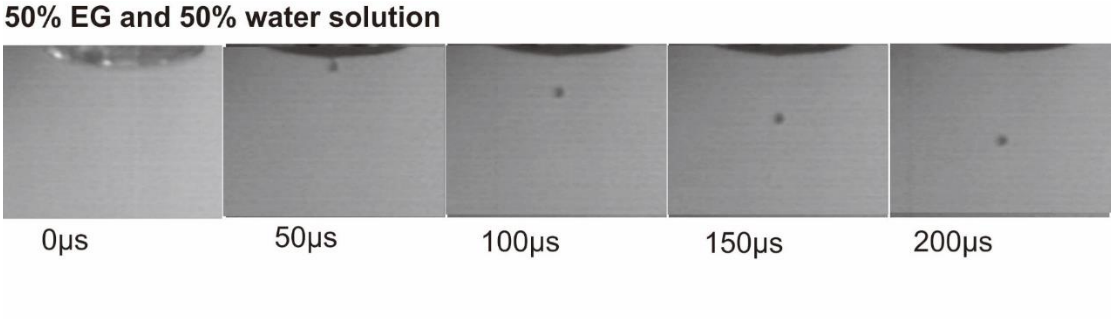

Figure 5.11. Photo sequence for droplet formation for the 0.5w%-cosolvent ink with a water & EG-dual-solvent system (volume ratio 1:1). The driving voltage was 33V. The pulse duration was 5 µs.

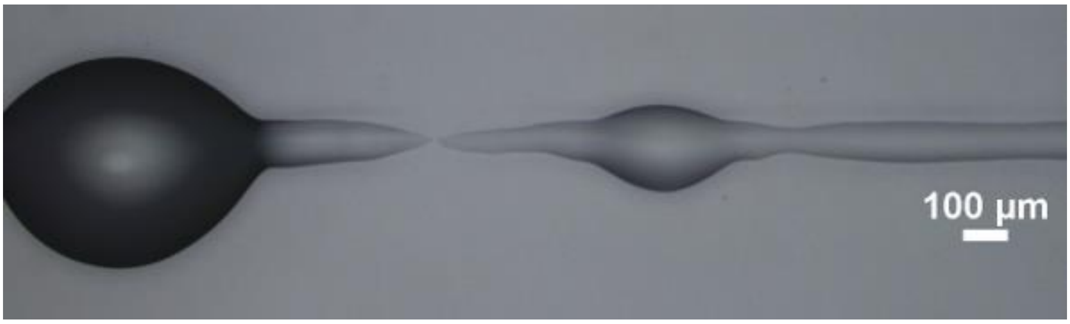

Figure 5.12. Optical microscopic image of 0.5w% cosolvent ink, with a dual-solvent system (water: EG=1:1), inkjet-printed onto the PET substrate with a line-shaped pattern. The original designed line-shaped pattern formed bulging structures. And the overlarge bulging structures separated the line into pieces due to the low wettability of both EG and water to the plastic substrates, e.g., PET.

Therefore, only the three-solvent system can form the inkjet-printing ink of the copolymer p[MBP-co-MATAC].

5.3 Determination of the Components of the Three-solvent System for Coffee-ring-free Inkjet Printing of Metal Platable Copolymer Thin Film

5.3.1 Determination of the Proportion of the Slow-evaporation-rate Cosolvent

After countless experiments, we found that the printing effect was good when we set the ingredient-mass-ratio of the three-solvent-copolymer systems to be 89 w% of DMF, 4w% of EG, and 7w% of water. However, when we increased the low-evaporation-cosolvent (EG) concentration to a level of more than 4 w%, the ink will flow on the copolymer pattern, as shown in Figure 5.13. And the flowing of the excessive slow-evaporation-rate cosolvent (EG) leads to irregular thickness distribution of the copolymer pattern.

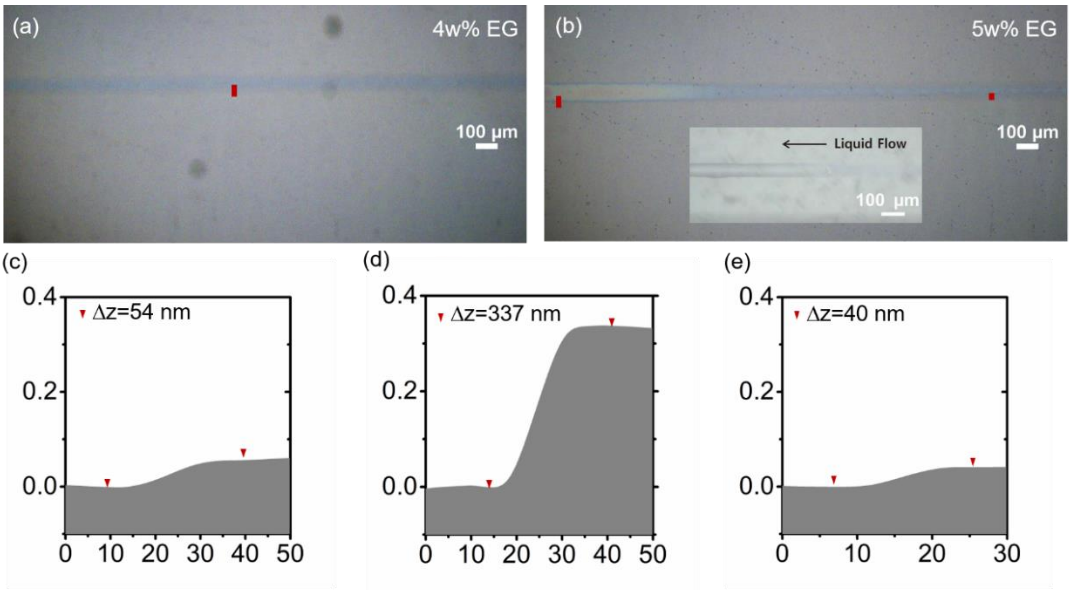

Figure 5.13. The residual EG flows along with the printed pattern caused uneven thickness distribution. a) Optical image of the inkjet-printed line-shaped pattern using copolymer ink with components, i.e., DMF, EG, and water, mixed at a ratio of a) 89:4:7, and b) 88:5:7. Insert: drying process of excessive EG accompanied with flowing along with the pattern. AFM profile showing the cross-sectional thickness of the inkjet-printed copolymer ink with c) 4w% d-e) 5w% of EG.

The cosolvent with a slow-evaporation rate is not easy to evaporate entirely for the firstly printed patterns. And they will immerge with slow-evaporation-rate cosolvent in the second inkjet-printed pattern and become a thin sheet of liquid with the self-levelling ability to form a uniform sheet of copolymer thin film shown in Figure 5.14.

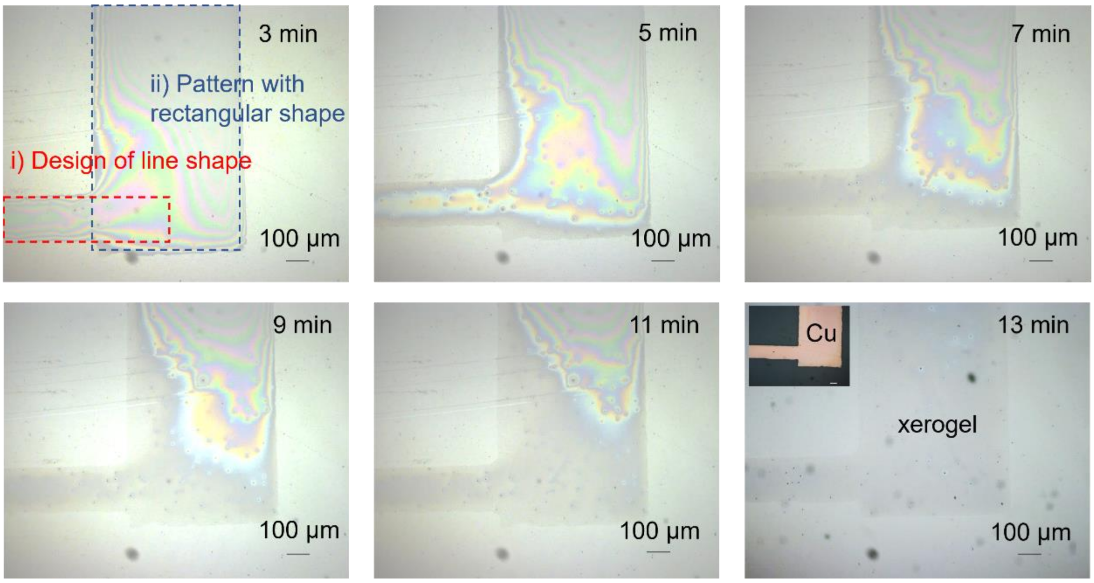

Figure 5.14. A series of microscopic images showing the drying process of a inkjet-printed pattern i) with the design of line shaped and a pattern with ii) the design of rectangular shaped joint together after drying for 30 min, 32 min, 34 min, 36 min, 38 min, and 40 min. The concentration of the cosolvent EG was 4w%. This pattern is on the PET substrate. The inset shows the xerogel-based Cu electrode grown on the inkjet-printed copolymer pattern (scale bar: 100 μm).

When we increased the concentration of EG from 4w% to 5w%, the redundant solvent, with a high evaporation rate, will flow on the pattern and initiate uneven deposition of the copolymer solute, as shown in Figure 5.15. Most of the solute deposited in the centra area left a pattern with an irregular thickness distribution. The uniformity of the inkjet-printed pattern is still not as good as the pattern printed by the copolymer ink with 4w% of the slow-evaporation-rate solvent due to the significant accumulation of non-volatile solvents in the original printed parts. As shown in Figure 5.16, when we further increase the proportion of the slow-evaporation-rate cosolvent (EG) to 7w%, the irregularity of the thickness distribution will be further improved and finally leading to irregular metal deposition. As the copolymer solute contains a bonding set for the catalyst, the Cu is grown in a position where the organic layer is relatively thick. When the organic layer is too thin, it will not cause Cu electroless deposition. Therefore, the slow-evaporation-rate cosolvent proportion is crucial and needs always be at a constant level. Because for the ink with the weight ratio of copolymer solute of only 0.5w%, 7w% of slow-evaporation rate cosolvent occupied an absolute volume proportion in the printed pattern, which will significantly impact the printed film. For the inkjet-printable p(MBP-co-MATAC) ink for Cu electrode deposition, the slow-evaporation-rate cosolvent (EG) proportion should always be 4w%.

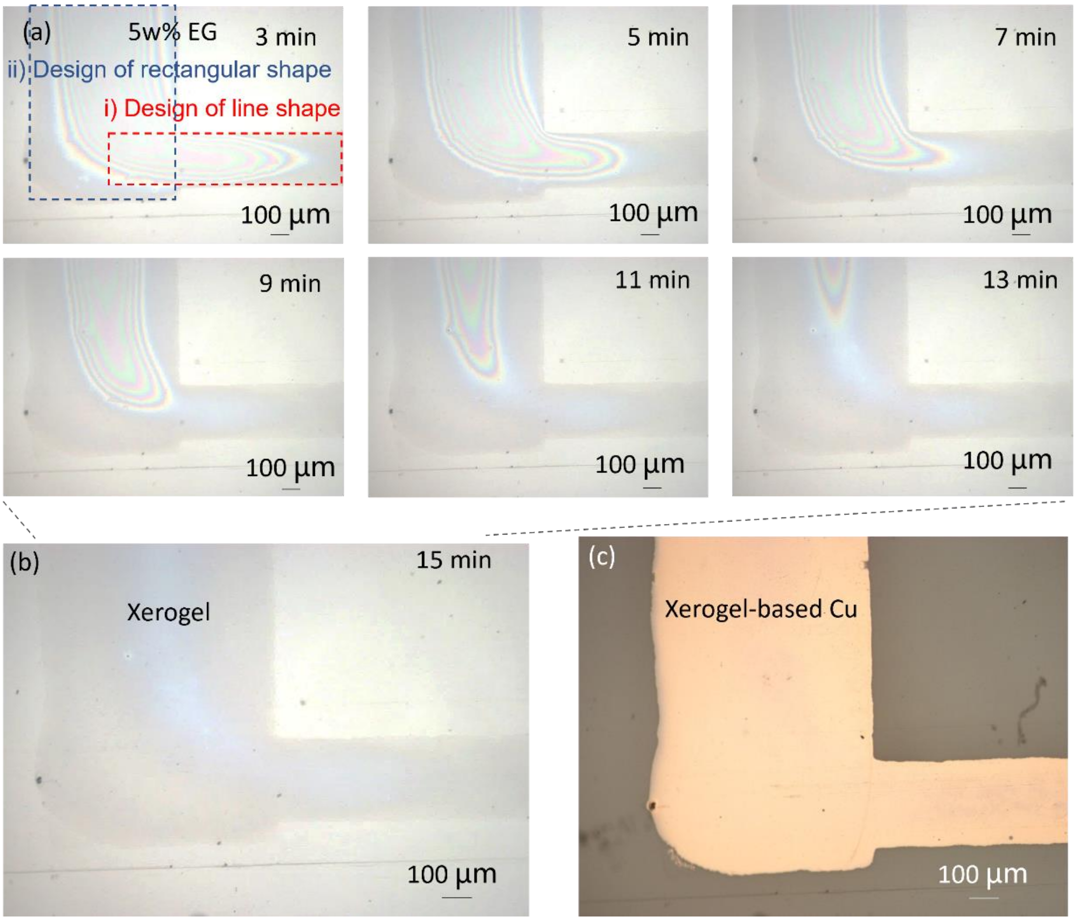

Figure 5.15. The solvent residual flows on the printed pattern formed uneven thickness distribution when increasing EG's concentration to 5w%. a) A series of microscopic images showing the drying process of an inkjet-printed pattern i) with the design of line shaped and a pattern with ii) the design of rectangular shaped joint together after drying for 35 min, 37 min, 39 min, 41 min, 43 min, and 45 min. The copolymer ink contains 5w% of the cosolvent EG, with slow-evaporation-rate. This pattern was inkjet-printed on the PET substrate. b) Optical microscopic image of the inkjet-printed pattern in (a) dried for 50 min. c) The optical microscopic image of the xerogel-based Cu electrode grown on the inkjet-printed copolymer pattern (b) (scale bar: 100 µm).

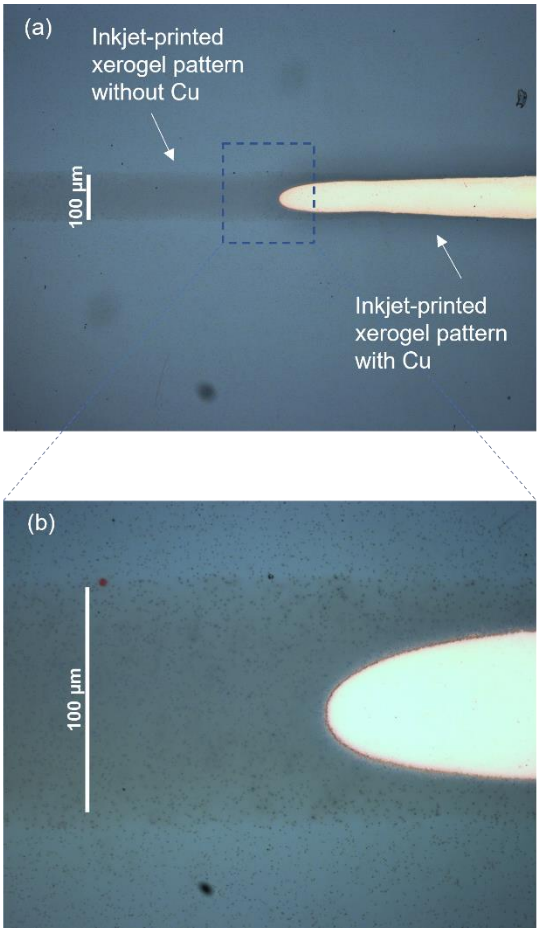

Figure 5.16. Optical microscopic image of Cu electroless deposition result on the inkjet-printed line-shape pattern formed by the three-solvent copolymer ink with slow-evaporation-rate cosolvent (7w%). The uneven thickness distribution of copolymer thin film caused the failure of the Cu deposition on the copolymer thin film with ultra-thin thickness. The flowing of the excessive cosolvent causes irregular Cu deposition with a low evaporation rate.

5.3.2 Determination of Proportion of the Water

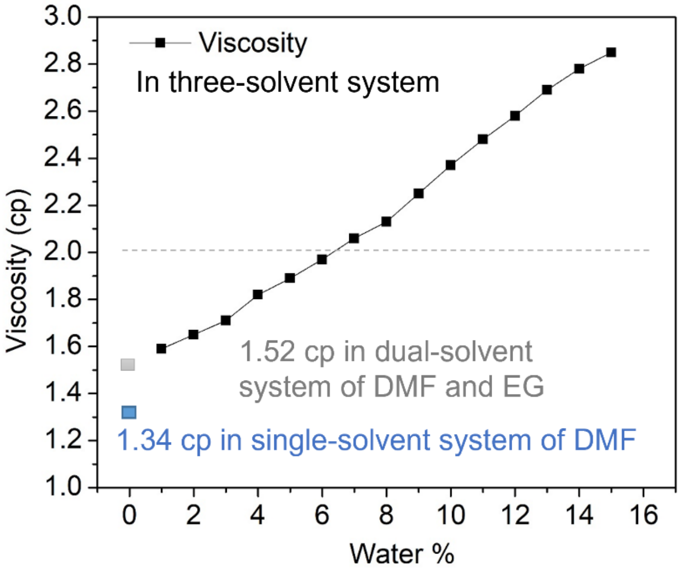

Figure 5.17. The viscosity change of P[MBP-co-MATAC] copolymer ink using different solvent systems. The blue dot represents 0.5w% copolymer dissolved in DMF single solvent. Gray dot demonstrates DMF and EG cosolvent mixed the ratio of 96:4. Black dots indicate the viscosity of copolymer inks with the addition of DI water in the proportions of 1% to 15%. Adding water concentration to around 7w% can achieve the ideal viscosity for inkjet-printing ink (2cp). The concentration of copolymer solute was all fixed to be 0.5w%.

As shown in Figure 5.17, the 0.5w% copolymer ink with a single solvent system formed by DMF had a viscosity of 1.34 cp, while the 0.5w% copolymer ink with a two-solvent system, composed of 96w%-DMF and 4w%-EG, had a viscosity of 1.52cp. Although increasing the proportion of EG can increase the viscosity to the most appropriate viscosity for inkjet printing, which is around two cp, the concentration of slow-evaporation-rate cosolvent, EG, has to be fixed 4w% to prevent irregular thickness distribution on the inkjet-printed patterns. Therefore, another cosolvent can act as a viscosity modifier to increase the viscosity of copolymer ink to around 2cp to improve the inkjet printability of the copolymer ink. We found that adding water can significantly increase the viscosity of the copolymer ink. As shown in Figure 5.17, the viscosity of the three-solvent copolymer ink increased from 1.6 cp to 2.8 cp when we added the proportion of water from 0w% to 15w%. The proportion of the Slow-evaporation-rate cosolvent EG always be 4w% when changing the proportion of water and the corresponding proportion of the DMF. Therefore, if we want to make the copolymer ink with the best inkjet printability, the water concentration should always be 7w%.

5.4 Drying Process of Three-Solvent-Copolymer Ink

The three-solvent copolymer ink can achieve coffee-ring free inkjet printing. This premium property benefits from the existence of ethylene glycol, which is a solvent with an extremely low evaporation rate. Therefore, there will be a liquid sheet that dries slowly during the final period of the drying process. Here we demonstrated the drying process of there-solvent copolymer ink on the PET substrate. During testing, 0.4 μL of the three-solvent copolymer ink was dropped onto the surface of the PET substrate to minimize the real inkjet-printing process. KRUSE contact angle meter captured the profile images for the droplet dry on the substrate. We assume that the droplet always presents a perfect circle. Therefore, the equation can express the droplet volume:

$$V = \frac{\pi}{3}(3d - h)h^2$$

H is the distance from the top of the droplet to the substrate. *D* is the radius of the droplet bottom cycle center. The following equation can express the surface area:

$$S = \pi \times (h^2 + d^2)$$

And the evaporation rate per unit surface area *E* can be expressed by the equation:

$$\mathrm{E} = \frac{V_n - V_{n-1}}{(S_n + S_{n-1})/2}.$$

As shown in Figure 5.18, the droplet drying process can be roughly divided into three drying processes with different solvent-evaporation rates. Table 2 lists the first and second processes that show a noticeable fitted linear relationship. The first drying period has the highest evaporation rate (i.e., 0.01399 μL/min), whiles the evaporation rate has decreased when entered the second and third drying processes. The liner relation indicated that the evaporation of one cosolvent mainly induces the evaporation with the highest evaporation rate (i.e., DMF with the evaporation rate of 0.3 (nBuAc=1)). As the number of DMF decreases, the evaporation of water (with a slower evaporation rate, 0.2 (nBuAc=1)) formed a gradually slowing of the solvent evaporation rate. Finally, the evaporation of the cosolvent with the slowest evaporation rate constitutes the final period of evaporation.

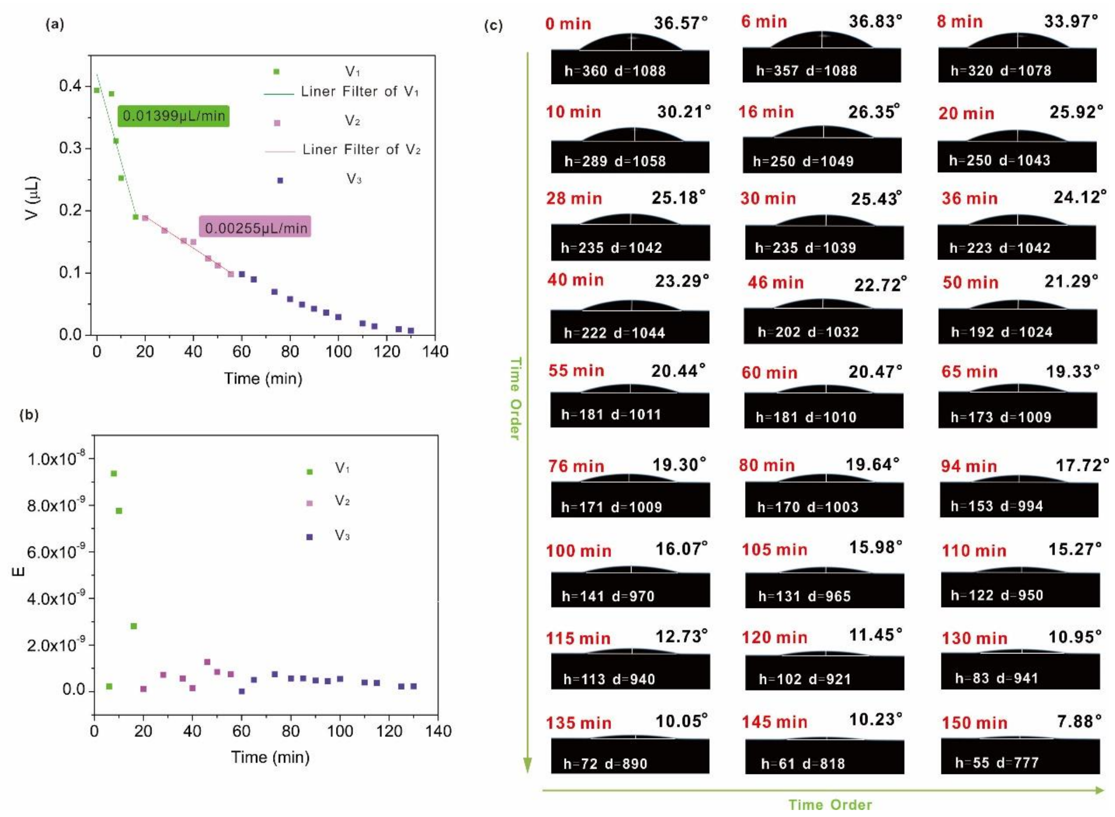

Figure 5.18. (a) Volume change during the drying process of three-solvent copolymer ink. (b) Evaporation rate per unit surface area E versus time. (c) Droplet profile captured by KRUSE contact angle meter during the droplet drying process of the three-solvent copolymer ink with an original volume of 4 μl.

Table 5.3. Fitting parameters of two drying periods

	Intercept	intercept	slope	slope	Statistics
	Value	Error	Value	Error	Adj. R-Square
Period 1	0.41942	0.0308	-0.01399	0.00323	0.81657
Period 2	0.2418	0.00677	-0.00255	1.6511×10-4	0.97537

And the drying speed is also shown not stable. The inter-fluid may still exist. During the last period of the drying process, the drying speed gradually decreases. It may cause by the component of the ink tend to be a single solvent, i.e., EG.

Three-solvent ink is complex during drying. Therefore, the measurement of droplet volume change during the drying process provided evidence for our estimation that there will remain a thin sheet of liquid ink that dried slowly and can forming uniform boundaries.

5.5 Slow-evaporation-rate Cosolvent for Leveling the Joint of the Inkjet-Printed Patterns

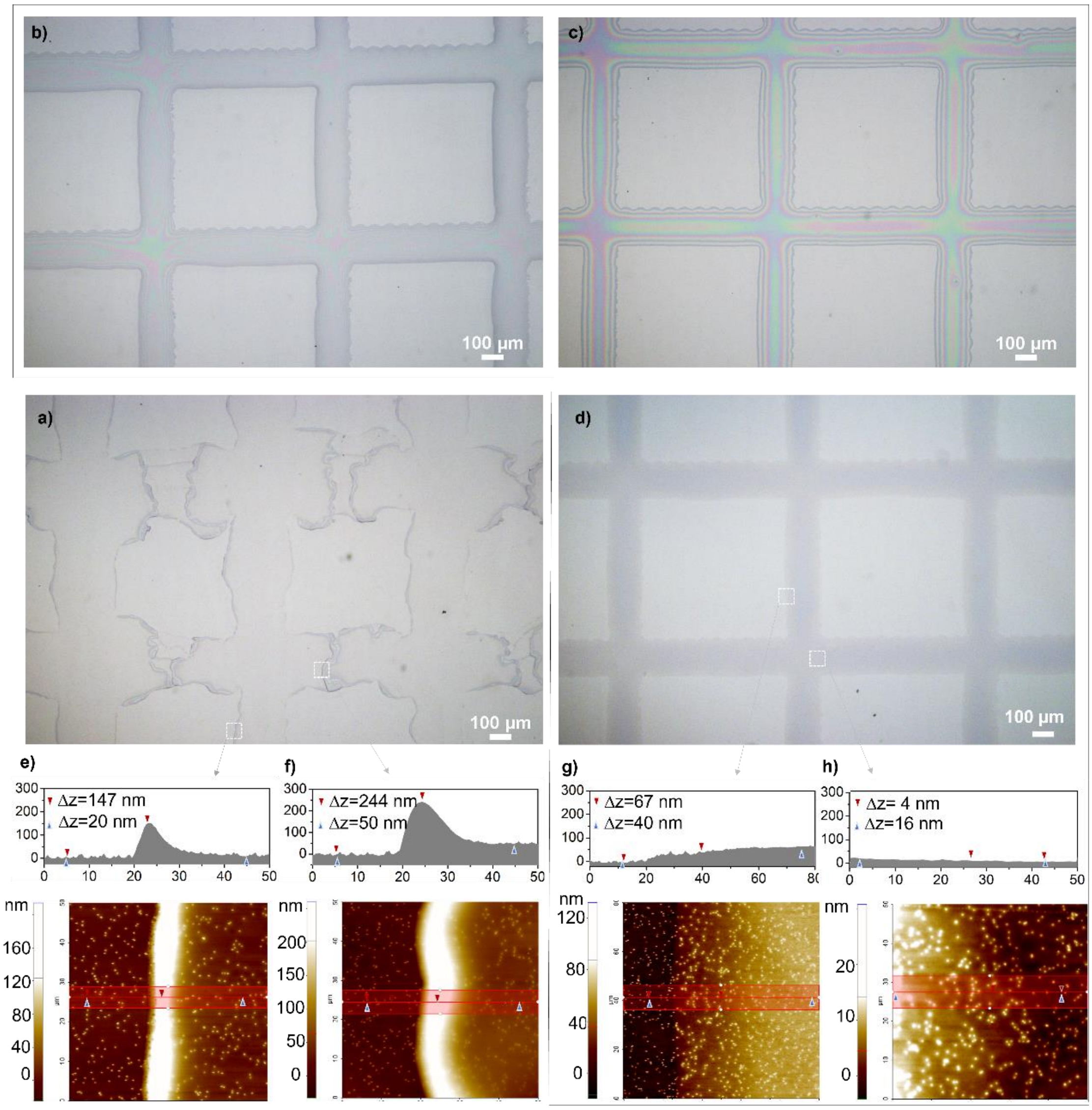

Figure 5.19. a) Optical microscopic image of the inkjet-printed mesh pattern, formed by the vertical (first printed) and horizontal (second printed) parallel lines printed, by the original 2-methoxyethanol based ink. b-d) Optical microscopic image of the inkjet-printed pattern, with the similar pattern design in (a), using the three-solvent copolymer ink, after drying at the ambient environment for b) 20 min. c) 30 min, and d) 70 min. AFM topographic image and corresponding cross-sectional profile images of e) a boundary area, in (a), f) a joint of vertical and horizontal lines, in (a), g) a boundary area, in (d), and h) a joint of vertical and horizontal lines, in (d).

As shown in Figure 5.19, the original copolymer ink for inkjet printing is easy to form polymer thin films without smooth surface morphology.[19a] The joint of the first inkjet-printed horizontal parallel lines and the second inkjet-printed vertical parallel lines had an extremely thick polymer distribution after drying the solvent. On the contrary, the inkjet-printed copolymer pattern formed by the three-solvent copolymer ink has a smooth joint. Figure 5.19b and Figure 5.19c demonstrating the inkjet-printed pattern after drying for 20 min and 30 min, respectively. A thin sheet of solvent at the end of the drying process levelled the joint of the overlapping area of the vertical and horizontal lines. As the three-solvent copolymer ink contained a slow-evaporation-rate cosolvent (i.e., EG), the main component of this liquid residue should be EG.

The self-levelling effect is crucial for the PAMD-based Cu electrode because the metal electroless deposition process will increase the unevenness of the inkjet-printed pattern. For example, as shown in Figure 5.20, the thickness of the irregular stain deposited in the joint increased from 244 nm to 1.7 μm after electroless metal deposition. In addition, the copolymer matrix contained the bonding set of the catalytic moieties, which can generate regional violent chemical reactions during the metal deposition process to further increase the deposited pattern's irregularity. Therefore, the self-levelling thin sheet of low-evaporation-cosolvent is crucial for inkjet printing of smooth Cu electrodes.

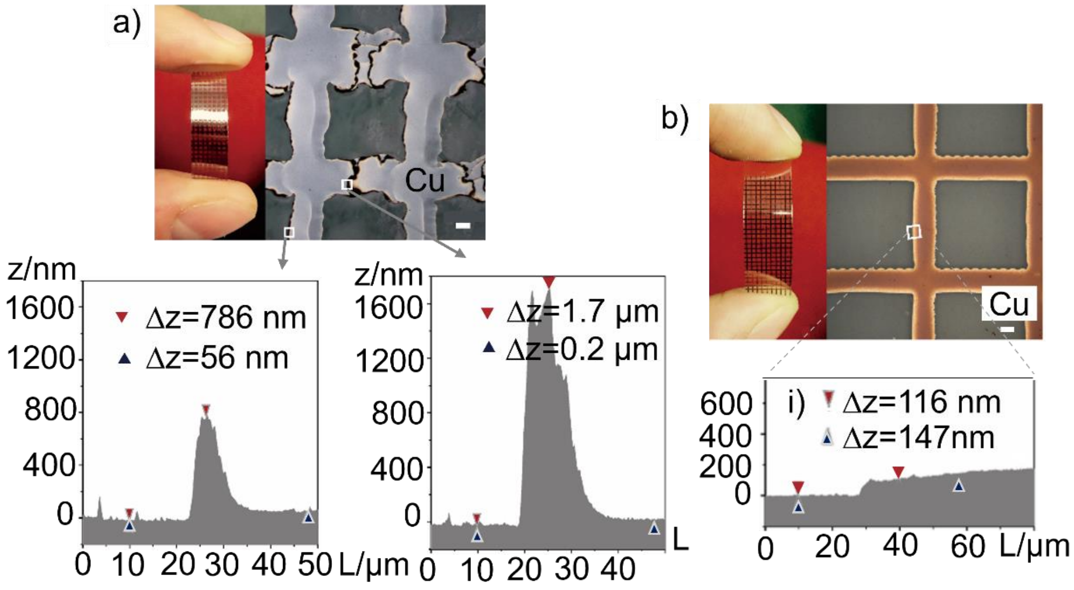

Figure 5.20. Optical microscopic images and corresponding AFM cross-sectional image of the inkjet-printed Cu mesh on the PET substrate using a) original copolymer

ink dissolved in a single solvent, 2-methoxyethanol, with single solvent, and b) three-solvent-based ink with slow-evaporation-rate cosolvent.

5.6 Inkjet-printing of Patterns with Uniform Boundary by Copolymer Ink with Slow-evaporation-rate Cosolvent

With the addition of the slow-evaporation-rate cosolvent, the inkjet-printing ink has a special function in levelling the inkjet-printed thin film patterns. And a unique inkjet-printing method can help to improve the uniformity of the inkjet-printed patterns.

5.6.1 Low limitation of Droplet Spacing for Printing Line-shaped Pattern

For the normal copolymer ink, the uniformity of the inkjet-printed lines is strongly related to the droplet spacing. The smaller droplet spacing will lead to forming a bulging structure, whilst the larger droplet spacing will lead to scalloped or individual drops, as shown in Figure 5.2.[80] However, we found the uniformity of the pattern inkjet-printed by the copolymer ink with three-solvent copolymer ink was minimally affected by the droplet spacing. As shown in Figure 5.21, the inkjet-printed line-shaped pattern had no apparent shape verification when changing the droplet spacing from 44 µm to 82 µm. Only the thickness has dramatically decreased (interred from the depth of the color of the copolymer thin film) when increased the droplet spacing. It indicated that the copolymer ink based on the three-solvent-cosolvent system could keep the shape of the original print pattern unchanged, i.e., without subtraction of the TCL line. And it could conserve a part of the solution on the surface of the printed pattern and finally form a smooth thin film without huge irregularity of the thickness distribution. The orifice diameter of the inkjet-printing head was 80 µm. The pattern was inkjet-printed on the spin-coated PVP thin film with uniform surface morphology. It indicated a strong tolerance to changes in solution volume when maintaining the uniformity of the boundary of the pattern.

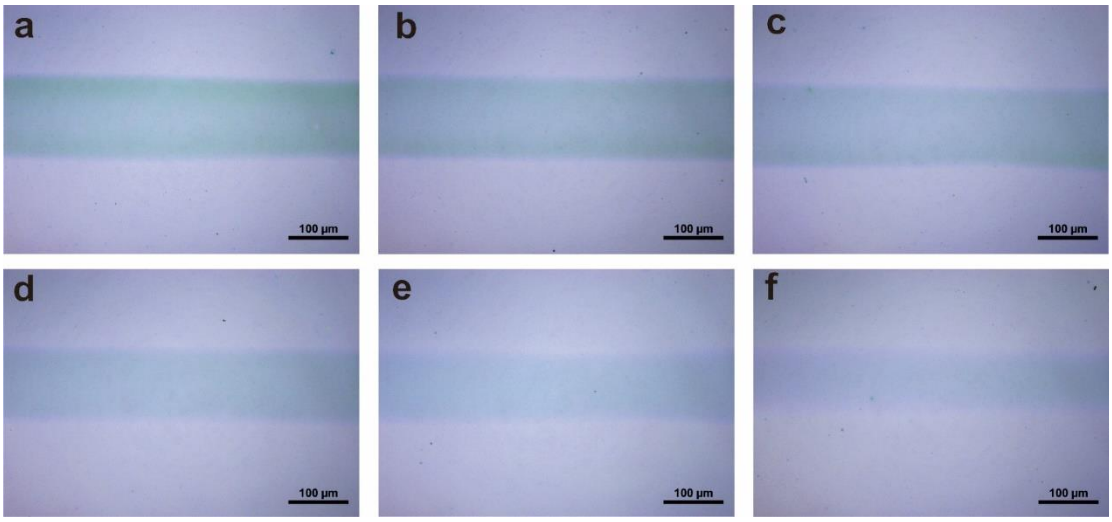

Figure 5.21. Optical images of the inkjet-printed copolymer paste lines with drop spacing of a) 42, b) 44, c) 48, d) 62, e) 72, f) 82 µm using the three-solvent copolymer ink with a slow-evaporation-rate cosolvent. In this strategy, the inkjet-printed lines did not have bulging or scalloped structures[80] on the line boundary. Thus, the drop spacing and drop volume only impact the pattern thickness but have almost no drastic impact on the boundary uniformity of the inkjet-printed pattern.

5.6.2 A Method to Inkjet Print Uniform Boundaries for Two-dimensional Patterns

Only line-shaped designs can achieve inkjet printing of the patterns with absolute uniform boundaries. As shown in Figure 5.22, using the ink with the high inkjet printability accompanying the stable droplet, the pattern formed by a single line can achieve high-resolution inkjet printing of the channel structure with a channel length of around 80 µm. And the slow-evaporation-rate cosolvent prevented the formation of irregular thickness deposition in the joint when compared with the electrode formed by the original single solvent copolymer ink.

However, there is no practical method for maintaining the boundary uniformity for the inkjet-printed patterns with complex two-dimensional designs. When we utilized the multi-lines to form a pattern with a thicker lines structure, the uniformity of the pattern became difficult to be perfectly controlled.

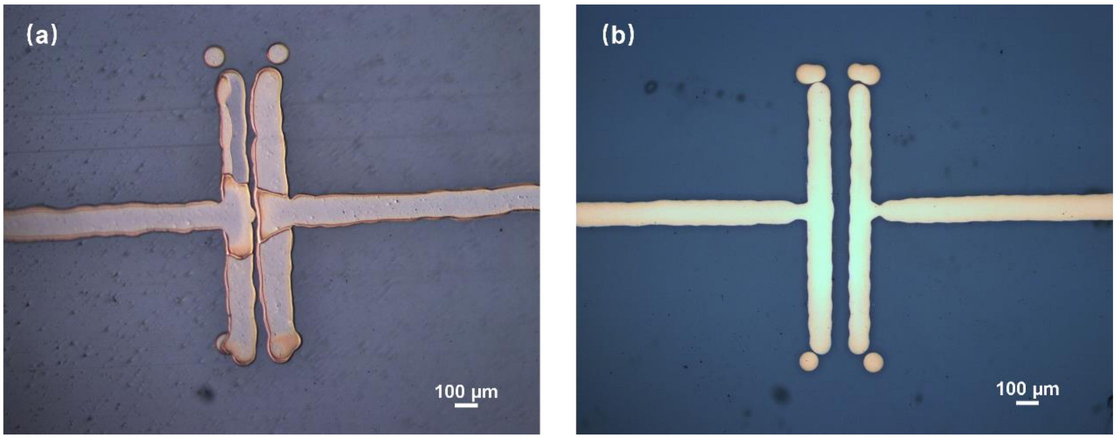

Figure 5.22. Optical microscopic image of the Cu electrode formed by a) original inkjet-printing ink with a 2-Methoxymethanol-based single solvent, and b) three-solvent copolymer ink with the addition of the slow-evaporation-rate cosolvent EG.

We found that for a pattern formed by the inkjet-printed parallel lines, only one boundary formed by the last printed line is uniform. We designed the pattern formed by inkjet-printing the parallel lines from outside to the inner side, aiming to form a channel structure with a uniform boundary for both electrodes, as shown in Figure 5.23. No matter how irregular the other three boundaries were, the internal two boundaries that formed the channel structure were uniform, as shown in Figure 5.23i. The success rate for inkjet-printing the electrode with a uniform channel is high, even with strip-shaped impurities destroying the outer edges' uniformity. This inkjet printing method is repeatable. The uniformity of the internal two boundaries remains unaffected. The droplet spacing and line spacing of the vertical lines were 42 µm.

We assume that using this technique, a channel with a shorter channel length can be inkjet-printed by only changing the sequence of inkjet-printing. As a proof-of-concept, we inkjet-printed two electrodes (originally designed to be a rectangular shape) following with the droplet printing sequence as shown in Figure 5.24. All the parallel lines' printing sequences were started from the bottom and stopped at the top. Both the electrodes had a bulging structure at the end of the first line because the inertial force of the slow-evaporation-rate cosolvent forced all the solutions flown to one end and made the ink beyond the original graphic boundary.

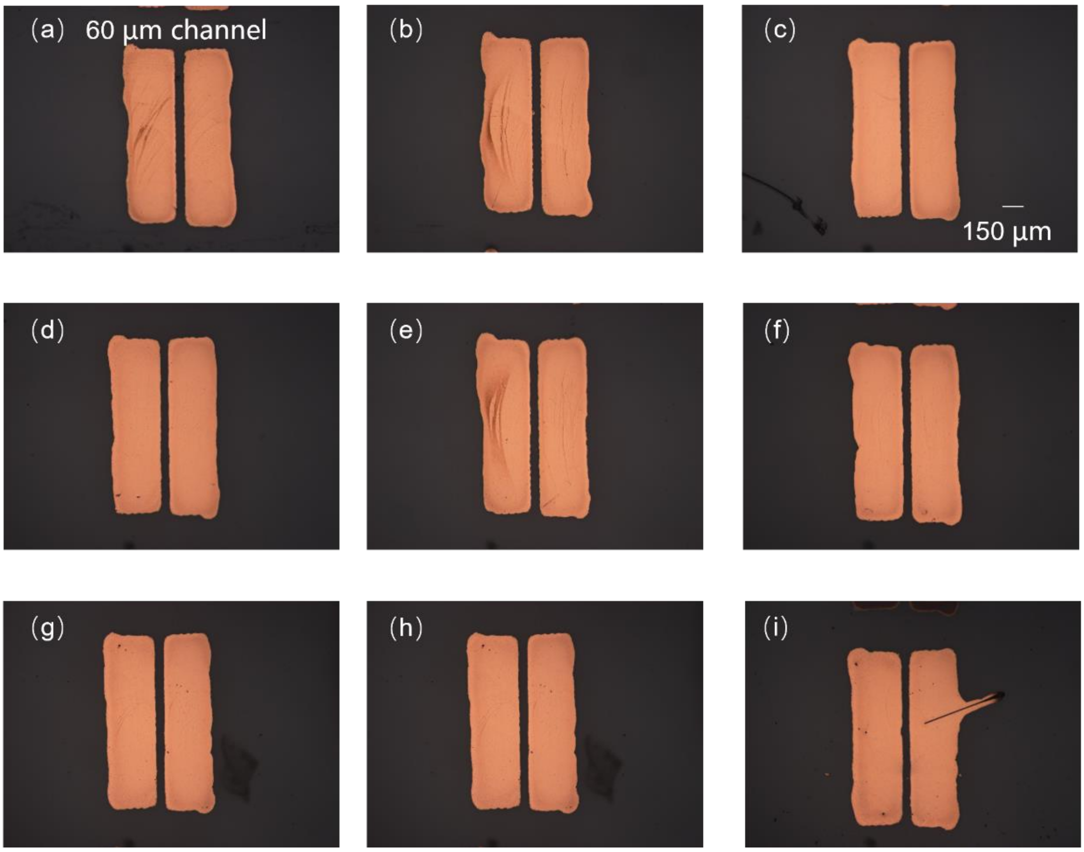

Figure 5.23 Optical microscopic images of nine pairs of inkjet-printed Cu electrodes forming channel structure on PVP substrate. The inkjet-printed drop arrays with a unique printing sequence printing vertical parallel lines from the outer side gradually approaching the channel boundary. The printing sequence for each drop array was from the bottom to the top. The lastly printed vertical line formed the channel boundary with high uniformity. Thus, this printing method can form a uniform channel structure with high repeatability by changing the inkjet-printing sequence.

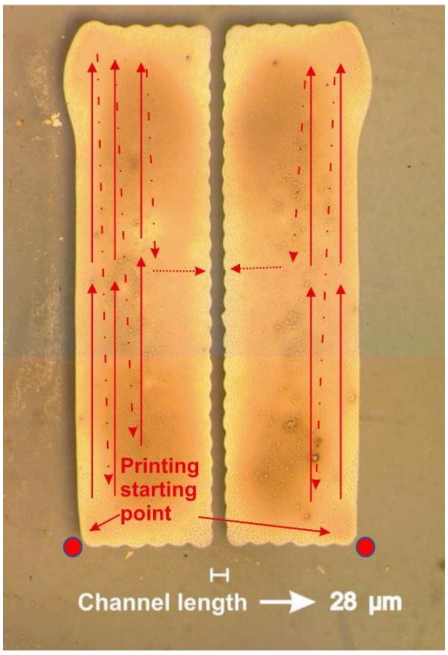

Figure 5.24 Optical microscopic image of the inkjet-printed Cu electrode forming a uniform channel structure by a special inkjet printing sequence marked by the red lines. Two red dots on the bottom demonstrate the initiation point of the inkjet printing.

To further improve the inkjet-printing resolution of the channel structure, we increased the droplet spacing appropriately. The droplet spacing and the line spacing were all set to be 48 μm. Although some scalloped[80] structures appeared on the well-controlled boundaries, the final printed lines were almost entirely in line with the designed printing pattern. There was no uncontrollable boundary appeared on the pure inkjet-printed electrode. Although some bulging[80] structures appeared on the rest three boundaries, the channel area reminds clear and uniform.

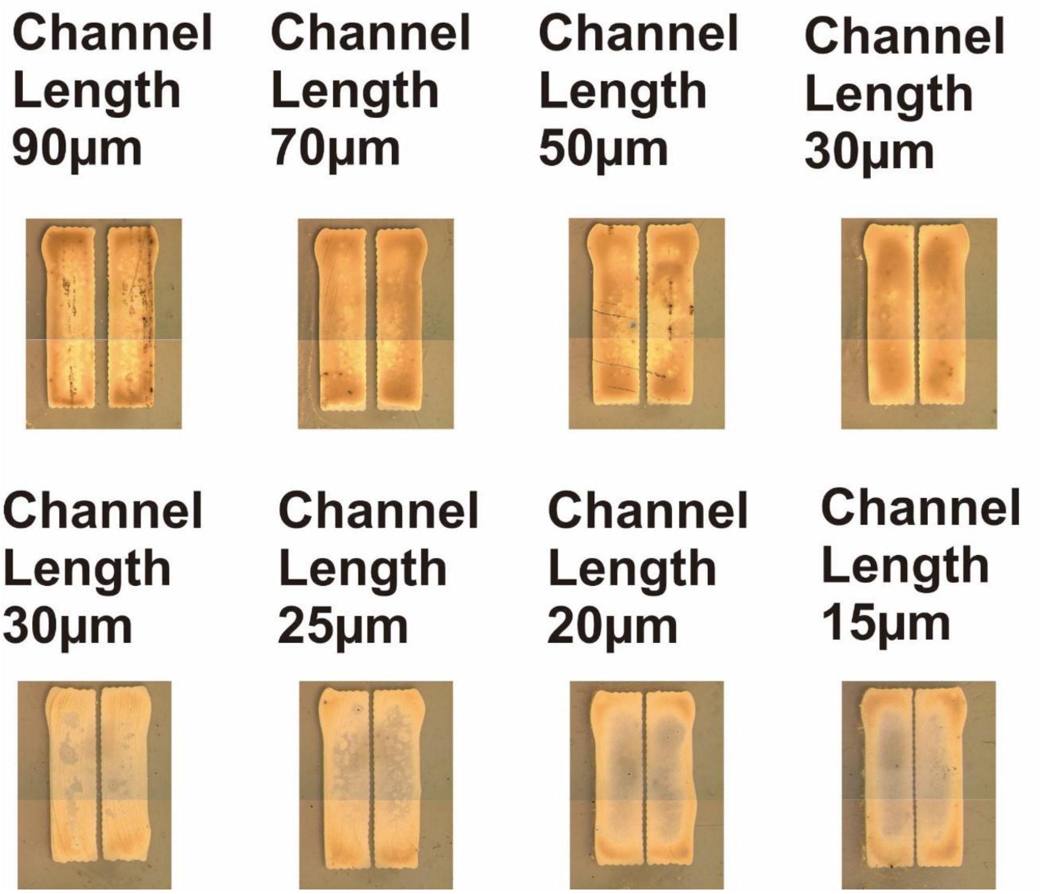

Figure 5.25 Optical microscopic images of the inkjet-printed electrodes forming channel structures with different channel lengths. The minimum channel length can reach 15 μm.

Because of the absolute uniformity of the inkjet-printed final line of the rectangular pattern formed by the parallel lines, we can further use this technique to decrease the inkjet-printed channels' channel length. As a proof of concept, we successfully inkjet-printed channel structure with the minimum channel length of 15 μm without any help from any other evaporation or etching technologies, as shown in Figure 5.25. This technique showed excellent repeatability and can fabricate all-inkjet-printed thin-film devices, such as OETCs and OTFTs, for higher electrical performance.

5.5 Conclusion

The modern inkjet-printing technique can print uniform droplets with similar volume, shape, and falling speed. And the resolution of the falling position can reach less than 1 μm benefit from the high-resolution platform controlled by stepper motors. However, the inkjet-printed pattern still has an irregular boundary and rough surface due to the complex drying and immerging phenomenon when ink droplets fall onto the substrate. In this chapter, we took metal platable three-solvent copolymer ink as an example to introduce a pattern self-levelling mechanism by introducing a slow-evaporation cosolvent to smooth the inkjet-printed pattern in joint. A thin sheet of solvent with an ultra-slow-evaporation rate formed and self-levelled the joint of the overlapping patterns. The commonly existing structure for inkjet-printed patterns, e.g., stacked coins or coffee-ring stains, were eliminated. In addition, with this special copolymer ink, a new inkjet-printing sequence can achieve high-resolution inkjet printing of channel structure. The first report systematically defines boundary control for two-dimensional patterns instead of original one-dimension designs with a line-shape pattern. Using two of the well-controlled boundaries, a high-resolution channel with a minimum channel length of 15 µm (the droplet size is ~80 µm) can be directly inkjet-printed by only changing the printing sequence. This simple technique can enhance the printing accuracy of specific areas and play a role in printed electronics such as high-performance OECTs and OTFTs. A smaller size orifice of the inkjet-printing head may further improve the inkjet-printing resolution.

Chapter 6. Potential Applications for the Inkjet-printed Xerogel-Based Cu Electrode

6.1 Xerogel-based Cu Electrode with Smooth Surface Morphology Used for Fabrication of Functional Electronic Devices

This inkjet-printed xerogel-based Cu electrode without coffee-ring stain can fabricate functional electronic devices. We assume the smooth morphology of the xerogel-based Cu electrode can enable spin-coating or inkjet printing of the functional materials directly on the surface of the electrode without leakage through the upper thin films prepared by simple-solution ways. As a proof-of-concept, we fabricate organic thin-film transistors (OTFTs) by simply inkjet printing of PVP dielectric layer and spin coating regioregular poly(3-hexylthiophene-2,5-diyl) (rr-P3HT) semiconductive layer on the top of the smooth xerogel-based Cu electrode to form OTFT device, as shown in Figure 6.1a1. This tentative experiment successfully produced a flexible OTFT with an *I-V* response (Figure 6.1a2).

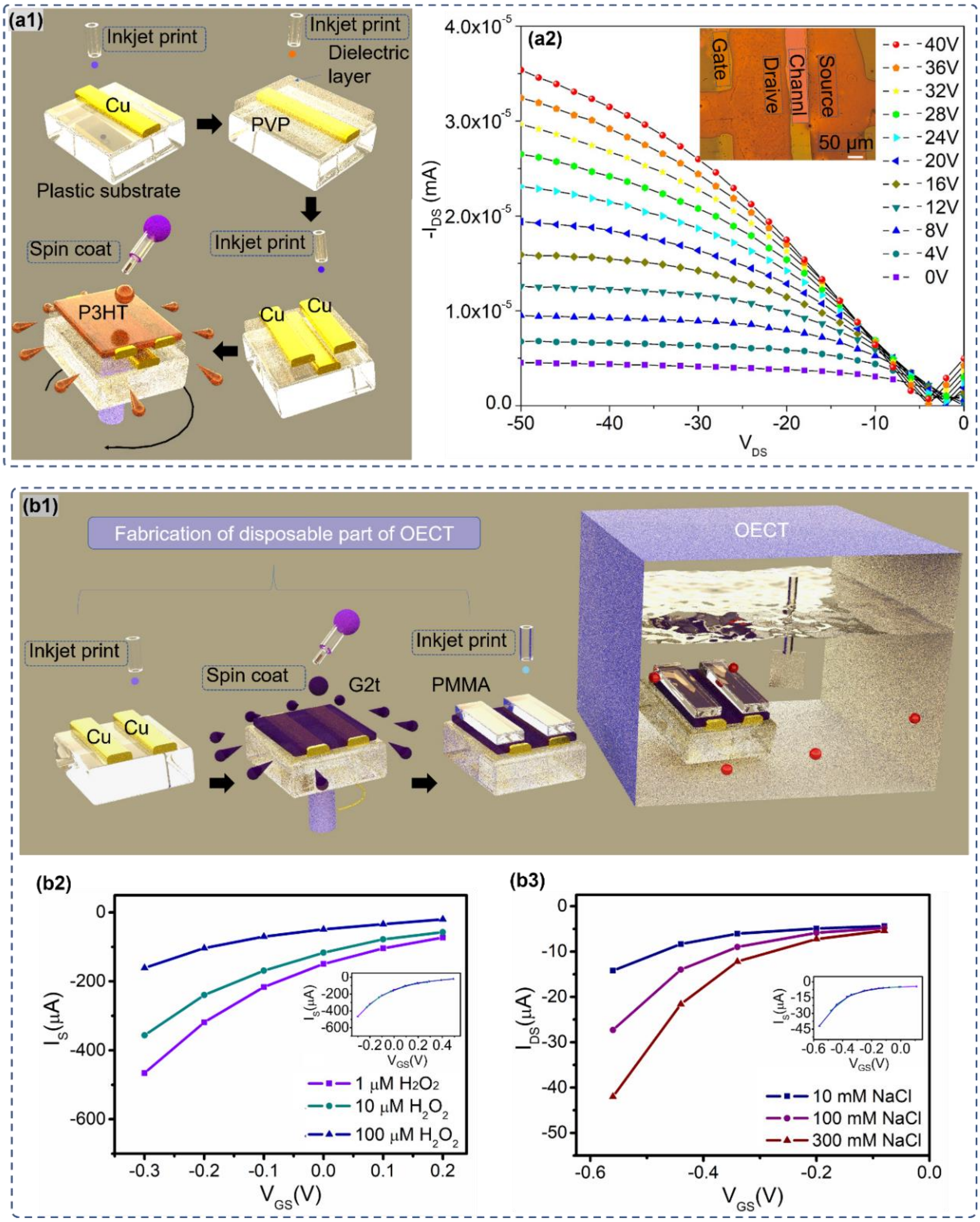

Figure 6.1. a1) Schematic diagram of the all-solutional fabrication process of the organic thin-film transistors (OTFTs) on a plastic substrate without the help of any other subtractive patterning technique. a2) *I*-*V* characteristic of OTFT (*L* = 604 μm, *W*=65 μm), using inkjet-printed Cu electrode as the gate electrode, measured at a variable gate voltage, changing from 0 V to -40 V, with a step of -4 V. Insert: optical microscopic image of the channel structure of the all-solution prepared OTFT. b1) The schematic diagram showing the fabrication process of the disposable part of the OECT fabricated by all-solution methods, i.e., inkjet printing method and the spin coating method. b2-b3) Transfer characteristics of a disposable OECT measured in PBS

solution with different b2) H_2O_2 concentrations and b3) NaCl concentrations. Inset: a universal transfer characteristic curve generated from the original curves that were scaled in the x-axis. V_d = -0.1V during testing.

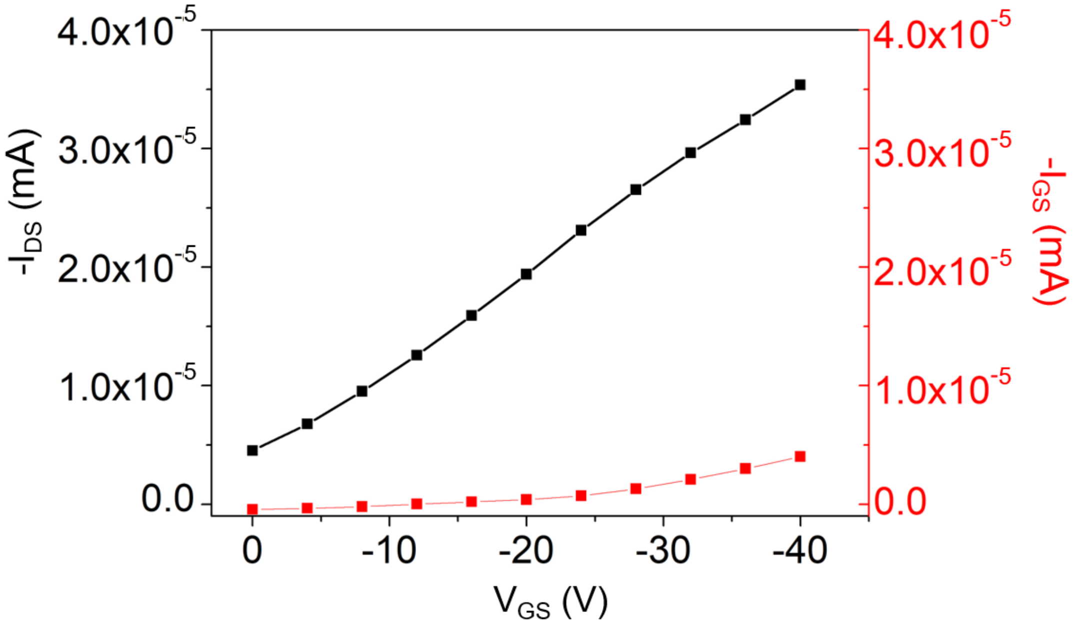

Figure 6.2 The curve of I_g and I_d vs V_g at a constant V_d of -50 V demonstrating the integrity of the triode function. I_g (leakage current) was in a reasonable range.

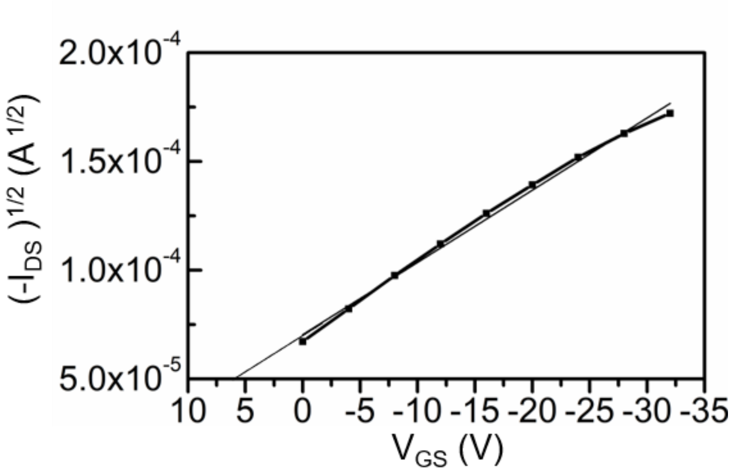

Figure 6.3. The curve of $(-I_{DS})1/2$ vs V_{GS} curve at a fixed V_{DS} of -50V. The line fitness for extracting the threshold voltage V_T.

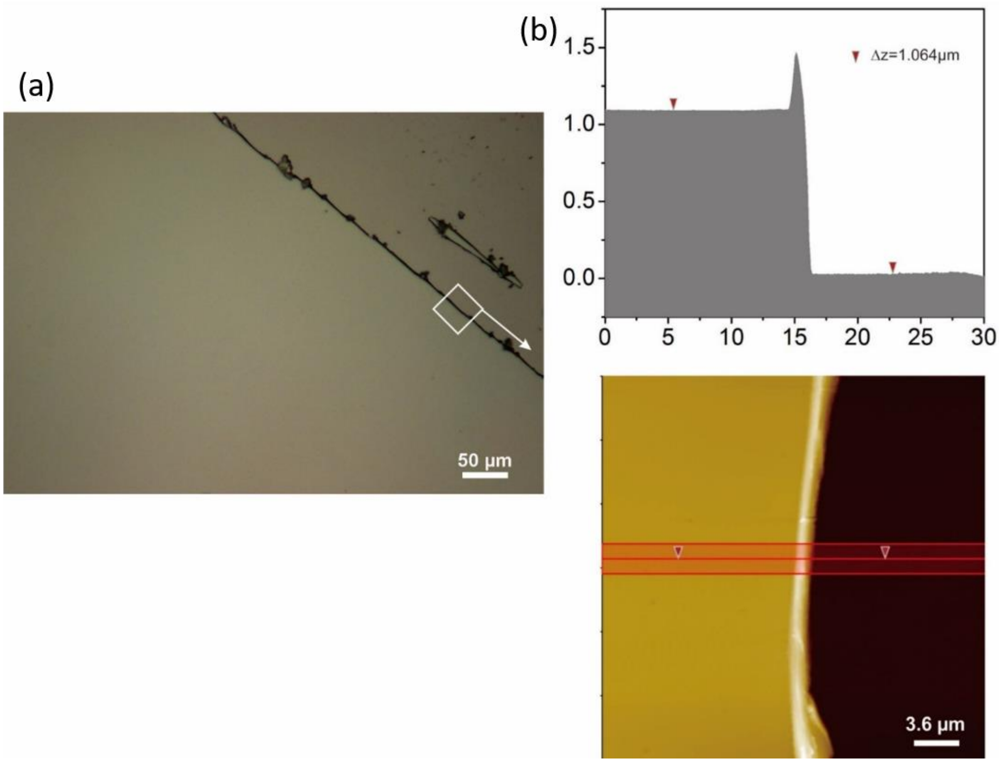

Figure 6.4 a) Optical microscopic image of the inkjet-printed PVP thin film with a scratch formed by a tweezer for thickness identification. The PVP layer is formed on the glass substrate by an inkjet printer. b) AFM image and the cross-sectional profile at the edge of a scratch trace.

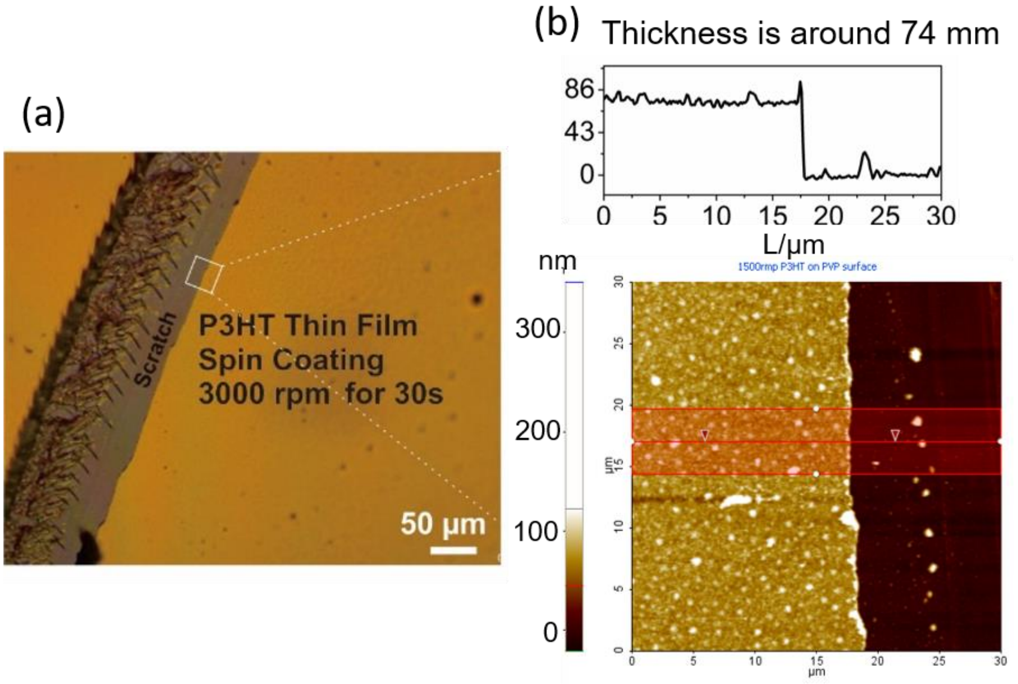

Figure 6.5. a) Optical microscopic image of the spin-coated P3HT thin film on the surface of the PVP film spin-coated on PEN substrate. The scratch-made by a tweezer

for identification of the thickness of the P3HT thin film. b) AFM image and cross-sectional profile at the edge of a scratch.

Figure 6.2 shows the I_g and I_d vs V_d at a constant V_g of -50 V, showing its triode function. From the $(-I_{DS})^{1/2}$ *vs* V_{GS} curve, the extract threshold voltage V_T was 6V, as shown in Figure 6.3. And the field-effect mobility can be calculated by the function[135]:

$$I_{DS} = \frac{W}{2L} C_i \mu (V_{GS} - V_T)^2$$

where C_i represents the capacitance per unit area that can be expressed by:

$$C_i = \frac{\varepsilon_0 K_{PVP}}{d_{PVP}}$$

where d_{PVP} is the thickness of the inkjet-printed PVP thin film, which is around 1.1μm (Figure 6.4). ε_0 represent for permittivity of vacuum space. K_{PVP} is the dielectric constant that can be set to 3.5 for PVP. Then, we extracted the mobility to be 1.2×10^{-3} cm^2/(V·s). Nevertheless, the on/off ratio is not high, possibly due to the low aspect ratio (*W/L*=9.3) and the P3HT (Figure 6.5) adoption by water and O_2 during the transporting process. Finally, the sample moved from the glove box (spin-coating and sintering of P3HT) to the vacuum chamber of the probe station (connected with Keithley 2400 for output analysis of the OTFT). This tentative experiment proves that inkjet printing or spin-coating can fabricate functional thin-film devices using inkjet-printed xerogel-based Cu electrodes.

The organic electrochemical transistors (OECTs) developed from the organic electrochemical transistor (OTFTs) have promising applications in chemical and biological sensors, benefit from the advantage of the application of a liquid electrolyte, low operation voltage (<1V), and a variable and straightforward structure.[21c] Figure 6.8b1 demonstrates the fabrication process of the disposable part of the OECTs for signal detection underwater using the inkjet-printed xerogel-based Cu as the source and the drain electrodes.

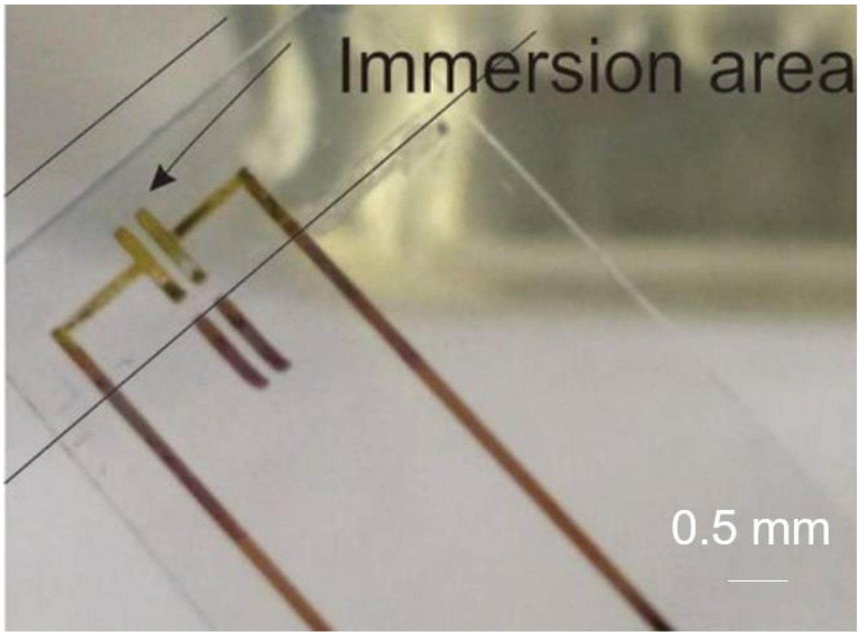

Figure 6.6. An optical image of the inkjet-printed xerogel-based Cu electrodes on the PET substrate passed the partially immersed in the electrolyte of the OECT for 5 min. Corrosion appeared in the part of the Cu electrode with a V_{DS} of 0.6V during the immersion operation.

Table 6.1. Chemical composition of the electrolyte of the OECT under testing.

Salt	NaCl	KCl	Na_2HPO_4	KH_2PO_4
Concentration (mmol/L)	137	2.7	1.0	2
Concentration (g/L)	8	0.2	1.44	0.24

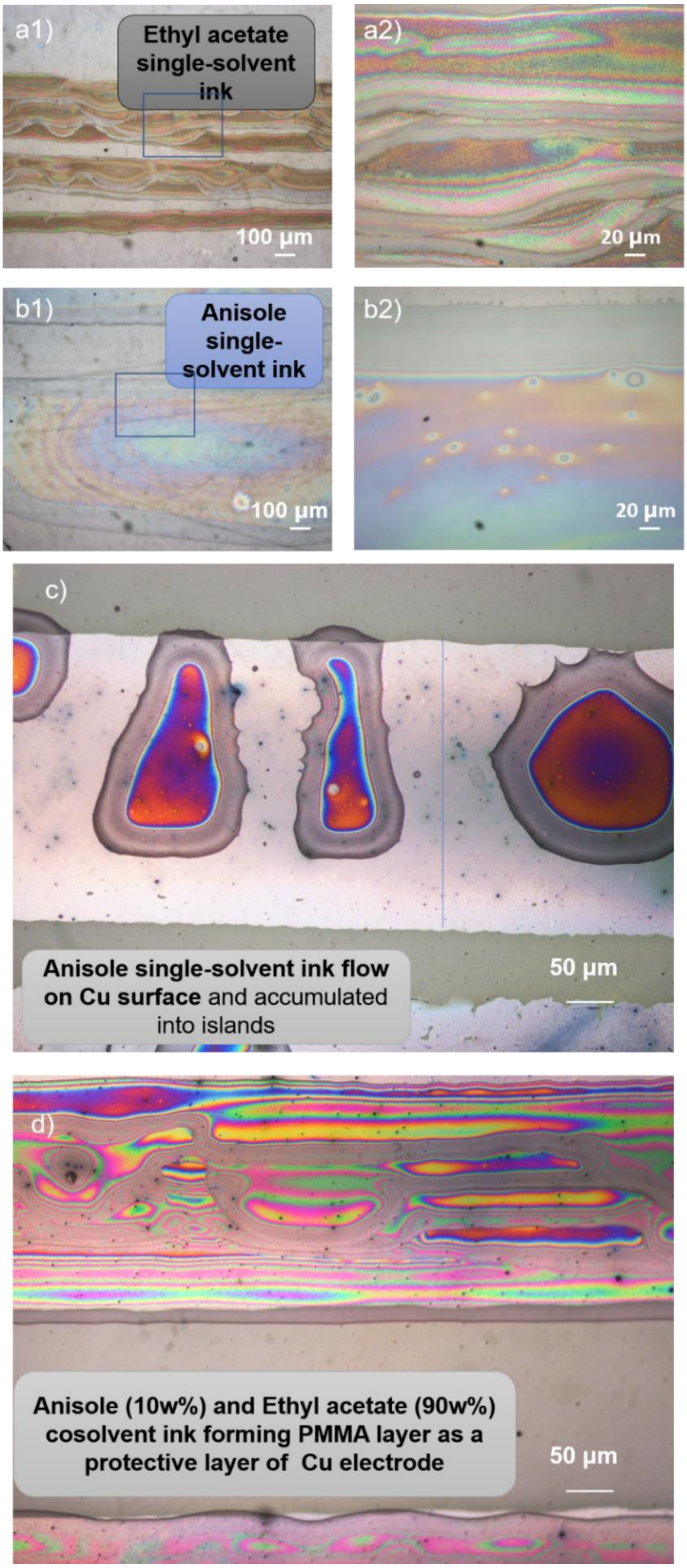

Figure 6.7. (a1) Normal and (a2) enlarged optical microscopic image of the inkjet-printed PMMA thin film formed by ethyl acetate single solvent ink on PEN substrate. (b1-b2) Inkjet-printed PMMA thin film formed by anisole single solvent ink. c) Optical

microscopic image of inkjet printing anisole single solvent PMMA ink on xerogel-based Cu electrode. Showing the incompatibility of the anisole with the surface of the Cu electrode. d) Optical microscopic image of the inkjet-printed PMMA cosolvent ink, composed of 10 w% anisole and 90 w% ethyl acetate on the surface of the Cu electrode. It can be a waterproof coating encapsulation for xerogel-based Cu electrodes.

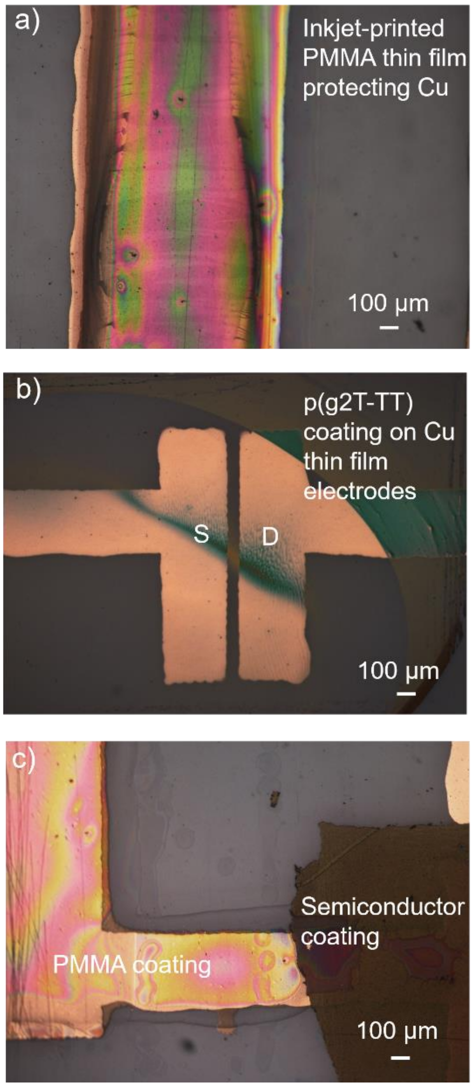

Figure 6.8. a) Optical microscopic images of the xerogel-based Cu electrode, on the disposable part of the OECTs, with a PMMA water thin film coat on its surface as a waterproof barrier. b) Optical microscopic image of the channel area of the disposable part of the OECT coated with a semiconductive (g2t-TT) layer on the xerogel-based Cu electrodes. c) Optical microscopic image of the joint of the coatings of the PMMA thin film and the semiconductor thin film on the disposable part of the OECT.

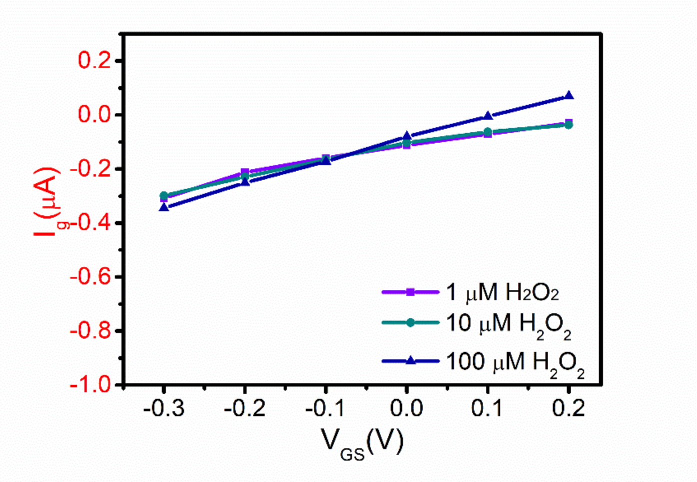

Figure 6.9. *Ig* (leakage current) vs *Vg* curve demonstrating the low level of the gate leakage current of the specific OECT during H_2O_2 concentration sensing.

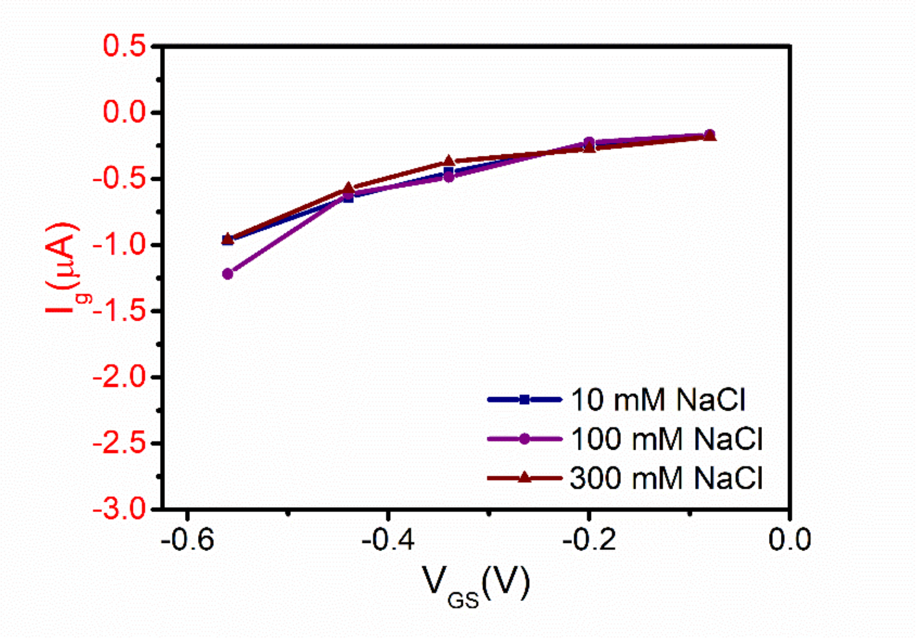

Figure 6.10. *Ig* vs *Vg* curve demonstrating the low level of the gate leakage current of the specific OECT during NaCl concentration sensing.

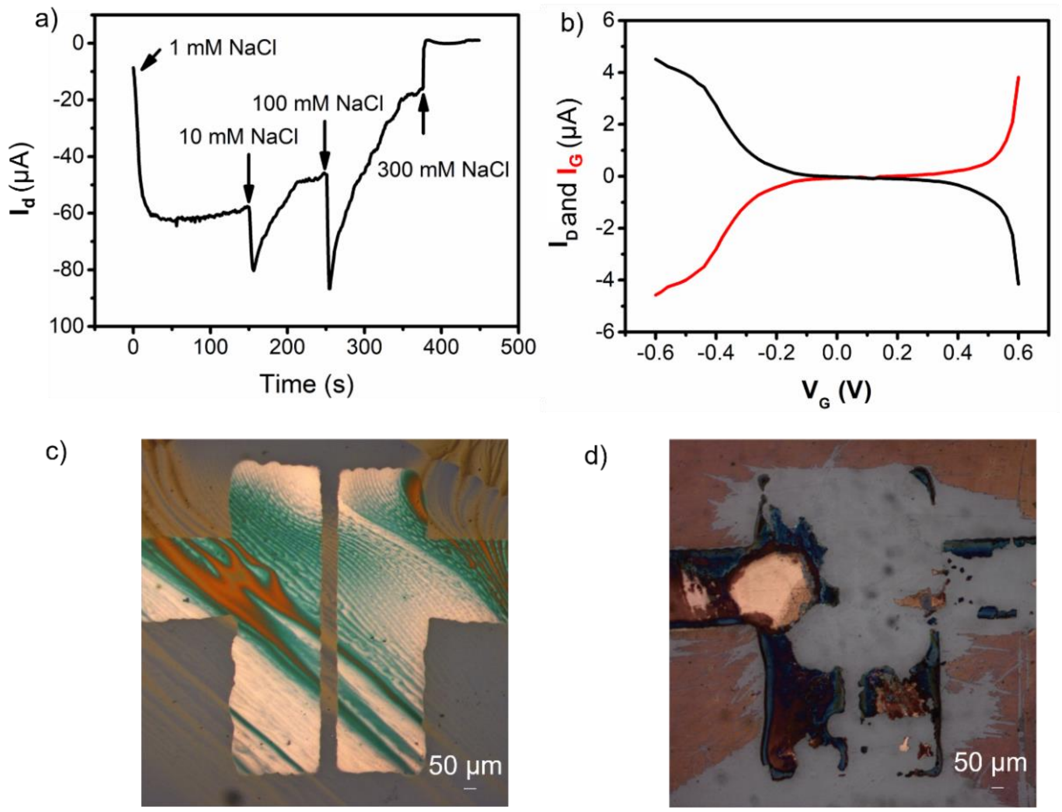

Figure 6.11. a) a) I_D vs time curve (with V_{DS} of -0.5V and V_{GS} of -0.4V) in sensing NaCl concentration. Although there was an obvious signal response when changing the NaCl concentration, the measuring system is not stable due to the slow corrosion of the Cu electrode. b) I_G-V_G and I_D -V_G curve of a specific disposable part of OECT after immersing in PBS solution for 450s with V_{DS} of -0.5V and V_{GS} of -0.4V. The value of I_G, the leakage of current, is like the value of I_D. This phenomenon indicated a large leakage current passed through the semiconductor thin film, and almost all the source currents came from the gate electrode. Optical microscopic image of the channel region of the disposable part of the OECTs c) before and d) after a 450-second immersion in PBS solution with V_{DS} of -0.5V and V_{GS} of -0.4V.

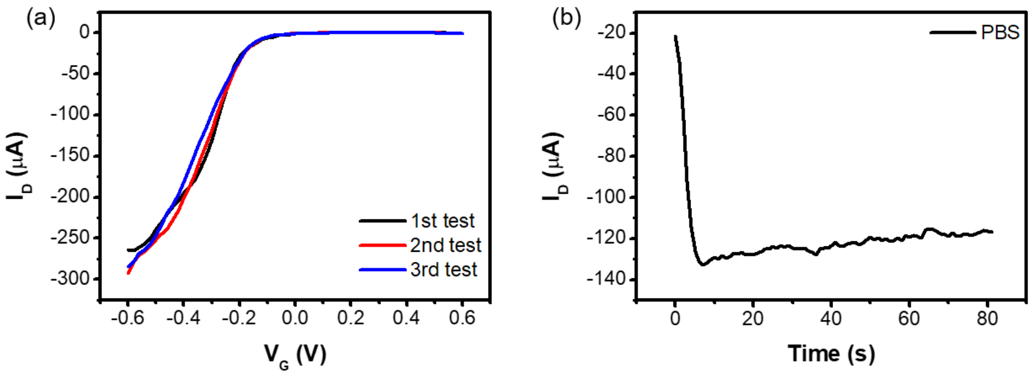

Figure 6.12. Stability test for the low-cost OECT, with the all-solutional, prepared disposable part with source and drain electrodes. a) I_V repeating test (in PBS solution). The time interval for each test is 20 seconds. b) I_D vs time curve (with V_{DS} of -0.5V and V_{GS} of -0.4V), showing the system is relatively stable in PBS solution for a short amount of time.

We developed bi-solvent inkjet printing ink of PMMA that can form a water-proof thin film. It can exposed electrodes to extend the device's service life underwater (Figure 6.6 and 6.7) because of the corroding phenomenon of Cu electrode in PBS solution (Table 6.1). Thanks to the uniform morphology of the xerogel-based Cu electrode, the glycolated thiophene (g2T-TT) semiconductor layer can be directly fabricated on the channel area (Figure 6.8) by spin-coating without leakage (Figure 6.9and Figure 6.10). Although such disposable OECT still cannot be placed in the electrolyte for an ultra-long time when the voltage is applied (Figure 6.11), the rapid measurement of solution concentration through the Id-Vg curve can still be easily achieved (Figure 6.12). As shown in Figure 6.81b2, the reusable flat platinum electrode and the combination of all-solution prepared disposable parts, with low production cost, can quickly measure the concentration of H_2O_2. As shown in Figure 6.81b3, this structure can measure the NaCl concentration as well.

6.2 Attempt to Inkjet Print Xerogel-Based Cu Electrode onto Plastic Bags

Plastic bags are the most common items in our daily lives. Most plastic bags we used for shopping thermoplastic PE. They cannot be a substrate for inkjet-printing of electrodes formed by metal nanoparticle inks that require a high-temperature sintering process to form metal thin film electrodes with good electrical conductivity and sort of adhesiveness to the substrate. Even with the minimum sintering temperature (150 °C), the high-temperature sintering process can still melt the plastic bags. Here, we successfully inkjet-printed Cu electrode on the plastic substrate using xerogel-based Cu electrode, benefit from its room-temperature preparing mechanism, as shown in Figure 6.13. The Cu electrode has a rough surface morphology formed due to the intrinsically irregular surface morphology of the surface of the plastic bag. Although the xerogel-based Cu electrode had a rough surface morphology, it can be used as a highly conductive thin film electrode to form a closed loop to illuminate a LED light, as shown in Figure 6.13c.

Figure 6.13. a) Optical photo of the inkjet-printed Cu electrode on a plastic bag. b) Optical microscopic image of the enlarged view of the surface of the xerogel-based Cu electrode on the plastic bag. c) Optical photo of the inkjet-printed circuit on a plastic bag forming a closed loop that can power a LED light.

6.3 Attempt to Inkjet Print Xerogel-Based Cu Electrode onto Stretchable Substrates

Latex material is one of the most common materials in our daily lives. Latex material has excellent stretchability. It can return to its original length without any damage after been stretched to 200% of its original length. However, when the temperature rosed up to 40 °C, the thin latex film would interact with the air's oxygen. And this aging process will turn the thin latex film harder and gradually lose stretchability. Therefore, they cannot be a substrate for inkjet printing of electronic devices. The commonly used printable inks need a high-temperature sintering process to form metal thin film electrodes with good electrical conductivity and sort of adhesiveness to the substrate. The high-temperature sintering process with the minimum sintering temperature, around 150 °C, will directly initiate the aging of the latex. Here, we successfully inkjet-print Cu electrode on the surface of latex substrate, benefit from the property of room-temperature fabrication of the xerogel-based Cu electrode. As shown in Figure 6.14, the latex membrane with a pre-stretching of 150% was a substrate for inkjet printing of the Cu electronic circuit. The original single-solvent copolymer ink (based on 2-methoxyethanol) has better wettability on latex substrate than the three-solvent-based ink. The Cu electroless metal deposition on a latex substrate was more difficult than Cu electroless deposition on a smooth substrate like PET. The metal was difficult to deposit on the latex substrate until increased copolymer concentration to 5 w%. The Cu electroless depositing time was 30 min.

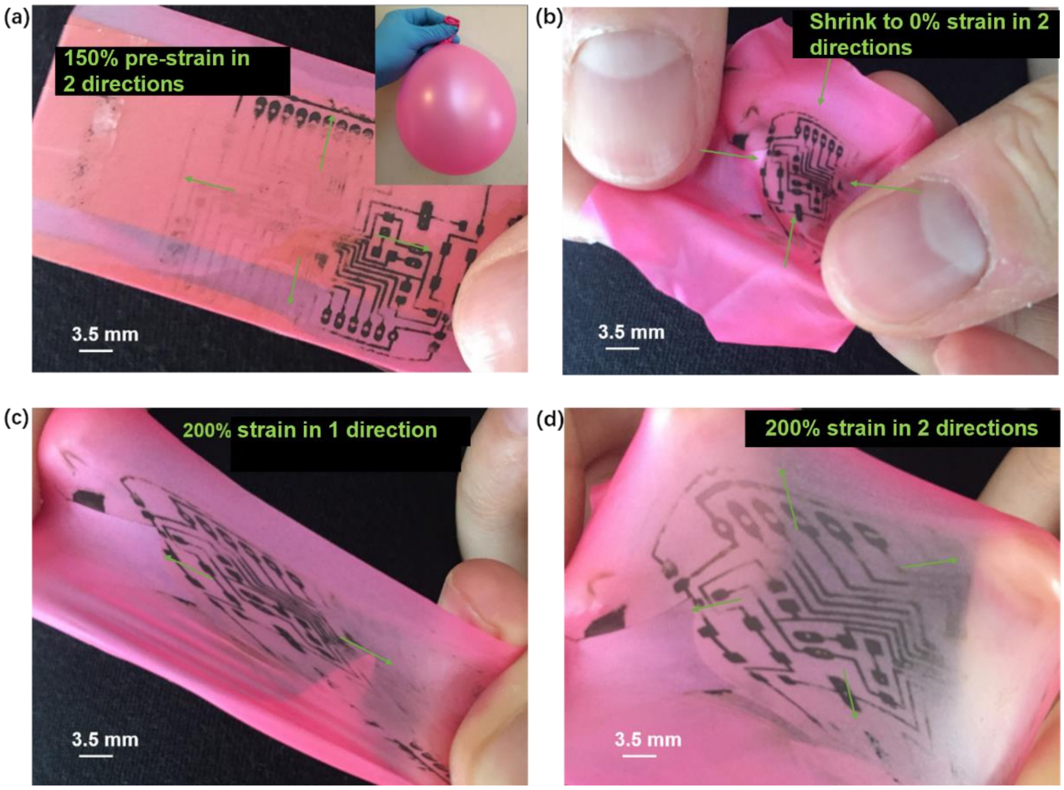

Figure 6.14. Inkjet-printed Cu circuit on the surface of a rubber balloon (latex film). a) Latex film formed an inkjet-printed circuit on its surface. The latex film maintained a stretching state of 150% in two directions after the whole metal electrode fabrication process. b) The latex film after releasing of its stretching extent. c) Photos of the latex film under pulling to 200% of its original size in c) one-dimension and d) two-dimension simultaneously.

The first several experiments failed when using low-concentration copolymer ink (0.5w%). Then we tried to print the copolymer ink with the copolymer centration of 2w%. The pattern started to grow on latex substrate, as shown in Figure 6.14. However, only half the copolymer buffer thin film successfully initiated Cu electroless deposition after immersion in the ELD solution for 30 min. In addition, only the small-sized Cu crystals (exhibit black color) were deposited on the inkjet-printed gel pattern. The pure-metal layer failed to be generated even past such a long-term electroless deposition. And the electrical conductivity of this kind of electrode was around 0.3 S/m (without stretching), which is ignorable.

When we increased the concentration of the copolymer ink to 5w%, the upper, pure metal layer started to grow because the pattern started to turn dark yellow, as shown in

Figure 6.15. And we found that the double-cycle inkjet-printing of the copolymer ink(can form thicker copolymer film) will increase the electrical conductivity. The conductivity of the pattern formed on the one-printing cycle was 2×10^3 S/m, whilst the conductivity of the sample with two-printing processes can reach 6×10^3 S/m. The thicker copolymer matrix was making the Cu with fewer wrinkles.

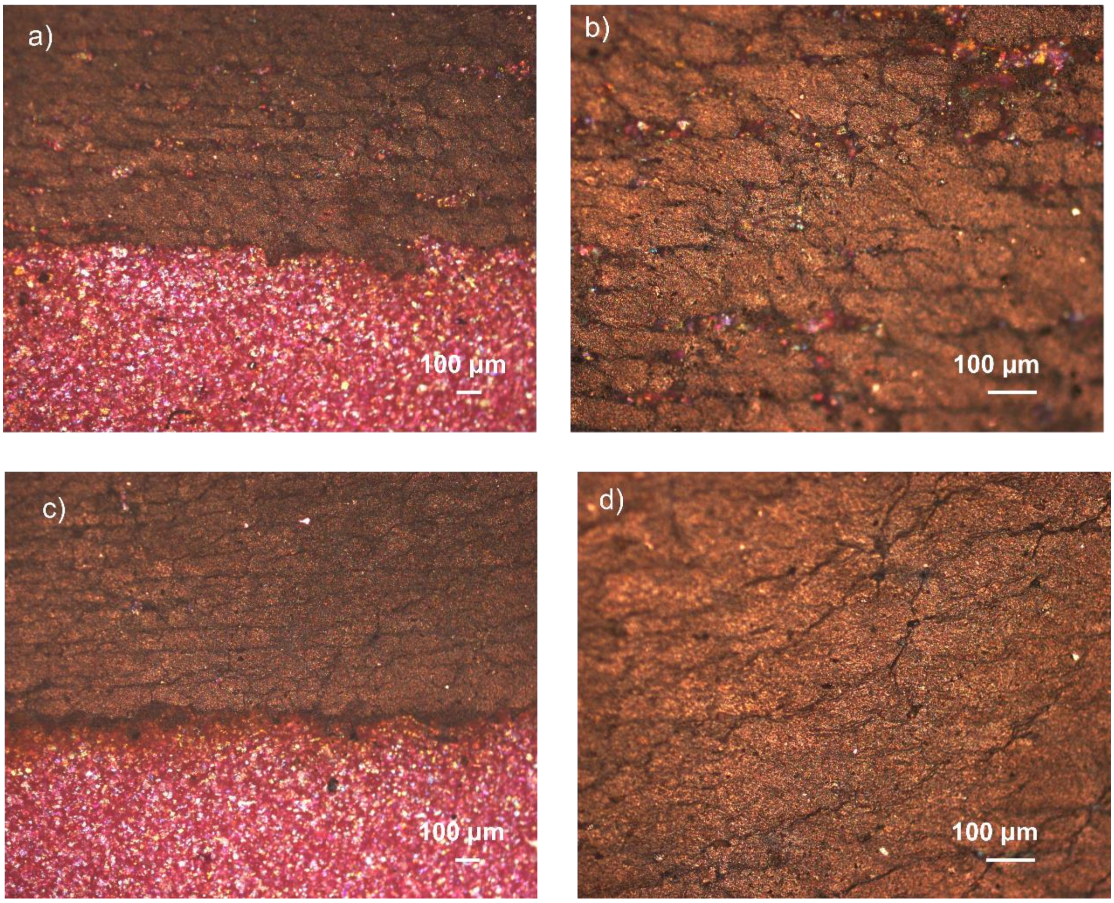

Figure 6.15. Optical microscopic image of the Cu thin film coated on latex film with a-b) one-time and c-d) two-times inkjet-printing of 5w% copolymer ink in the three-solvent-copolymer system.

As shown in Figure 6.16, the difficulties in the formation of the Cu electrode on the latex surface may result from the rough surface of the rubber film. The over large surface roughness leads to small-sized metal flakes instead of continuous metal thin films. Therefore, increasing the surface uniformity of the thin latex film is very important for the fabrication of Cu electrodes on the latex membrane.

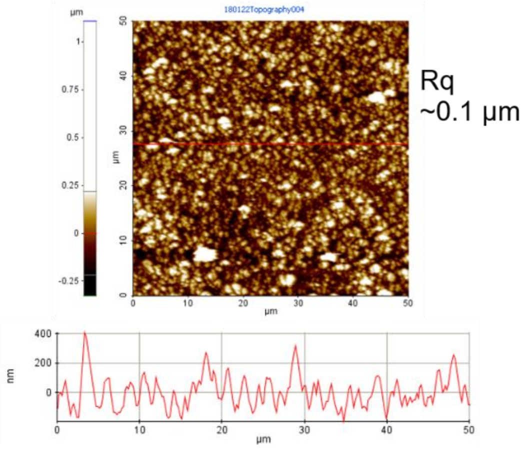

Figure 6.16. AFM image and cross-sectional roughness of the surface of the thin latex membrane.

Spin-coating of the latex solution onto a glass slide can form the thin latex film. The spin-coating was at 2000 rpm for 20 s. After a half-hour drying in a hot oven, the thin latex membrane became free-standing and stretchable. Then the three-solvent based copolymer ink was inkjet printed on the surface of the smooth latex membrane. The root means square roughness of the pattern was 0.1 µm, as shown in Figure 6.16.

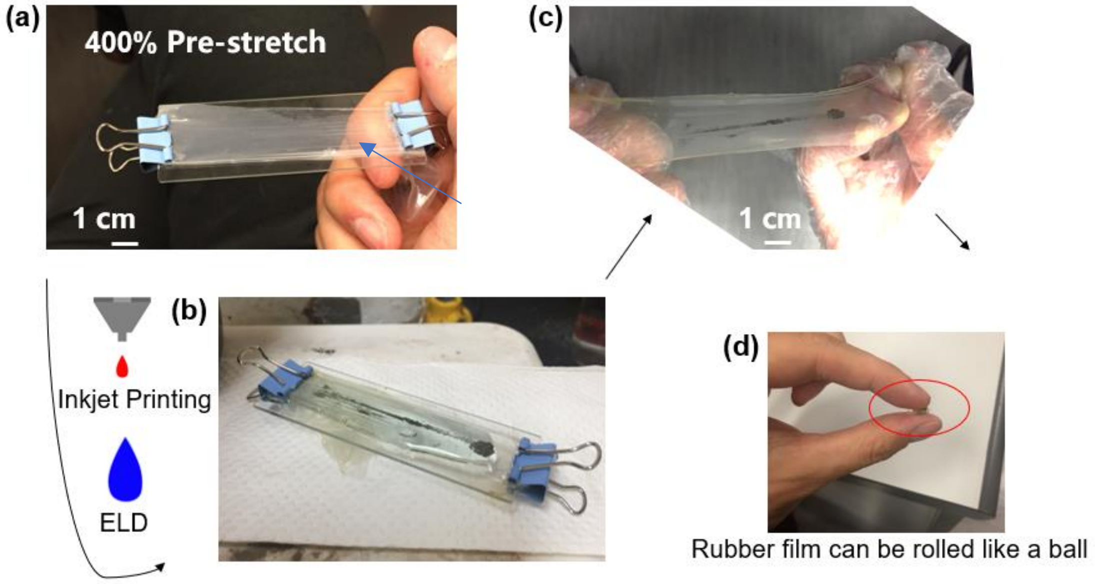

Figure 6.17. a) Optical images of the latex thin-film pre-stretched to 400% of its original size. b) Optical photo of the Cu electroless deposited on the xerogel, patterned by an inkjet printer. Left inset: schematic diagram of the simplified preparation steps for fabrication of the stretchable electrode on latex. c) Optical microscopic image of pull the thin latex film with Cu coating. d) The ultra-flexible Cu thin-film conductors on the

free-standing latex thin film can be rolled like a ball without damaging its electrical conductivity.

After 1-hour electroless deposition, the Cu thin film grows slowly on the surface of the thin rubber film. The recorded highest electrical conductivity of this kind of Cu electrode was 1.1 × 10^3 S/min. However, the Cu electrode in the stretched stage was not detected well because of the lack of the joining material to form well connected with the thin film electrode in the stretching state.

The following points influence the quality of the Cu patterns:

1. Rough printing result. The inkjet printing head must be resized to a relatively high altitude to avoid colliding with the printing head. However, the far distance between the printing head to the substrate is more likely to cause the reduction of the inkjet-printing resolution.
2. The wettability of thin latex film is poor for three-solvent copolymer ink. Therefore, the boundary of the printed lines was rough. The flowing of the copolymer ink on the surface of the membrane caused this phenomenon.
3. Pre-stretching easy to cause wrinkle of the membrane. The wrinkle will cause serious difficulties for inkjet printing. The printed ink will accumulate in the lower please of wrinkles and make the pattern discontinue. Stretching the membrane in 2 or more directions will tackle this problem.

To deal with the difficulties mentioned above. An easy way, namely pre-stretching based on a card, was invented to pre-stretched membrane uniformly in two directions to avoid wrinkles, as shown in Figure 6.18. Moreover, maintaining the stretching state without introducing the tools, i.e., clamps, with the high altitude reduced the change of collision with the inkjet-printing head. And it can make the follow-up operation steps, such as catalyst bath and electroless metal deposition, easy to operate.

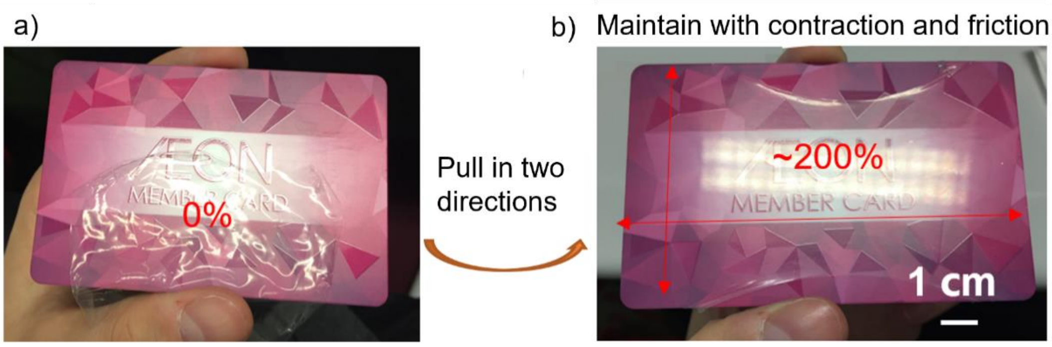

Figure 6.18. Optical images of thin latex film a) without and b) with ~200% stretch in two directions using an ordinary purchasing plastic card. The latex film can firmly attach to the card by its intrinsic contracting force and high friction force.

6.4 RFID Antenna Made by Inkjet-Printed Xerogel-Based Cu Electrode

Radiofrequency identification (RFID) is a technology that allows data transmission wirelessly through electromagnetic waves in radio frequencies. It can be a signal transmission unit for all kinds of wearable electronic and smart packaging and manufactured in large quantities. However, current inkjet-printing ink made by Noble-metals, which had high production costs, prevented the widespread application of this technology. Here, we report a method to inkjet-print xerogel-based Cu electrode on PET substrate to form a functional RFID antenna with a low-production cost.

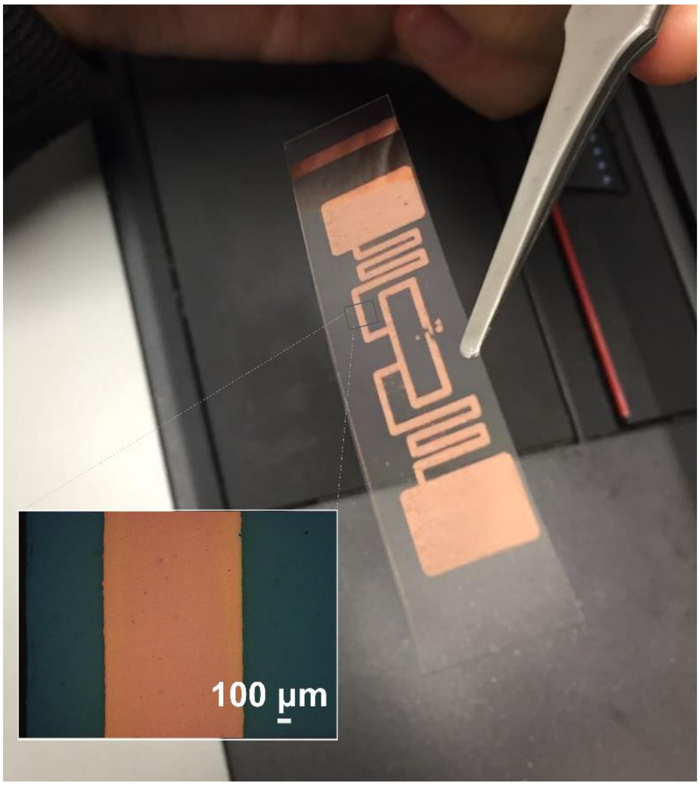

Figure 6.19. Optical photo image of the inkjet-printed RFID antenna formed by xerogel-based Cu electrode. Insert is an enlarged visual microscopic image showing the uniformity of the inkjet-printed pattern.

As shown in Figure 6.19, the RFID antenna can be inkjet-printed on the surface of the transparent PET substrate with a printing resolution of around 50 µm. The size of the inkjet-printed Cu antenna of the high-frequency RFID tape (AZ-B44) was 10.33 mm × 44.45 mm. A functional RFID tape was fabricated after mounting the chip, M4QT, to the antenna. The RFID detector (LJYZN-101) can transmit 902~928MHZ ultra-high frequency signals outwards, with the frequency-hopping spread spectrum (FHSS) mode. When an RFID tap with an operating frequency within this frequency range, the indicator will light up, and the buzzer will beep. When the RFID tap in an area less than 5 meters above the RFID detector, the alarm light will activate the alarm mechanism.

6.5 Triboelectric Generator Made by PAMD-based Cu Electrodes

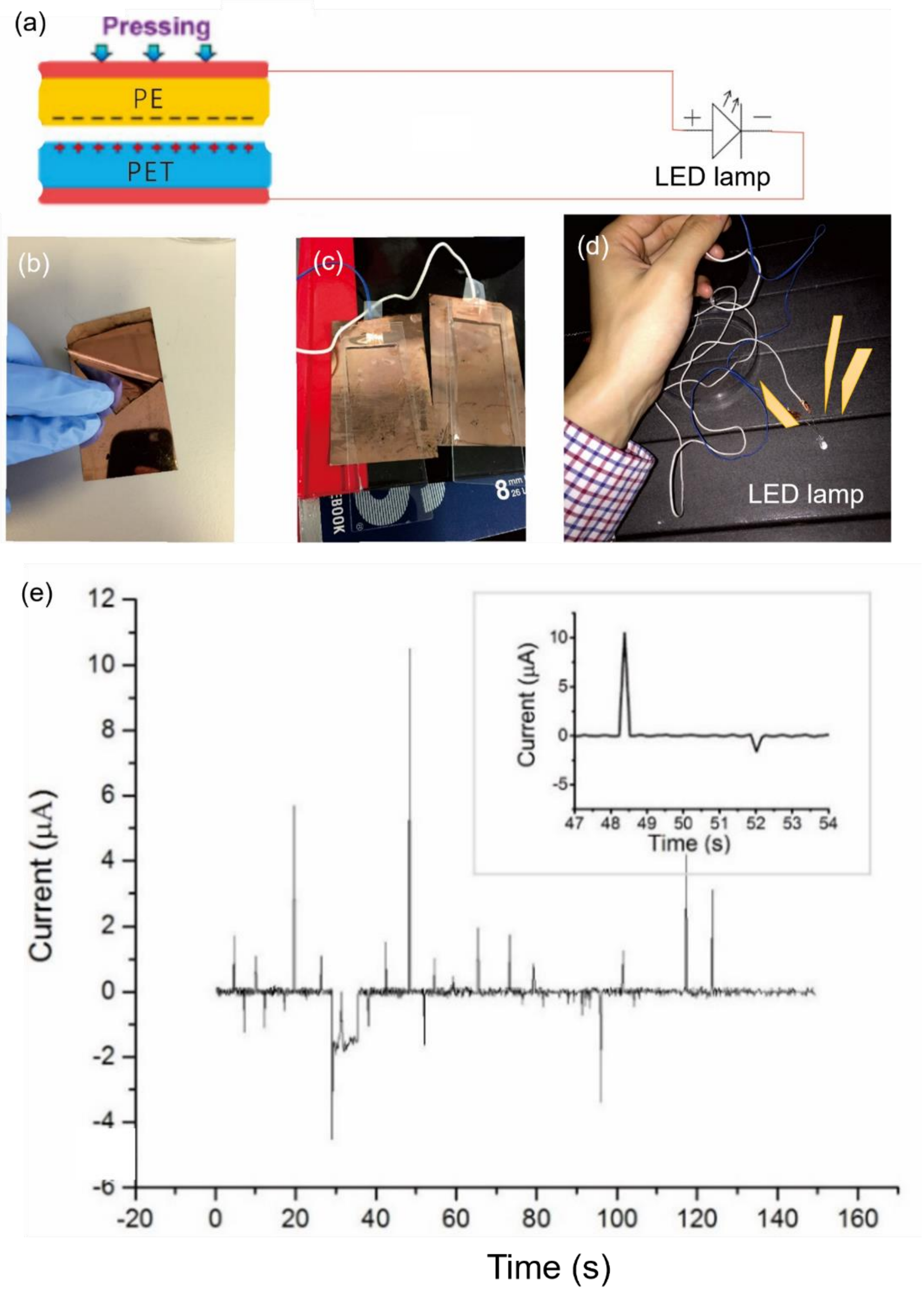

Figure 6.20 a) Schematic diagram showing the working principle of the triboelectric generator. b-c) Optical photos of the triboelectric generator using PE and PET as the dielectric layer and PAMD-based Cu as conductor. d) Photo of the LED lamp instantaneously illuminated by electrical energy generated from the triboelectric generator. e) Current vs time curve of the energy generated by the triboelectric generator during continuously separating and closing the two dielectric layers. Insert current vs time curve on a specific separating & closing cycle.

The triboelectric nanogenerator (TENG) uses contact charging and electrostatic induction to generate electronic energy. As shown in Figure 6.20a, the two dielectric parts obtain potential differences after their physical contact. The static charge on the surface of dielectric films will induce the charge accumulation at the metal electrode. After the reconnection of two dielectric layers, the outer face of the dielectric layer becomes electrically neutral. At this moment, the current will flow through the connected electrodes to balance the current state.

The triboelectric generator has two dielectric components. Each component comprises a 50-µm-thick plastic film and a 150-nm-thick metal coating. The PAMD technique offered the substantial compatibility of a thin metal film and the plastic layer for both PE and PET thin films. Therefore, the triboelectric generator was resilient and flexible and suitable to be developed to be a wearable component that can fix on clothes. The operation of quick separation and merging of two dielectric components can induce electronic potential between two electrodes if we layer apart or attach two films. As a proof-of-concept, we connected the triboelectric generator to the 2 pins of a LED bulb. The electrical energy generated by the triboelectric generator can instantaneously illuminate LED (figure 6.20d). We used the oscilloscope (KEITHLEY 2400) to measure the maximum electric energy of this triboelectric generator. The maximum charge density on the PE or PET were around 10 $\mu C/m^2$ for one testing cycle, as shown in Figure 6.20e.

Although this triboelectric generator does not have a nanostructure (not TENG), the charge density can still reach a high level. It may benefit from the introduction of solid glue, as shown in Figure 6.21. As the actual contact area for two plastic dielectric layers was very small, the introduction of solid glue can dramatically increase their real contact area. The charging and discharging on all the real-contacted points worked together to enhanced instant electrical potential on two electrodes. The TENG usually has a limited lifespan due to the wearing and shedding of nanostructures.

On the contrary, the glue-based triboelectric generator does not need to worry about the wear of thin glue film. However, the design with the introduction of glue increases the frictional force in the direction of relative displacement (horizontally) between the two dielectric layers. A mechanical structure with automatic reduction capability may be able to solve this problem well.

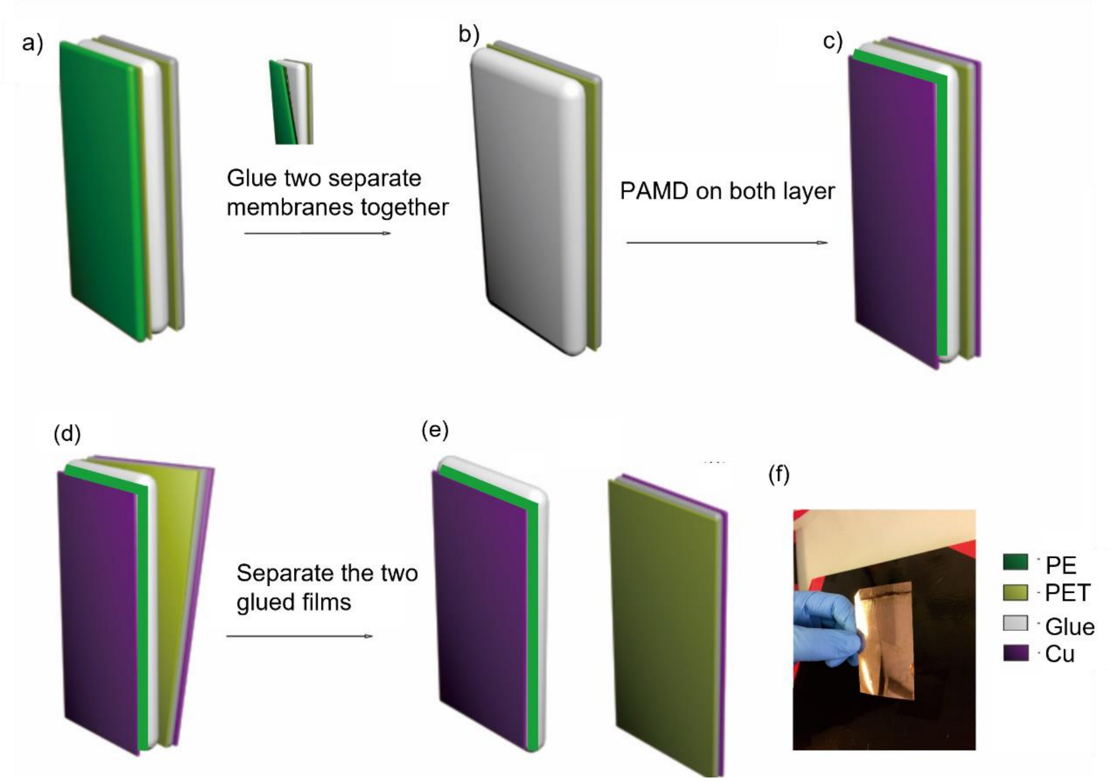

Figure 6.21 a-e) Schematic diagram showing the structure and the fabrication process of the triboelectric generator with a PAMD-based Cu electrode. The solid flue thin film is sandwiched between PE and PET dielectric layers to enhance the real contact area. f) Optical image of the real triboelectric generator.

6.7 Conclusion

PADM-based Cu electrodes can apply to the fabrication of many functional electronic devices, including biological sensing, smart packaging, RFID, stretchable conductors, and triboelectric generators. It is approved that the PAMD-based Cu electrode is good enough to replace Au or Ag nanoparticle ink in printed electronics. The Cu electrode prepared by this technology is cheap, durable, and have high adhesiveness to the plastic substrate. The future is an electronic era. This low-cost energy generation system can collect mechanical energy lost by human movement and transfer them to electrical energy to power the microelectronic devices.

CHAPTER 7. CONCLUSIONS AND OUTLOOK

7.1 Conclusions

In this thesis, the formation mechanism of problems, such as high surface roughness, low-printing accuracy, and low-deposition uniformity, was investigated for the original PAMD-based Cu electrodes patterned by inkjet-printer. Here, reported many methods enabled preparing inkjet-printed Cu electrodes with smooth surface morphology and uniform boundary. Furthermore, multiple technologies, including TEM, SEM and AFM, investigated the microstructural properties of the area where the electrode connects to the plastic substrate. It is also the first-time investigation of the adhesiveness of the PAMD-based Cu electrode by nanoindenter. Finally, the inkjet-printed Cu electrode with smooth surface morphology enabled the low-cost production of the all-solution prepared OECTs and OTFTs. In addition, a newly invented inkjet-printing mechanism, together with the new ink, helped inkjet-printing of a high-resolution channel.

In chapter 4, A new treatment step, namely EtOH treatment, made the traditional gel-based Cu electrode to the xerogel-based Cu electrode accompanied by a shrinkage of half of its original thickness. Then, instruments, including AFM, TEM, underwater AFM, nanoindenter, profile, demonstrated the 3-dimensional structure of the xerogel. The xerogels have a mesoporous structure. The pore size is bigger than 20 nm but smaller than 50 nm. Cu electrode grew on the xerogel, shown large adhesive energy to the plastic substrate. The adhesive energy of xerogel based Cu was 0.7 J/m^2. Compared with the gel-based Cu electrodes, with adhesive energy of 0.06 J/m^2, it has an advantage. The strengthening of the polymer cluster during the EtOH treatment step may form this considerable toughness of xerogel. On the one hand, the xerogel formed an extremely rough surface morphology that helps closely combined with the pure-metal layer on the top. On the other hand, the xerogel matrix has a thicker polymer cluster when compared with the gel matrix. Therefore, the mesoporous xerogel matrix acted as a tough binder between the plastic substrate and the pure-metal layer on the top.

In chapter 5, the three-solvent copolymer ink with a slow-evaporation-rate cosolvent can initiate a self-levelling mechanism to smooth the original irregular thickness distribution in the joint of the inkjet-printed patterns. The proportion of the slow-evaporation-rate cosolvent needs to be 4w% because an excessive amount of slow-evaporation-rate cosolvent will flow on the copolymer pattern causing irregular thickness distribution. Similarly, a too-small amount of slow-evaporation-rate cosolvent cannot initiate a self-levelling mechanism. In addition, a special inkjet printing sequence showed the ability to improve the uniformity of the inkjet-printed pattern in one boundary. This method needs to use the ink with the addition of slow-evaporation-rate cosolvent. Two of these pure inkjet-printed boundaries can form a uniform channel with a minimum channel length of 15 µm without the help of any other patterning methods.

In chapter 6, PAMD-based Cu electrodes replaced the Au or Pt electrodes in fabricating electronic devices, including disposable OECTs, OTFTs, RFID antennas, and triboelectric generators. The functional materials can be directly spin coat on the inkjet-printed Cu electrode to form functional OTFTs and OECTs without short-circuiting current between the thin films prepared by the solution methods. The smooth surface morphology of the inkjet-printed Cu electrode ensured the integrity of the thin films coatings on the top. In addition, this PAMD-based Cu electrode was successfully printed on heat-sensitive substrates, e.g., plastic beg (PE thin film) and thin latex film, to form flexible and stretchable electrodes. Thus, the new generation of PAMD-based Cu electrodes has excellent potential to be applied in many research areas such as intelligent packing, flexible robots, electronic skin, etc.

7.2 Outlooks

This thesis introduced an inkjet-printing technique for Cu electrode preparation approaching maturity. This PAMD-based Cu electrode can be inkjet-printed on a plastic substrate and maintain the high uniformity of the pattern boundary and the smooth surface morphology. This high-quality Cu printing technique can replace the popular Noble metal inkjet-printing ink in some application areas and save this limited material resource consumption. And this technique has the potential to reduce the production cost of the printed electronics industry, maintaining the premiums uniformity, flexibility and electrical conductivity as well. We have already found a way to fabricate an inkjet-printed source and drain channel with a channel length of 15 µm using the inkjet printing head with an orifice of 50 µm. More narrow channels patterned by pure inkjet printing technique may appear by applying smaller orifices in the inkjet printing head. In addition, the method of the PAMD-based Cu deposition does not require a vacuum environment, high-temperature evaporation, or sintering steps that need high energy consumption.

This method only relays chemical energy for Cu deposition. Therefore, it is possible to be the final choice of people in the era of energy crisis. Furthermore, without the sintering process (≥150 °C), this technique is also very the potential to be applied on lots of heat-sensitive substrates, including latex and PE. Maybe some biological or textile thin-film material with bridal mechanical properties can also be used as the substrate for PAMD-based Cu electrodes in the future.

Reference

[1] a) S. R. Quake, A. Scherer, *Science* **2000**, 290, 1536; b) Y. a. Chaug, J. E. Haubrich, M. Sereda, R. Liang, *MRS Online Proceedings Library Archive* **2004**, 814; c) J. Mei, M. R. Lovell, M. H. Mickle, *IEEE transactions on electronics packaging manufacturing* **2005**, 28, 265; d) J. H. Cho, J. Lee, Y. Xia, B. Kim, Y. He, M. J. Renn, T. P. Lodge, C. D. Frisbie, *Nat Mater* **2008**, 7, 900; e) D.-H. Kim, J.-H. Ahn, W. M. Choi, H.-S. Kim, T.-H. Kim, J. Song, Y. Y. Huang, Z. Liu, C. Lu, J. A. Rogers, *Science* **2008**, 320, 507; f) S. Pralle, J. Boscarino, *Review of Policy Research* **2011**, 28, 323.

[2] G. Deokar, J. Avila, I. Razado-Colambo, J.-L. Codron, C. Boyaval, E. Galopin, M.-C. Asensio, D. Vignaud, *Carbon* **2015**, 89, 82.

[3] D. M. Mattox, *Handbook of physical vapor deposition (PVD) processing*, William Andrew, **2010**.

[4] a) J. Dijksman, *Journal of Fluid Mechanics* **1984**, 139, 173; b) S. B. Fuller, E. J. Wilhelm, J. M. Jacobson, *Journal of Microelectromechanical systems* **2002**, 11, 54; c) B. J. de Gans, P. C. Duineveld, U. S. Schubert, *Advanced materials* **2004**, 16, 203; d) M. Singh, H. M. Haverinen, P. Dhagat, G. E. Jabbour, *Advanced materials* **2010**, 22, 673.

[5] a) T. Sekitani, Y. Noguchi, K. Hata, T. Fukushima, T. Aida, T. Someya, *Science* **2008**, 321, 1468; b) S. K. Vashist, D. Zheng, K. Al-Rubeaan, J. H. Luong, F.-S. Sheu, *Biotechnology advances* **2011**, 29, 169; c) C. B. Jacobs, M. J. Peairs, B. J. Venton, *Analytica Chimica Acta* **2010**, 662, 105; d) K. Chen, W. Gao, S. Emaminejad, D. Kiriya, H. Ota, H. Y. Y. Nyein, K. Takei, A. Javey, *Advanced materials (Deerfield Beach, Fla.)* **2016**.

[6] J. Li, F. Ye, S. Vaziri, M. Muhammed, M. C. Lemme, M. Östling, *Advanced materials* **2013**, 25, 3985.

[7] a) C. K. Chiang, C. Fincher Jr, Y. W. Park, A. J. Heeger, H. Shirakawa, E. J. Louis, S. C. Gau, A. G. MacDiarmid, *Physical review letters* **1977**, 39, 1098; b) H. Shirakawa, E. J. Louis, A. G. MacDiarmid, C. K. Chiang, A. J. Heeger, *Journal of the Chemical Society, Chemical Communications* **1977**, 578; c) R. H. Friend, *Conductive Polymers II: From Science to Applications*, iSmithers Rapra Publishing, **1993**; d) D. Kumar, R. Sharma, *European polymer journal* **1998**, 34, 1053; e) M. H. Al-Saleh, U. Sundararaj, *Carbon* **2009**, 47, 2.

[8] G. Zou, J. Yan, F. Mu, A. Wu, J. Ren, A. Hu, Y. Zhou, *Open Surface Science Journal* **2011**, 3, 70.

[9] A. Hu, J. Guo, H. Alarifi, G. Patane, Y. Zhou, G. Compagnini, C. Xu, *Applied Physics Letters* **2010**, 97, 153117.

[10] B.-J. Kim, T. Haas, A. Friederich, J.-H. Lee, D.-H. Nam, J. R. Binder, W. Bauer, I.-S. Choi, Y.-C. Joo, P. A. Gruber, *Nanotechnology* **2014**, 25, 125706.

[11] a) P. Peng, A. Hu, A. P. Gerlich, G. Zou, L. Liu, Y. N. Zhou, *ACS Appl. Mater. Interfaces* **2015**, 7, 12597; b) J. Liang, K. Tong, Q. Pei, *Adv Mater* **2016**, DOI: 10.1002/adma.201600772; c) Y. Zhang, H. Dai, *Applied Physics Letters* **2000**, 77, 3015; d) B. H. Hong, S. C. Bae, C.-W. Lee, S. Jeong, K. S. Kim, *Science* **2001**, 294, 348.

[12] M. Kanzaki, Y. Kawaguchi, H. Kawasaki, *ACS Appl. Mater. Interfaces* **2017**, 9, 20852.

[13] M. Zenou, O. Ermak, A. Saar, Z. Kotler, *Journal of physics D: Applied physics* **2013**, 47, 025501.

[14] J. Ryu, H.-S. Kim, H. T. Hahn, *Journal of Electronic Materials* **2011**, 40, 42.

[15] S.-J. Joo, S.-H. Park, C.-J. Moon, H.-S. Kim, *ACS Appl. Mater. Interfaces* **2015**, 7, 5674.

[16] Y.-T. Hwang, W.-H. Chung, Y.-R. Jang, H.-S. Kim, *ACS Appl. Mater. Interfaces* **2016**, 8, 8591.

[17] a) L. Jiang, Virginia Tech, **2010**; b) J. G. Bai, G.-Q. Lu, *IEEE Transactions on device and materials reliability* **2006**, 6, 436; c) S.-P. Chen, Z.-K. Kao, J.-L. Lin, Y.-C. Liao, *ACS Appl. Mater. Interfaces* **2012**, 4, 7064.

[18] a) C. Zhu, E. Chalmers, L. Chen, Y. Wang, B. B. Xu, Y. Li, X. Liu, *Small* **2019**, 1902440; b) Y. Yu, C. Yan, Z. Zheng, *Advanced Materials* **2014**, 26, 5508; c) J. Wu, R. Roberts, N. C. Tien, D. Li, presented at SENSORS, 2014 IEEE **2014**; d) R. Guo, Y. Yu, Z. Xie, X. Liu, X. Zhou, Y. Gao, Z. Liu, F. Zhou, Y. Yang, Z. Zheng, *Adv Mater* **2013**, 25, 3343; e) R. Guo, Y. Yu, Z. Xie, X. Liu, X. Zhou, Y. Gao, Z. Liu, F. Zhou, Y. Yang, Z. Zheng, *Advanced Materials* **2013**, 25, 3343; f) X. Liu, X. Zhou, Y. Li, Z. Zheng, *Chem. Asian J* **2012**, 7, 862; g) J. R. Lancaster, J. Jehani, G. T. Carroll, Y. Chen, N. J. Turro, J. T. Koberstein, *Chemistry of Materials* **2008**, 20, 6583; h) O. Azzaroni, Z. Zheng, Z. Yang, W. T. Huck, *Langmuir* **2006**, 22, 6730.

[19] a) Y. Yu, X. Xiao, Y. Zhang, K. Li, C. Yan, X. Wei, L. Chen, H. Zhen, H. Zhou, S. Zhang, Z. Zheng, *Adv Mater* **2016**, DOI: 10.1002/adma.201505119; b) K. Fukuda, T. Sekine, D. Kumaki, S. Tokito, *ACS Appl. Mater. Interfaces* **2013**, 5, 3916.

[20] a) H. Hu, R. G. Larson, *The Journal of Physical Chemistry B* **2006**, 110, 7090; b) D. Kim, S. Jeong, B. K. Park, J. Moon, *Applied Physics Letters* **2006**, 89, 264101; c) R. D. Deegan, O. Bakajin, T. F. Dupont, G. Huber, S. R. Nagel, T. A. Witten, *Nature* **1997**, 389, 827.

[21] a) P. Lin, F. Yan, H. L. Chan, *ACS Appl. Mater. Interfaces* **2010**, 2, 1637; b) G. Horowitz, *Advanced materials* **1998**, 10, 365; c) P. Lin, F. Yan, *Advanced materials* **2012**, 24, 34.

[22] Z.-T. Zhu, J. T. Mason, R. Dieckmann, G. G. Malliaras, *Applied Physics Letters* **2002**, 81, 4643.

[23] T. Ji, P. Rai, S. Jung, V. K. Varadan, *Applied Physics Letters* **2008**, 92, 208.

[24] a) Q. Zhang, V. Subramanian, *Biosensors and Bioelectronics* **2007**, 22, 3182; b) L. Jagannathan, V. Subramanian, *Biosensors and Bioelectronics* **2009**, 25, 288; c) Q. Zhang, L. Jagannathan, V. Subramanian, *Biosensors and Bioelectronics* **2010**, 25, 972.

[25] H. U. Khan, M. E. Roberts, O. Johnson, R. Förch, W. Knoll, Z. Bao, *Advanced Materials* **2010**, 22, 4452.

[26] H. S. White, G. P. Kittlesen, M. S. Wrighton, *Journal of the American Chemical Society* **1984**, 106, 5375.

[27] D. A. Bernards, G. G. Malliaras, *Advanced Functional Materials* **2007**, 17, 3538.

[28] S. Chao, M. S. Wrighton, *Journal of the American Chemical Society* **1987**, 109, 6627.

[29] S. Y. Yang, F. Cicoira, R. Byrne, F. Benito-Lopez, D. Diamond, R. M. Owens, G. G. Malliaras, *Chemical Communications* **2010**, 46, 7972.

[30] C. Liao, C. Mak, M. Zhang, H. L. Chan, F. Yan, *Advanced Materials* **2015**, 27, 676.

[31] P. Lin, X. Luo, I. Hsing, F. Yan, *Advanced Materials* **2011**, 23, 4035.

[32] V. Kantola, J. Kulovesi, L. Lahti, R. Lin, M. Zavodchikova, E. Coatanéa, *Bit Bang* **2009**, 63.

[33] H. Al-Chami, University of British Columbia, **2010**.

[34] H. Kipphan, *Handbook of print media: technologies and production methods*, Springer Science & Business Media, **2001**.

[35] C. R. Heurich, W. A. Runck, Google Patents, 1981.

[36] A. Karwa, **2006**.

[37] R. E. Nisbett, T. D. Wilson, *Journal of personality and social psychology* **1977**, 35, 250.

[38] P. Cosseddu, A. Bonfiglio, *Thin Solid Films* **2007**, 515, 7551.

[39] P. Cosseddu, Universita'degli Studi di Cagliari, **2007**.

[40] J. A. Rogers, R. G. Nuzzo, *Materials Today* **2005**, 8, 50.

[41] D. Chrisey, A. Pique, J. Fitz-Gerald, R. Auyeung, R. McGill, H. Wu, M. Duignan, *Applied surface science* **2000**, 154, 593.

[42] R. A. McGill, R. Chung, D. B. Chrisey, P. C. Dorsey, P. Matthews, A. Piqué, T. E. Mlsna, J. L. Stepnowski, *IEEE transactions on ultrasonics, ferroelectrics, and frequency control* **1998**, 45, 1370.

[43] J. Bohandy, B. Kim, F. Adrian, *Journal of Applied Physics* **1986**, 60, 1538.

[44] A. Mette, P. Richter, M. Hörteis, S. Glunz, *Progress in Photovoltaics: Research and Applications* **2007**, 15, 621.

[45] A. M. El-Toni, T. Yamaguchi, S. Shimizu, Y. Fujishiro, M. Awano, *Journal of the American Ceramic Society* **2008**, 91, 346.

[46] D. A. Berlincourt, D. R. Curran, H. Jaffe, *Physical Acoustics: Principles and Methods* **1964**, 1, 247.

[47] L. Rayleigh, *Proceedings of the London mathematical society* **1878**, 1, 4.

[48] E. Tekin, P. J. Smith, U. S. Schubert, *Soft Matter* **2008**, 4, 703.

[49] a) E. B. Secor, P. L. Prabhumirashi, K. Puntambekar, M. L. Geier, M. C. Hersam, *The journal of physical chemistry letters* **2013**, 4, 1347; b) Y. Li, L. Lan, P. Xiao, S. Sun, Z. Lin, W. Song, E. Song, P. Gao, W. Wu, J. Peng, *ACS Appl. Mater. Interfaces* **2016**, 8, 19643.

[50] P. Chen, H. Chen, J. Qiu, C. Zhou, *Nano Research* **2010**, 3, 594.

[51] K. Abe, K. Suzuki, D. Citterio, *Analytical chemistry* **2008**, 80, 6928.

[52] G. Wei, H. Zhou, Z. Liu, Y. Song, L. Wang, L. Sun, Z. Li, *The Journal of Physical Chemistry B* **2005**, 109, 8738.

[53] Y. Zhou, A. Hu, *Open Surface Science Journal* **2011**, 3, 32.

[54] P. Peng, A. Hu, Y. Zhou, *Applied Physics A* **2012**, 108, 685.

[55] Y. Zhou, W. Gale, T. North, *International Materials Reviews* **1995**, 40, 181.

[56] Y. Li, K.-s. Moon, C. Wong, *Science* **2005**, 308, 1419.

[57] J. F. Lancaster, *Metallurgy of welding*, Elsevier, **1999**.

[58] W. Qi, M. Wang, *Materials chemistry and physics* **2004**, 88, 280.

[59] J. Perelaer, B. J. de Gans, U. S. Schubert, *Advanced materials* **2006**, 18, 2101.

[60] E. C. Garnett, W. Cai, J. J. Cha, F. Mahmood, S. T. Connor, M. G. Christoforo, Y. Cui, M. D. McGehee, M. L. Brongersma, *Nat Mater* **2012**, 11, 241.

[61] T. Tokuno, M. Nogi, M. Karakawa, J. Jiu, T. T. Nge, Y. Aso, K. Suganuma, *Nano research* **2011**, 4, 1215.

[62] S. Magdassi, M. Grouchko, O. Berezin, A. Kamyshny, *ACS Nano* **2010**, 4, 1943.

[63] P. Calvert, *Chemistry of materials* **2001**, 13, 3299.

[64] C. B. Hurd, *Chemical Reviews* **1938**, 22, 403.

[65] S. Kistler, *The Journal of Physical Chemistry* **1932**, 36, 52.

[66] R. Roy, *Journal of the American Ceramic Society* **1956**, 39, 145.

[67] C. J. Brinker, G. W. Scherer, *Sol-gel science: the physics and chemistry of sol-gel processing*, Academic press, **2013**.

[68] H. Schmidt, *Journal of Non-Crystalline Solids* **1985**, 73, 681.

[69] P. J. Flory, *Principles of polymer chemistry*, Cornell University Press, **1953**.

[70] a) H. Dislich, E. Hussmann, *Thin Solid Films* **1981**, 77, 129; b) J. Livage, M. Henry, C. Sanchez, *Progress in solid state chemistry* **1988**, 18, 259; c) Ö. Ouchterlony, *APMIS* **1953**, 32, 231.

[71] M. A. B. Meador, E. F. Fabrizio, F. Ilhan, A. Dass, G. Zhang, P. Vassilaras, J. C. Johnston, N. Leventis, *Chemistry of Materials* **2005**, 17, 1085.

[72] J. Zarzycki, *Journal of Sol-Gel Science and Technology* **1997**, 8, 17.

[73] G. W. Scherer, *Journal of the American Ceramic Society* **1990**, 73, 3.

[74] T. Shaw, *Journal of the American Ceramic Society* **1986**, 69, 27.

[75] R. Dwivedi, *Journal of materials science letters* **1986**, 5, 373.

[76] T. Kawaguchi, J. Iura, N. Taneda, H. Hishikura, Y. Kokubu, *Journal of Non-Crystalline Solids* **1986**, 82, 50.

[77] C. Brinker, W. Drotning, G. Scherer, *MRS Online Proceedings Library Archive* **1984**, 32.

[78] J.-K. Hong, H.-S. Yang, M.-H. Jo, H.-H. Park, S.-Y. Choi, *Thin Solid Films* **1997**, 308, 495.

[79] R. D. Deegan, *Physical review E* **2000**, 61, 475.

[80] D. Soltman, V. Subramanian, *Langmuir* **2008**, 24, 2224.

[81] X. Shen, C.-M. Ho, T.-S. Wong, *The Journal of Physical Chemistry B* **2010**, 114, 5269.

[82] L. Cui, Y. Li, J. Wang, E. Tian, X. Zhang, Y. Zhang, Y. Song, L. Jiang, *Journal of Materials Chemistry* **2009**, 19, 5499.

[83] T. P. Bigioni, X.-M. Lin, T. T. Nguyen, E. I. Corwin, T. A. Witten, H. M. Jaeger, *Nat Mater* **2006**, 5, 265.

[84] M. Anyfantakis, Z. Geng, M. Morel, S. Rudiuk, D. Baigl, *Langmuir* **2015**, 31, 4113.

[85] P. J. Yunker, T. Still, M. A. Lohr, A. Yodh, *Nature* **2011**, 476, 308.

[86] W. Ristenpart, P. Kim, C. Domingues, J. Wan, H. Stone, *Physical Review Letters* **2007**, 99, 234502.

[87] J. A. Lim, W. H. Lee, H. S. Lee, J. H. Lee, Y. D. Park, K. Cho, *Advanced functional materials* **2008**, 18, 229.

[88] M. Majumder, C. S. Rendall, J. A. Eukel, J. Y. Wang, N. Behabtu, C. L. Pint, T.-Y. Liu, A. W. Orbaek, F. Mirri, J. Nam, *The Journal of Physical Chemistry B* **2012**, 116, 6536.

[89] H.-Y. Ko, J. Park, H. Shin, J. Moon, *Chemistry of materials* **2004**, 16, 4212.

[90] M. Kuang, J. Wang, B. Bao, F. Li, L. Wang, L. Jiang, Y. Song, *Advanced Optical Materials* **2014**, 2, 34.

[91] B. Su, C. Zhang, S. Chen, X. Zhang, L. Chen, Y. Wu, Y. Nie, X. Kan, Y. Song, L. Jiang, *Advanced Materials* **2014**, 26, 2500.

[92] M. Layani, M. Gruchko, O. Milo, I. Balberg, D. Azulay, S. Magdassi, *ACS Nano* **2009**, 3, 3537.

[93] Z. Zhang, X. Zhang, Z. Xin, M. Deng, Y. Wen, Y. Song, *Advanced Materials* **2013**, 25, 6714.

[94] J. Stringer, B. Derby, *Journal of the European Ceramic Society* **2009**, 29, 913.

[95] P. Q. Nguyen, L.-P. Yeo, B.-K. Lok, Y.-C. Lam, *ACS Appl. Mater. Interfaces* **2014**, 6, 4011.

[96] J. Wang, Z. Zheng, H. Li, W. Huck, H. Sirringhaus, *Nat Mater* **2004**, 3, 171.

[97] L. Wu, Z. Dong, M. Kuang, Y. Li, F. Li, L. Jiang, Y. Song, *Advanced Functional Materials* **2015**, 25, 2237.

[98] A. Mahajan, W. J. Hyun, S. B. Walker, J. A. Lewis, L. F. Francis, C. D. Frisbie, *ACS Appl. Mater. Interfaces* **2015**, 7, 1841.

[99] D. Stüwe, D. Mager, D. Biro, J. G. Korvink, *Advanced Materials* **2015**, 27, 599.

[100] H. Dong, W. W. Carr, J. F. Morris, *Physics of fluids* **2006**, 18, 072102.

[101] a) S. Bull, D. Rickerby, *Surface and Coatings Technology* **1990**, 42, 149; b) S.-Y. Chang, H.-L. Chang, Y.-C. Lu, S.-M. Jang, S.-J. Lin, M.-S. Liang, *Thin Solid Films* **2004**, 460, 167.

[102] https://www.polyu.edu.hk/umf/facility/cleanrooms/96-probe-station-with-semiconductor-parameter-analyzer/, accessed.

[103] H. Tang, F. Yan, P. Lin, J. Xu, H. L. Chan, *Advanced Functional Materials* **2011**, 21, 2264.

[104] H. Kang, H. Park, Y. Park, M. Jung, B. C. Kim, G. Wallace, G. Cho, *Scientific reports* **2014**, 4, 5387.

[105] J. Hast, M. Tuomikoski, R. Suhonen, K. L. Väisänen, M. Välimäki, T. Maaninen, P. Apilo, A. Alastalo, A. Maanineny, presented at SID Symposium Digest of Technical Papers **2013**.

[106] a) S. Brady, K. Lau, W. Megill, G. Wallace, D. Diamond, *Synthetic metals* **2005**, 154, 25; b) J. R. Windmiller, J. Wang, *Electroanalysis* **2013**, 25, 29.

[107] D.-Y. Shin, Y. Lee, C. H. Kim, *Thin Solid Films* **2009**, 517, 6112.

[108] X. Liu, X. Zhou, Y. Li, Z. Zheng, *Chem Asian J* **2012**, 7, 862.

[109] O. Prucker, C. A. Naumann, J. Rühe, W. Knoll, C. W. Frank, *Journal of the American Chemical Society* **1999**, 121, 8766.

[110] J. Byerley, W. Teo, *Canadian Journal of Chemistry* **1969**, 47, 3355.

[111] P. Li, Y. Zhang, Z. Zheng, *Advanced Materials* **2019**, 1902987.

[112] K. Tanaka, K. Gunji, T. Katayama, *Computer Methods and Experimental Measurements for Surface Effects and Contact Mechanics VIII* **2007**, 55, 303.

[113] P. Burnett, D. Rickerby, *Thin solid films* **1987**, 154, 403.

[114] J. Ye, N. Kojima, K. Ueoka, J. Shimanuki, T. Nasuno, S. Ogawa, *Journal of applied physics* **2004**, 95, 3704.

[115] D. Stojanović, A. Orlović, M. Zrilić, I. Balać, C. Tang, P. Uskoković, R. Aleksić, *Polymer composites* **2013**, 34, 1710.

[116] G. Pharr, *Materials Science and Engineering: A* **1998**, 253, 151.

[117] W. C. Oliver, G. M. Pharr, *Journal of materials research* **1992**, 7, 1564.

[118] a) A. Ternovskii, V. Alekhin, M. K. Shorshorov, M. Khrushchev, V. Skvortsov, *Zavodskaya Laboratoriya* **1973**, 39, 20; b) S. Bulychev, V. Alekhin, M. K. Shorshorov, A. Ternovskij, G. Shnyrev, *Zavodskaya Laboratoriya* **1975**, 41, 1137.

[119] A.-Y. Jee, M. Lee, *Polymer Testing* **2010**, 29, 95.

[120] B. Briscoe, L. Fiori, E. Pelillo, *Journal of Physics D: Applied Physics* **1998**, 31, 2395.

[121] B. R. Lawn, A. G. Evans, D. Marshall, *Journal of the American Ceramic Society* **1980**, 63, 574.

[122] M. Ayatollahi, A. Karimzadeh, *International journal of fracture* **2012**, 175, 193.

[123] G. Anstis, P. Chantikul, B. R. Lawn, D. Marshall, *Journal of the American Ceramic Society* **1981**, 64, 533.

[124] a) R. Keller, J. Phelps, D. Read, *Materials Science and Engineering: A* **1996**, 214, 42; b) H. Hirakata, O. Nishijima, N. Fukuhara, T. Kondo, A. Yonezu, K. Minoshima, *Materials Science and Engineering: A* **2011**, 528, 8120.

[125] a) H.-C. Tsai, Y.-S. Chang, S.-Y. Chang, *Microelectronic Engineering* **2008**, 85, 1658; b) A. Volinsky, N. Moody, W. Gerberich, *Acta materialia* **2002**, 50, 441.

[126] L. Qian, M. Li, Z. Zhou, H. Yang, X. Shi, *Surface and Coatings Technology* **2005**, 195, 264.

[127] P. Ilgin, H. Durak, A. Gür, *Polymer-Plastics Technology and Engineering* **2015**, 54, 603.

[128] L. He, M. Janner, Q. Lu, M. Wang, H. Ma, Y. Yin, *Advanced Materials* **2015**, 27, 86.

[129] L. Cui, J. Zhang, X. Zhang, L. Huang, Z. Wang, Y. Li, H. Gao, S. Zhu, T. Wang, B. Yang, *ACS Appl. Mater. Interfaces* **2012**, 4, 2775.

[130] T. M. D. Dang, T. T. T. Le, E. Fribourg-Blanc, M. C. Dang, *Advances in Natural Sciences: Nanoscience and Nanotechnology* **2011**, 2, 015009.

[131] H. Sirringhaus, T. Kawase, R. Friend, T. Shimoda, M. Inbasekaran, W. Wu, E. Woo, *Science* **2000**, 290, 2123.

[132] Y.-Y. Noh, N. Zhao, M. Caironi, H. Sirringhaus, *Nature nanotechnology* **2007**, 2, 784.

[133] W. R. Cox, T. Chen, C. Guan, D. J. Hayes, R. E. Hoenigman, B. T. Teipen, D. L. MacFarlane, presented at OSA Diffractive Optics and Micro-Opticas Topical Meeting (Hawaii) **1998**.

[134] D. Jang, D. Kim, J. Moon, *Langmuir* **2009**, 25, 2629.

[135] I. Mejia, M. Estrada, M. Avila, *Microelectronics Reliability* **2008**, 48, 1795.